

White Dwarfs in the SPY and HQS Surveys

An Analysis of a Large Set of White Dwarf Spectra and a
Search for Variable ZZ Ceti White Dwarfs

Dissertation
zur Erlangung des Doktorgrades
der Mathematisch-Naturwissenschaftlichen Fakultät
der Christian-Albrechts-Universität
zu Kiel

vorgelegt von
Björn Voss

Kiel
2006

Referent: Prof. Dr. D. Koester

Koreferent: Prof. Dr. R. Wimmer-Schweingruber

Tag der mündlichen Prüfung: 5. Juli 2006

Zum Druck genehmigt: Kiel, 19. Juli 2006

Der Dekan

Abstract

White dwarfs are the final evolutionary stage of 99% of all stars and thus among the most common stellar objects. Their study can reveal information about their progenitor main sequence stars, and white dwarfs are an important tool for different kinds of astrophysical studies, e.g., in the determination of cosmological parameters. In the last years a large amount of data on White Dwarfs has been gathered by different surveys, and the data of one of these survey projects, “SPY”, are analysed in this thesis. The SPY spectra are characterized by an especially high resolution compared to the data of other recent investigations of white dwarfs. Thus, they allow the so far most sensitive study of weak spectral features in a large set of white dwarf spectra. Among the results that are obtained only because of the high spectral resolution are the discoveries of several helium-atmosphere white dwarfs with small admixtures of hydrogen in their atmospheres, and of a hot helium-atmosphere white dwarf that weakly exhibits HeII in its spectrum which is a novel feature for white dwarfs of this type.

Another main focus of the SPY analysis is the assembly of a catalogue of parameters of about 750 white dwarfs, the largest white dwarf sample that has so far been studied using high-resolution spectra. A χ^2 fitting routine is used to fit white dwarf model spectra to the SPY data, and parameters of the stellar atmospheres are obtained from the fits.

Such a catalogue can be employed to select white dwarfs with certain temperatures at which they are expected to exhibit pulsations. These pulsating white dwarfs of the ZZ Ceti type are interesting objects since the study of their pulsations allows to investigate the interior structure of the stars. The second part of this thesis therefore aims at a considerable increase of the known sample of such pulsating white dwarfs.

Candidate ZZ Ceti stars are identified based on the atmosphere parameters of the SPY objects, as well as from the data of another survey, the Hamburg Quasar Survey (HQS). The HQS data are coarse and do not allow a direct identification of probable pulsators. Therefore, photometric observations of a large number of HQS stars are carried out and analysed, yielding more precise stellar parameters for these objects.

The resulting sample of probable ZZ Ceti stars, selected from both the SPY and HQS stars, is studied in time-resolved photometric observations. 15 new variables of this kind are discovered, increasing the known sample of bright ($B < 17$) stars of this kind by 50%.

Zusammenfassung

Weißer Zwerge sind die Endstadien der Entwicklung von 99% aller Sterne, und damit eine der häufigsten Arten von Sternen. Die Untersuchung Weißer Zwerge kann Informationen über ihre Vorläufer, die Hauptreihen-Sterne, ergeben, und Weißer Zwerge sind wichtige Werkzeuge astrophysikalischer Studien verschiedener Art, z.B. in der Ermittlung kosmologischer Parameter. In den letzten Jahren wurde in diesem Zusammenhang eine große Menge von Daten Weißer Zwerge in verschiedenen Durchmusterungen gesammelt, und die Daten eines dieser Projekte, "SPY", werden in dieser Arbeit analysiert. Ein wesentliches Merkmal der SPY-Spektren ist ihre im Vergleich zu den Daten anderer bisheriger Studien sehr hohe Auflösung. Daher ermöglichen die Spektren die bisher empfindlichste Untersuchung schwach ausgeprägter spektraler Merkmale anhand eines großen Datensatzes von Spektren Weißer Zwerge. Unter den Ergebnissen die dank der hohen spektralen Auflösung erzielt wurden ist die Entdeckung zahlreicher Weißer Zwerge mit heliumreichen Atmosphären die Spuren von Wasserstoff enthalten, sowie eines heißen Weißen Zwerge mit heliumreicher Atmosphäre, dessen Spektrum eine schwach ausgeprägte HeII-Linie aufweist; ein Merkmal das bei solchen Sternen bisher nicht gefunden wurde.

Ein weiteres Ziel der Analyse der SPY-Daten ist die Erstellung eines Katalogs von Parametern von etwa 750 Weißen Zwergen, der bisher größten Sammlung von Daten Weißer Zwerge die aus Spektren hoher Qualität ermittelt wurden. Eine χ^2 -Fit-Routine wurde eingesetzt um Modellspektren Weißer Zwerge an die SPY-Daten anzupassen und daraus Parameter der Atmosphären abzuleiten.

Aus einem solchen Katalog können Weißer Zwerge in einem bestimmten Temperaturbereich ausgewählt werden, innerhalb dessen sie Pulsationen aufweisen sollten.

Solche pulsierenden Weißen Zwerge des ZZ-Ceti-Typs sind interessante Objekte, da aus einer Untersuchung der Pulsationen Erkenntnisse über den inneren Aufbau dieser Sterne gewonnen werden können. Der zweite Teil dieser Arbeit hat daher eine Erweiterung der bekannten Anzahl solcher variabler Weißer Zwerge zum Ziel.

Vermutlich pulsierende Weißer Zwerge wurden anhand der Atmosphären-Parameter der SPY-Objekte ausgewählt, sowie aus den Daten einer weiteren Durchmusterung, dem Hamburg Quasar Survey (HQS), ermittelt. Die HQS-Daten sind zu grob als daß sie eine direkte Auswahl wahrscheinlicher ZZ-Ceti-Sterne ermöglichen würden. Daher wurden photometrische Beobachtungen einer großen Anzahl von Sternen des HQS durchgeführt und aus den Beobachtungsdaten wurden genauere Parameter dieser Weißen Zwerge bestimmt.

Die sich ergebende Auswahl wahrscheinlicher ZZ-Ceti-Sterne, basierend auf den SPY- und auf den HQS-Daten, wurde schließlich in zeitaufgelösten photometrischen Beobachtungen untersucht. 15 neue ZZ-Ceti-Sterne wurden entdeckt, was eine Vergrößerung der

bekannten Anzahl hellerer Sterne dieser Art ($B < 17$) um 50% darstellt.

Contents

Abstract	iii
Zusammenfassung	v
I Introduction	1
1 White Dwarfs	3
1.1 Formation and Basic Characteristics of White Dwarfs	3
1.2 Observational Properties of White Dwarfs	5
1.3 The Analysis of White Dwarfs in the SPY Survey	7
1.4 White Dwarfs in the HQS Survey	7
1.5 ZZ Ceti Stars	9
1.6 Observations of ZZ Ceti Stars	10
II SPY	13
2 The SPY Project	15
2.1 A Search for Supernova Ia Progenitors	15
2.2 This Work: A Re-use of the SPY Data	15
2.3 The SPY Observations	16
2.4 Data Reduction	17
3 Overview of the Analysis Method	19
3.1 The Model Spectra	20
3.2 The Fitting Routine	21
3.3 Adjustment of the Models to the Continuum	23
3.4 Different Fitting Solutions for each Object	24
3.5 The Analysis Pipeline	25
4 Results of the DA Star Fits	27
4.1 Fit Uncertainties	31
4.2 Comparison with other Investigations	32
4.3 The Influence of Continuum Level Changes	34
4.4 Comparison to Koester et al. 2001	36
4.5 DA Mass Distribution	38

4.6	DA+dM Binaries	42
4.7	Identification of Probable New ZZ Ceti Stars	43
5	DB Star Fit Results	47
5.1	Remarks on DBA, Cool DB, and DB+dM Fits	47
5.2	DB Fit Accuracy	48
5.3	DB Masses	49
6	Objects Without Model Fits	51
7	Comments on Individual Objects	53
7.1	Magnetic DA Stars	53
7.2	Peculiar Helium-rich White Dwarfs	59
7.3	Subdwarf Stars	63
8	New White Dwarfs	65
III Search for ZZ Ceti Candidate Stars Among the HQS Objects		67
9	Calar Alto 1.23m Observations	69
9.1	Layout of the Observations	69
9.2	Data Reduction	71
9.3	Data Analysis	71
9.4	Results of the 1.23 m observations	74
10	BUSCA Observations	79
10.1	Photometry versus Spectroscopy	79
10.2	BUSCA	81
10.3	The Observations	83
10.4	Reduction of the BUSCA Data	84
11	Analysis of the BUSCA photometry	85
11.1	Correction for Effects of the Atmosphere	85
11.2	Correction for Instrumental Effects	86
11.3	$u - b$ vs. $b - y$ Analysis	87
11.4	$u - b$ vs. $b - I$ Analysis	91
IV Lightcurve Observations of New ZZ Ceti Stars		101
12	Early Lightcurve Observation Attempts	103
12.1	Three New Variables from Observations by Collaborators	103
12.2	Observations at Observatoire Haute-Provence	103

13 The NOT Observations	105
13.1 Setup of the Observations	105
13.2 Data Reduction and Analysis	106
13.3 Observing Conditions	109
14 The NOT Results: 12 New ZZ Ceti Variables	113
14.1 Overview of the New Variables	113
14.2 NOV Objects	113
14.3 Individual Discussion of the New ZZ Ceti Stars	115
14.4 Results and Discussion	121
15 Summary and Outlook	127
A Hydrogen Atmosphere Fit Results	129
B Fit Results for DA+dM Composite Spectra	141
C Helium Atmosphere Fit Results	145
D List of Objects without a Fit	149
E CA 1.23m observation log	153
F Results of the BUSCA Observations: Parameters for 223 New WD	155
G Graphical Representation of the SPY Spectra Fits	161
G.1 DA Stars	161
G.2 DA+dM Binaries	217
G.3 DB Stars	221
G.4 DBA Stars	231

List of Figures

1.1	Stellar evolution and the formation of white dwarfs	4
1.2	An example HQS objective prism spectrum	8
2.1	Example SPY DA spectrum	17
2.2	Example SPY DB spectrum	18
3.1	DA model spectra	21
3.2	DB model spectra	22
4.1	Examples of typical spectra	29
4.2	Examples of spectra with problematic fits	30
4.3	Comparison of $\log g$ from two spectra of an object	32
4.4	Comparison of T_{eff} from two spectra of an object	33
4.5	Comparison with literature T_{eff} & $\log g$	35
4.6	Comparison of T_{eff} with Koester et al. 2001	37
4.7	Comparison of $\log g$ with Koester et al. 2001	38
4.8	The DA mass distribution	40
4.9	The smoothed DA mass distribution	41
4.10	DA masses with respect to temperature	42
4.11	Example fits of DA+dM binaries	43
4.12	DA stars in and near the ZZ Ceti instability strip	45
5.1	DB and DBA mass distributions	50
7.1	The spectrum of HS 1031+0343	54
7.2	The $H\beta$ Zeeman triplet of HS 1031+0343	55
7.3	Zeeman triplets of two DAH stars from Koester et al. (2001)	56
7.4	$H\alpha$ triplets of four other known weak-field DAH stars	58
7.5	Zeeman triplets of the three new DAH stars with weak fields	59
7.6	The split $H\alpha$ line of WD 0453–295	60
7.7	The spectrum of the DAB HE 2149–0516	61
7.8	The full spectrum of the cool DO star WD 2142–169	62
7.9	The central part of the spectrum of the cool DO star WD 2142–169	63
9.1	CA 1.23 m time-series photometry of known variables	75
9.2	Distribution of the CA1.23m observations with respect to the variability indicators	77

10.1	Two-color diagram with the Strömgen colors of known ZZ Ceti stars . . .	81
10.2	The transmission curves of the BUSCA dichroics	82
11.1	The transmission curves of the BUSCA filters	87
11.2	The quantum efficiency of the BUSCA CCDs	88
11.3	Fits of the BUSCA to the Strömgen data points	90
11.4	The model atmosphere grids for $u - b$ vs. $b - y$	91
11.5	The results of the $u - b$ vs. $b - y$ analysis	92
11.6	The calibration of the first run data	94
11.7	The calibration of the second run data	95
11.8	The calibration of the third run data	96
11.9	The calibration of the fourth run data	96
11.10	The calibration of the fifth run data	97
11.11	The calibrated observation results of the first run	97
11.12	The calibrated observation results of the second run	98
11.13	The calibrated observation results of the third run	98
11.14	The calibrated observation results of the fourth run	99
11.15	The calibrated observation results of the fifth run	99
11.16	The observed ZZ Ceti and nonvariable stars	100
13.1	Example display of time-series imaging data	106
13.2	The FTs of individual target-reference combinations	110
13.3	Differential and absolute magnitude with thin clouds	111
14.1	Lightcurve and FT of WD 1342–237	117
14.2	The FTs of HS1441+3219: An indication of possible variations	118
14.3	The FT of HS1625+1231	118
14.4	Changes in the FT of HS 0733+4119	120
14.5	Changes in the FT of HE 0344–1207	121
14.6	Lightcurves and FTs of the 7 new ZZ Ceti stars of the first run	122
14.7	Lightcurves and FTs of the 5 new ZZ Ceti stars of the second run	123
14.8	The temperatures and gravities of the new variables and NOV objects . . .	125
14.9	The temperatures and gravities of the cDAV and hDAV variables	126

List of Tables

1.1	Spectral Types of White Dwarfs	6
3.1	Spectral intervals of the fitting process	25
4.1	Objects with hydrogen model fits	28
4.2	Comparison with literature T_{eff} & $\log g$	34
4.3	Tests of the effects of continuum level changes	36
4.4	Comparison to the results of Koester et al. 2001	37
5.1	Properties of the DB mass distribution	50
6.1	Objects without a fit: Numbers per type	51
7.1	DAH field strengths derived from the SPY spectra	60
8.1	New white dwarfs	66
9.1	Probable ZZ Ceti stars detected in the CA 1.23 m observations	76
10.1	Log of the BUSCA observation runs	83
11.1	The “grid transformation”	89
12.1	Properties of the targets observed at OHP	104
13.1	Properties of the targets observed at the NOT	107
13.2	NOT observing log	108
14.1	Pulsation properties of the new ZZ Ceti stars	114
14.2	NOV objects	116
A.1	Fit results for hydrogen atmosphere stars	130
B.1	Fit results for DA+dM binaries	142
C.1	Fit results for stars with He atmosphere fits	146
D.1	Individual listing of objects without a fit	150
E.1	CA 1.23 m Observation Log	154

F.1 BUSCA observations results 156

Part I
Introduction

Chapter 1

White Dwarfs

White dwarfs are the endpoints of the evolution of 99% of all stars. When stars with masses less than $\sim 7 M_{\odot}$ (solar masses, $M_{\odot} = 1.989 \times 10^{33}$ g) leave the main sequence they form dense cores composed of Carbon and Oxygen that are subsequently exposed when the stars lose their hydrogen-rich envelopes. These exposed Carbon-Oxygen (CO-) cores, which retain only very thin helium or hydrogen surface layers, are the white dwarfs.

1.1 Formation and Basic Characteristics of White Dwarfs

The evolution of a star to the final white dwarf stadium is shown in Fig. 1.1. Stars on the main sequence are stabilized against the compressing force of gravity by the energy release from central hydrogen fusion. This is a long lasting evolutionary phase, of about 9×10^9 years for a star of one solar mass. The following phases in which the central hydrogen fusion is replaced by a succession of other fusion sources are of much shorter duration. First, after the core becomes depleted of hydrogen, H fusion takes place in a shell around the core. As a consequence, the stellar luminosity is multiplied while the effective temperature of the surface is reduced. The star becomes a “red giant” with an increasingly hot and degenerate helium core. At a certain threshold core temperature, helium fusion in the degenerate core is ignited explosively (“helium flash”) and the star quickly changes its structure. The luminosity of the resulting star with central helium fusion is smaller than that in the preceding red giant phase, and the temperature is higher. These stars are found on the so-called “horizontal branch” in the temperature-luminosity diagram (Fig. 1.1). For most stars, the development from the main sequence to a red giant is then repeated, now starting from the horizontal branch: After depletion of the helium in the stellar core, helium fusion takes place in a shell around the core and the stellar luminosity is strongly enhanced once more, again at decreasing temperature. The star is now found in the so-called “asymptotic giant branch” (AGB) phase. This short evolutionary phase is characterized by a succession of alternating episodes of helium and hydrogen shell fusion, the “thermal pulses”. The outer layers become unstable in this phase and strong mass loss occurs, by up to $\dot{M} = 10^{-4} M_{\odot} \text{ yr}^{-1}$. When the hot core, now composed of the helium fusion products C and O, becomes exposed, the star evolves at constant luminosity towards exceedingly high temperatures ($T_{\text{eff}} > 10^5$ K) of the visible surface. The H/He envelope is almost completely lost when the “planetary nebula” phase

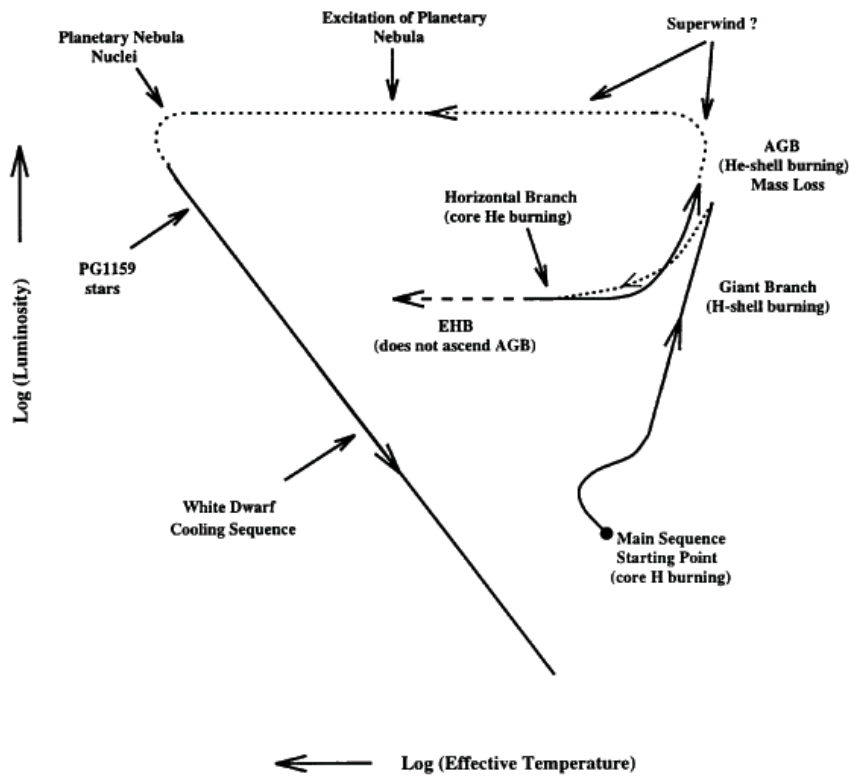


Figure 1.1: The evolutionary path of a star from the main sequence to the final stage on the white dwarf cooling sequence. Stars evolve very quickly in some phases, and can thus not easily be observed in these stages. The corresponding parts of the evolutionary track are shown as dotted lines. (taken from Bannister 2001)

is reached. Subsequently, the star is devoid of any nuclear energy sources. The star is now in its final and longest lasting evolutionary stage, as a White Dwarf. It slowly shrinks and cools, evolving towards increasingly low luminosities and temperatures along the “white dwarf cooling track”, on timescales of several 10^9 years. White dwarfs are thus found over a broad range of temperatures, from $\sim 10^5$ K to a few times 10^3 K. They will cool down to even lower temperatures, eventually becoming hypothetical “black dwarfs”, but since the age of the universe poses an upper limit on the age of white dwarfs and thus a lower limit on their cooling temperature, none have yet been able to cool to temperatures below 2000 K.

Most white dwarfs are found to have masses close to $0.6 M_{\odot}$, i.e., the progenitor star has lost most of its mass in its AGB evolutionary phase. The remaining mass is concentrated in a volume of about $\sim 10^{-6}$ of that of the star on the main sequence. The density of a white dwarf is thus very high, typically $1.5 \times 10^7 \text{ g cm}^{-3}$ in the center. At these densities the matter is fully ionized and the electrons are relativistically degenerate. Their degeneracy pressure is the counteracting force that balances gravity in white dwarfs. An equilibrium is only possible for white dwarfs of masses smaller than $1.44 M_{\odot}$, the Chandrasekhar limiting mass, named after its discoverer. For even more massive stellar cores, inverse beta decay will occur, creating a neutron star as the final evolutionary stage.

Considering their high densities, white dwarfs are “laboratories” in which matter at extreme conditions can be studied. In fact, when the nature of the first white dwarfs was discovered in the early 20th century, these stars provided the first proof that matter can exist in such a state.

The degeneracy causes an inverse relationship of stellar mass and radius, unlike that of non-degenerate stars, $R \propto M^{-1/3}$. Thus, massive White Dwarfs have smaller radii than less massive ones. The radii of White Dwarfs are typically $\sim 1.5 \times 10^{-2} R_{\odot}$ (solar radii, $R_{\odot} = 6.96 \times 10^{10}$ cm). When they shrink and cool, the radius changes only by a small amount, and thus the decreasing luminosity mainly depends on the decreasing temperature, $L \propto T_{\text{eff}}^4$. The luminosities of white dwarfs range over several orders of magnitude, from more than $10 L_{\odot}$ for the youngest and rarest objects down to less than $10^{-4} L_{\odot}$ (solar luminosities, $L_{\odot} = 3.826 \times 10^{33}$ erg s $^{-1}$).

Besides the interest in white dwarfs themselves, they are employed as important tools in different kinds of astrophysical investigations. The age of a stellar population, e.g., that of the disk of the Milky Way galaxy, or that of a stellar cluster, can be determined from the ages of the oldest White Dwarfs in the population. Cool white dwarfs are believed to provide a share of the dark matter in the universe, and this can be investigated in studies of cool White Dwarfs in the halo of the Milky Way galaxy. Furthermore, white dwarfs are the progenitors of Supernovae of the type Ia, which in turn are important for cosmological research (see chapter 3), and thus white dwarfs play a role in the recent determination of cosmological parameters.

1.2 Observational Properties of White Dwarfs

White dwarfs do retain a tiny fraction of the former stellar envelope, i.e., they have a thin atmosphere comprising about 10^{-2} of the stellar mass that is composed either of helium, or of both hydrogen and helium. Therefore, the CO cores can not be observed directly, but only the atmospheres. The outer layer of the atmosphere that can be observed is normally composed of one element only, He or H, because gravitational separation causes the lightest element to float on top of the atmosphere. Thus, only absorption lines of either hydrogen or helium are seen in the spectra of most white dwarfs. The lines are strongly broadened by the high surface gravity of typically $g \sim 10^8$. Trace elements are found in the spectra of some white dwarfs, which can either be accreted from the interstellar medium (e.g., hydrogen can be accreted and appear as trace constituent of a helium layer, or Ca may be accreted and may show CaII lines in hydrogen atmospheres), or mixed up into the atmosphere by convection that occurs in cooler white dwarfs (e.g., Carbon bands are found in some cool White Dwarf spectra). Furthermore, heavy elements can be radiatively levitated in the atmospheres of hot white dwarfs. Thus, although about 80% of the White Dwarfs show only Balmer lines in their optical spectra, there are several other types of white dwarf spectra for which a classification system has been developed by Sion et al. (1983). In this classification system, the first letter “D” in each type designation stands for a degenerate star, followed by a letter that describes the principal features of the optical spectra. The types according to this classification system are listed in table 1.1.

A second letter may be appended to indicate secondary spectral features. Common types of this kind are DBA stars, i.e., helium atmosphere white dwarfs with an admix-

Table 1.1: Spectral Types of White Dwarfs

Type	Description
DA	Balmer lines only, the most frequent type
DB	Lines of neutral helium only
DO	Lines of neutral and ionized helium
DQ	Carbon features, i.e., either C ₂ bands or atomic carbon lines
DZ	“Metal” lines, i.e., such of any element heavier than He, except C
DC	Featureless spectra

ture of hydrogen, or DAZ/DBZ/DBAZ stars, i.e., White Dwarfs that have accreted metals from the interstellar medium. Other combination types, e.g., DAB, or DAO, also exist but are less frequent. It is important to note that the principal feature in the spectrum is not always the main constituent of the atmosphere, which is always either H or He. Therefore, the DC, DQ, and DZ types are in fact white dwarfs with a helium atmosphere and with temperatures below $\sim 10\,000$ K, at which He is not visible in the spectra. Concerning the He-atmosphere types, there is thus an evolutionary cooling sequence from DO to DB to DC/DQ/DZ, and one would expect the DO population to smoothly transition to that of the DB stars at temperatures around $38\,000$ K below which HeII becomes invisible in the spectra. This is however not the case; DO stars are only found at temperatures $T_{\text{eff}} > 45\,000$ K, and DB stars only with $T_{\text{eff}} < 30\,000$ K. In between lies the region of the so-called “DB gap” where no helium-atmosphere white dwarfs are found. It is currently not certain why this is the case. One possible explanation is that even the seemingly hydrogen-devoid DO and DB stars do have a small fraction of hydrogen in their atmospheres which only floats up and forms an opaque layer, rendering the He invisible, in the DB gap temperature region. At higher and cooler temperatures, the trace amount of hydrogen would not be spectroscopically visible either because gravitational separation is not yet finished (in the DO), or because the hydrogen is mixed into the much thicker He layer by the onset of convection in the cooling atmosphere. This scenario would however require a very small fine-tuned amount of the hydrogen in such stars, which is difficult to reconcile with the results of stellar evolution calculations.

In addition to the classification of the spectra based on their constituents, the letters “H” or “P” may be appended if the spectra either show a Zeeman splitting or a polarisation of the spectral lines, due to the presence of a magnetic field. Furthermore, the letter “V” is employed to indicate a variable white dwarf, i.e., one that exhibits nonradial pulsations which is generally the case for DB stars at temperatures around $23\,000$ K and for DA stars in the so-called ZZ Ceti instability strip at temperatures of about $11\,000 - 12\,000$ K.

Important for the study of white dwarfs is the determination of parameters of their atmospheres, i.e., temperatures and surface gravities. These can be derived either by sampling the spectrum at certain wavelengths and analysing the so-obtained stellar “colours” (see chapter 10), or by recording the full spectrum and analysing the strength and shape of the H or He absorption lines (see chapter 3). Both techniques have been employed in different parts of this work. Subsequently, derived quantities like the stellar mass can be computed using the known theoretical relation of mass and radius, as well as the theoretical cooling tracks. The first part of this work is an analysis of this kind that was conducted

for a large set of White Dwarf spectra of high resolution that had been obtained in the course of the “SPY” survey project.

1.3 The Analysis of White Dwarfs in the SPY Survey

SPY is a radial velocity survey that was designed to identify binary White Dwarf systems and determine their properties. An atmosphere analysis based on the spectra was not the original aim of that project, but the data proved to be well suited for such a study, and contain a wealth of information on white dwarfs of different types. The main motivations for such an analysis of the SPY spectra are the amount of data, which is larger than that of any other study of white dwarf spectra so far, except that of the SDSS survey, and the resolution of the SPY spectra which is higher than that of other studies that investigate an appreciable number of white dwarfs.

The SPY data are described in chapter 2, and the analysis method is presented in chapter 3: Model spectra for DA, DB, and DBA white dwarfs were fitted to the data, using a χ^2 fitting routine. The fit results are presented in chapters 4 and 5, for the DA and DB stars, respectively, and in chapter 6 the white dwarfs of other types for which no fit results were obtained are summarized. A catalogue of temperatures, gravities, and masses of the 750 DA and DB white dwarfs was created from the fit results, and the mass distributions of both types of stars are discussed. Among the DA stars, several objects that are placed in the region of the ZZ Ceti instability strip and that are thus probable new variable white dwarfs are found. Among the helium-atmosphere stars, a large number with small traces of hydrogen in the atmosphere is found. These DBA stars are more numerous than it had been found so far in other studies, due to the high spectral resolution of the SPY data that allows to detect comparatively small traces of hydrogen.

In addition to the model atmosphere fit results, a visual inspection of all spectra was carried out to identify possible peculiarities. Some such objects with special features are discussed in chapter 8. Among these are ten magnetic DA stars for which the field strengths are derived from the Zeeman splitting of the Balmer lines, as well as one of the first known objects that is found in the temperature region of the DB gap.

Another result of the SPY spectra analysis is the identification of several new white dwarfs, which are objects that were assumed to be white dwarfs but not spectroscopically identified as such before. These objects are presented in chapter 9.

1.4 White Dwarfs in the HQS Survey

The second part of this work is based on data of the Hamburg Quasar Survey (HQS, Hagen et al. 1995). This survey is aimed at the identification of extragalactic objects, but also provides a wealth of new detections of stars of different types. Numerous white dwarfs are detected in such surveys that search for blue extragalactic objects because the white dwarfs are hot and thus show blue colours as well. Other surveys of this kind besides the HQS are Hamburg ESO survey (HES, Wisotzki et al. 1996), as well as the Sloan Digital Sky Survey (SDSS). The colour criteria by which white dwarfs can be selected from such survey samples do not exclusively extract white dwarfs, but also stars of similar characteristics. Among these are the hot progenitors of White Dwarfs, the so called PG 1159

stars, as well as the “subdwarf” stars, objects on the horizontal branch that do not have a sufficient mass to evolve on to the AGB but directly evolve from the horizontal branch towards the white dwarf cooling sequence.

The HQS data comprises both photographic photometry data and objective prism spectra. The objective prism spectra have a low resolution and thus only allow a tentative selection of objects as white dwarfs as well as only an approximate determination of temperatures. Homeier (2001) derived a sample of 3000 HQS objects that are probable new white dwarfs. An example spectrum of such an object is shown in Fig. 1.2.

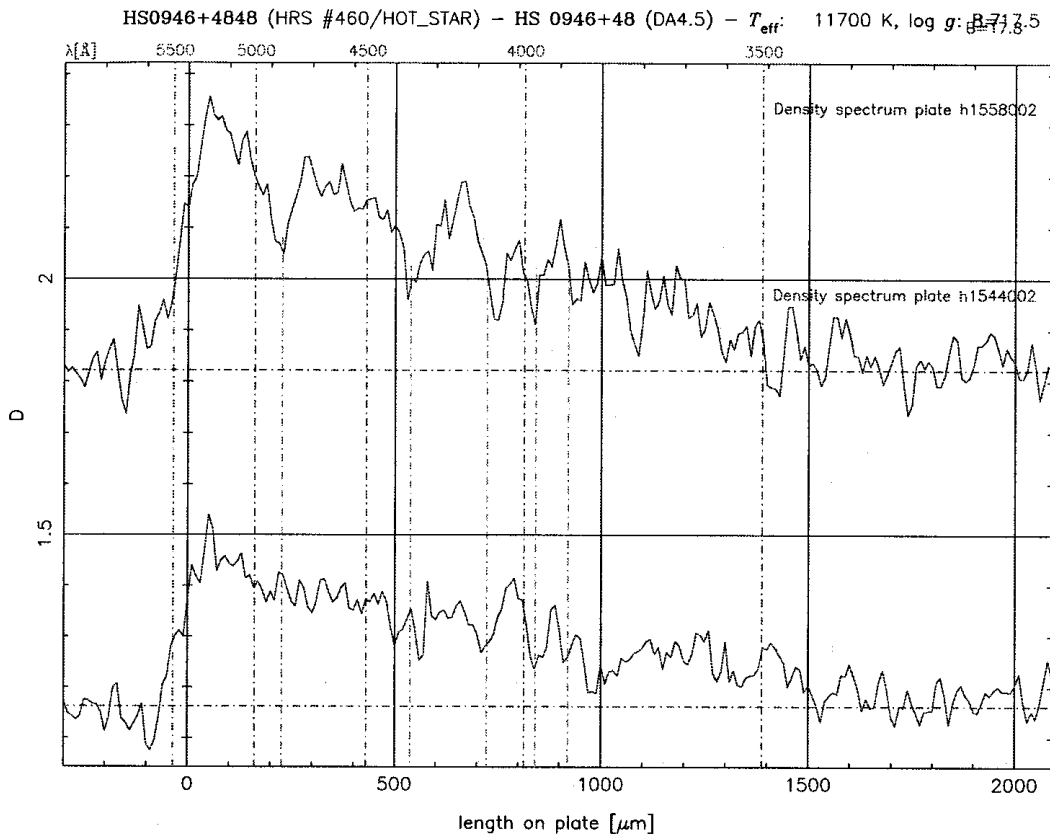


Figure 1.2: An example HQS objective prism spectrum of a DA white dwarf, taken from Homeier (2001). In this plot, the density of the image on the photographic plate, which is a measure of the flux, is plotted against the position on the plate, which is a measure of the wavelength. The wavelength increases towards the left and is cut off near 5500 Å. The wavelengths of the Balmer lines H β through H8 are indicated by vertical dot-dashed lines.

There are about 1000 cool objects in Homeier’s sample, i.e., such for which he derived temperatures lower than 16 000 K. Taking the large uncertainty of the objective prism temperatures into account, any of these stars might be placed in the region of the ZZ Ceti instability strip. Thus, the 1000 cool objects contain a potentially large number of variable white dwarfs. The second part of this work is the identification of such new ZZ Ceti stars.

1.5 ZZ Ceti Stars

ZZ Ceti stars are DA white dwarfs that show variations of their luminosity. The first such object, HL Tau 76, was discovered in 1968 by Landolt, but the star ZZ Ceti was the first of its kind to be studied in detail and has thus become the prototype of this class of variable stars (Robinson, Nather & MacGraw 1976, Nather 1978). The luminosity variations are due to non-radial pulsations for which gravity is the restoring force.

In a diagram of effective temperature vs. surface gravity, these stars are found in an instability strip between temperatures of ~ 10700 K and ~ 12100 K, (Bergeron et al. 2004; Mukadam et al. 2004b). Pulsators near the cool temperature limit, referred to as cDAV stars, generally show longer periods with higher amplitudes than their hot limit counterparts, called hDAV stars. The known oscillation periods range from 71 s (G 185–32, Kepler et al. 2000) up to 1466 s (HS 0952+1816, Mukadam et al. 2004a), with amplitudes of the pulsation modes ranging from a fraction of a percent up to about five percent.

The ZZ Ceti pulsations can be employed to reveal characteristics of the interior structure of a pulsator, e.g., the thickness of the outer hydrogen layer. Such studies require observations of very highly resolved pulsation frequency spectra of ZZ Ceti stars. Observations of this kind are only possible in huge coordinated efforts of many observatories that are necessary to record the pulsations over the course of several days without interruptions by daylight. The Whole Earth Telescope (WET, see Nather et al. 1990) collaboration has obtained such data for several ZZ Ceti stars and important results were derived from the pulsation spectra. Such an analysis was most recently carried out for the star HL Tau 76 by Dolez et al. (2006) and Pech et al. (2006). However, the small number of excited pulsation modes is a drawback in such investigations. Kleinman (1999) has demonstrated that considering the combined pulsation modes of the all DAV stars instead of those of individual objects offers the possibility of a more detailed analysis of these stars as a group. This leads to an interest in the discovery of new ZZ Ceti stars.

Besides such contributions to stellar astrophysics, white dwarf pulsations are a useful tool in a number of different other research areas. The white dwarf cooling rates are controlled by the mass of the H layer. Therefore determinations of stellar population ages from white dwarf temperatures benefit from a better knowledge of the white dwarf cooling rates through an improved knowledge of white dwarf H layer masses. Furthermore, the short-period oscillations of hDAV pulsators are very stable ($\dot{P} \simeq 4 \times 10^{-15}$, Kepler et al. 2005) and can thus be used to detect planets that orbit such white dwarfs, from variations of the observed arrival times of the pulses. For such projects, a more substantial number of ZZ Ceti stars that are sufficiently bright and show the right pulsational properties, e.g., hDAV pulsations for planet searches, would be an advantage.

These reasons are the main motivations of a search for new ZZ Ceti stars. Only 32 variables of this type were known when this work was begun, but in the last two years, detections of about 70 new ZZ Ceti stars were reported. These new pulsators are objects of rather faint magnitudes, $B \sim 18$, that have been detected based on data from the SDSS by Mukadam et al. (2004a), Mullally et al. (2005), Kepler et al. (2005b), and Castanheira et al. (2006b). Although the number of known ZZ Ceti stars has thus been tripled as a result of the overall richness of the detection of new white dwarfs by the SDSS, the new ZZ Ceti stars that are found in the SPY and HQS samples by this work are still a valuable addition because they are on average two magnitudes brighter ($B \sim 16$) than those discovered from

the SDSS. Therefore, these stars are better suited for further in-depth studies.

Another motivation is that the purity of the ZZ Ceti instability strip has been questioned by Mukadam et al. (2004b) based on the T_{eff} vs. $\log g$ distribution of SDSS ZZ Ceti and non-ZZ Ceti stars. From a theoretical point of view, all DA white dwarfs should go through a DAV phase when they cool down to the temperature region of the ZZ Ceti instability strip. Thus, the alleged discovery of an impure instability strip, i.e., of DA white dwarfs that do not pulsate at temperatures between 11 000 K and 12 000 K, is a challenge to the theory of white dwarf atmospheres. Furthermore the results that are derived from the study of ZZ Ceti pulsations are only applicable to the entire group of the DA stars if no intrinsic differences exist that might cause some DA not to pulsate at ZZ Ceti temperatures. Therefore a considerable increase of the number of DAV stars with parameters that are not derived from the SDSS spectra will be an important check of the alleged finding of an impure instability strip. New ZZ Ceti detections that are based on the SPY analysis results can contribute to this.

1.6 Observations of ZZ Ceti Stars

The identification of pulsating stars requires the recording of lightcurves of the stars, i.e., of a time-series measurement of the stellar flux, which is consuming a large amount of observation time. Therefore such observations are not feasible for a large number of objects of which only a small fraction is expected to be indeed variable, as it is the case for the white dwarfs in the HQS: The uncertainties of the HQS temperatures are ~ 6000 K, and the objects are approximately equally distributed over the temperature range. Thus, only about a sixth of the true temperatures will fall into the region of the ZZ Ceti instability strip, because it is 1000 K wide. Therefore, the expected “success fraction” is too low and the number of candidate stars too high to make lightcurve observations of all HQS stars feasible.

Thus it is necessary that methods to pre-select the most probable new variables among the HQS targets are found and applied to the sample, before actual lightcurve observations are carried out. First, time-series photometry data with a low time resolution, which is too low to directly show the possible pulsations, were obtained for the possible new variables. This requires much less observation time than obtaining a proper lightcurve. A technique to identify probable pulsators from such coarse time-series was developed, and several stars were identified as probable pulsators. These observations and their analysis are described in chapter 9. The motivation for this kind of observations was that a large amount of observation time at a telescope that allowed only such coarse photometric observations was available to the institute in Kiel in 2002.

That telescope became inoperative in 2003, and thus the pre-selection of the most probable ZZ Ceti candidate stars was continued by observations of a different kind at another telescope. Now, photometric colours of the HQS stars were measured and much more accurate temperatures than those from the HQS spectra were derived from the colour data. About 300 of the cool HQS stars were studied in this way, and 20 were identified as probable pulsators according to their temperatures, described in chapters 10 and 11.

After these pre-selection observations, the candidate ZZ Ceti stars needed to be identified as pulsators by direct observations of their pulsation lightcurves. Such observations

were first carried out by other observers to which the candidates had been forwarded, and three new variables were discovered. The first own lightcurve observations, obtained at Observatoire Haute-Provence, were less successful and did not yield any ZZ Ceti detections. These first lightcurve observations are described in chapter 12. The following chapter 13 describes similar but more successful observations using the Nordic Optical Telescope (NOT), in which 12 new variables were identified. Finally, these new variables are discussed in chapter 14.

Part II

SPY

Chapter 2

The SPY Project

2.1 A Search for Supernova Ia Progenitors

Supernovae (SNe) of the type Ia are important tools for cosmological research, especially but not only as the most successful standard candles in the investigation of the accelerated cosmic expansion (Tonry et al. 2003, Riess et al. 2001, Perlmutter et al. 1999). Therefore, their formation mechanism comes into focus. Although it is widely accepted that SNe Ia originate from thermonuclear ignition and burning of a CO white dwarf in a binary system, it is uncertain whether this is triggered by accretion from a hydrogen-rich companion or from a merger with another white dwarf (see Belczynski et al. 2005, Branch et al. 1995). The latter scenario, called double degenerate (DD) scenario (Webbink 1984, Iben & Tutukov 1984), requires that the binary has a total mass larger than the Chandrasekhar mass and that the separation of the components is sufficiently small to allow them to merge within a few billion years. The Supernova Ia Progenitor Survey (SPY, Napiwotzki et al. 2003) has been designed to test this scenario by searching for binary White Dwarf systems that qualify as supernova Ia progenitors. Spectra of more than 800 white dwarfs were obtained at two points in time to identify any radial velocity variations that would reveal the orbital motion, period, and mass of any SNIa progenitor system. As a result of this survey, it has now been established that SN Ia progenitors do indeed exist among the DD systems: One such object (WD 2020–425, Napiwotzki et al. 2005) and two “close candidates” with masses slightly below the Chandrasekhar limit (Karl et al. 2003, Napiwotzki et al. 2002) have so far been found. More than 30 further DD systems have been discovered by SPY, some of which were published by Napiwotzki et al. (2001), Nelemans et al. (2005), and Morales-Rueda et al. (2005).

2.2 This Work: A Re-use of the SPY Data

A “by-product” of this survey is a large collection of high-quality white dwarf spectra that can be employed for studies far beyond the original scope of SPY: Napiwotzki et al. (2004), Ströer et al. (2005), and Lisker et al. (2005) report on subdwarf stars in the SPY sample, and Werner et al. (2004) discovered a new DO and a new PG 1159 star from the survey data. Pauli et al. (2003) have studied the kinematics of the WD observed by SPY, deriving their memberships of the different stellar components that make up the Milky

way galaxy. Koester et al. (2005a; 2005b) analysed the SPY spectra of DAZ stars and of a peculiar DAZB object, and Berger et al. (2005) investigated the rotational broadening of CaII lines of DAZ white dwarfs. Most relevant to this work, Koester et al. (2001) published an analysis of the atmosphere parameters of a preliminary sample of about 200 SPY objects.

The first part of this work is a continuation of the study that was begun in that paper; an analysis of the SPY spectra of DA and DB stars, now using the final complete data sample.

2.3 The SPY Observations

This chapter describes the SPY observation setup and the data reduction procedures, as they were already presented by Napiwotzki et al. (2003) and Koester et al. (2001).

The SPY survey was implemented as a low priority service mode “filler” program, which takes advantage of non-perfect observing conditions, e.g., bright moonlight, bad seeing, or thin clouds, in which many other projects with higher requirements would not have been feasible. Since such high-requirement projects are often those that are also given a high priority, the way in which SPY was implemented made it possible that a large amount of observing time was allocated for this survey.

For each object, two spectra were obtained at different epochs with UVES, a high resolution echelle spectrograph at the ESO VLT UT2 telescope. This spectrograph splits the light beam of the telescope into two “arms”, one containing the UV (3000 Å) to blue wavelengths, and the other covering the red to IR (11000 Å) region of the spectrum. A dichroic beam splitter (UVES dichroic # 1) was used to operate both arms of the spectrograph in parallel, with a small gap of 80 Å width centered at 4580 Å, between the parts of the spectrum recorded by the two arms. The maximum resolution is $\frac{\lambda}{\Delta\lambda} = 110\,000$ in the red part of the spectrum, if a narrow slit with a width of 0.3” is used. For the SPY observations, a wider slit of 2.1” width was employed to take into account that the SPY observations are carried out even during periods of bad seeing, i.e., when stellar images are smeared out to large angular diameters by atmospheric effects. A wide slit is necessary under such conditions to avoid flux losses that would occur if the stellar image were more extended than the width of the slit. Using this 2.1” slit, the resolution is reduced to $\frac{\lambda}{\Delta\lambda} = 18\,500$, but in cases of favorable seeing with less extended stellar images, the resolution is higher than that value.

The spectra were recorded on 3 different CCD chips, one in the blue arm and two in the red. These CCDs (2 EEV and one MIT/LL CCD) have a resolution of 2K×4K and were read out with a 2 × 2 binning to decrease the readout noise. Between the spectral intervals that are covered by the two CCDs in the red arm, a second gap occurs at 5640 Å, with a width of $\Delta\lambda \approx 80$ Å, similar to the gap between the data of the two arms.

Stars down to a magnitude of Johnson $B = 16.5$ were observed, with typical exposure times of 10 min, or shorter for brighter objects. A signal to noise ratio per binned pixel (0.05 Å) of $S/N = 15$ or higher was achieved for most spectra.

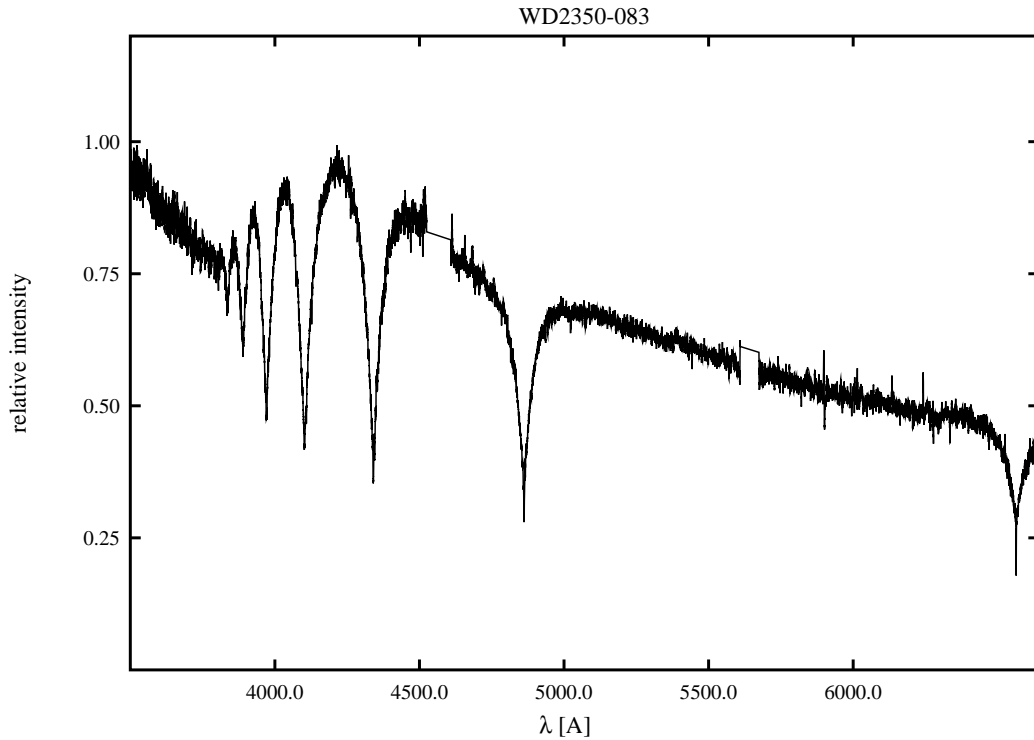


Figure 2.1: A typical DA spectrum, of WD 2350–083. The spectrum has been rebinned to a stepsize of 1 Å for this plot. The instrumental gaps in the spectrum are obvious. The data are shown to their full extent on the red side of the spectrum, and cut off at 3750 Å on the blue end.

2.4 Data Reduction

The spectra were reduced with the ESO pipeline for UVES, which includes basic image reduction steps such as background subtraction, flatfielding and rebinning, as well as the merging of the echelle orders and the wavelength calibration, using ThAr calibration spectra. Koester et al. (2001) found that the quality of these automatically extracted spectra is very good, except for a quasi-periodic wave-like pattern that occurs in some of the spectra. This has since been largely removed by additional processing that has been done at the astronomical institute of the University of Erlangen-Nürnberg, the Dr.-Remeis-Sternwarte in Bamberg, by collaborators of the SPY project. Another part of the additional processing was the removal of large-scale sensitivity variations by applying an instrumental response function to the data, which was derived from nearly featureless spectra of DC stars, as well as from sdO star spectra with very narrow spectral lines.

Still, some artifacts and unremoved sky features remain in the data, most of which do not significantly affect the spectral analysis. Among these are different night sky lines, and some artifacts that are caused by defects of the CCD chips, which appear in some spectra, e.g., near 5890 Å and 4690 Å. One type of artifact that causes some concern are changes of the continuum level that are found in certain places of some spectra, mostly near 4050 Å or 4230 Å. The origin of these features is unclear; they might affect the fitting process because unlike the other artifacts, they are not limited to a few adjacent data points.

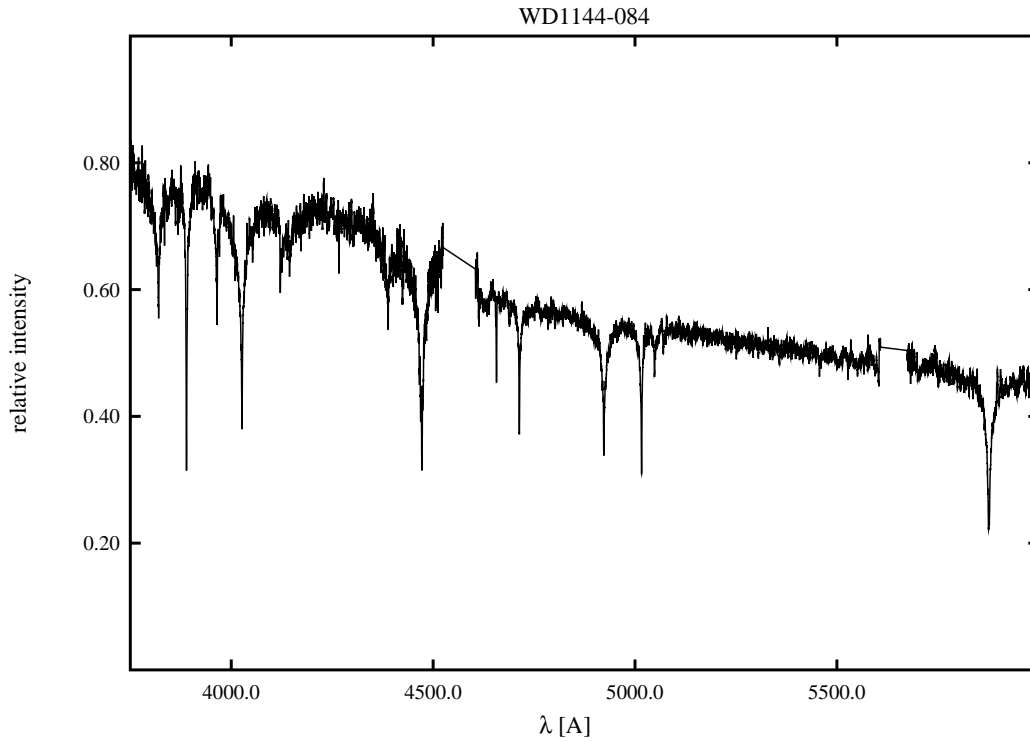


Figure 2.2: The spectrum of WD 1144–084, a typical DB white dwarf. The shown spectral range is that to which model atmospheres were fitted in the analysis, from 3750 Å up to the HeI 5876 Å line. The spectrum has been rebinned to a stepsize of 1 Å for this plot.

For this analysis, the data have been rebinned to a stepsize of 0.1 Å, both to further reduce the noise in the spectra as well as to reduce the huge data volume. This is in contrast to the preliminary analysis of Koester et al. 2001, who used a rebinning to 1 Å. Therefore, the objects of their sub-sample are included in this analysis, now using the data with the smaller stepsize.

Chapter 3

Overview of the Analysis Method

The aim of this analysis is a determination of the effective temperature T_{eff} and the surface gravity, given in its logarithmic form $\log g$. For the simple monoelemental composition of the atmospheres of most white dwarfs, these two parameters completely characterize the stellar atmosphere.

The temperature of the atmosphere acts on the observable spectrum in two ways: First, the distribution of the continuum flux depends on the temperature similar to the way in which the radiation of a black body does. As a second effect, which is more relevant to this analysis, the shape of the absorption lines of hydrogen or helium is affected by the temperature. The strength of the lines first increases with the temperature up to a maximum line strength near $T_{\text{eff}} \approx 12\,500\text{ K}$ or $T_{\text{eff}} \approx 20\,000\text{ K}$ for hydrogen and helium, respectively. A further increase of the temperature then leads to a decrease of the line strengths.

The effect of the other atmosphere parameter, $\log g$, on the observed spectrum is the pressure broadening of the lines, which increases with the surface gravity.

The continuum slope of the spectra cannot be used to determine the effective temperatures because the SPY data are not spectrophotometrically calibrated, i.e., it is not certain that the continuum slope accurately reflects the flux distribution of the stellar spectrum. It may instead be affected by atmospheric and instrumental effects. Therefore only the profiles of the spectral lines allow a reliable determination of the atmosphere parameters, provided that the effects of possibly incorrect continuum slopes and curvatures can be avoided.

The line profiles are analysed by fitting the observed profiles with theoretical profiles that are derived from atmosphere models for different temperatures and surface gravities. The theoretical profiles are first scaled to the level of the observed continuum on each side of a line, thus removing any effects of possibly incorrect flux levels of the continuum. Then, the atmosphere model whose so adjusted profiles best reproduce the observed line shapes is determined.

The analysis method is very similar to that employed by Koester et al. (2001) and Homeier et al. (1998), and therefore some additional details on the fitting process that are not mentioned here can be found in these publications.

3.1 The Model Spectra

The model spectra are computed from model atmospheres that were developed by D. Koester over several years. They are described in detail in Finley et al. (1997). The atmospheres are modeled assuming local thermodynamical equilibrium (LTE), which is a valid assumption for most of the temperature range over which the SPY objects are distributed. Only for temperatures in excess of 40 000 K, non-LTE effects become noticeable, but the impact on the fitting results is small (Koester et al. 2001); the temperatures and gravities are generally overestimated by the LTE fit results, but at 40 000 K only by a minor amount of less than 100 K for the temperature and less than 0.03 dex for $\log g$. A serious impact on the fitting results is only found for temperatures higher than 60 000 K, where the temperature and gravity are overestimated by more than 1500 K, and more than 0.05 dex by the LTE models (Napiwotzki et al. 1999; Liebert et al. 2005). Less than 3% of the observed objects are found at temperatures $T_{\text{eff}} > 60\,000$ K; so for almost all studied objects the LTE parameters will be precise within the expected uncertainties of a few 100 K and a few 0.01 dex.

The models that are employed here are composed of either pure hydrogen or helium, or of helium with small admixtures of hydrogen, for the DA, DB, and DBA stars, respectively. The hydrogen model grid covers a temperature range from 5000 K to 95 000 K, in steps of 500 K below temperatures of 21 000 K, followed by 1000 K steps up to 26 000 K, a 2000 K stepsize up to 30 000 K and steps of 5000 K width above that temperature. For each of these temperatures, models with $\log g = 5.0, 5.5, 6.0, 6.5, 7.0, 7.25, 7.5$, up to 8.5 in steps of 0.1, 8.75 and 9.0 dex were used.

For the models with helium as the main constituent of the atmosphere, temperatures from 10 000 K to 50 000 K are covered. Here the models are spaced by 1000 K below 20 000 K and 2000 K up to 40 000 K, followed by a 50 000 K model, and $\log g$ is covered from 7.0 to 9.0 in steps of 0.25 dex.

Energy transport by convection is important in the atmospheres of cool white dwarfs. It is taken into account in the model atmospheres following the mixing length approximation, with a certain combination, designated as ML2, of the parameter values that characterize this approximation, and with a value of the main parameter, the ratio of mixing length to the pressure scale height, $\alpha = 0.6$. This combination of parameters of the mixing length approximation has been shown by Bergeron et al. (1995) and Koester & Vauclair (1997) to give the best simultaneous reproduction of both the UV and the optical line profiles of DA stars with convective atmospheres.

The broadening of the spectral lines is calculated according to the Stark broadening by charged perturbers. Line broadening by neutral perturbers due to van der Waals interactions is not included in the models. It becomes important at temperatures of less than $T_{\text{eff}} \sim 9000$ K in hydrogen atmospheres and below $T_{\text{eff}} \sim 15000$ K in helium-dominated atmospheres. At temperatures below these values, the reproduction of the observed line profiles by the models is therefore not perfect, and becomes increasingly inaccurate for lower temperatures.

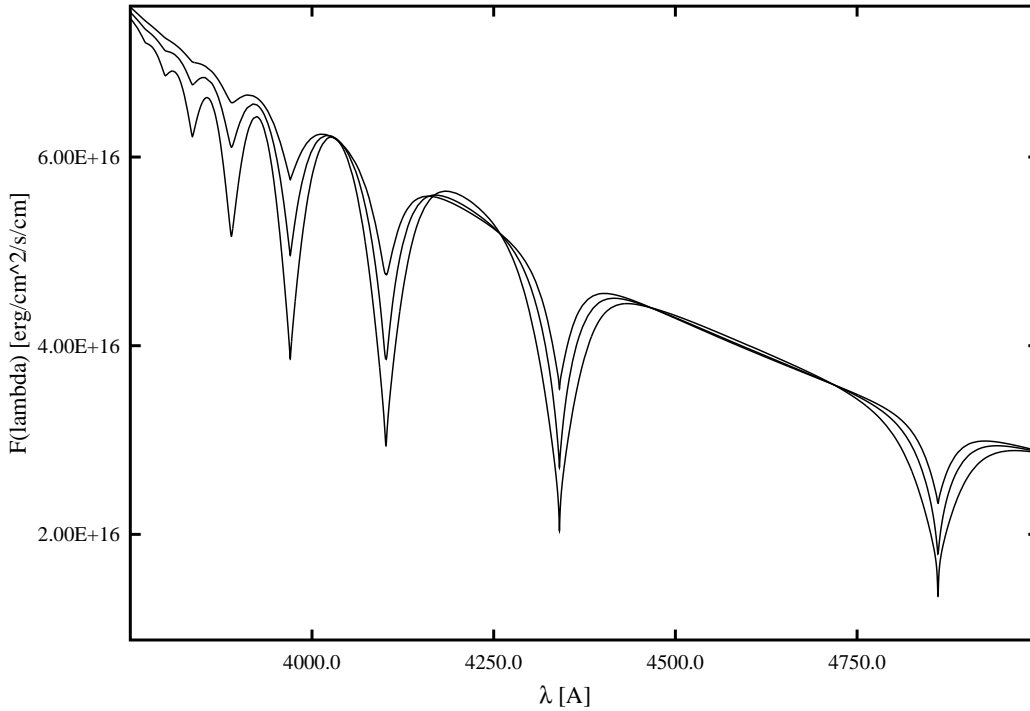


Figure 3.1: The spectral region of the lines H8 to H β of DA model spectra for $T_{\text{eff}} = 20\,000$ K, showing the strongest lines, 30 000 K, and 40 000 K, all for $\log g = 8.0$. To illustrate the differing line shapes at increasing temperatures, the spectra have been adjusted to the flux levels of the 40 000 K spectrum, i.e., the given flux units are correct only for that spectrum.

3.2 The Fitting Routine

The fitting routine that was used in this work is implemented as a FORTRAN program that was developed by D. Koester, using routines from Press et al. (1992). It carries out a χ^2 fit, i.e., the best-fitting model spectrum f_{th} is determined by minimizing the quantity

$$\chi^2 = \sum_{i=1}^n \left(\frac{f_{\text{ob}}(\lambda_i) - f_{\text{th}}(\lambda_i, T_{\text{eff}}, \log g, r_v)}{\sigma_i} \right)^2$$

where f_{ob} is the observed spectrum, and r_v is an additional parameter of the fit that takes any wavelength shift into account. Such a shift is normally present due to a radial movement of the observed object, due to a gravitational redshift which is important at the high gravities of white dwarfs, and possibly also due to any unwanted calibration or instrumental effect on the wavelength scale. σ_i is the uncertainty of each measurement, i.e., the spectral noise at each point i of the spectrum.

χ^2 is thus the difference between the observed spectrum and a certain model spectrum, summed over the data points and weighted by the spectral noise at each wavelength. Not all data points are used in this sum, but only those within certain spectral intervals that contain the spectral lines; as mentioned before, the continuum between the lines cannot be used for the fitting.

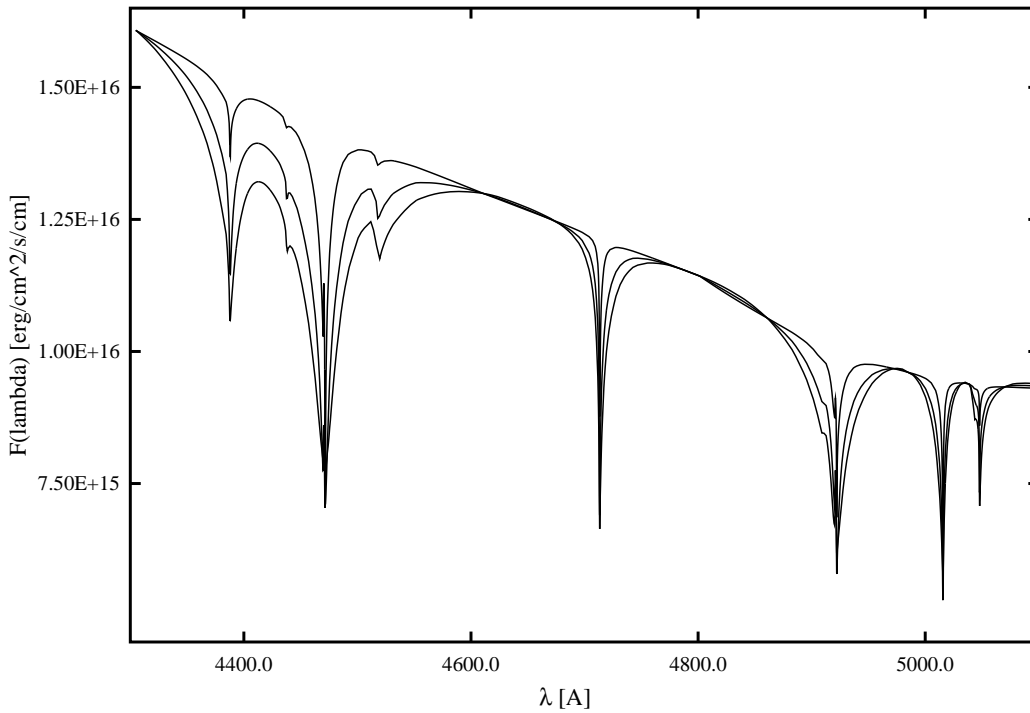


Figure 3.2: The same as Fig.3.1, for a spectral region of DB model spectra near one of the strongest HeI lines at 4471 \AA . The temperatures of the models are $T_{\text{eff}} = 20\,000 \text{ K}$, with the strongest and broadest lines, $17\,000 \text{ K}$, and $14\,000 \text{ K}$, all for $\log g = 8.0$. The spectra have been adjusted to the flux levels of the coolest spectrum.

The expectation value of the χ^2 distribution is equal to the number N of degrees of freedom of the distribution, which in this case is

$$N = n_{\text{ob}} - n_{\text{th}}$$

where n_{ob} is the number of data points and n_{th} is the dimension of the model grid, i.e., here $n_{\text{th}} = 2$, corresponding to the two “directions” of the model grid, T_{eff} and $\log g$. The quantity χ^2/N , called reduced χ^2 , has the expectation value 1, which one expects to find for a good fit. Any fit with a reduced χ^2 that is much higher than that indicates a bad reproduction of the observed data and therefore an uncertain fit result.

A large χ^2 is sometimes also due to the presence of one or a few bad data points (“cosmics”) with a very high value. The fit is normally good in spite of such bad points, and the *relative* values of χ^2 for different models still allow an identification of the best model, but the *absolute* value of χ^2 is not useful as an indicator of the fit quality in such a situation.

The determination of the best-fitting model from the values of χ^2 is based on the Levenberg-Marquardt algorithm (Press et al. 1992). This algorithm iteratively proceeds from a $(T_{\text{eff}}, \log g)$ starting point down the slopes and “valleys” of the two-dimensional function $\chi^2(T_{\text{eff}}, \log g)$ towards a local minimum. The algorithm is a combination of the steepest descent method that only follows the gradient at each iteration point, and an inversion of the Hessian Matrix, which allows a more precise step towards a local minimum, but only if the local geometry of the χ^2 surface is well approximated by a quadratic form.

That is normally only true near the minimum, and therefore the algorithm continuously switches from the steepest descent method at the beginning of the iteration to the Hessian matrix inversion near the minimum.

In each iteration step, a position in the model grid is predicted, at a place in between the grid points, and a model spectrum is created for that $(T_{\text{eff}}, \log g)$ position by a bilinear interpolation of the model spectra of the three closest grid points. Subsequently, the derivatives with respect to both parameters are computed, and χ^2 is determined for the new grid position. The derivatives serve to predict the direction of the next iteration step, and the difference of χ^2 from one step to the next determines the distance of the following step.

σ_i which has to be known for the χ^2 computation is determined from the squared difference of f_{ob} to a smoothed version of the data, which is calculated by a Savitzky-Golay filtering of f_{ob} . The resulting summed σ is averaged in certain spectral intervals, placed next to each spectral line, and a continuous function $\sigma(\lambda)$ is interpolated from these discrete averaged values.

After the iteration converges to a minimum, the formal standard deviations of the resulting parameters are obtained from the covariance matrix.

3.3 Adjustment of the Models to the Continuum

The model spectra need to be adjusted to the continuum level of the observed spectrum near each Balmer line, thereby removing the effects that a possibly incorrect continuum slope or curvature might have on the following determination of χ^2 . This is an important step of the fitting process, also because only an appropriate choice of the wavelengths at which the adjustment is done, the so called continuum placement, permits a proper working of the fitting routine. Since there is no precise a priori knowledge about the wavelengths that are appropriate, some iterative experimentation is necessary to determine the best continuum placement.

Spectral regions on both sides of each line are used to determine the local averaged continuum levels, and an interpolation between these mean continuum levels is used to determine a continuum level for all wavelengths, to which the model spectra are scaled. The continuum regions for the DA fits are placed individually for the lines from $H\alpha$ up to $H\gamma$, and on both sides of the spectral interval from $H\delta$ to 3700 Å. For the DB stars, the continuum is similarly adjusted on both sides of each isolated line or on both sides of each spectral region that contains several narrowly spaced lines.

One difference between this analysis and the earlier study of Koester et al. (2001) is that a quadratic interpolation of the continuum flux is used here, while they used a linear interpolation. Since the SPY data have not been flux calibrated, not only the continuum slopes but also the continuum curvatures might not correctly represent the stellar flux distribution, and under these conditions a quadratic interpolation can yield better results because it provides the additional degree of freedom that is necessary to correct not only for an incorrect continuum slope but also for an incorrect curvature.

Concerning the continuum placement, the mentioned changes of the continuum level near 4040 Å and 4230 Å are somewhat problematic. The latter feature appears only in a small number of spectra, and any effects on the fitting process were avoided by placing

the continuum regions closer to the possibly affected lines $H\delta$ and $H\gamma$. The feature near 4050 \AA , on the other hand, is weakly present in as many as a third of the SPY spectra. It generally has the effect that the observed flux in the spectral region from 4030 \AA to 4060 \AA is higher than the model fit in these cases. This cannot be avoided because for all possible alternative continuum placements, even if multiple continuum regions between $H\delta$ and $H\epsilon$ are used, an inaccurate fit of either the blue wing of $H\delta$ or the red wing of $H\epsilon$ is the consequence. As the effect is weak and localized in most spectra, the uncertainty of the parameters that are derived from most of these fits is most probably not increased by this effect. However, there is a small number of spectra in which this continuum change is very pronounced and where it is therefore not certain that accurate parameters can be determined. Thus, these cases are investigated more closely in section 4.3.

3.4 Different Fitting Solutions for each Object

As mentioned above, the Balmer lines reach their maximum strength around $T_{\text{eff}} = 12\,500 \text{ K}$, and the maximum strength of the HeI lines is found near $20\,000 \text{ K}$. Therefore two solutions for the fit of a spectrum are normally possible, one on either side of the line strength maximum. In the immediate vicinity of the temperature of maximum line strength, the χ^2 surface may show an even more complex shape with multiple shallow minima. Three T_{eff} starting values were used for the DA fitting, $15\,000 \text{ K}$, $12\,000 \text{ K}$, and $9\,000 \text{ K}$, and two for the helium atmosphere fits, $25\,000 \text{ K}$ and $15\,000 \text{ K}$, to cover all possible solutions. The resulting degeneracy of the solution can be lifted by using not only the relative values of χ^2 , like it is done by the Levenberg-Marquard algorithm, but also the absolute χ^2 values of each individual solution. This allows to select the global minimum from the different local minima.

For some DA stars, two solutions close to the Balmer line maximum are found which have an almost equal χ^2 and an equally well fitting visual appearance, so that no single solution can be selected. In these cases the Johnson or Strömgren colours of these objects that are published in McCook & Sion (1999) are used to decide which solution is the correct one. The observed colours are compared to a grid of theoretical colours that are computed by convolving the Koester model atmospheres with the Johnson or Strömgren filter transmission functions. This method always allows an easy decision between the hotter and cooler solutions. Only seven objects remain for which no observed colors are published and where thus two possible solutions remain. For these objects, both solutions are given in the list of the fit results in the appendix.

If one of the two spectra of each object has a much higher noise than the other, or shows any strong artifacts, the fit result of the higher quality spectrum is used as the final result for that object. For the stars with two spectra of similar quality, the individual fit results were averaged, weighted by their individual uncertainties, to yield the final parameters of the object.

Both selections, that of the best-fitted spectrum and that of the fit with the best starting temperature, were checked by a visual inspection that was carried out on all spectra and their different fits. The formal uncertainties and the values of χ^2 were found to be reliable indicators of the spectral and fit quality, respectively. Another aim of the visual inspection was to ascertain any peculiarities, especially for the objects for which neither hydrogen

Table 3.1: The spectral intervals that were used in the fitting process. For the DBA stars, the DB intervals were combined with the DA intervals that surround $H\alpha$ and $H\beta$. The wavelengths are given in \AA .

Purpose	DA, λ_{start}	DA, λ_{end}	DB, λ_{start}	DB, λ_{end}
χ^2 fitting	3700	4175	3770	4180
	4240	4440	4350	4500
	4720	5000	4675	4800
	6480	6640	4820	5115
			5800	5950
σ determination	3670	3760	3750	3770
	4180	4240	3910	3930
	4420	4470	4180	4210
	4670	4720	4315	4335
	5100	5140	4500	4520
	6400	6450	4640	4670
	6620	6640	4800	4820
			5115	5140
			5750	5770
			5960	5990
Continuum estimation	3670	3730	3750	3770
	4010	4030	3905	3920
	4170	4190	3980	3990
	4220	4260	4070	4090
	4440	4460	4180	4200
	4480	4500	4330	4350
	4640	4660	4410	4430
	4680	4720	4500	4510
	5000	5040	4660	4675
	5200	5250	4800	4820
	6350	6400	4960	4980
	6460	6480	5115	5140
	6620	6640	5790	5800
		5950	5970	

nor helium models yielded a good fit, but also for the seemingly common DA and DB stars.

3.5 The Analysis Pipeline

The spectral fitting that has been described so far is embedded into a reduction pipeline which includes the merging of the three parts of each spectrum, the fitting of the spectra itself, and the plotting of the fitted models together with the observations.

Additional steps of the pipeline are the determination of the final parameters as described above, and the archiving of the results in an SQL database that was used to store

not only the fit results but also all other relevant information on each object, including any comments on peculiarities or literature references. The tables in the appendices were created from this database. For each object, stored are:

- Name
- Final fit results:
 - $T_{\text{eff}}, \sigma(T_{\text{eff}})$
 - $\log g, \sigma(\log g)$
 - $r_v, \sigma(r_v)$
 - χ^2
- the number of individual fit results that were averaged for the final result
- the ID(s) of the spectrum or spectra from which the final result is derived
- the date and time of the recording of the spectrum or spectra
- the starting value or values that yielded the best fit
- the white dwarf classification of the object, according to this analysis
- information from the SPY input catalog:
 - the celestial coordinates
 - the magnitude, usually Johnson B or V
 - the color, usually Johnson $B - V$
 - the white dwarf classification of the object in the input catalog
 - any aliases of the object name
- any comments on peculiarities
- literature references

Chapter 4

Results of the DA Star Fits

Of a total number of 848 objects for which spectra were analysed, a hydrogen atmosphere model fit was obtained for 694 objects. The different classes of stars that are found in this sub-sample are listed in table 4.1. The fit results for most objects are given in appendix A. An exception are the DA+dM stars, i.e., binary systems composed of a DA white dwarf and a late-type main sequence star, for which the results listed in appendix B. All objects, including double degenerate binary stars and magnetic DA stars that exhibit Zeeman splitting of the Balmer lines, have been fitted as single nonmagnetic stars. The additional uncertainties that are introduced by this should be small for the single-lined binaries for which only one component contributes significantly to the flux, as well as for most of the magnetic stars, since those for which a fit was achieved show weak field strengths and thus only a moderate line splitting with a separation of the components of only a few Å.

The double-lined binaries are more difficult cases, because the line cores of both components are visible in the spectra. If the model spectrum of a single star is fitted to these data, like it is done here, effectively only average parameters of both components are determined. A more proper treatment of these objects would require to fit them with a set of two model spectra, as it has been done, e.g., by Napiwotzki et al. (2002) and Karl et al. (2003). For such an analysis it would however be necessary to derive some stellar parameters, e.g., the masses, beforehand from an orbital analysis, in order to be able to keep them fixed during the fitting process. Such an orbital analysis is beyond the scope of this work, and thus only the single-model fitted average parameters are determined for these objects.

Besides the white dwarfs there are several subdwarf stars in the analysed sample. Most SPY observations of sdB stars (subdwarf stars with Balmer and HeI lines in their spectra) have been studied earlier by Lisker et al. (2005), who derived temperatures and surface gravities that are in very good agreement with those from this analysis. The SPY spectra of sdO and sdOB stars (i.e., hot subdwarfs showing HeII lines in their spectra) have been investigated by Ströer et al. (2006). The fit results for the subdwarf stars are listed together with those for the hydrogen-atmosphere white dwarfs in appendix A.

The fits with very high and very low temperatures show deviations from the observed line profiles, due to NLTE effects for $T_{\text{eff}} > 40\,000$ K, and caused by the onset of increased line broadening by van der Waals interaction for $T_{\text{eff}} < 9000$ K. For many very cool objects no fit could be achieved, because without an inclusion of the increased broadening

Table 4.1: Types and numbers of objects with DA model fits. The seven “other” objects are peculiar objects such as DAB or DA+DB stars.

Object Type	Number of Objects
Single, nonmagnetic DA	589
DA+dM binaries	44
Double degenerate binaries	22
Magnetic DA	10
sdO, sdOB	12
sdB	8
DAO	3
Other types	7

in the models, the fitting routine converges towards models of exceedingly high $\log g$. For a few very cool and very hot objects for which no fit could be achieved with a quadratic interpolation of the continuum levels, a linear interpolation allowed a reasonable fit. In such cases, these linear-interpolated continuum results are given in table A.1, with an according remark.

Some typical example fits of spectra with different S/N are shown in Fig. 4.1. Examples of problematic fits at high and low temperatures, and also of objects for which the continuum on the blue side of $H\delta$ is not properly fitted (see sections 2.4 and 3.3), are displayed in Fig. 4.2. In this figure, NLTE effects can be recognized in the line cores of one of the example spectra, and differences of models and observations are obvious in the example spectra of very cool objects, especially for the $H\alpha$ line.

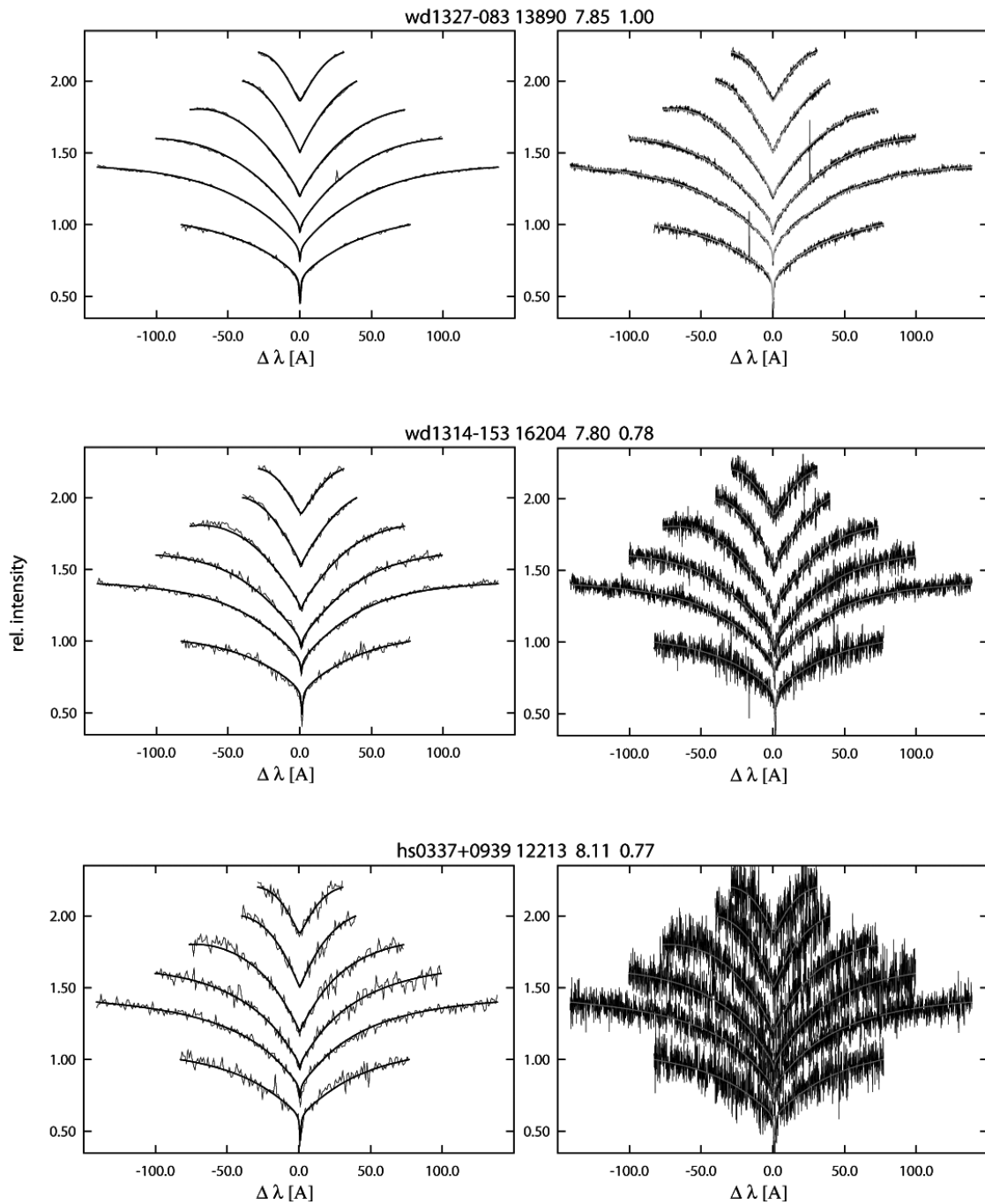


Figure 4.1: Some example fits of spectra of high, typical and low S/N . The Balmer lines from H α to H δ (bottom to top) are shown. The relative intensity scale is correct for H α and has been displaced by 0.4 for H β and by an additional 0.2 for each higher line. On top of each panel, the fit results (T_{eff} , $\log g$ and χ^2) are given. The right panels show the data with the full 0.1\AA resolution, as thin black lines, and the model fits as overplotted gray lines. In the left panels, the same data are shown with a binning of 1\AA , as thin lines, and the model fits as thick lines. For the highest S/N spectra, the binned data (top left panel) are indistinguishable from the fits. The objects in the middle and the lower panels show weak cases of the elevated flux in the blue wing of H δ .

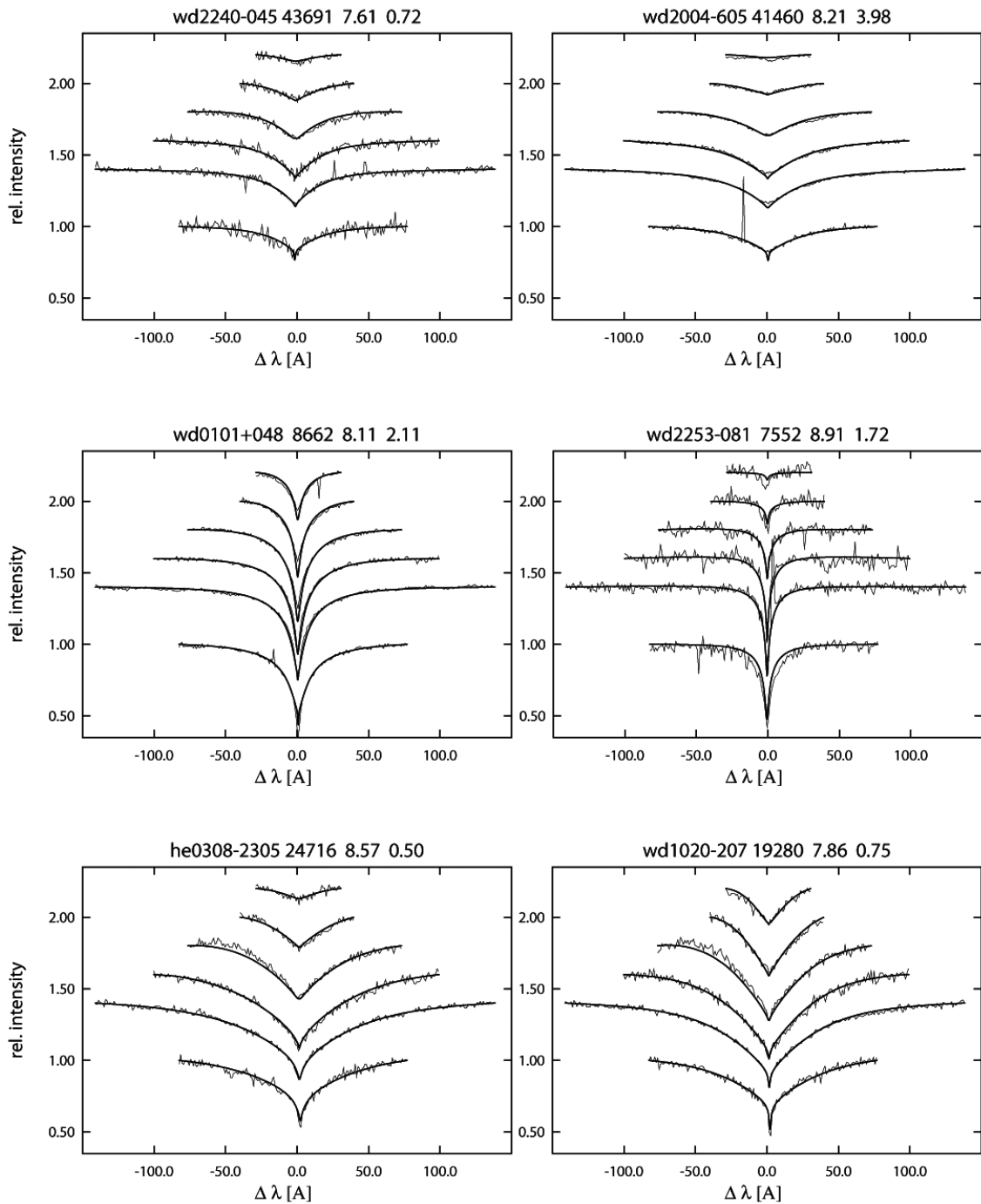


Figure 4.2: Some examples of problematic fits. The plotting and labeling is similar to Fig. 4.1. In the upper panels, both an NLTE-affected spectrum with filled-up line cores (right) and an unaffected object of similar temperature (left) are shown. The middle panels show low-temperature fits, of which the one on the right side is not perfect, especially for H α . The lower panels show spectra in which an elevated flux in the blue wing of H δ is strongly present.

The third fitting parameter, the radial velocity, was used only to allow a correction of the wavelength scale, without which the fitting process would not have worked properly.

Since the wavelength scale of the spectra has not been corrected for the motion of the earth, the radial velocity values that result from the fits are a superposition of the stellar, solar, and earth velocities. It was not intended to yield precise results of the stellar radial velocities from these values. Such precise data of the stellar velocities have already been derived earlier from the SPY spectra by Napiwotzki et al. (in preparation).

4.1 Fit Uncertainties

The uncertainties of the atmosphere parameters that are given in table A.1 are the formal uncertainties from the χ^2 fitting routine. They are mostly low, and normally amount to only a few times 10 K. They do not include systematic errors, which might be introduced by the data reduction, or by the lack of a flux calibration of the data. Thus the true uncertainties of the fit results are generally underestimated by these *internal* uncertainties of the fitting process.

This has been demonstrated by Napiwotzki et al. (1999), who compared the results that different investigations derived for common objects. They concluded that typical *external* uncertainties of state-of-the-art atmosphere analyses of white dwarfs are almost an order of magnitude larger than the formal fitting errors. They found typical external uncertainties of

$$\sigma(T_{\text{eff}}) / T_{\text{eff}} \sim 3.3 \%$$

and

$$\sigma(\log g) \sim 0.07$$

An approximate value of the external uncertainty can be obtained from the different fit parameters of the two independent SPY spectra of each object. This method tends to overestimate the uncertainties, because the spectra are not of uniform quality, and therefore the fit results of a spectrum with high S/N would often be compared to the results of another spectrum with lower quality. A similar situation occurs if one of the two spectra shows artifacts that might have affected the fitting process. To minimize such an overestimation of the uncertainty, only those pairs of fit results for which both spectra are of similar quality, in terms of the S/N as well as concerning the presence of artifacts, are used.

180 such pairs of DA fit results were selected, and this subsample was further reduced to those 142 objects that are neither cooler than 10 000 K nor hotter than 40 000 K. This avoids the temperature regimes where NLTE effects or broadening by neutral particles become important and where the fit results are thus less certain than for the more typical white dwarfs at intermediate temperatures. The resulting mean differences of the effective temperatures and surface gravities are

$$\langle \Delta \log g \rangle = 0.070 \text{ dex}$$

and

$$\langle \Delta T_{\text{eff}} / T_{\text{eff}} \rangle = 1.94 \%$$

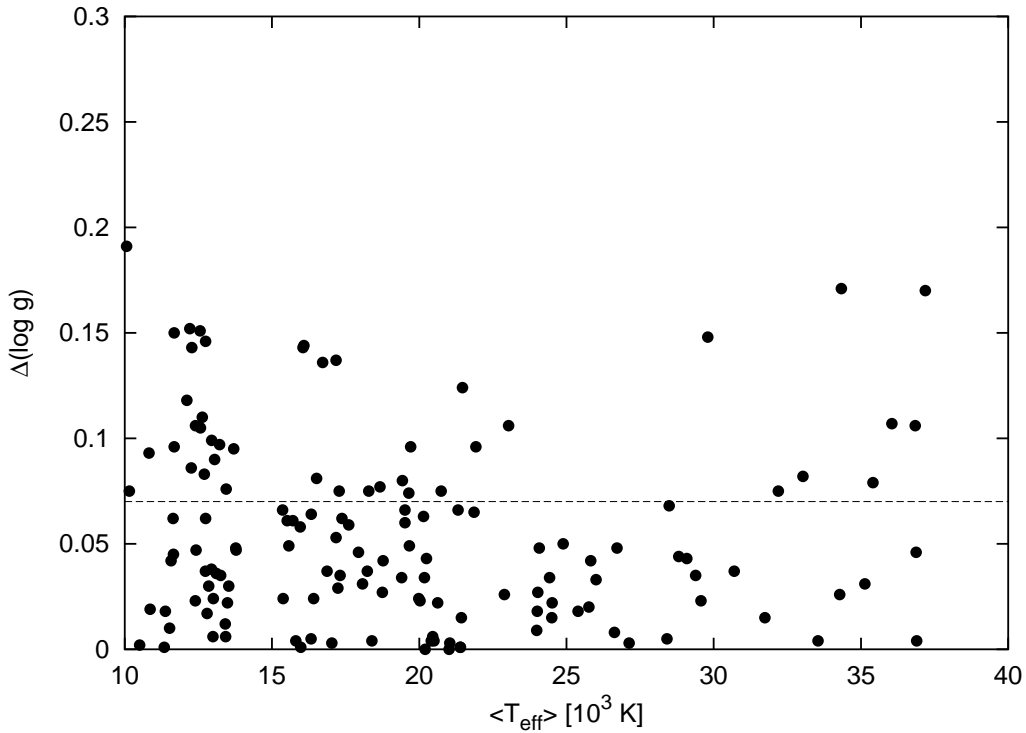


Figure 4.3: The distribution of $\Delta(\log g)$ of the DA fits with respect to T_{eff} , derived from the fit results of two different spectra. The average difference of 0.07 dex is shown as a dashed line.

The distributions of $\Delta \log g$ and ΔT_{eff} with respect to T_{eff} are shown in Figs. 4.3 and 4.4.

Another estimate of the external uncertainty that is introduced by the fitting process can be derived by comparing the results to those of a second, independent fitting method. Such an independent fitting method was developed and used by D. Koester to fit the models to the data without employing the Levenberg-Marquard algorithm. Instead, first a value of χ^2 for each point of the model grid is computed, and then a paraboloid is fitted to the points around the minimum of the resulting χ^2 surface. The fit results are derived by interpolating between the grid points to the position of the paraboloid minimum.

A comparison of the results that were obtained with this method for a subset of 274 objects to the results of the original, more tested and tried method, yields differences of $\langle \Delta T_{\text{eff}} / T_{\text{eff}} \rangle = 0.56 \pm 2.10\%$ and $\langle \Delta(\log g) \rangle = 0.006 \pm 0.064$. The systematic shifts are insignificantly low, while the scatter of the differences is very similar to that found in the above comparison of the results of the two spectra per object. Thus, the general uncertainty of the T_{eff} results seems to be similar to 2% and that of $\log g$ similar to 0.07 dex.

4.2 Comparison with other Investigations

Similar to the work of Napiwotzki et al. (1999), the external uncertainties can also be judged from the differences of the SPY results to those that other investigations found for

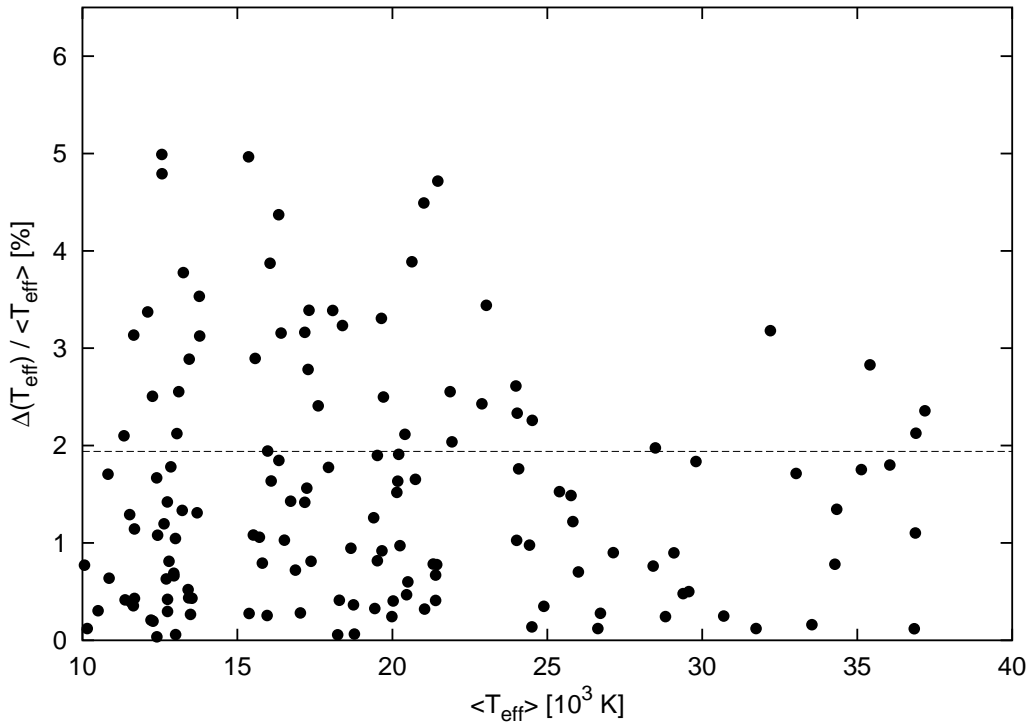


Figure 4.4: The same as Fig. 4.3, for $\Delta(T_{\text{eff}}) / \langle T_{\text{eff}} \rangle$, and with the average difference of 1.94 % shown as a dashed line.

common objects. The fitting results are compared to those of Bergeron et al. (1992, 2004), Finley et al. (1997), Marsh et al. (1997), Vennes et al. (1996, 1997a, 1997b, 1999), and Liebert et al. (2005). All these investigations employed analysis methods that are similar to that of this work, i.e., atmosphere parameters of the objects were derived from model spectra fits to the Balmer line profiles of optical spectra. Finley et al. (1997) and Marsh et al. (1997) used grids of Koester model atmospheres for their fits, while the remaining authors used a different set of model atmospheres that are described in Bergeron et al. (1992; also used by Liebert et al. 2005 and Vennes et al. 1999). As in the previous section, only objects with temperatures ranging from 10 000 K to 40 000 K are used. The results are listed in table 4.2 and are displayed in Fig. 4.5.

The comparison to the data of Liebert et al. (2005) should be considered as the most significant one, not only because the number of their objects that are in common with SPY is the largest of all other investigations, but also because their sample is one of homogeneously obtained and analysed spectra with a comparatively high S/N . While their T_{eff} data is on average in good agreement with the SPY results, their $\log g$ values seem to be systematically higher by 0.051 dex. This confirms a trend that they found when they compared their results to that of other authors; their mean surface gravity is higher by $\Delta \log g \sim 0.08$ dex than that of all but one of the five other studies that they compare their results to.

The mean difference of the results of this work to those of the other investigations if they are considered altogether are small: Both T_{eff} and $\log g$ are on average higher in the literature than in these results by insignificantly small amounts of 0.16 % and 0.019 dex, respectively.

Table 4.2: Results of the comparison of the data of this work to those of other investigations. The values are the mean and the 1σ scatter of the differences of (SPY - other) data for each other investigation. The last column gives the number n of SPY objects that are in common with the literature sample. The Bergeron et al. (1992) data of one object, WD 0339–035, is derived from a fit that clearly terminated on the wrong side of the maximum strength of the Balmer lines, and the data of this object were therefore not used.

Sample	$\Delta(\log g)$	$\Delta(T_{\text{eff}})[\%]$	n
Bergeron et al. 1992	-0.042 ± 0.096	-0.83 ± 2.76	41
Finley et al. 1997	0.033 ± 0.083	0.23 ± 1.98	31
Marsh et al. 1997	0.076 ± 0.081	2.37 ± 3.70	15
Vennes et al. 1996/7/9	0.001 ± 0.120	-1.20 ± 1.68	22
Bergeron et al. 2004	-0.007 ± 0.084	0.06 ± 1.99	11
Liebert et al. 2005	-0.051 ± 0.089	-0.20 ± 3.33	80

The comparison results lie in the same range of values, especially for the scatter of the differences around their mean, that Napiwotzki et al. (1999) derived in their investigation of the external uncertainties of white dwarf atmosphere parameters. They found, by comparing their results to those of Marsh et al. (1997), Vennes et al. (1997b), and Finley et al. (1997), systematic shifts (their data - other data) of $\langle \Delta(T_{\text{eff}})/T_{\text{eff}} \rangle = -2.3\%$, 3.2% , and 0.7% , as well as $\langle \Delta(\log g) \rangle = -0.112$, -0.001 , and -0.064 . The overall value that they determine for the scatter of the individual differences around the mean is, as mentioned before, 3.3% for T_{eff} and 0.07 dex for $\log g$. The comparison results of this work agree with their findings.

4.3 The Influence of the Continuum Level Changes on the Fitting Process

It is important to check if the stronger kind of continuum level changes that appear in some spectra (see section 2.4 and 3.3, as well as Fig. 4.2) has an influence on the reliability of the fit results. One indicator of the quality of the results is the degree of their consistency with data for the same objects that are found in the literature. From 9 objects for which this effect is strongly present and that are in common with the objects analysed by Liebert et al. (2005), a shift of $\langle \Delta(\log g) \rangle = -0.050$ is found, which is not significantly different from the value for the complete sample of common objects (see table 4.2). For the temperatures, there seems to be a more significant change of $\langle \Delta(T_{\text{eff}}) \rangle = 2.09\%$, but even this is within the range of values of the different systematic shifts to the other literature samples.

This result is listed in the first line of table 4.3, labeled as “4020” because 4020 \AA is the central wavelength of the spectral region in which the continuum level was determined.

As it was mentioned in section 3, it would have been possible to use different spectral regions to fit the continuum, and this was tested for the objects of this sub-sample by first using a spectral region centered on 4055 \AA (“4055” in table 4.3), and in another test,

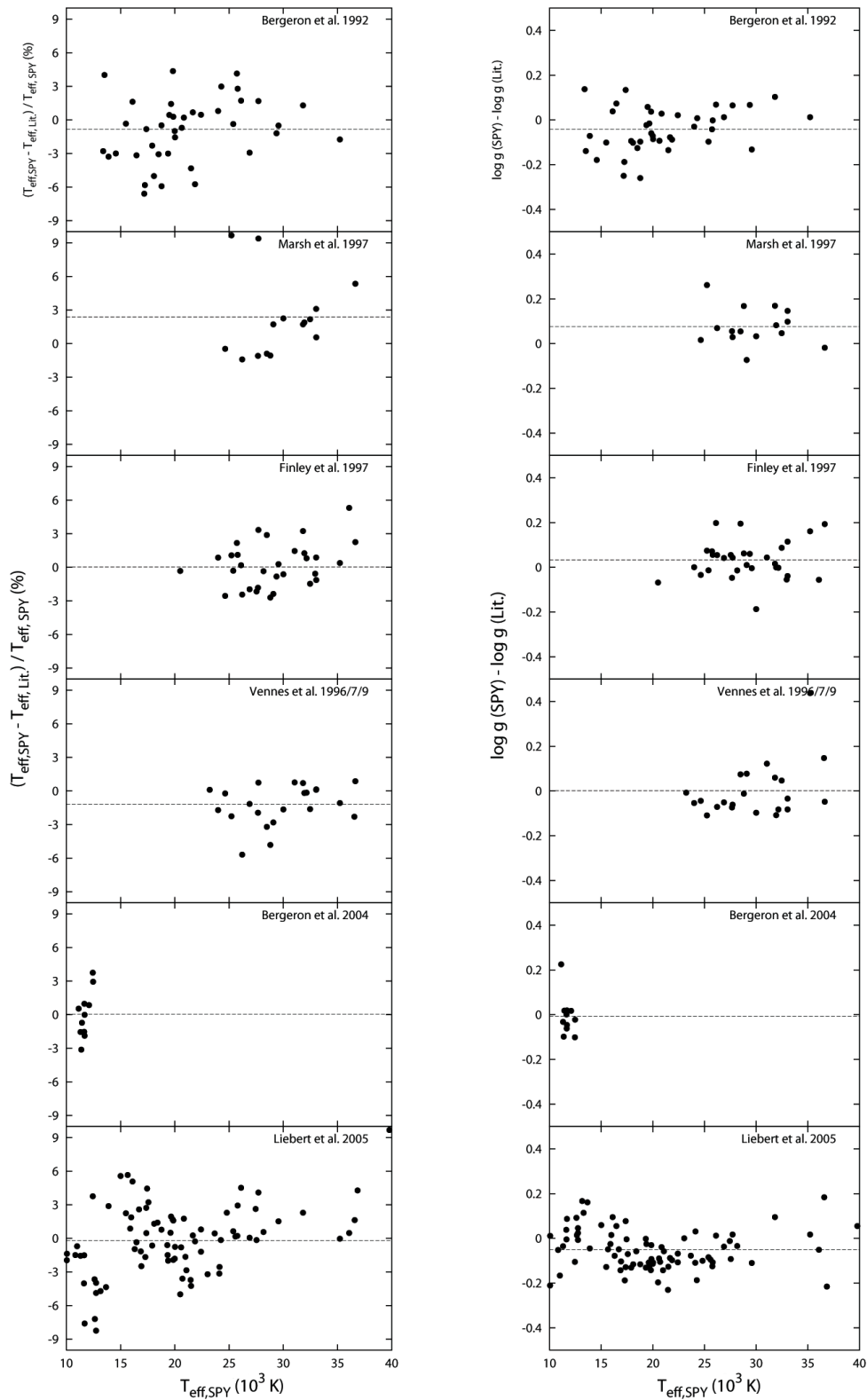


Figure 4.5: Comparison to the parameters derived by other investigations for common objects. The dashed lines give the average differences.

Table 4.3: Comparisons of different re-analyses of the data of this work to a sub-sample of the Liebert et al. (2005) data.

Sample	$\Delta(\log g)$	$\Delta(T_{\text{eff}})[\%]$	n
4020	-0.050 ± 0.051	2.09 ± 2.45	9
4055	-0.230 ± 0.074	-3.31 ± 2.73	9
Three regions	-0.154 ± 0.069	-0.92 ± 2.87	9

by fitting the continuum around H ϵ and H δ using a set of three spectral regions centered on 3930 Å, 4005 Å, and 4055 Å, labeled “three regions” in the table. Although the test with three intervals yields a better agreement with the literature for T_{eff} , both results for $\log g$ are in strong disagreement with the literature results. This is consistent with the interpretation that the continuum around 4020 Å indeed represents the continuum levels of the adjacent Balmer lines, while that around 4055 Å is a generally less correct region of the spectra. The value of χ^2 is on average not significantly improved by any of the alternative continuum placements.

A different test of the influence that the observed continuum discontinuities might have on the results is an investigation of the average value of $\log g$ in an affected and an un-affected sub-sample of the SPY spectra. The average values are $\langle \log g \rangle = 7.915$ for such a sample of unaffected objects and $\langle \log g \rangle = 7.880$ for a sample of strongly affected objects where the fit quality near H δ is bad. The difference of 0.035 dex is small compared to the estimates of the uncertainty that were derived in the previous section. Like the comparison to literature data, this is consistent with the assumption that even for the fits of the most problematic spectra, the derived parameters are not unreliable.

4.4 Comparison to Koester et al. 2001

A comparison of the results to those of Koester et al. 2001 is different from the literature comparisons of section 4.2 since largely the same analysis procedure and the same data that they used are employed here. Only the results for those 108 objects for which Koester et al. used the same spectra as this work are regarded. Any object for which the final results are derived from newer spectra that were unavailable in their study are left out. Furthermore, five objects for which the Koester et al. (2001) fits clearly terminated on the wrong side of the temperature of maximum Balmer line strength are left out.

As displayed in Figs. 4.6 and 4.7, a systematic shift and scatter of $\Delta(T_{\text{eff}}) = -1.65 \pm 3.142\%$ and $\Delta(\log g) = 0.05 \pm 0.10$ (2001 - this work) is the result. These differences are larger than expected, and similar to those found in the comparisons with other, completely independent samples. Thus, the results of this work seem to be not more closely related to the 2001 results than to the other literature results.

To investigate the source of this unexpected effect, not only the final results are compared to those of 2001, but also results of a subset of the data that were analysed by

- (a) using not a quadratic continuum fit, but a linear fit like it was done in 2001, which is the main difference of both analyses in terms of the fitting method,

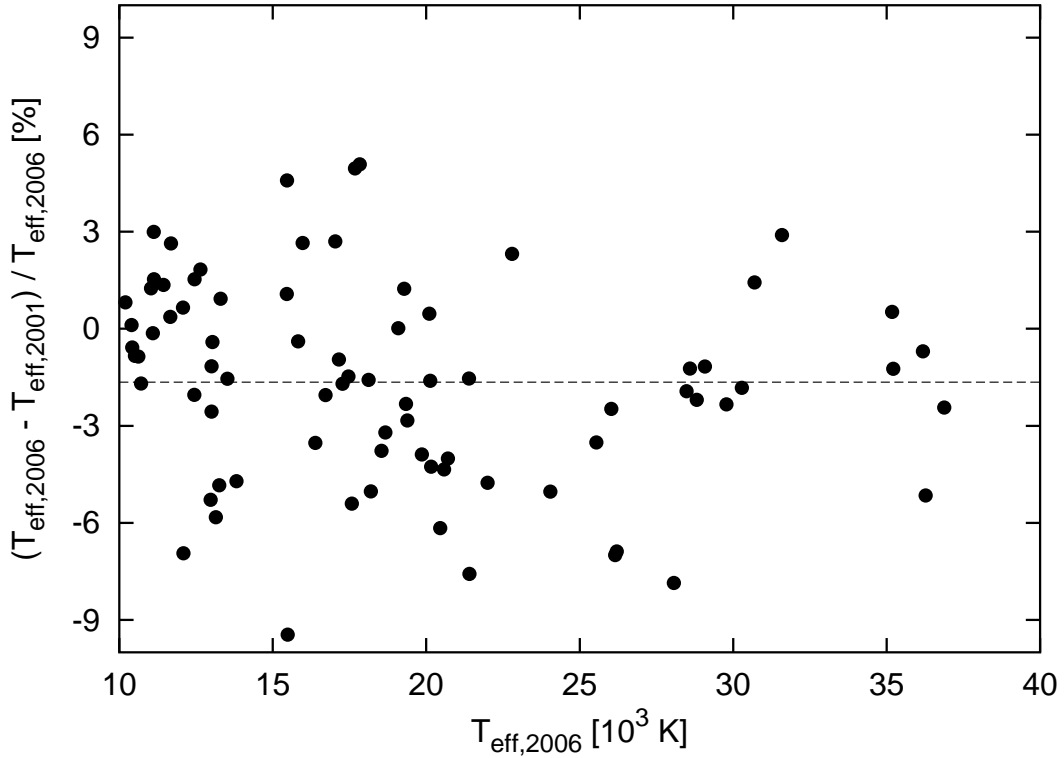


Figure 4.6: The differences in T_{eff} between these data and those of Koester et al. 2001. The dashed line represents the mean difference of -1.65%.

- (b) in addition to (a), using versions of the recent (2006) spectra that are rebinned to a lower resolution as it was employed in 2001, and
- (c) in addition to (a), using the same lower-resolution spectra that were used in 2001, i.e., not the current re-reduced versions of the spectra (see section 2) but the original versions.

Table 4.4: Results of the comparison of the results of this work to those of Koester et al. 2001.

2001 - ...	$\Delta(\log g)$	$\Delta(T_{\text{eff}})$ [%]	n
This work	0.050 ± 0.099	-1.65 ± 3.14	108
Sample (a)	-0.024 ± 0.052	-2.23 ± 2.75	60
Sample (b)	-0.017 ± 0.054	-2.29 ± 2.95	60
Sample (c)	-0.017 ± 0.045	-0.70 ± 1.21	60

Each of these steps should take the results closer to those of Koester et al. (2001), and thus decreasing systematic shifts are expected with each step. The results for all four comparisons are listed in table 4.4, and they are largely as expected: Especially the change of the fit method and the use of the re-reduced spectra seem to increase the difference between these results and those of 2001. The major effect seems to be the new reduction of the spectra. Given the systematic shift that has to be a consequence of the new reduction, and the fact that this shift is comparable in size with that of other, completely

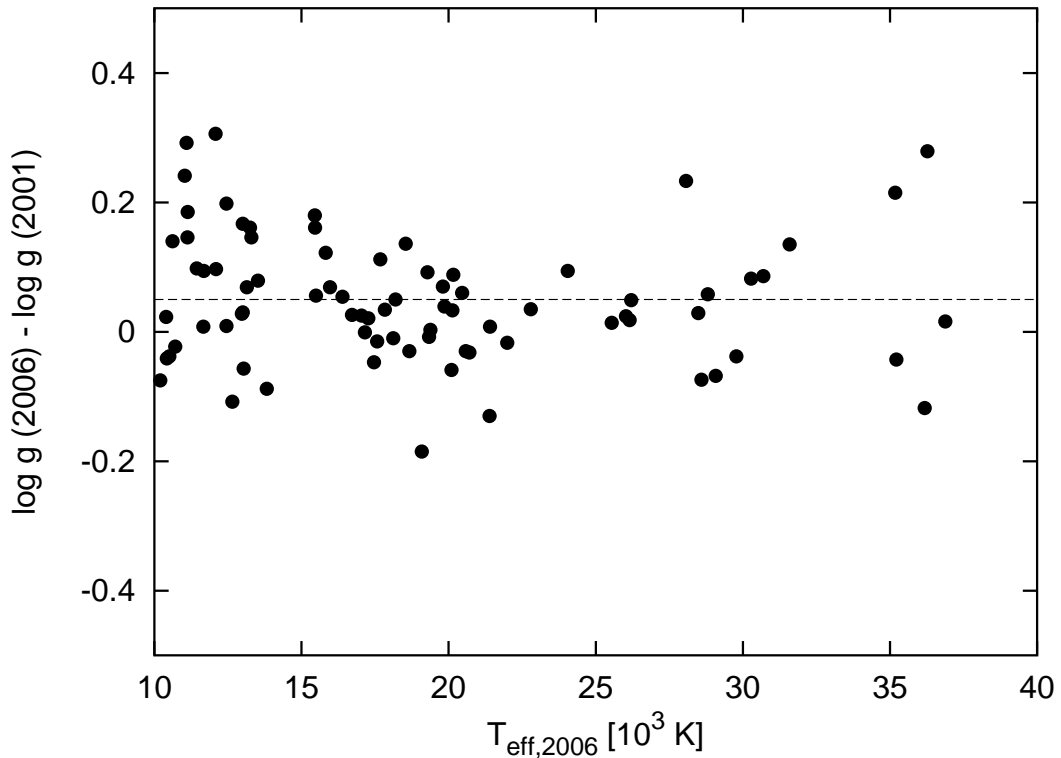


Figure 4.7: The same as Fig.4.6, for $\log g$, with an average difference of 0.05 dex.

independent investigations, the conclusion that the re-reduced spectra constitute a set of data that is practically independent from that of Koester et al. (2001) might be drawn.

It is found that the 2001 fits for which the disagreement with the new results is largest are less accurate than the new fits. This is mostly based on flaws in the early versions of the spectra. One can therefore be confident that the new fit results are indeed improved results, compared to those of 2001, and that this is the reason of the rather large differences of the resulting atmosphere parameters.

4.5 DA Mass Distribution

Masses for all objects with DA atmosphere fits were computed using the cooling tracks of Wood (1995). These tracks tabulate the evolution of the decreasing effective temperatures T_{eff} and radii R during the aging of a white dwarf, and are calculated for a number of given masses M of the white dwarf as well as for a number of given hydrogen and helium mass fractions.

Each track describes a function $R_M(T_{\text{eff}})$ for a certain stellar mass. Thus, given the fitted effective temperature, a radius R_M can be obtained from each track. The surface gravities for each track mass and the given temperatures are then computed,

$$\log g_M = \log(G M / R_M^2)$$

and finally, a function $M(\log g)$ is interpolated from the $\log g_M$ values, and the mass of the object can be obtained from this function. The overall uncertainty of 0.07 dex of the surface gravities leads to a typical uncertainty of the masses of $0.05 M_{\odot}$.

The cooling tracks that are used are those that were calculated for “thick” hydrogen envelopes, i.e., for an H envelope mass of $M_{\text{H}} = 10^{-4} M_{*}$ in units of the stellar mass, and He envelopes of $M_{\text{He}} = 10^{-2} M_{*}$.

For a statistical analysis, only single DA with effective temperatures below 40000 K are used, in order to exclude objects for which NLTE effects are important. Furthermore, a considerable increase of the average $\log g$ and mass below a temperature of ~ 13000 K is found, as shown in Fig. 4.10. This is an effect that has been observed in other samples before, most recently in those of Liebert et al. (2005) and Kleinman et al. (2004). It is probably not due to a truly increased gravity of these objects. Although it might indeed be possible that the progenitors of the oldest white dwarfs had a comparatively high mean mass, such an effect would only be expected to be found for white dwarfs with much higher cooling ages and much lower temperatures than $T_{\text{eff}} \sim 13000$ K. Therefore it is assumed that the increased masses are not real but probably an effect of the onset of convection below these temperatures; either through mixing of helium into the atmosphere and thus an increased pressure broadening of the Balmer lines (Bergeron et al. 1990a, 1992), or through systematic errors of the models. Such errors would however have to be present and similar in different, independent sets of model atmospheres, since the same results have been found using models of different authors. In either case, a higher $\log g$ is most probably only mimicked by other effects and therefore objects in which such effects might be present should not be included in a mass distribution. Thus, only objects with $T_{\text{eff}} > 13000$ K are used here to assemble a mass function.

For the resulting sample of 395 objects, the average surface gravity is $\langle \log g \rangle = 7.874$ dex with a one sigma variance of 0.241 dex. The average mass of the distribution is $0.572 M_{\odot}$ with a variance of the entire distribution of $0.122 M_{\odot}$. The large variance is due to the extended shape of the distribution; the width of the main peak is much lower. The mass distribution is plotted in Fig. 4.8. Besides the main peak just below $0.6 M_{\odot}$, it exhibits a secondary peak close to $0.4 M_{\odot}$. This feature is already well known from earlier studies; it is attributed to helium-core white dwarfs that can emerge from the evolution of binary star systems (Iben & Tutukov 1986). Another secondary peak is centered on $0.8 M_{\odot}$; it is comparable to similar peaks in the mass distributions of the samples of Bergeron et al. (1992), Liebert et al. (2005) and Napiwotzki et al. (1999). In those samples it appeared however not very pronounced, either only as a high-mass “shoulder” of the main peak in Liebert et al. (2005), or as an isolated peak that comprises only an insignificantly small number of objects in the other two studies. Here, the $0.8 M_{\odot}$ feature extends to approximately $0.9 M_{\odot}$, and contains more than 40 stars, while only five objects with even higher masses are found in the SPY sample. Thus, in this mass distribution there is clearly no distinct high-mass component extending from $0.9 M_{\odot}$ upwards to $1.2 M_{\odot}$, like it is found in the Marsh et al. (1997) sample.

The origin of the $0.8 M_{\odot}$ peak is uncertain. It is even more pronounced than the peak of He-core White Dwarfs. It might be a real feature; this possibility is supported by considering a “smoothed” mass distribution, shown in Fig. 4.9. This smoothed plot was derived as the average of five mass distributions with a binning of $0.5 M_{\odot}$. The binning for each of the distributions was shifted by $0.1 M_{\odot}$, yielding the five different distributions. These were then averaged by computing the mean value of all five distributions in $0.1 M_{\odot}$ steps. The smooth appearance of the $0.8 M_{\odot}$ peak in the smoothed plot indicates that it is not merely an artifact of the binning. However it cannot be interpreted with certainty as a

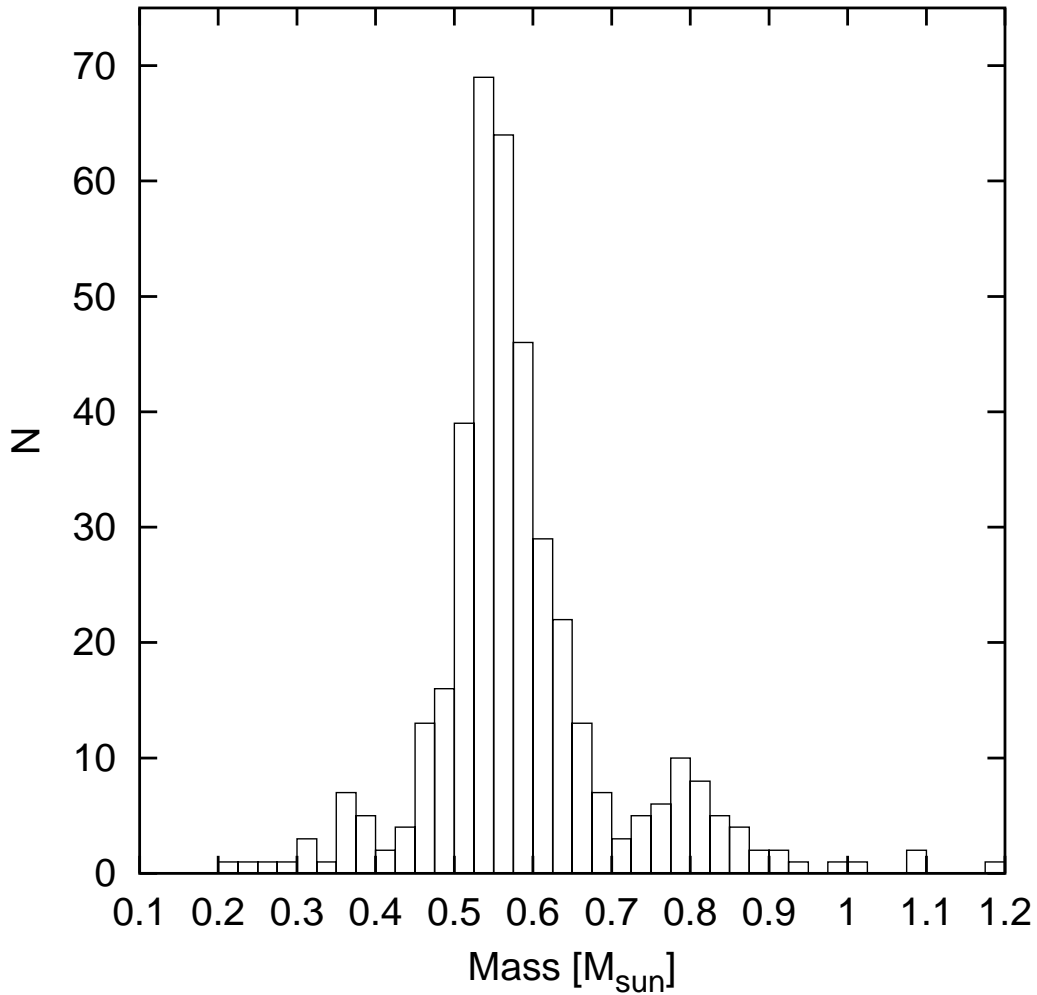


Figure 4.8: The DA mass distribution, determined from 395 single DA with $13000 \text{ K} < T_{\text{eff}} < 40000 \text{ K}$. The mean mass is $0.572 \pm 0.122 M_{\odot}$.

real feature.

There is no explanation for such a bi-modal mass distribution of the CO-core white dwarfs as a result of single star evolution. Some authors (Marsh et al. 1997, Vennes 1999) have suggested that high mass peaks that they find in their samples at masses of $\sim 1 M_{\odot}$ and $\sim 1.2 M_{\odot}$ might be due to mergers of white dwarfs as the result of binary star evolution, and that the $\sim 1 M_{\odot}$ peak might be explained by mergers of a He-core with a CO-core white dwarf, and the $\sim 1.2 M_{\odot}$ peak by mergers of two CO-core white dwarfs. The mass of the $0.8 M_{\odot}$ peak is too low to be connected to such processes, but some of the objects in this mass range might be the result of mergers of two He-core white dwarfs.

Compared to the results of the two largest other studies of this kind, the average mass of the SPY DA stars is about $0.031 M_{\odot}$ smaller than that found by Liebert et al. (2005) from their investigation of objects of the PG sample, and $0.008 M_{\odot}$ smaller than the mean mass found by Giovannini et al. (2005) from an analysis of the SDSS DA fit results of Kleinman et al. (2004).

The mass distributions of several other earlier investigations show mean masses ranging from 0.56 up to more than 0.60 solar masses, and although the SPY peak mass is

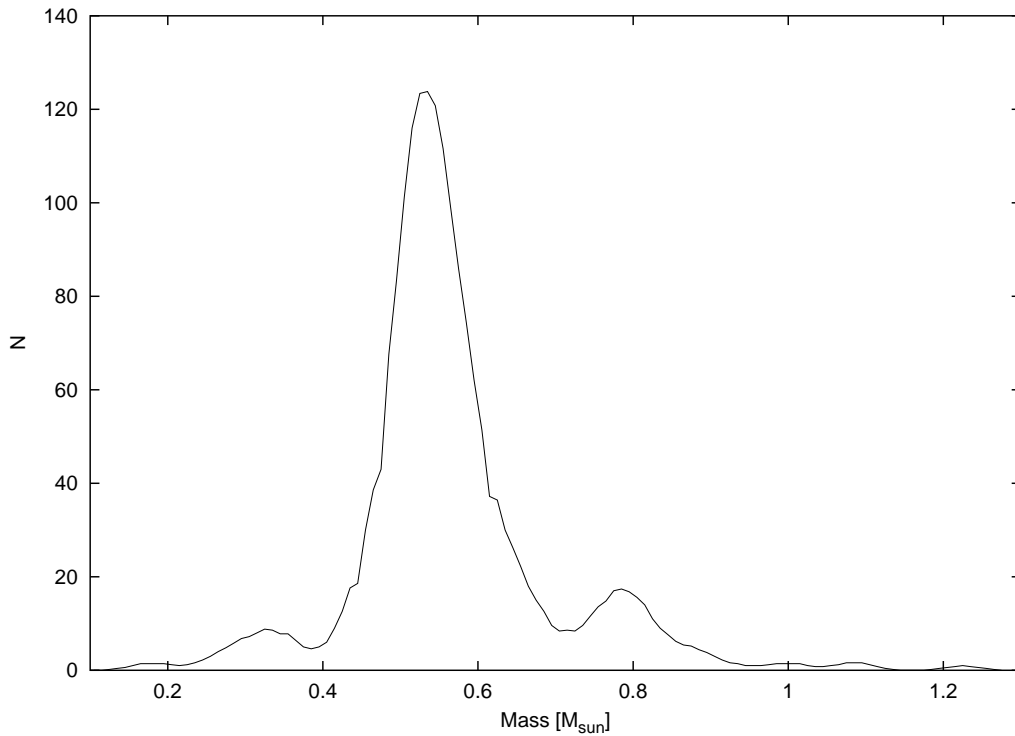


Figure 4.9: The smoothed DA mass distribution, determined as the average, computed at $0.1 M_{\odot}$ steps, of five mass distributions of the same sample but with a shift of the $0.5 M_{\odot}$ binning by $0.1 M_{\odot}$ with respect to each other. The N value for a certain mass is the number of objects that are found in a mass bin of $0.5 M_{\odot}$ width that is centered on that mass value.

somewhat lower than that of the two largest other such samples, it is placed within the range of mean masses of the earlier studies. The SPY results are in agreement with, e.g., those of Bergeron et al. (1992) and Marsh et al. (1997).

There seems to be some confusion in the literature concerning the mean masses of such samples since often simply a “peak mass” is given which is determined by fitting a gaussian to the bins that make up the central peak. Such a peak mass is of course lower than the mean mass because the DA mass distributions of all recent studies show an asymmetric distribution with more objects at high masses than at low masses. Giovannini et al. (2005) compare their mean mass ($0.58 M_{\odot}$) to that which Madej et al. (2004) derived for the SDSS sample (i.e., the same data) but without noting that the Madej et al. value is a peak mass, not a mean mass.

Koester et al. (2001) found a mean mass of $0.59 M_{\odot}$ from the SPY data, but no low-temperature cutoff was used for their sample, and thus, objects which exhibit the unexplained high gravities at temperatures below 13000 K were included. If the same range of temperatures as in Koester et al. (2001) is used here, a mean mass of $0.60 M_{\odot}$ is the result.

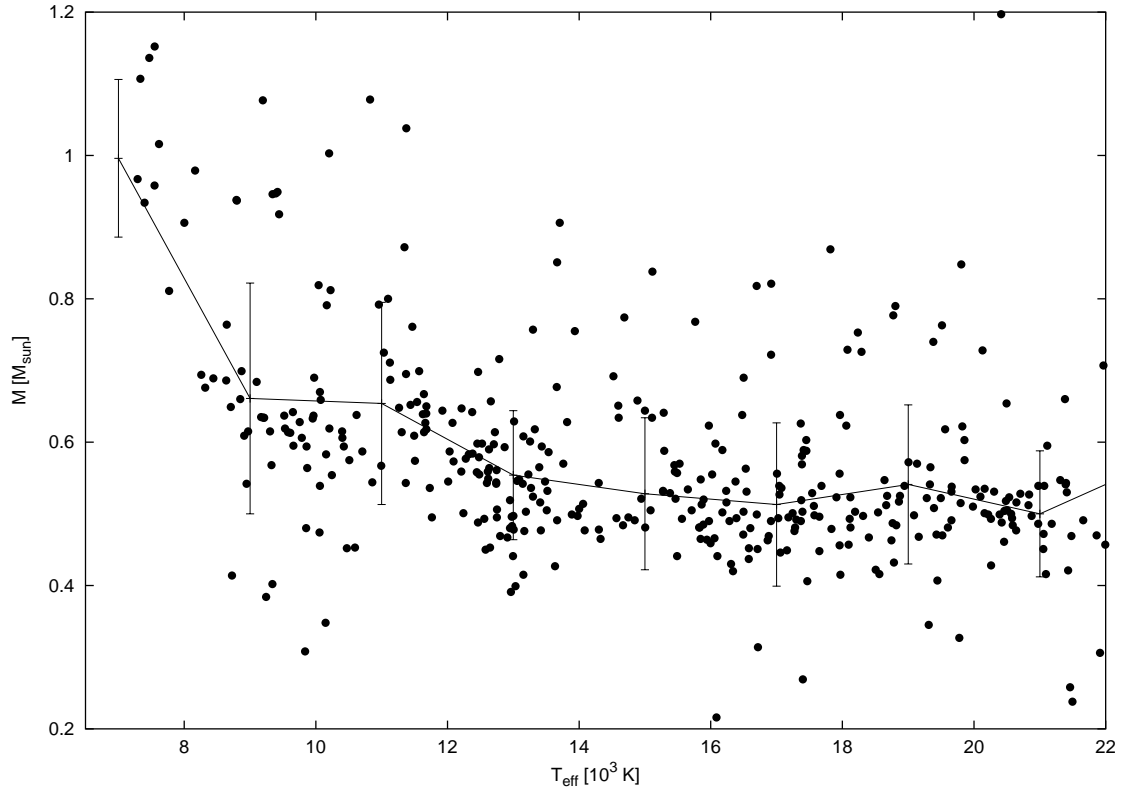


Figure 4.10: The DA masses plotted with respect to effective temperature, for lower temperatures and including those below 13 000 K that were omitted in the mass distribution in Fig. 4.8. The average masses in 2000 K-wide temperature bins are plotted, showing the increase of the mean mass near 13 000 K. The error bars display the 1σ variances of the subsample mass distributions of each temperature bin. The masses at very low temperatures ($T_{\text{eff}} < 8000$ K) are erroneous due to the strong line broadening that is not included in the models.

4.6 DA+dM Binaries

The DA+dM binaries are fitted separately from the other hydrogen-rich spectra. $H\alpha$ and $H\beta$ are not used for these fits but only the higher Balmer lines, since the red part of the spectrum is normally dominated by the companion while the bluer part of the spectrum is usually governed by the white dwarf flux. The lines higher than $H\beta$ are completely unaffected by the companion in many DA+dM spectra, and even in those spectra where this is not the case, meaningful fits can mostly be achieved. These results are listed in table B.1, where also an estimate of the degree of contamination by companion features is given, (a) for clean DA spectra, (b) for mild contaminations, mostly by filled-up line cores due to H emission, and (c) for considerable contamination and thus doubtful fit results. This is illustrated in Fig. 4.11.

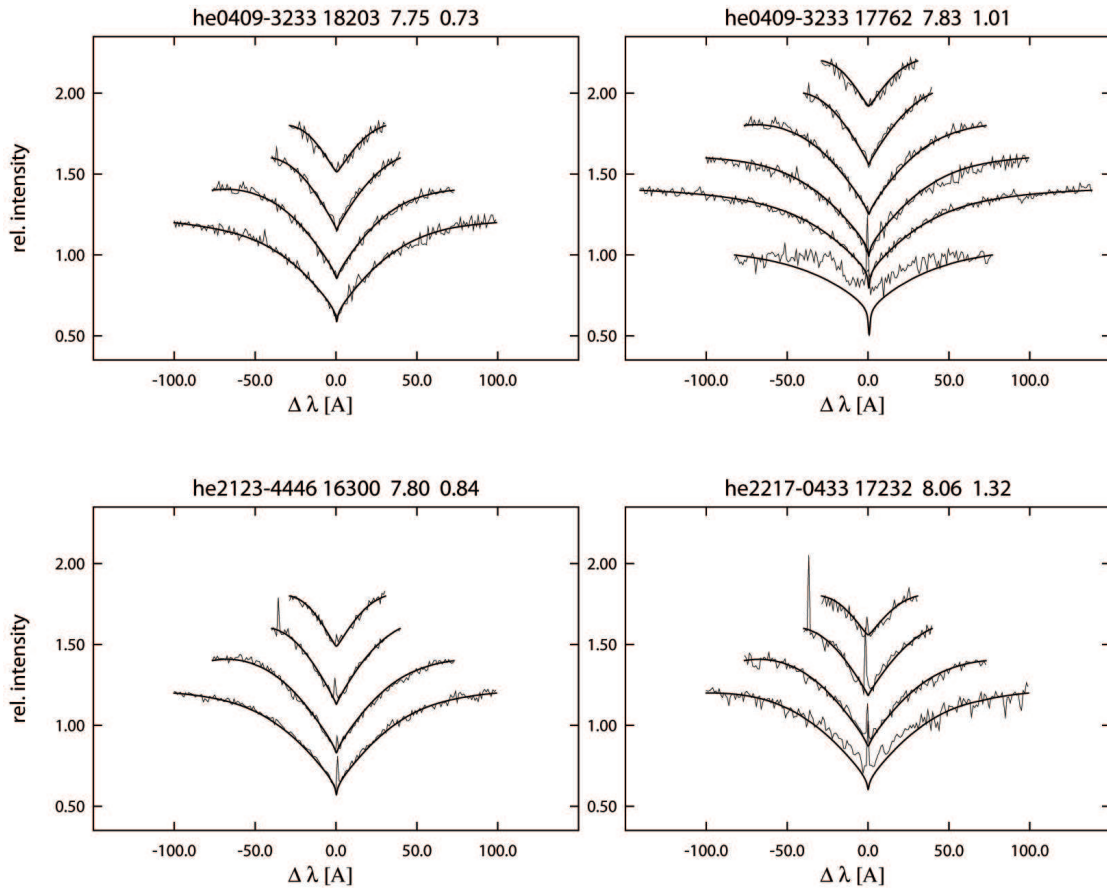


Figure 4.11: Example fits of DA+dM binaries with spectra where the higher Balmer lines show no presence of the companion (upper left, type 'a'), where only the line cores are affected (lower left, type 'b') and where the companion flux is strong and affects the shapes of even the higher Balmer lines (lower right, type 'c'). As a comparison, the upper right panel shows a fit of the same spectrum as in the upper left panel, but including $H\alpha$ and $H\beta$.

4.7 Identification of Probable New ZZ Ceti Stars

Numerous DA are placed in the region of the ZZ Ceti instability strip by their atmosphere parameters, some of which are previously known ZZ Ceti pulsators. Three stars have earlier been identified as new variables by Fontaine et al. (2003) and Bergeron et al. (2004), based on the SPY parameters that were published by Koester et al. (2001).

Fig. 4.12 shows the temperatures and gravities of the DA stars in the region of the instability strip; several of them had not been checked for variations when this work was begun. Since then, time-resolved photometry observations have been obtained for several of them, resulting in the publication of six new ZZ Ceti stars that are based on these SPY results by Silvotti et al. (2005), Castanheira et al. (2006b) and Voss et al. (2006). In addition, further 3 new SPY-derived DAV stars were recently detected. They are published here for the first time. These lightcurve observations and their results are described in part IV. Not all stars that are placed within or near the empirical edges of the ZZ Ceti instability

strip have yet been checked for pulsations; they are therefore interesting objects for further studies.

The distribution of the variable and non-variable objects in Fig. 4.12 can be studied to derive a further constraint on the accuracy of the atmosphere fit results. The non-variable stars would be expected to be found outside of the plotted empirical edges of the instability strip, the hDAV stars (see section 9) would be expected in the high-temperature part of the strip, and the cDAV pulsators closer to the red edge. This is not exactly the case, since some pulsators are found at higher temperatures than the blue edge, and the cDAV and hDAV pulsators are not separated at the center of the strip. Both is however consistent with the assumption of an overall temperature uncertainty of $\sigma(T_{\text{eff}}) \approx 2\%$ which amounts to approximately 230 K in the region of the instability strip. Also the occurrence of three non-variable objects within the blue edge is consistent with such an uncertainty, but the two non-variables that are found near the center of the strip (according to the Bergeron edges) would require much larger temperature uncertainties to be possibly indeed placed outside the strip. These two object are therefore crucial for the judgement of the fit accuracies. The Mukadam edges would give a better match to these two stars since the required temperature uncertainties are smaller for those edges. On the other hand, the Bergeron edges offer a better overall match of the object distributions, especially because the temperatures of the hottest three pulsators are not reproduced well by the Mukadam edges.

It is possible that the two seemingly non-variable stars in the center of the strip are in fact variable but simply did not show their pulsations when they were observed because of beating effects, or because their pulsations are weaker than the upper limits that were derived for any variations. The first object, HS 0926+0828, has been observed only on one occasion, and an upper limit for intensity changes of 0.6% was derived (Mukadam et al. 2004a). The other object, WD 1026+023, was observed on multiple occasions and an upper limit of 0.3% was found by Kepler et al. (1995). The second star is thus a more reliable non-variable than the first, but both might well pulsate below the limits. An example for this possibility is WD 1116+026 which is not variable according to Kepler et al. (1995) with a limit of 0.3%, but was later found to show weak variations of about 0.1% (Gianninas et al. 2005).

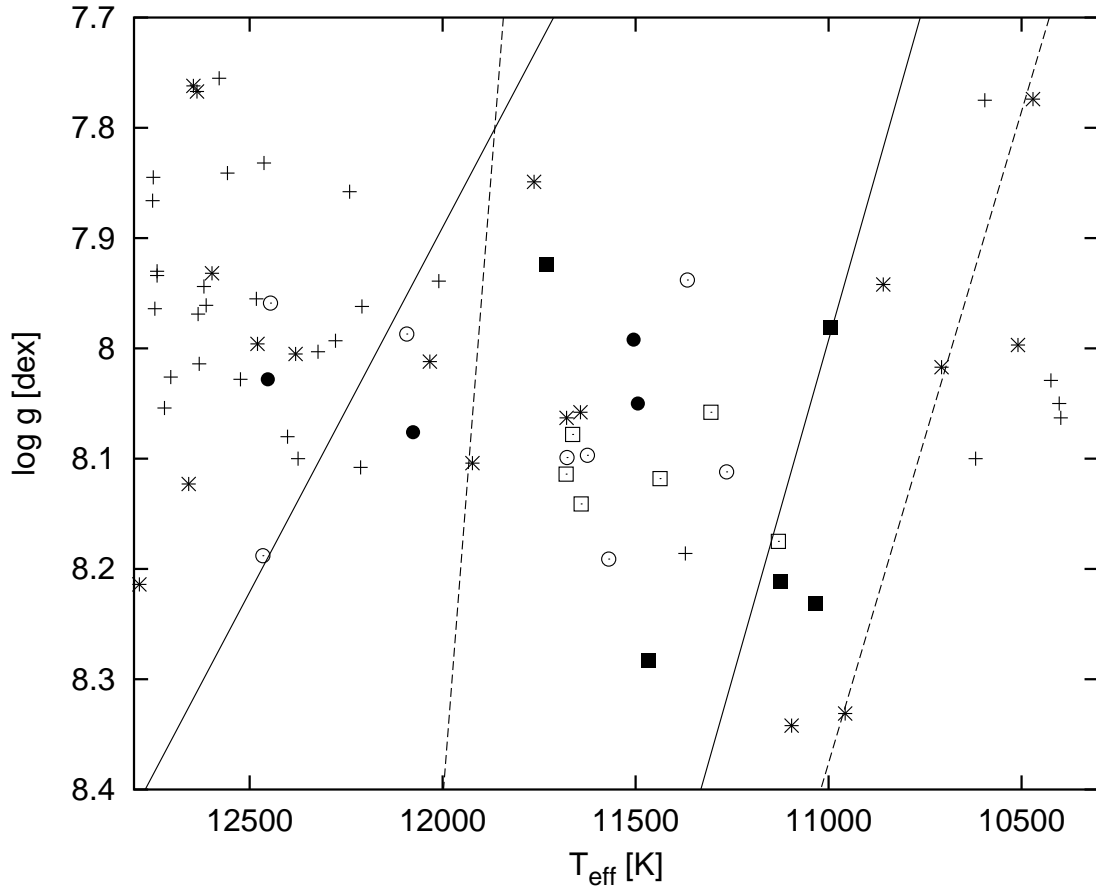


Figure 4.12: SPY parameters of DA stars in the region of the ZZ Ceti instability strip. Open and filled symbols are ZZ Ceti variables; the filled symbols show those that have been newly detected based on this work. Asterisks indicate objects for which no variations could be found, and objects shown as crosses have not yet been checked for pulsations. The empirical edges of the instability strip according to Bergeron et al. (2004) and Mukadam et al. (2004b) are plotted as solid and dashed lines, respectively. Squares are cDAV variables, and circles are variables of the hDAV subtype.

Chapter 5

DB Star Fit Results

There are 59 DB stars in the SPY sample for which fit results are obtained. Of these, 23 show only helium lines in their spectra, and 32 are DBA stars that show traces of hydrogen, mostly only an $H\alpha$ line. 9 of the DBA stars also show metal lines in their spectra. The four remaining helium-rich objects are two DBZ stars without hydrogen, and two DB+dM binaries.

5.1 Remarks on DBA, Cool DB, and DB+dM Fits

DBA spectra: The DBA spectra were not fitted with the grid of pure helium model atmospheres, but with model spectra from 4 grids of atmospheres with admixtures of hydrogen, $N_{\text{He}}/N_{\text{H}} \equiv y = 10^2, 10^3, 10^4, \text{ and } 10^5$, respectively. Each of the DBA was fitted with all 4 model grids. The best of the 4 resulting solutions was selected based on the χ^2 , and based on a visual inspection of the fits. For many objects the differences of χ^2 or of the visual appearance are small, and no decision for one best fit, i.e., one best $\log y$, was possible. However, two of the model fits of different $\log y$ could always be selected as upper and lower limits of the hydrogen abundance. If no single solution was selected, the upper and the lower limit solution are given in the table, C.1.

The SPY spectra of 14 stars that were classified as DB before show weak hydrogen lines, mostly $H\alpha$ only, and according to the model atmosphere fits the hydrogen abundances of only one of these stars is larger than $\log y = 5$, all others have $\log y \geq 5$. This is smaller than the abundances of the DBA stars that have so far been observed and are found in the literature; the high resolution and S/N of the SPY spectra allows to detect smaller traces of hydrogen than it was possible from the spectra of earlier investigations. Among the new DBA is one of the few known DBV variable stars, WD1115+158, with $\log y = 4$.

The detection of low hydrogen abundances in such a large number of spectra significantly increases the fraction of the DBA stars among the white dwarfs with helium-rich atmospheres; the ratio of the numbers of DBA and DB stars is $N_{\text{DBA}} / N_{\text{DB}} = 0.22$ in the catalogue of McCook & Sion (1999), but here it is five times as large, $N_{\text{DBA}} / N_{\text{DB}} = 1.5$, i.e., 60% of all helium atmosphere SPY spectra also show hydrogen lines.

Traces of H in hot He atmospheres: The visibility of hydrogen in a helium-rich atmosphere depends on the temperature; Balmer lines of equal strength correspond to higher abundances at higher temperatures. If the effective temperature is lower than $T_{\text{eff}} \approx 20\,000$ K, even small hydrogen abundances of $y > 10^5$ produce clearly visible Balmer lines, and thus such abundances can be excluded if no H features are present in the spectrum. For the hotter DB, the absence of H lines only allows to exclude $y \leq 4$, since a hydrogen fraction of 10^{-5} in the atmosphere would be invisible at temperatures above 20 000 K. Therefore, the spectra of these hot DB stars were also fitted with the $y = 10^5$ grid, since even the presence of an invisibly small amount of hydrogen affects the strength of the He lines and thus adds uncertainty to the pure He atmosphere fit results of these spectra. The $N_{\text{He}}/N_{\text{H}} = 10^5$ results are also listed in table C.1. The average difference of the fit result with hydrogen to that without hydrogen is consistent with zero, i.e., the average of $T_{\text{eff}, \log y=5} - T_{\text{eff}, \text{pure He}}$ is an order of magnitude smaller than the scatter of these values, and the same for the values of $\Delta \log g$.

DB+dM spectra: There are two stars in the DB sample that show composite spectra. These DB+dM binaries were treated like the DA+dM stars, i.e., the red part of the spectra was not used in the fits and only the HeI lines at short wavelengths of $\lambda < 4500\text{\AA}$, where the flux of the late-type companion is low, were fitted.

Spectra of cool DB stars: The broadening of the He lines is not accurately described by Stark broadening alone in cool atmospheres. The models which only take Stark broadening into account therefore do not produce accurate fits if $T_{\text{eff}} < 15000$ K. This is similar to the effect that was already pointed out concerning the cool DA white dwarfs; van der Waals interaction is becoming important at low temperatures. For even cooler atmospheres of $T_{\text{eff}} < 14000$ K, no fit is achieved since $\log g$ converges to exceedingly high values. In the same way as for the cool DA, this happens because the strong broadening mimicks line broadening that is caused by very high gravity.

There are several objects in the SPY sample that only show weak HeI 5876 Å and/or H α lines, and for which no fit can be achieved. These are probably cool white dwarfs with He-dominated atmospheres. All these not fitted cool objects are listed in table D.1.

5.2 DB Fit Accuracy

As for the DA stars, the accuracy of the fit can be judged if the fit results of two spectra of one object are compared. This has been done for 24 DB and DBA stars for which two spectra of similar qualities are available. The resulting mean differences are larger than that of the DA star fit results: $\langle \Delta T_{\text{eff}} / T_{\text{eff}} \rangle = 3.33\%$ and $\langle \Delta \log g \rangle = 0.081$ dex. The large $\langle \Delta T_{\text{eff}} \rangle$ is dominated by two outliers at high temperatures. If these are omitted, the results are $\langle \Delta T_{\text{eff}} / T_{\text{eff}} \rangle = 1.05\%$ and $\langle \Delta \log g \rangle = 0.077$ dex, which is almost surprisingly small.

A comparison of the DB fit results to those that are found in the literature for some common objects shows a different picture: The differences are much larger than for the DA stars, pointing to more uncertain results. In a comparison to the samples of Beauchamp et al. (1999) and Castanheira et al. (2006a) large systematic shifts are

found; the SPY temperatures are considerably lower than those in the literature: $\langle \Delta T_{\text{eff}} \rangle = 1293 \pm 2302$ K, $\langle \Delta \log g \rangle = 0.035 \pm 0.104$ dex (Beauchamp et al. (1999) – SPY), and $\langle \Delta T_{\text{eff}} \rangle = 1500 \pm 2600$ K, $\langle \Delta \log g \rangle = 0.1 \pm 0.6$ dex (Castanheira et al. (2006a) – SPY). However, these comparisons are problematic, because both of these studies do not treat the hydrogen abundances in DBA stars as accurately as this work, i.e., they only fit all stars with a pure He model and with one low hydrogen admixture model. Furthermore, the Beauchamp et al. sample only includes objects for which they find $T_{\text{eff}} > 20\,000$ K, and the Castanheira parameters are derived from fits of UV spectra.

The uncertainties of the DB fit results are thus much less well known than those for the DA; they might be very low as suggested by the differences of the results of different SPY spectra or very high and biased towards low temperatures as it is found from comparisons to other studies.

5.3 DB Masses

Masses for the DB were derived analogously to the masses of the DA stars, using the mass-radius relation from Wood (1995) but now for helium envelopes with $M_{\text{He}} = 10^{-4} M_*$, and without hydrogen.

The average mass of all DB stars is $0.606 M_{\odot}$; that is about $0.03 M_{\odot}$ larger than that of the SPY DA stars, but well within the typical masses of DA white dwarfs. The DB mean mass of this analysis is also much lower than the unexplainedly high value of $0.77 M_{\odot}$ that was found for the DB stars by Koester et al. (2001); since the same fit methods, model atmospheres and mass-radius relations that they used were also employed here, their large value remains unexplained. Beauchamp et al. (1996) found that the distribution of the DB masses is narrower than that of the DA stars, only 5% of their DB stars are placed outside of a mass interval from $0.5 M_{\odot}$ to $0.65 M_{\odot}$. Here, a fraction of 25% of the DB is found outside that interval, which is not too different from the 32% of the SPY DA stars that have masses below $0.5 M_{\odot}$ or above $0.65 M_{\odot}$.

The average masses and surface gravities of different sub-samples are listed in table 5.1. It can be seen that the mean mass is higher for the DBA than for the DB stars. The on average higher masses of DBA stars were already pointed out earlier; they might be due to an increased accretion of hydrogen by stars with higher mass, and possibly also to a decreased dilution of the accreted hydrogen in a convection zone that is thinner in high mass stars (Beauchamp et al. 1996). Among the DBA, a comparison of objects with higher hydrogen abundances to those with lower abundances shows an increase of the mean mass with the hydrogen abundance. However, the differences of the mean masses are smaller than the typical mass uncertainties $\sigma(M) \sim 0.5 M_{\odot}$, and thus the samples are not significantly different, although there is a clear trend towards higher masses of DBA stars.

The DB and DBA mass distributions are shown in Fig. 5.1. They appear to be considerably different, but the numbers of objects in each bin is small and thus the differences are probably insignificant. The DBA exhibit a sharp peak at masses of $0.6 M_{\odot} - 0.65 M_{\odot}$ compared to the DB stars that show a much broader peak at lower masses, i.e., a distribution that is more similar to that of the DA. It can also be recognized that the distribution of DBA stars with low hydrogen abundances (the filled parts of the DBA mass distribution

bins) is similar to that of the remaining DBA stars with high hydrogen abundances.

Table 5.1: Properties of the DB mass distribution and different subsamples.

Sample	$\langle \log g \rangle$	$\langle M \rangle [M_{\odot}]$	$\sigma(M) [M_{\odot}]$	N
All DB	8.011	0.606	0.088	55
DB without H	7.965	0.580	0.084	25
All DBA	8.037	0.620	0.076	29
DBA with $\log y \leq 5$	8.034	0.614	0.059	18
DBA with $\log y > 5$	8.042	0.631	0.097	11

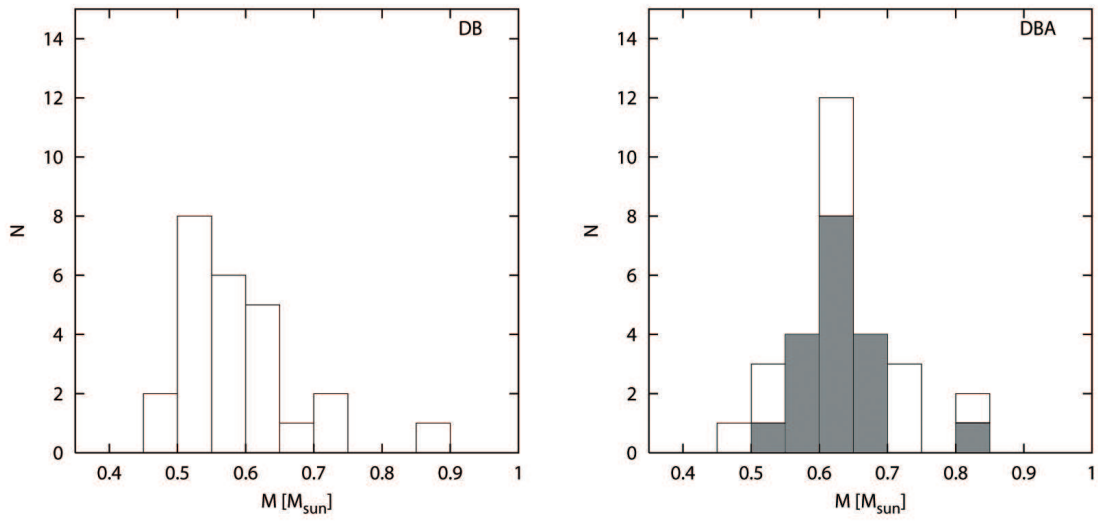


Figure 5.1: The mass distributions of DB stars without traces of hydrogen (left) and DBA stars (right). The grey parts of the DBA mass distribution bins indicates the fraction of each bin that is made up by DBA stars with low hydrogen abundances, $\log(N_{\text{He}}/N_{\text{H}}) \geq 5$.

Chapter 6

Objects Without Model Fits

There are 95 objects in the SPY sample for which neither a hydrogen nor a helium atmosphere fit could be achieved. The types of these objects were determined by a visual inspection, and the numbers of objects of each type is given in table 6.1.

Table 6.1: Types and numbers of objects without a model atmosphere fit. The “other” objects include 2 PG 1159 stars, 2 DAB and 3 He-sdO subdwarfs.

Object Type	Number of Objects
Cool DA	19
High-field DAP & DABP	7
Hot DAO	3
Cool DB & DBA	9
DZ & DZA	12
DQ, DQA & DQZ	14
DC	13
Hot DO & DOZ	10
Other	9

Many of these are objects without hydrogen or helium lines in their spectra: DQ, DZ and DC white dwarfs, i.e., helium-atmosphere white dwarfs that are too cool to show helium lines. Featureless DC spectra served calibration purposes during the SPY data reduction; this is the reason why objects which were known to exhibit featureless spectra had been included in the SPY target list.

Other objects for which no fit results were obtained are hot DAO and DO White Dwarfs whose temperatures are outside of the temperature range that is covered by the employed He and H model atmosphere grids, i.e., larger than 50 000 K and 100 000 K, respectively.

Besides that, there are several objects that show only weak HeI or Balmer lines, mostly only $H\alpha$ and/or HeI 5876 Å. These are probably cool objects for which the lines are too weak, or too broadened by neutral scattering, to yield a fit. For the spectra of this type, a fit result of low temperature is obtained if $\log g = 8.0$ is kept fixed during the fit, and if only the lines that are present in the spectrum are fitted, e.g., in some cases only $H\alpha$. These fits with fixed $\log g$ are rather inaccurate and do not reproduce the line profiles

correctly. However, such fits with fixed $\log g$ for which all Balmer lines up to H8 were used agree within ~ 500 K with the results of model fits in the literature, which use a more appropriate broadening theory. On the other hand, the fits that only employ $H\alpha$ usually differ from the better literature data by more than 1000 K.

The types, and, if available, the temperatures that were derived with fixed $\log g$ for each of these objects is listed in table D.1.

The stars that are listed there as “cool DA” but only show a weak $H\alpha$ line, and were previously classified as DC white dwarfs, may be helium-atmosphere white dwarfs that are too cool to show helium in their spectra, and would thus possibly be classified as DBA stars if they were hotter.

Chapter 7

Comments on Individual Objects

7.1 Magnetic DA Stars

There are four magnetic DA stars in the SPY sample that have not been published before, HS 0051+1145, HE 1233–0519, HS 1031+0343, and WD 2051–208, as well as two objects that were published first as DAH stars in Koester et al. (2001), WD 0058–044 and WD 0239+109. Five of these white dwarfs have field strengths below 1 MG. The logarithm of the surface gravity of three of them is about 7.9 dex and thus rather usual for a DA, while HE 1233–0519 and WD 2051–208 show high gravities of $\log g = 8.29$ dex and $\log g = 8.98$ dex, respectively. WD 2051–208 is the object with the highest fitted gravity in the SPY sample. Since the field strengths of both high-gravity objects are low, the model atmosphere fits are reliable even though they do not reproduce the split of the line cores.

Below, these six objects and some additional white dwarfs of the SPY sample that are already known to be magnetic, but are not well studied so far, or are of special interest are discussed. Besides these stars, there are 6 more known DAH and one known DBAH object in the SPY data, of which most have field strengths in excess of 10 MG. They are already well studied and thus they are not discussed further.

HS 1031+0343 This object is a new magnetic DA star. The only Zeeman triplet that is completely present, and for which the three components are well discernible, is that of $H\beta$. The σ^- , π , σ^+ components are found at 4771 Å, 4851 Å, and 4905 Å. The components of the higher lines are blended together, and the σ^+ component of $H\alpha$ is shifted by an amount that places it outside of the observed spectral range; thus only the σ^- and π components of $H\alpha$ are available in the SPY data, at 6560 Å and 6420 Å.

The components of $H\beta$ can be used to derive an approximate field strength from the linear splitting of $H\beta$, $\Delta\lambda_L = (\lambda_{\sigma^+} - \lambda_{\sigma^-})/2$. From

$$\Delta\lambda_L [\text{Å}] = 4.67 \cdot 10^{-13} \cdot \hat{g} \cdot \lambda_0^2 [\text{Å}] \cdot B [\text{G}] \quad (7.1)$$

(e.g., Unsöld & Baschek 2002), with $\hat{g}=1$ and $\lambda_0 = 4861$ Å for the σ components of $H\beta$, and with the observed separation $\Delta\lambda_L = 67$ Å, $B = 6.1 \pm 0.3 \times 10^6$ G is found. The uncertainty of the field strength is derived from a conservatively estimated accuracy of ± 3 Å of λ_{σ^+} and λ_{σ^-} . The additional shift due to the quadratic splitting Ze was neglected

here as it is approximately equal for both σ components and thus adds to their separation only by a much smaller amount than the measurement accuracy. Assuming the field strength that is derived from $\Delta\lambda_L$, and using

$$\Delta\lambda_Q [\text{\AA}] = -4.98 \times 10^{-23} \lambda_0^2 [\text{\AA}] (n^4 - n'^4) (1 + m^2) B^2 [\text{G}] \quad (7.2)$$

(Surmelian & O'Connell 1974), with $\lambda_0 = 4861 \text{\AA}$, $n = 4$, $n' = 2$, and $m = 0, 1$ for π, σ of $\text{H}\beta$, the expected quadratic shifts are $\Delta\lambda_{Q,\sigma} = -20_{-3}^{+1} \text{\AA}$ and $\Delta\lambda_{Q,\pi} = -10_{-1.5}^{+0.5} \text{\AA}$. The measured values are $\Delta\lambda_{Q,\sigma} = \lambda_0 - (\lambda_{\sigma^+} + \lambda_{\sigma^-})/2 = -23 \text{\AA}$, and $\Delta\lambda_{Q,\pi} = \lambda_0 - \lambda_{\pi} = -9 \text{\AA}$, which is within the assumed uncertainties of the predicted values.

For $\text{H}\alpha$, $\Delta\lambda_L = -123 \pm 6 \text{\AA}$, $\Delta\lambda_{Q,\sigma} = -10 \pm 1 \text{\AA}$, and $\Delta\lambda_{Q,\pi} = -5 \pm 1 \text{\AA}$ are analogously predicted. The linear shift cannot be measured independently from the quadratic shift since the σ^+ component is not available. Therefore only $\lambda_{\pi} - \lambda_{\sigma^-} = -138 \pm 5 \text{\AA}$ can be measured, which is consistent with the expected value, $\Delta\lambda_L + \Delta\lambda_{Q,\sigma} - \Delta\lambda_{Q,\pi} = -128 \pm 8 \text{\AA}$. For the π component, $\lambda_0 - \lambda_{\pi} = -2 \pm 1 \text{\AA}$ can be measured. The small discrepancy with the expected shift of -5\AA might be explained by a doppler shift of about $+3 \text{\AA}$, which would however be in disagreement with the findings from $\text{H}\beta$. Nevertheless, a field strength of $B = 6.1 \pm 0.3 \times 10^6 \text{ G}$ is generally consistent with the observed features.

The shape of the shifted components, especially of $\text{H}\beta$, is quite asymmetric and will be useful for any more detailed study of the field geometry, which is however beyond the scope of this work. The components have a different shape in the three SPY spectra, which might be due to different rotational phases of the object at the epochs of the spectra.

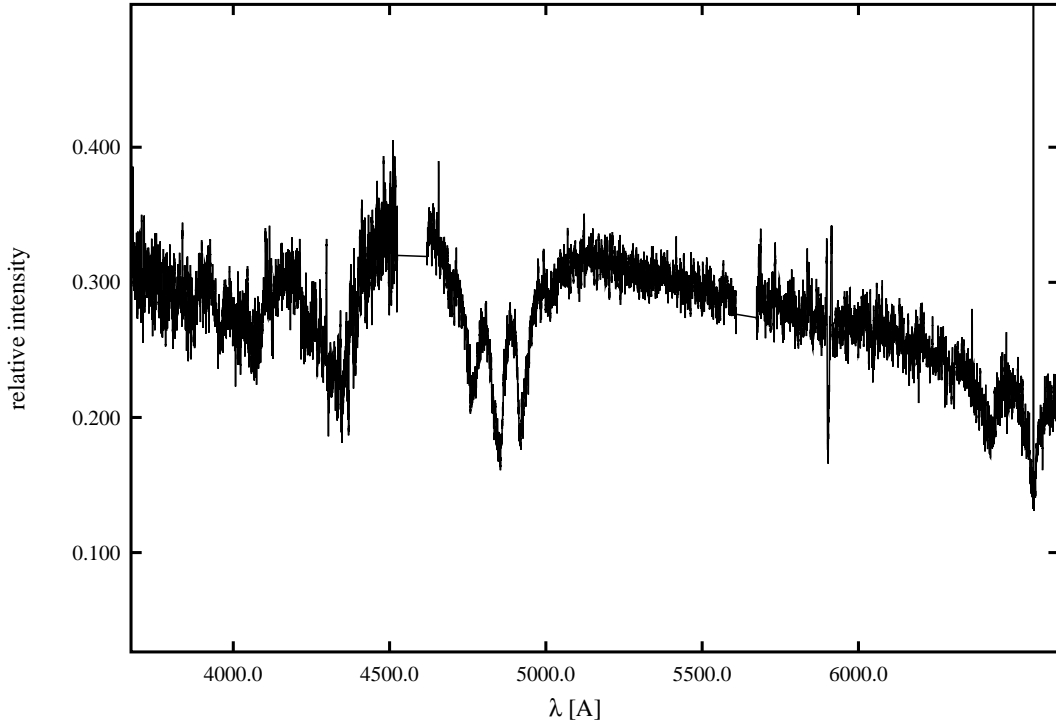


Figure 7.1: The spectrum of HS 1031+0343, binned to a resolution of 1\AA . $\text{H}\alpha$ shows a strong emission core.

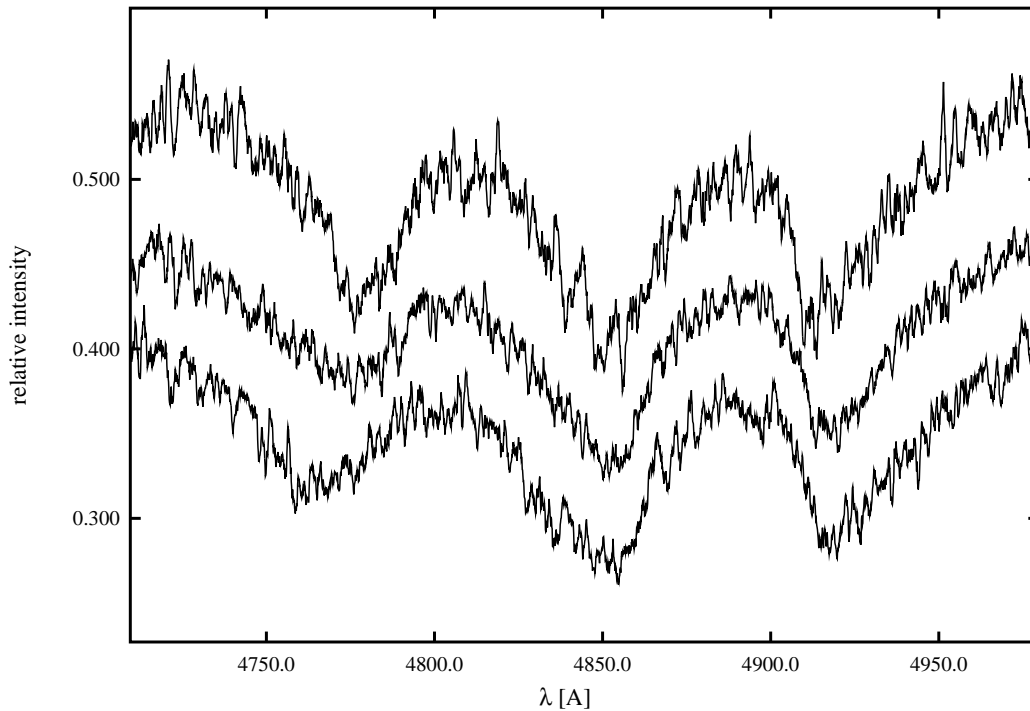


Figure 7.2: The $H\beta$ Zeeman triplet of HS 1031+0343 in the three SPY spectra of this object, binned to a resolution of 1 \AA .

WD 0058–044 This star has been published as a magnetic DA by Koester et al. (2001). The shifts of the σ components with respect to the π components are $6.2 \pm 0.3 \text{ \AA}$ and $3.6 \pm 0.3 \text{ \AA}$, for $H\alpha$ and $H\beta$, respectively. The components of the higher Balmer lines are blended. The quadratic splitting of the lines is negligible here since the split is small and thus the field strength has to be low. The strength of the B field is determined from equation 7.1 to be $B = 3.3 \pm 0.3 \times 10^5 \text{ G}$, as determined from $H\alpha$, and $B = 3.1 \pm 0.2 \times 10^5 \text{ G}$, as determined from $H\beta$.

WD 0239+109 Greenstein & Liebert (1990) recognized an unusual line shape for this object, and suggested a magnetic field as one of the possible reasons. Bergeron et al. (1990b) interpreted the spectrum as that of an unresolved DA+DC binary. The SPY spectra in Koester et al. (2001) revealed the presence of Zeeman splitting of $H\alpha$ and thus proved the magnetic nature of the object. In the first SPY spectrum, the $H\alpha$ components are placed at 6576.6 \AA , 6562.3 \AA , and 6548.4 \AA , and those of $H\beta$ at 4868.9 \AA , 4861.0 \AA , 4853.0 \AA , and from that field strengths of $7.0 \pm 0.2 \times 10^5 \text{ G}$, from $H\alpha$, and $7.2 \pm 0.3 \times 10^5 \text{ G}$, from $H\beta$, can be derived. The separation is slightly stronger in the second spectrum, the σ components of the two lines are placed at 4870.0 \AA , 4851.7 \AA , 6577.5 \AA , and 6546.3 \AA , but the values for $H\beta$ are very uncertain since the S/N is much lower than in the first spectrum. Therefore, the resulting field strengths of $8.3 \pm 1 \times 10^5 \text{ G}$ ($H\beta$) and $7.8 \pm 0.7 \times 10^5 \text{ G}$ ($H\alpha$) are not significantly stronger than those derived from the first spectrum.

WD 0257+080 Bergeron et al. (1997) found a flat-bottom $H\alpha$ core for this object which is typical for white dwarfs with a low-strength magnetic field, but they were not able to

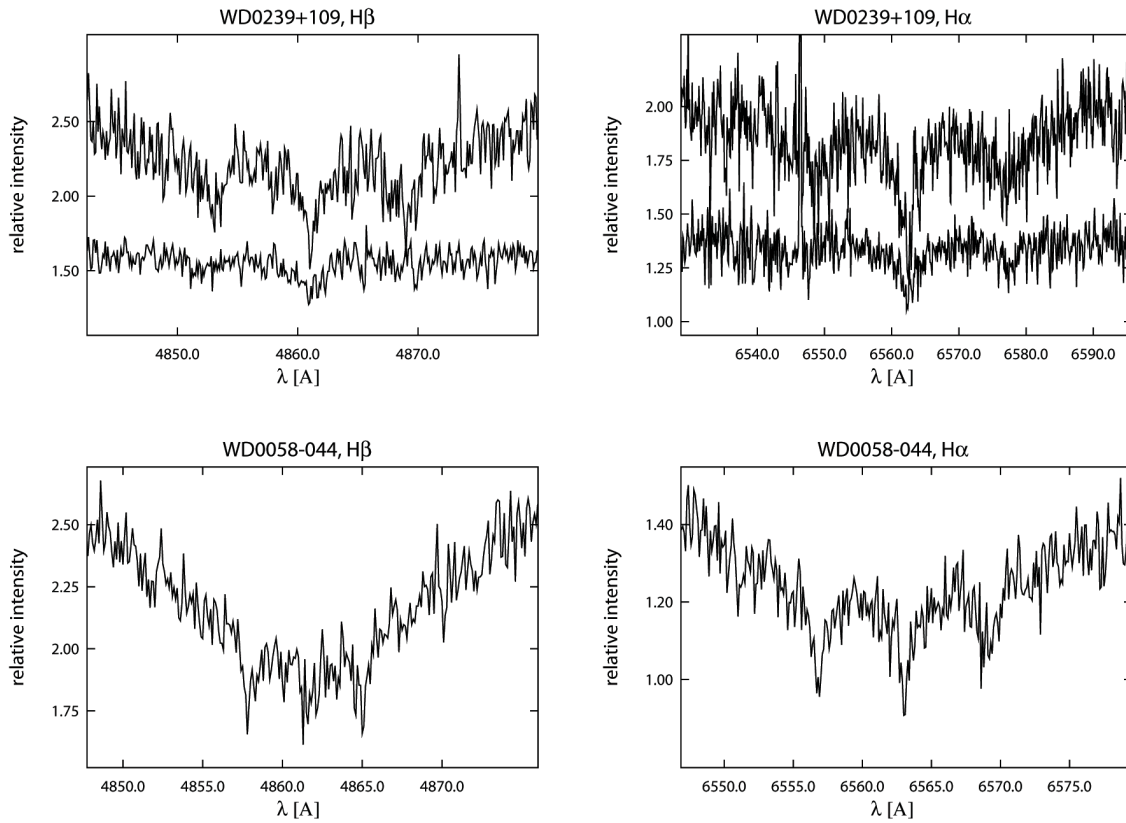


Figure 7.3: The $H\alpha$ and $H\beta$ triplets of the two DAH that were first presented by Koester et al. (2001). For WD 0239+109, both SPY spectra are shown. The lower spectrum has been displaced downward by 0.3 units, thus the relative intensity scale is correct only for the upper spectrum.

identify a Zeeman triplet and estimated the field strength to be ~ 100 kG.

One of the two SPY spectra of WD 0257+080 clearly shows an $H\alpha$ triplet. In the other spectrum, which has a slightly lower S/N , only the σ^- component is discernible. The $H\alpha$ components of the first spectrum are split by $\Delta\lambda_L = 1.8 \pm 0.3 \text{ \AA}$, from which $B = 90 \pm 15 \text{ kG}$ can be derived, a more precise value than the previous estimate. However, the split is not symmetrical, since the components are placed at 6562.4 \AA , 6564.5 \AA , and 6565.9 \AA , and therefore this value is only a rough estimate.

WD 1953–011 A weak Zeeman-split triplet of $H\alpha$ was found by Koester et al. (1998), from which they derived a field strength of 93 kG. Maxted et al. (2000) had noticed a variable depression in the wings of $H\alpha$ which they identified as additional Zeeman-split $H\alpha$ features, which led them to assume a non-simple field geometry with a strong spot-like field of ~ 500 kG combined with a weaker 70 kG dipole field.

Comparing the two SPY spectra, the $H\alpha$ wings appear deformed near 6550 \AA and 6575 \AA , which might allow a very rough estimate of field strengths similar to ~ 500 kG up to ~ 750 kG, if it is assumed that these features are of magnetic origin. However no variation of these features as described by Maxted can be found, the line shape is very similar in both SPY spectra. The central triplet however is obvious, and the splitting of

the core is $1.9 \pm 0.2 \text{ \AA}$. This corresponds to a dipole B field of $95 \pm 10 \text{ kG}$.

WD 2105–820 The spectrum of this star was found to show a flat-bottom $H\alpha$ core, probably due to a low magnetic field, by Koester et al. (1998), from which they derive a field strength of 43 kG . No Zeeman triplet is obvious in the SPY spectra as well, they also only exhibit the broadened, flat core; the full width of the core of 1.8 \AA in the SPY spectra is consistent with the field strength derived by Koester et al. (1998).

WD 2359–434 Koester et al. (1998) suspected that this DA could be magnetic due to its flat $H\alpha$ core, and a very low field of only 3 kG was polarimetrically found by Aznar Cuadrado et al. (2004). They selected this object as one of their program stars based on the criterion that the SPY spectra show no signs of Zeeman splitting; however they themselves note that flat Balmer line cores are present in the spectra of that object, and if these are caused by the B field, it would indicate a higher field strength than that derived from the polarimetry data.

The SPY spectra indeed do not only show a flat-bottom $H\alpha$ core, but within that core also a pronounced π component and less clear, broad σ components, centered at 6561.1 \AA , 6563.5 \AA , and 6565.8 \AA . Thus a field strength of $1.1 \pm 0.1 \times 10^5 \text{ G}$ can be derived. This is two orders of magnitude stronger than polarimetrically found by Aznar Cuadrado (2004). The reason for these different results is unclear.

WD 0446–789 and WD 1105–048 These objects are the two remaining of the three for which Aznar Cuadrado (2004) discovered magnetic fields of only a few kG from polarimetry data.

The $H\alpha$ core of WD 0446–789 appears slightly broadened, the width is 1.8 \AA which is slightly wider than the average line core width of $\sim 1 \text{ \AA}$, but this is far too insignificant to deduce the presence of a magnetic field. However if there were indeed a magnetic broadening of $\sim 0.8 \text{ \AA}$, this would correspond to a field strength on the order of 10 kG .

The line core of WD 1105-048 shows no peculiarities, it has a width of 1 \AA .

HS 0051+1145 This object has earlier been found as a blue source, PHL 886, but was not observed spectroscopically before SPY. It is a new magnetic DA. The SPY spectra have a rather low S/N and thus only the $H\alpha$ triplet of one of the spectra is resolved. The components are placed at 6558.9 \AA , 6563.6 \AA , and 6568.6 \AA , yielding an approximate field strength of $2.4 \pm 0.1 \times 10^5 \text{ G}$.

HE 1233–0519 This DA was published by Koester et al. (2001), but not recognized as a magnetic star. The SPY spectra have a low S/N so that only the $H\alpha$ triplet is discernible in one of the spectra. With the components at 6552.2 \AA , 6564.4 \AA , and 6576.6 \AA , a field strength of $6.1 \pm 0.1 \times 10^5 \text{ G}$ results.

WD 2051–208 Beers et al. (1992) published this object as a DA, but it was not further investigated since. It is a new magnetic DA, and shows a variable Zeeman split of $H\alpha$ and $H\beta$. The $H\alpha$ components in the two SPY spectra are found at 6562.0 \AA , 6566.6 \AA , 6570.7 \AA , and at 6560.2 \AA , 6566.6 \AA , 6571.9 \AA , respectively, and those of $H\beta$ at 4861.2 \AA ,

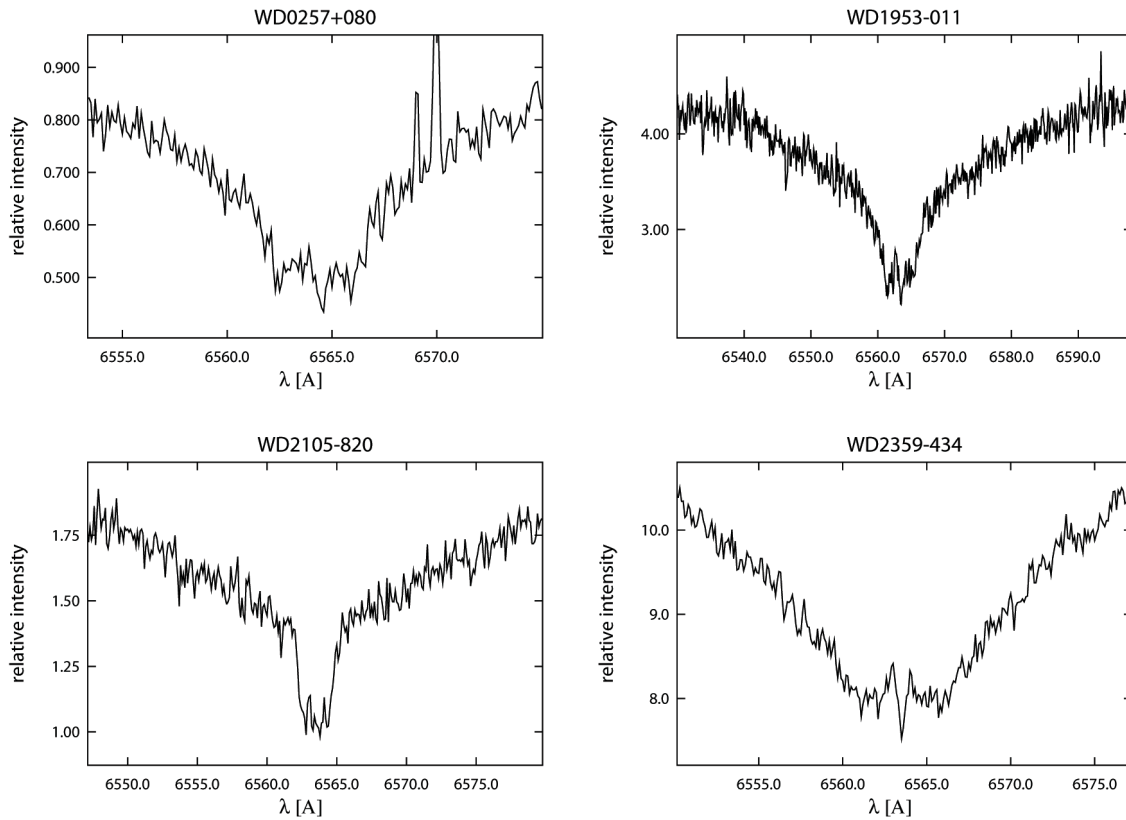


Figure 7.4: The $H\alpha$ triplets of four known DAH with weak fields. WD 0257+080 was known to exhibit a flat core of probably magnetic origin, and in the SPY spectrum the Zeeman components can be discerned. WD 1953–011 is believed to exhibit deformed line wings that indicate a complex field geometry, but this is not obvious from the SPY spectra who nevertheless show the splitting of the $H\alpha$ core. The $H\alpha$ core of WD 2105–820 is broadened but flat except for the spectral noise; no Zeeman components can be identified.

4864.0 Å, 4866.7 Å, and at 4861.0 Å, 4863.9 Å, 4866.9 Å. The resulting field strengths are $2.2 \pm 0.2 \times 10^5$ G and $2.9 \pm 0.2 \times 10^5$ G (from $H\alpha$) as well as $2.5 \pm 0.3 \times 10^5$ G and $2.7 \pm 0.3 \times 10^5$ G (from $H\beta$). The values derived from $H\alpha$ are significantly different, and each is consistent with the corresponding value from $H\beta$.

WD 2253–081 and WD 1344+106 Bergeron et al. (2001) suspected that shallow line cores which they find for these objects might indicate low-strength magnetic fields, and suggested that high-resolution spectroscopy should be employed to detect possible Zeeman splitting. The line cores of both objects have since been fitted with rotationally broadened line profiles, corresponding to projected rotation velocities of 36_{-7}^{+14} km s⁻¹ for WD 2253–081 (Karl et al. 2005) and 4.5 ± 2 km s⁻¹ for WD 1344+106 (Berger et al. 2005).

The $H\alpha$ line cores in the SPY spectra of both objects neither show Zeeman triplets nor flat bottoms that could indicate the presence of a B field. They are non-magnetic objects.

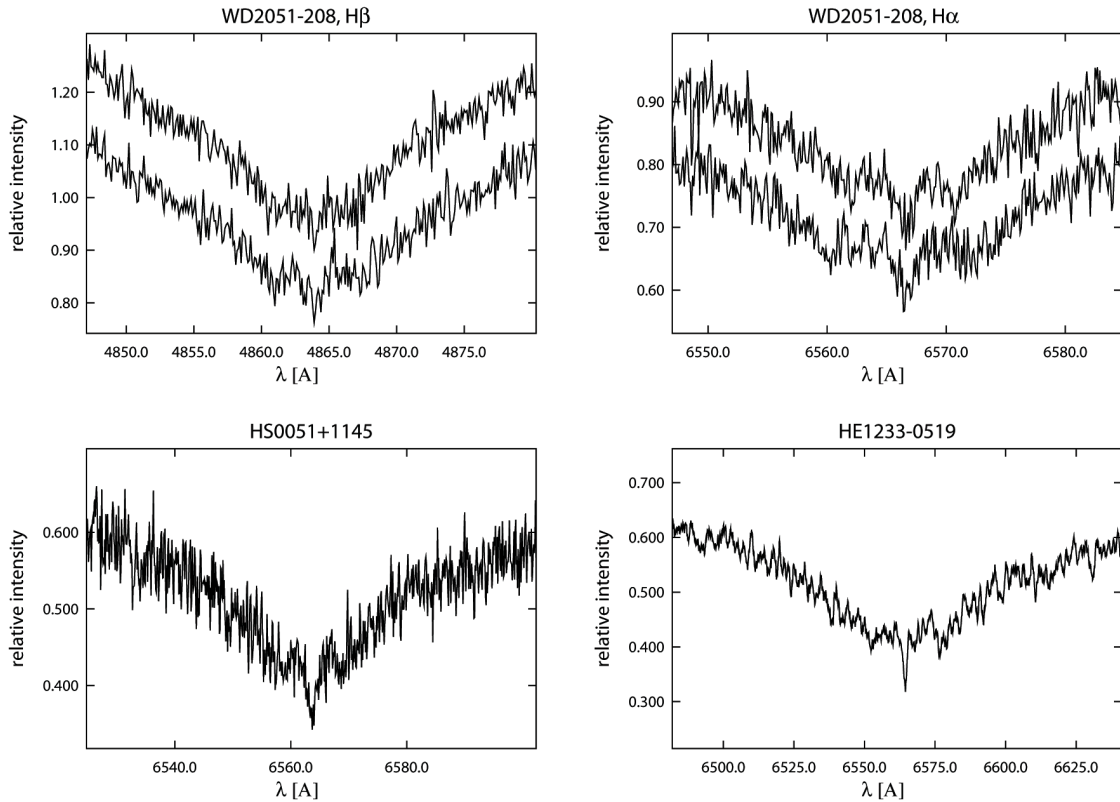


Figure 7.5: The Zeeman triplets of the three new DAH stars with weak fields. The $H\alpha$ triplet of HE 1233–0519 is shown with a resolution binned to 1 \AA , the others are displayed at the full resolution of 0.1 \AA . Both spectra have been plotted for WD 2051–208, and the upper spectrum has been displaced upward by 0.1 units, thus the relative intensities are correct only for the lower spectrum.

7.2 Peculiar Helium-rich White Dwarfs

WD0453-295 This apparent DAB white dwarf was studied by Wesemael (1994) and found to be a DA+DB binary, since no single-star atmosphere model is able to reproduce the UV flux distribution of this object. Although the SPY single-star DA atmosphere fit does not accurately reproduce the peculiar line profiles, the fit result, $T_{\text{eff}} = 27\,186 \text{ K}$, $\log g = 7.393$, is very similar to Wesemael’s single-star fit result. However, they discard that single-star model, and fit the spectrum with a DA+DB model, from which they derive $T_{\text{eff}} = 16\,360 \text{ K}$, $\log g = 7.44$ for the DA and $T_{\text{eff}} = 13\,330 \text{ K}$, $\log g = 7.70$ for the DB component.

The three SPY spectra of WD 0453–295 show variable line core shapes, due to the orbital motion of the components. One of the three spectra exhibits a split core of $H\alpha$. Thus the DB component is indeed a DBA or perhaps even a DAB star, whose H abundance has to be considerable, since the equivalent widths of $H\alpha$ of both the DA and its companion have to be comparable.

WD0127-311 This object has first been classified as a magnetic DA with a strong field of 176 MG by Reimers et al. (1996), but has been found to show a variable spec-

Table 7.1: DAH field strengths derived from the SPY spectra

Object	Zeeman Shift [\AA]		B [10^5 kG]		Comments
	H α	H β	H α	H β	
HS 0051+1145	4.9		2.4 ± 0.1		New DAH
WD 0058-044	6.2	3.6	3.3 ± 0.3	3.1 ± 0.2	
WD 0239+109	14.1	8.0	7.0 ± 0.2	7.2 ± 0.3	
	15.6	9.2	7.8 ± 0.7	8.3 ± 1.0	
WD 0257+080	1.8		0.9 ± 0.15		Asymmetric
HS 1031+0343		67		61 ± 3	New DAH
HE 1233-0519	12.2		6.1 ± 0.1		New DAH
WD 1953-011	1.9		0.95 ± 0.1		
WD 2051-208	4.4	2.8	2.2 ± 0.2	2.5 ± 0.3	New DAH
	5.9	3.0	2.9 ± 0.2	2.7 ± 0.3	
WD 2105-820	~ 0.9		~ 0.4		Flat core
WD 2359-434	2.4		1.1 ± 0.1		

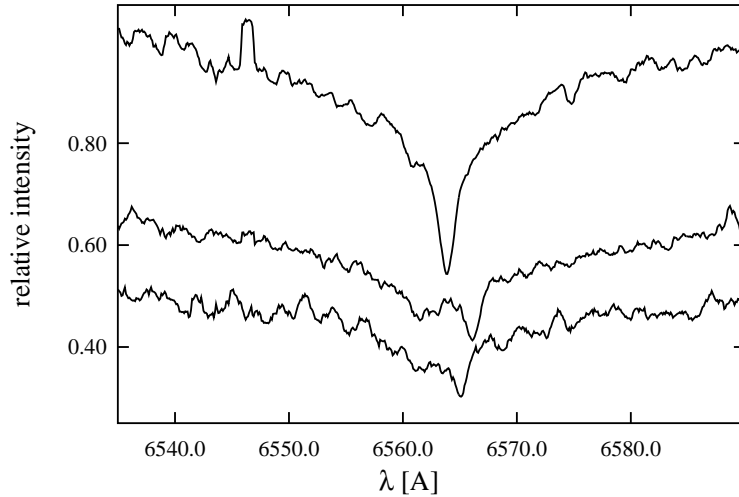


Figure 7.6: The H α line in the three SPY spectra of WD 0453-295. The middle spectrum shows two line cores. The spectra are shown rebinned to a resolution of 1\AA .

trum by Friedrich et al. (2000) that resembles that of a DB in their data; they derive $T_{\text{eff}} = 13\,800$ K, $\log g = 8.48$. Polarization measurements by Schmidt et al. (2001) revealed that the object is non-magnetic since no polarization was found. The SPY spectra of WD 0127-311 are DB spectra as well; they show the HeI 5876\AA , 4026\AA , and 3888\AA lines. HeI 6678\AA is outside of the spectral range of the SPY data, and HeI 4471\AA is not unambiguously present, however in that part of the SPY spectra the noise is higher than in the other spectral regions. WD 0127-311 is thus classified as a cool DB with $T_{\text{eff}} < 14\,000$ K, in agreement with Friedrich et al. (2000). No fit is obtained because of the low temperature.

WD0209+085 This DAB star is well studied since it is one of very few objects that exhibit helium features at a temperature that places it in the DB gap. Heber (1997) found a helium abundance that is variable at timescales of a few months, which has been interpreted as a sign of helium accretion from a clumpy interstellar medium. The equivalent widths of the HeI 4471 Å and 5876 Å lines show no significant differences between both SPY spectra, i.e., no variation of the abundance is found. This is however not surprising since the spectra were recorded within 3 days of each other.

HE2149-0516 The spectrum of HE 2149–0516 shows strong Balmer lines and weaker but strong HeI lines. It is a new DAB star. The pure hydrogen or helium atmosphere fits do not give a result since the line strengths are too strongly affected by the other constituent of the atmosphere; only a hydrogen fit that is limited to the H α line results in a reasonable temperature of 29 000 K to 30 000 K, but with a very low fitted gravity of $\log g \approx 6.9$, or 32 000 K if the gravity is kept fixed at $\log g = 8.0$. Although these fits are of course very inaccurate, both because of the presence of helium and because only a single line was used, the temperature is very similar to those that were derived for most other stars of this class, i.e., near the low-temperature edge of the DB gap.

6 DAB stars have been studied so far in detail in the literature, and an additional 5 new DAB stars were published, but without a closer investigation, by Kleinman et al. (2004). HE 2149–0516 is the twelfth DAB star.

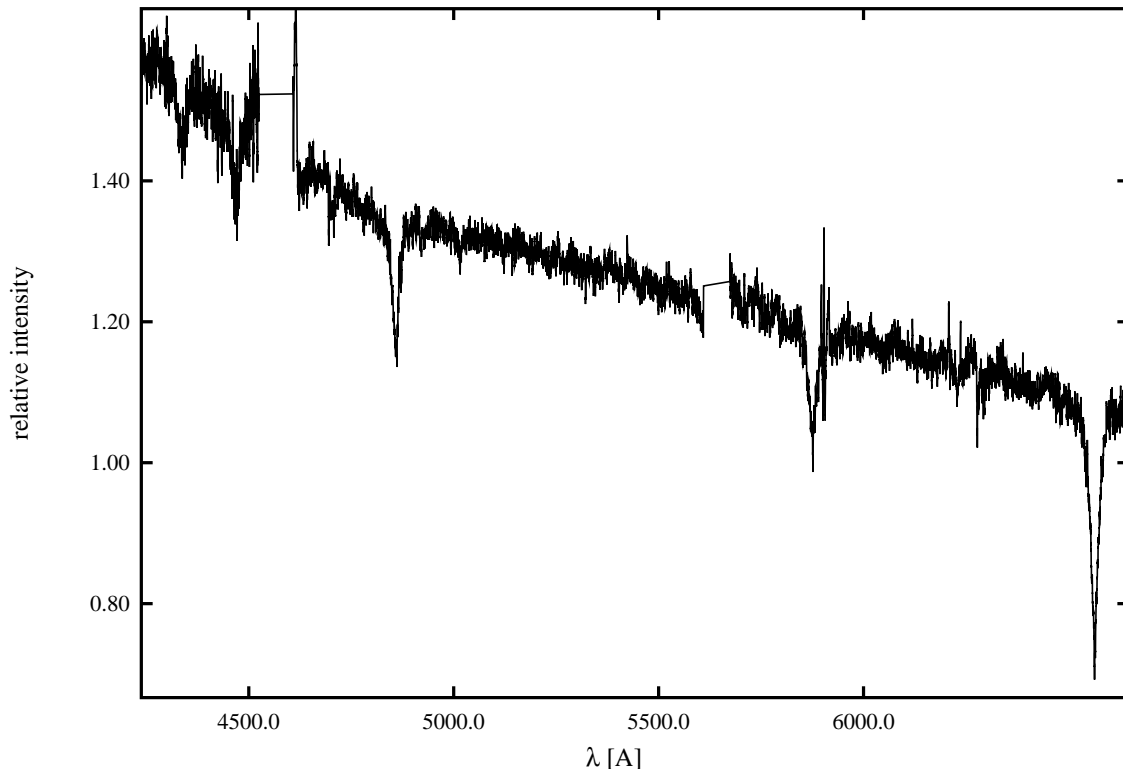


Figure 7.7: The part of the spectrum of the DAB HE 2149–0516, from H γ to H α .

The cool DO star WD 2142–169 The spectrum of WD 2142–169 is dominated by HeI lines, but also shows a weak HeII 4686 Å line, as well as H α , H β , and CaII lines. Accord-

ing to the WD classification system (e.g., Wesemael et al. 1993) it is thus a DO star. The presence of HeII indicates that the temperature can not be much smaller than 40 000 K, but the weakness of the line suggests that the temperature of WD 2142–169 is lower than that of the DO stars that were so far known, who all have $T_{\text{eff}} > 45\,000$ K.

WD 2142–169 is listed as a DB star of $T_{\text{eff}} = 15\,900$ K in Koester et al. (2005a), and in fact such a fit can be obtained at a moderate quality, $\chi^2 = 1.41$, and with a low hydrogen abundance of $\log y = 5$, but of course such a fit does not reproduce the HeII line. The best fit is achieved with a high hydrogen abundance, $\log y = 2$, it results in a temperature of $T_{\text{eff}} = 39\,100$ K and a gravity of $\log g = 7.74$ at $\chi^2 = 1.23$. This fit is shown in Figs. 7.8 and 7.9. The HeII line is slightly stronger in the fit than in the spectrum. The Balmer lines are not well reproduced by this fit; they are stronger in the observed spectrum than in the fitted model, and thus the H abundance is probably higher than fitted, i.e., $\log y < 2$. A fit with a model of a too low hydrogen abundance usually overestimates the temperature. Therefore it is possible that the temperature is slightly lower than 39 000 K, and this is supported by the fit of the HeII line which suggests a slightly lower temperature, since the line is weaker in the spectrum than in the fit.

WD 2142–169 is one of the coolest DO stars that are known and one of very few helium-rich objects that populate the DB gap. Only one similar object is known, SDSS J074538.1+312205, which was recently published by Eisenstein et al. (2006). Like WD 2142–169, it shows weak HeII and Balmer lines in a spectrum that is dominated by HeI. They derive a temperature of $39\,800 \pm 2000$ K from the SDSS photometry, but do not obtain a reliable fit of the spectra.

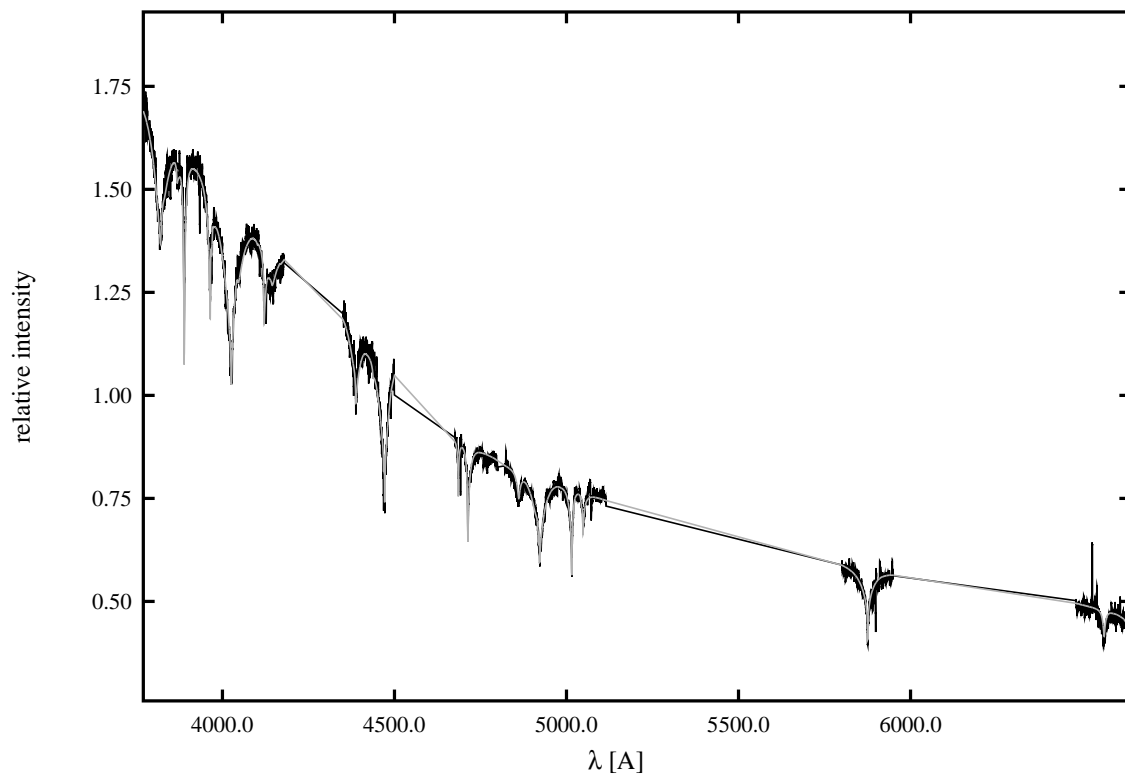


Figure 7.8: The spectrum of WD 2142–169, shown as a black line, and the fit, shown as light gray line.

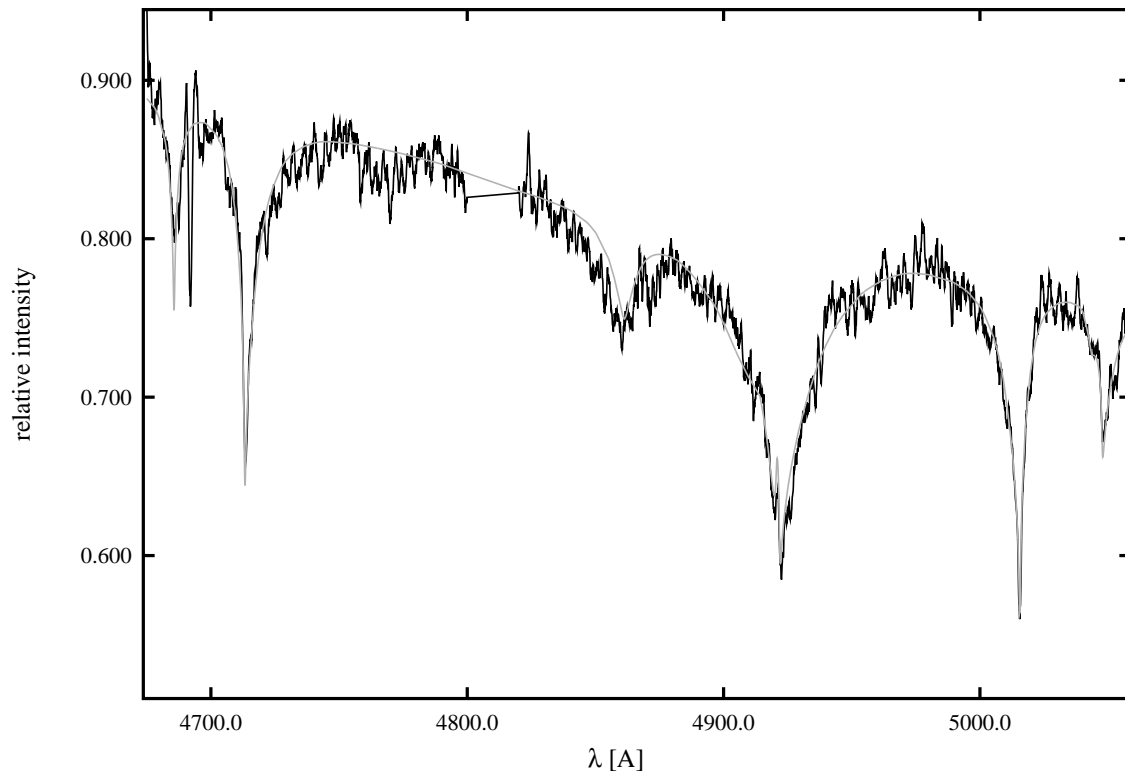


Figure 7.9: The part of the spectrum of WD 2142–169 that contains the HeII 4686 Å and H β lines. The spectrum is shown as a black line, and the fit as a light gray line. The feature at 4690 Å is a defect of the CCD that appears in many SPY spectra.

HS 0146+1847 This object was identified as a white dwarf with strong Balmer and CaII lines, and thus seemingly is a DAZ star. It was included as such in the analysis of SPY DAZ spectra of Koester et al. (2005a). However, the hydrogen model atmosphere fits of this work gave no proper fit of the line profiles for this star, and thus a peculiar composition of the atmosphere had to be assumed. Weak HeI lines are present, and a closer analysis conducted by D. Koester (Koester et al. 2005b) revealed that the atmosphere is indeed helium-rich, but at a low temperature at which helium lines are very weak. Hydrogen and the metals are therefore only minor constituents of the atmosphere. They achieved a much better fit, arriving at a temperature that is considerably lower than that from the hydrogen model atmosphere fits: $T_{\text{eff}} = 11500 \pm 300$ K. The surface gravity was kept fixed to $\log g=8$ in their analysis, but the true value is probably close to that.

7.3 Subdwarf Stars

WD 0944–090 Kilkenney (1997) lists this object as a hot DA, and Bergeron (1984) had earlier classified it as an sdB. The SPY spectra show HeII 4686 Å and the model atmosphere fit converges to $T_{\text{eff}} = 69208$ K, $\log g = 5.89$. Therefore this is an sdO star; however the fit of the line profiles is not good and the true atmosphere parameters might be quite different.

HE 0959–0828 In the PG survey (Green et al. 1986), this object was detected as an 'sdOD' star, meaning a subdwarf with a HeI-dominated spectrum with weak or absent H and HeII features, while the EC survey (Kilkenny et al. 1997) lists it as an 'sdB?' star since weak Balmer lines were probably detected. Sefako et al. (1999) find a featureless, hot spectrum for HE 0959–0828.

The SPY spectra show Balmer lines and weaker HeI and HeII 4686 Å lines, and thus an sdO spectrum. Since the H δ and the higher Balmer lines are blended with HeI lines, only the three Balmer lines up to H γ are fitted, with the results $T_{\text{eff}} = 78800$ K and $\log g = 6.75$ dex.

WD 1148–230 Stys et al. (2000) derive $T_{\text{eff}} = 41790$ K, $\log g = 5.84$ for this object and tentatively classify it as an sdO. However, they find that the far UV flux is not reproduced accurately by an atmosphere with these parameters and thus they speculate that it might be an unresolved binary. The SPY spectra show split H α cores, but since these appear very similar in both spectra, they are most likely emission cores and not a sign of binarity. The SPY model atmosphere fit points to an sdO atmosphere, in agreement with the optical spectrum analysis of Stys et al. (2000).

Helium-rich subdwarfs The three stars HE 1349–2320, WD 1632+222 and WD 2258+155 are hot helium-rich subdwarfs ('He-sdO') for which no fit is obtained because they are placed outside of the helium model atmosphere grid due to their low gravity, or in the case of HE 1349–2320 because of the high temperature of more than 50 000 K.

The spectrum of HE 1349–2320 only shows HeII lines; it has been classified as sdO by Christlieb et al. (2001) and Kilkenny et al. (1997) but no atmosphere parameters are given in the literature. No conclusions about the gravity can be drawn from the SPY helium atmosphere fit, because it converges towards high temperatures and not low gravities. Therefore this object is either a hot DO or a He-sdO star.

WD 1632+222 is listed as a DB in Green et al. (1986) and hence also in McCook & Sion (1999). It was found to be in fact a helium-rich subdwarf O by Bergeron et al. (2000), and the SPY spectra are similar to their spectrum, showing no hydrogen but only strong HeI and weak HeII lines.

The case is similar for WD 2258+155, which is a DB according to Wegner & Dupuis (1993), and, as a result, also according to McCook & Sion (1999). However, it had earlier been listed as an 'sdO(D)' by Kilkenny et al. (1988), which is a classification that is based on the PG survey classification system and indicates a HeI-dominated subdwarf spectrum with weak or absent HeII and hydrogen lines. The SPY spectra show HeI and HeII of about equal strength.

Chapter 8

New White Dwarfs

Most of the SPY objects were taken from the catalogue of McCook & Sion (1999), and are thus already known as white dwarfs. The same is true for the few objects that were selected from the Edinburgh / Cape (EC; Kilkeny et al. 1997) and Montreal / Cambridge / Tololo (MCT; LaMontagne et al. 2000) surveys.

This is different for about a third of all objects that are taken from the Hamburg ESO (HES; Wisotzki et al. 1996, Christlieb et al. 2001) and Hamburg Quasar (HQS; Hagen et al. 1995) objective prism surveys. Since the resolution of the objective prism spectra of these surveys is normally too low to allow an unambiguous identification of a white dwarf or a determination of accurate atmosphere parameters, only some HQS and HES objects that have been re-observed before this work are known to be white dwarfs. For the majority of the HQS and HES SPY observations, 171 objects, the SPY data is the first certain detection of these stars as white dwarfs.

154 of these are DA white dwarfs, 10 are DA+dM binaries and the remaining new objects have helium-rich atmospheres. These new objects are listed in table 8.1 in more detail.

Besides the new objects, there are some white dwarfs that were already known and are contained in McCook & Sion (1999), but with a spectral type that does not agree with the features that are visible in the SPY spectra. In most cases these are minor changes of the classification due to the detection of trace constituents of the atmosphere that were not discernible in the lower-resolution data of earlier studies:

Besides the 18 new DBA stars with weak hydrogen lines, and the DB WD 2142–169 in which HeII was found, both of which are discussed above, there are two DC stars in which weak hydrogen lines or carbon bands could be identified, and 2 former DQ stars in which CaII lines are found.

A more important change of the classification was found for WD 2207–625 which is a new DO white dwarf with $T_{\text{eff}} > 50\,000$ K; it is listed as a DC star in the literature but the SPY spectra clearly show HeI and HeII lines, as well as CaII.

Table 8.1: New white dwarfs

Source	Type	Number	Comments	
HQS	DA	75	Including two DAH stars and one DD star	
	DA+dM	2		
HES	DA	79	Including 3 DD stars	
	DA+dM	8		
	DBA	4		
	DB+dM	2		
	DAB	1		HE 2149-0516
	DB	1		
(WD	DC	1	WD 1520–340: First spectroscopic observation)	

Part III

Search for ZZ Ceti Candidate Stars Among the HQS Objects

Chapter 9

Remote Observations with the Calar Alto 1.23m Telescope

As it was mentioned in part I, a large number of probable white dwarfs had been identified from the objective prism spectra of the HQS by D. Homeier (2001), and the main use that can be made of this sample is the identification of new ZZ Ceti variables among those 1000 stars in his catalogue that are cool, i.e., that have temperatures $T_{\text{eff}} < 16\,000\text{ K}$ according to the objective prism spectra analysis. As these data are not very accurate, any of these objects might be a DA white dwarf with a temperature that places it in or near the ZZ Ceti instability strip, and thus any of these objects could be a new ZZ Ceti star. Due to the large number of objects and due to the large amount of observation time that is necessary to obtain a lightcurve that would allow to identify an object as a variable star, it is not feasible to search for ZZ Ceti stars among Homeier's objects directly. It is rather more feasible to first derive a subsample of the most probable new ZZ Ceti stars by conducting preparatory observations, and lightcurves will subsequently only be obtained for the objects of such a subsample.

One possibility of recognizing stars that are *probably* pulsating, but in a much shorter time than it would be required to definitely identify a pulsator by recording its lightcurve, is to obtain short sequences of photometric time series data. Such photometric sequences could show signs of any pulsation of a star even if the sequence is too short and has a too coarse temporal resolution to allow an identification of the pulsation period and amplitude. Such a short sequence might even have a sampling frequency that is lower than the pulsation frequency, and would still show that a pulsation is present. This is possible because the pulsation cycle will be sampled at different phases during the photometric sequence even if it is not resolved by the observations, provided that the sampling and pulsation frequencies are not too similar. Thus, a variation of the measured brightness would be recognizable during the sequence.

9.1 Layout of the Observations

Such observations were carried out in 2002 with the 1.23 m telescope of the Calar Alto observatory. This observatory is operated by the Max-Planck-Institut für Astronomie, together with the spanish Instituto de Astrofisica de Andalucia. The 1.23 m telescope

was operated jointly by the universities of Kiel and Hamburg in 2002, and had been refitted with remote observing capabilities by the Hamburger Sternwarte. About 50% of the observation time was made available to the institute in Kiel, and the telescope was remotely controlled from Kiel university. Using software that was written by H. Hagen at the Hamburger Sternwarte, an ssh connection to the observatory was established via Hamburg university, and commands entered in Kiel were dispatched to different on-site systems at Calar Alto. Although some typical difficulties were encountered during the observations, mainly connected to a lack of immediate awareness of weather changes and difficulties in dealing with on-site technical problems, the remote observing proved viable. Further observations with that telescope after the year 2002 were planned, but a major technical failure left the telescope inoperative since early 2003.

The telescope was equipped with a CCD camera with a 2K×2K SITE chip which has a field of view of 17.1' on the sky with an angular resolution of 0.5". The readout time of this camera for a full frame is approximately 3 minutes, which is too long even for the coarse temporal resolution that was planned. Instead, only a small section of the chip, a rectangle of typically about 2 or 3% of the chip area, was read out (*windowed readout*), strongly reducing the readout time to just over 10 s. The window was chosen so that several bright stars, ideally brighter than the target object, were included in the window. These would serve as references for the target flux during the data analysis. The exposure times, depending on the brightness of the target, were about ~ 40 s. Taking some overhead time for the necessary re-setting of the CCD into account, a cycle time of ~ 60 s was realized, and typically 40 frames were obtained for each object. The observations were carried out in white light, i.e., no filter was used, to maximize the recorded flux. Stars with magnitudes $B < 17$ mag could be observed at a S/N that would allow the smallest known amplitudes in ZZ Ceti stars to be detected. Under unfavourable observing conditions, e.g., clouds, or moonlight, this limit was about one magnitude lower. Thus, about half of the 1000 objects in Homeier's catalog could be observed, and even more than that if a slightly lower accuracy would be accepted at which only the higher-amplitude ZZ Ceti stars would be detectable.

The observations were carried out in three periods, in the nights from August 15th to September 6th, from September 19th to 21st, and from December 23rd to January 1st, 2003, with support by D. Koester, D. Schemioneck, and M. Hünsch. 33% of this time could not be used due to bad weather, and a fraction of 13% was lost to technical problems that were mostly caused by a failing connection to the computers at Calar Alto. In the remaining time, 124 candidate ZZ Ceti stars were observed, as well as 5 known ZZ Ceti stars that were included as a check of this method of detecting pulsations. Some other observing programs were carried out in parallel, but roughly 80% of the useful time was available for the ZZ Ceti candidate observations. An observation log of these observations is given in appendix E.

The observations and the data were organized with the help of some utility programs and an SQL database that were created for this purpose, e.g., automating the creation of object lists for a night, the data storage, and some other duties.

9.2 Data Reduction

The data reduction and analysis was originally intended to be carried out by a fully automated pipeline software. When it became obvious that the observation would not be continued, this pipeline had not yet been implemented in its fully automated version, but as a series of semi-automated separate programs that have to be executed sequentially. A perl script controls this reduction pipeline, as part of which the actual image reduction is carried out by IRAF¹ and additional photometry is obtained with the program “Source Extractor” (Bertin & Arnouts 1996).

The two basic steps of the data reduction that remove any sensitivity variation effects of the detector from the data, zero-correction and flatfielding, were conducted by IRAF, as well as the detection of the brightest sources in an image and the subsequent identification of the target object. Isolated stars with a sufficient flux, relative to that of the target, were automatically selected as possible reference stars. For the target and the reference stars, aperture photometry with three types of apertures was carried out:

- IRAF: Circular apertures of different radius, but with the same radii for all frames and all stars; the radius of the aperture was chosen as equal to the FWHM of the stellar image point spread function (PSF)
- IRAF: The same, but with a radius that was adapted for each frame to the PSF FWHM of the target star
- Source Extractor: Elliptic apertures with variable axes that were fitted to the each individual PSF in each frame

The photometry output of both programs is given in *magnitudes* (m), which are defined as negative logarithms of the fluxes. Thus, for historical reasons, smaller magnitudes correspond to higher fluxes. The magnitudes are determined by both programs from the counts c within the aperture that covers the area a , and it is corrected for the background count level b , i.e., the mean count rate in parts of the image that do not contain stars, and for the exposure time t :

$$m = -2.5 \log(c - a \cdot b) + 2.5 \log t \quad (9.1)$$

The uncertainty σ_m of m is calculated by the programs from the photon shot noise of c and b , and from the readout noise of the camera. The center position of the aperture might change during the sequence due to small errors in the movement of the telescope which, then, does not completely compensate for the earth’s rotation. Thus it is important to re-determine the position of each star in each frame, and reposition the photometry apertures accordingly. This is done as part of the reduction pipeline.

9.3 Data Analysis

Differential magnitudes were calculated from the photometry output, for all three types of photometry. The advantage of such differential magnitudes $m_{\text{diff}} = m_{\text{target}} - m_{\text{reference}}$ is

¹Image Reduction and Analysis Facility, see <http://iraf.noao.edu>

that they are largely independent from variations of the atmospheric observing conditions, and have much smaller uncertainties. This can be seen when the correction is considered that is necessary to take the effects into account that the atmosphere has on a photometric measurement m :

$$m_{\text{corr}} = m + w_1 + w_2 \cdot X + w_3 \cdot (B - V) + w_4 \cdot (B - V) \cdot X \quad (9.2)$$

where the coefficients w_1 to w_4 are the zeropoint of the observations, the extinction coefficient, the “colour term” and the differential extinction coefficient. X , the “Airmass”, is a measure of the length of the light path through the atmosphere, relative to observations to the zenith ($X_{\text{zenith}} = 1$). $(B - V)$ describes the colour of a star, which is defined as the difference of the flux that is measured through two filters with different effective wavelengths. In this case, B and V are the fluxes measured through filters of the same name of the Johnson photometric system, but in principle any combination of filters can be used. Since the measurements that are analysed here were recorded without any filters, no stellar colours can be derived from the measurements and it is therefore not possible to correct the photometry according to equation 9.2. That correction would furthermore have required extensive observations of “standard stars”, i.e., stars of precisely known magnitudes and colours, to determine the coefficients. Fortunately there is no need to use equation 9.2 since one is dealing with differential photometry here. Because the coefficients as well as X are equal for all sources in an image, equation 9.2 becomes

$$m_{\text{corr,diff}} = m_{\text{diff}} + w_3 \cdot (B - V)_{\text{diff}} + w_4 \cdot (B - V)_{\text{diff}} \cdot X \quad (9.3)$$

where $(B - V)_{\text{diff}} = (B - V)_{\text{target}} - (B - V)_{\text{reference}}$. Thus two of the largest sources of uncertainty, the correction for the zeropoint and that for atmospheric extinction, are eliminated. If furthermore not the absolute value of $m_{\text{corr,diff}}$ is of interest but only its temporal variation, also the w_3 term can be omitted because $(B - V)$ is constant. Thus, only the last term, the *differential extinction*, might affect the photometry results. This is relevant for white dwarf observations because white dwarfs are mostly hotter and thus bluer than the average field stars which will naturally provide most reference stars. Thus, one expects to find a small, slow change of m_{diff} due to differential extinction, as the celestial elevation and thus the airmass of the observation changes during the recording of the time series data. A more abrupt and stronger change of the differential magnitude may occur if thin clouds are present. However, such changes will be much smaller than those that the absolute magnitudes would show at the same time. The differential extinction can not be properly corrected for according to equation 9.3 because neither a value of w_4 can be determined for the white light observations nor can $(B - V)_{\text{diff}}$ be derived from the data. Nevertheless, the slow change of the differential magnitude due to the changing elevation can be approximated as a linear function. Therefore a linear trend was removed from each time series. Furthermore, although larger variations of m_{diff} because of clouds cannot be corrected for, they can normally at least be recognized, and the affected part of the time series can be discarded.

Multiple reference stars were observed together with each target, which is important to exclude the possibility of using an unknown variable star as the reference. Another advantage of using multiple references is that a sum of the individual differential magnitudes

will have smaller uncertainties than the individual values. This sum s , in which the individual magnitudes are weighted by the inverse square of their uncertainties, is computed as

$$s = -2.5 \log \frac{\sum_{i=1}^{n_{\text{references}}} 10^{-0.4(m_{\text{target}} - m_{\text{ref},i})} \times [(\sigma_{\text{target}}^2 + \sigma_{\text{ref},i}^2) \cdot 10^{-0.8(m_{\text{target}} - m_{\text{ref},i})}]^{-1}}{\sum_{i=1}^{n_{\text{references}}} [(\sigma_{\text{target}}^2 + \sigma_{\text{ref},i}^2) \cdot 10^{-0.8(m_{\text{target}} - m_{\text{ref},i})}]^{-1}} \quad (9.4)$$

where σ_{target} and $\sigma_{\text{ref},i}$ are the shot noise uncertainties of the individual photometric measurements of the target and the reference stars. The temporal average of the uncertainty of s , σ_s , is determined as well:

$$\langle \sigma_s \rangle = \frac{1}{n_{\text{frames}}} \sum_{i=1}^{n_{\text{frames}}} \sqrt{\left(\frac{\partial s}{\partial \sigma_{\text{target}}} \right)^2 \sigma_{\text{target}}^2 + \sum_{i=1}^{n_{\text{references}}} \left(\frac{\partial s}{\partial \sigma_{\text{ref},i}} \right)^2 \sigma_{\text{ref},i}^2} \quad (9.5)$$

The temporal variance σ_t of the time-series data was then derived from the sum s of frame i , $s(i)$, and the temporal average of s , $\langle s \rangle$:

$$\sigma_t = \sqrt{\left[\sum_{i=1}^{n_{\text{frames}}} (s(i) - \langle s \rangle)^2 \right] \times (n_{\text{frames}} - 1)^{-1}} \quad (9.6)$$

σ_t constitutes the most important quantity of this analysis since it should be similar to $\langle \sigma_s \rangle$ for a non pulsating object, and will be larger if the object is pulsating, provided that $\langle \sigma_s \rangle$ is small compared to the amplitude of the pulsation. Thus, if the ratio of the two quantities is large,

$$\frac{\sigma_t}{\langle \sigma_s \rangle} \gg 1 \quad (9.7)$$

this indicates probable pulsations. It is however unknown which value of this ratio can be considered as a threshold value above which one can expect an object to show pulsations, because there may be additional sources of uncertainty. These could be introduced e. g. by the flat field correction or by any differential extinction due to thin clouds. The latter effect was largely avoided by checking for the characteristic variations that this would induce to the differential magnitude, to the background count level of an image, and to the extent of the PSF of the stars. Nevertheless, it can not be excluded that some additional uncertainty is present and will lift the threshold value above $\sigma_t / \langle \sigma_s \rangle = 1$. The observations of known variables were used to determine which values of $\sigma_t / \langle \sigma_s \rangle$ can be considered as indication of variations.

The distribution of the s values in a time series was used as a second indicator of possible variability. For a non variable object for which the individual values of sum are different only because of the shot noise, a gaussian distribution of the values with a variance of $\langle \sigma_s \rangle$ would be expected. For an intrinsically variable object however, a non-gaussian distribution should be found because the flux changes are not randomly distributed. This means that not only a variance that is larger than the expected $\langle \sigma_s \rangle$ may

indicate pulsations of an object, but also a shape of the s distribution that is deviating from a gaussian. Thus, a χ^2 test is used to evaluate the agreement of the measured distribution with the assumption of a gaussian distribution.

For this test, the range of values of s is split into several intervals i , and for each of the intervals the number N_i of measurements in the interval is determined. The width of the expected gaussian distribution is given by $\langle\sigma_s\rangle$ and its scale by the total number of measurements $\sum_i N_i = n_{\text{frames}}$. The resulting scaled gaussian distribution function is used to determine the number of expected measurements in each interval, n_i . The degree of the agreement of both distributions is then given by

$$\chi^2 = \sum_i \frac{(N_i - n_i)^2}{n_i} \quad (9.8)$$

As for the ratio $\sigma_i / \langle\sigma_s\rangle$, it is not a priori known which value of χ^2 will constitute a threshold that can be used to separate expected variables from expected non variable stars, and thus the observations of known ZZ Ceti stars will serve as a calibration for this second indicator of possible pulsations as well.

9.4 Results of the 1.23 m observations

The analysis of the three types of photometry showed that the Source Extractor photometry yields better results than the IRAF photometry. The IRAF absolute photometry was found to vary by several percent, more than expected, for most targets. Source Extractor, on the other hand, produced the constant results that were expected of non variable stars. This indicates that for the small apertures that were used (a few arcseconds wide) an individual fitting of each PSF as it is done only by Source Extractor is necessary. A fixed aperture, or one that is allowed to vary with time but not from one star to another, gives less precise results because the shape and extent of the PSF can vary over time if the atmospheric conditions (the “seeing”) are unfavourable.

For some measurement series, even the Source Extractor absolute photometry varied by more than 10%. For these observations it was realized that clouds were affecting the measurements, and such data were discarded. They could not be used because of the effects of differential extinction that were expected for cloudy conditions; in such cases, variations of the absolute magnitude were found to be accompanied by much smaller synchronous changes of the differential magnitude. For the data of 24 of the 124 observed objects such variations that can be traced back to clouds were present, and thus the number of objects with useful observations is reduced to 100.

The accuracy of the remaining observations is mostly as high as necessary to detect the faintest known ZZ Ceti pulsations, i.e., better than 0.01 mag, but some observations of faint targets were achieved only with higher uncertainties. The five known variables that were included could all be detected using the two diagnostic methods. In Figure 9.1 the time series values s of four of the known variables are plotted; it can be seen that for those with high amplitudes and long periods it is even possible to record a proper lightcurve, while the variations of G226-29 with a shorter period are undersampled. The detections of four of the five known variables are the most significant detections of all observed targets.

Thus, if these four variables would be used to define a threshold above which any new pulsators are found, no detections would be made.

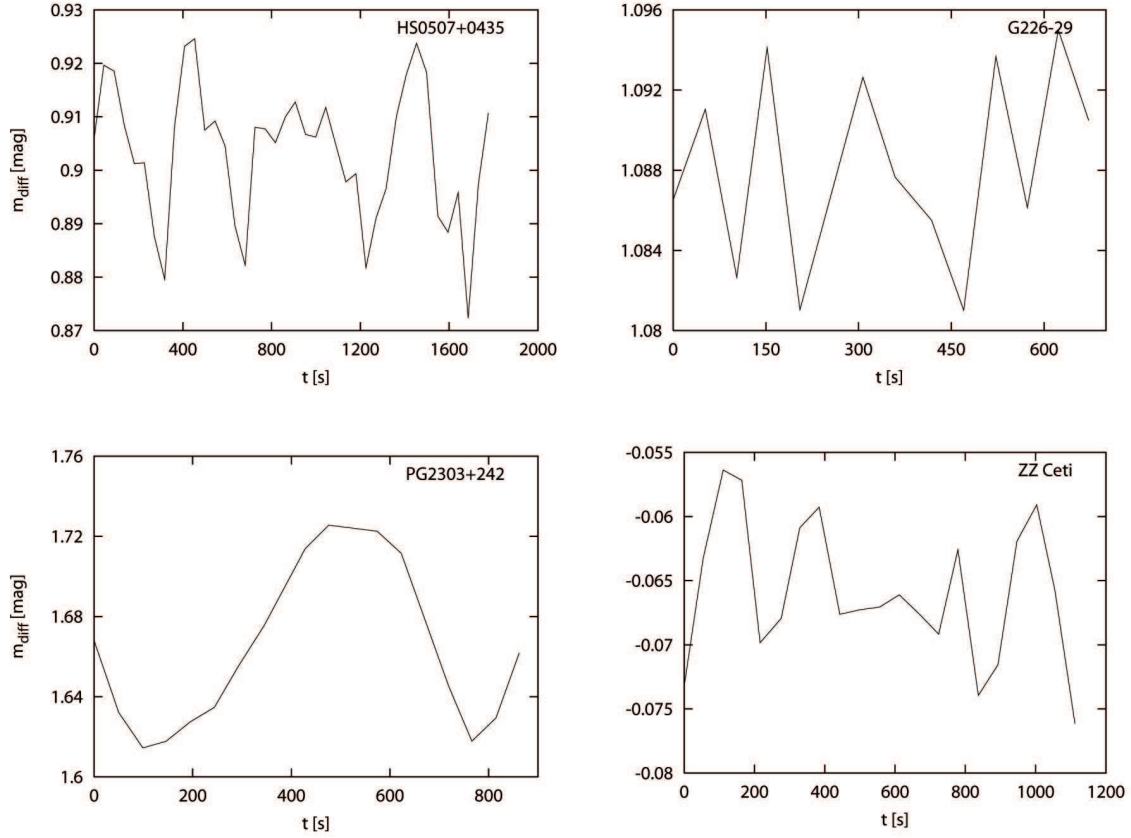


Figure 9.1: The Source Extractor photometry time series data of four of the five observed known variables. G226-29 is a pulsator with one of the shortest periods P and lowest amplitudes A that are known for ZZ Ceti stars, $P = 109$ s and $A = 0.6\%$. The lightcurve is undersampled, as it was expected, but the variation is clearly detected from the scatter of the data. For PG 2303+242 and HS 0507+0435, the lightcurves are resolved and it is possible to recognize the amplitudes and frequencies of the pulsations.

However one of the observed known variables, ZZ Ceti, is detected at an only intermediate level of significance. The results for this star, $\sigma_t / \langle \sigma_s \rangle = 1.58$ and $\chi^2 = 7.64$, can be employed as more meaningful threshold values, because these are the highest possible threshold values which, if applied to all observations, select all known variables as possibly pulsating stars.

Eight of the sample stars have a χ^2 larger than ZZ Ceti, as well as $\sigma_t / \langle \sigma_s \rangle > 1.58$, and might thus be variable. The analysis results for these eight most probable new detections, and those of the five known variables, are listed in table 9.1. The table also includes the time series scatter of the absolute magnitude of the brightest reference star, σ_{single} . If this quantity is large, it may indicate possible changing atmospheric conditions and thus, although no presence of clouds could be ascertained in these cases, a detection is less reliable if σ_{single} is large.

If both cutoffs that are obtained from the analysis results of ZZ Ceti are not applied at

Table 9.1: The analysis results of probable new ZZ Ceti stars detected in the CA 1.23 m observations, below the line, and of the observed known variables, above the line. σ_{single} is the times series variance of the *absolute* photometry of the brightest reference star.

Object	B [mag]	$\langle\sigma_s\rangle$ [mag]	σ_t [mag]	$\langle\sigma_s\rangle / \sigma_t$	χ^2	σ_{single} [mag]
ZZ Ceti	14.3	0.003	0.005	1.582	7.63	0.012
HS 0507+0435	15.6	0.004	0.012	3.063	24.02	0.048
G 226–29	12.4	0.002	0.011	5.805	25.72	0.009
PG 2303+242	15.6	0.004	0.038	7.780	30.46	0.003
G 29–38	13.2	0.002	0.016	6.339	41.61	0.015
HS 0007+1917	16.7	0.005	0.011	2.046	10.00	0.017
HS 0116+0449	17.2	0.008	0.022	2.546	14.29	0.005
HS 0143+2139	15.5	0.004	0.007	1.646	8.67	0.055
HS 0246+0607	17.3	0.013	0.021	1.633	10.42	0.009
HS 1607+1436	16.9	0.003	0.006	1.692	9.35	0.003
HS 1652+2357	17.1	0.009	0.014	1.612	9.29	0.006
HS 2054+0610	16.8	0.010	0.018	1.737	10.30	0.013
HS 2301+0127	17.1	0.028	0.052	1.822	8.62	0.004

the same time, but individually, one additional candidate is found from the ratio criterion and further twelve objects would be detected as possible variables from their large χ^2 . Thus the χ^2 is the weaker criterion. This is shown in Fig. 9.2, which displays the distribution of the observed objects with respect to the values of $\sigma_t / \langle\sigma_s\rangle$ and χ^2 . Four of the five known variables are found in the rightmost bins of each panel, and the other objects in those bins have a lower χ^2 or lower ratio value than any of the known variables. This could be interpreted in such a way that none of these stars can unambiguously be considered as a new variable, and that therefore the most significant detections, i.e., the objects in the right three bins of each panel of Fig. 9.2, are possible but not highly probable new variables.

As mentioned in the introduction, one would expect to find variations in about a sixth of the stars of the cool subsample of the Homeier catalogue, and thus more than ten new variables should be among the 100 objects that were analysed. This is similar to the number of the best candidates that are detected by both methods with a higher significance than that of the detection of ZZ Ceti. But only if most of these eight candidates could indeed be confirmed as new ZZ Ceti variables, the final result would be as expected. Further studies of the candidate variables would thus have been necessary, and it might have been possible to derive time series with a longer duration and maybe even with a shorter cycle time at the Calar Alto 1.23 m telescope. This was however not possible any more after the telescope became inoperative. Later, lightcurve observations at the better equipped NOT telescope were obtained, but at that time there were already several other, better constrained candidate ZZ Ceti stars of therefore higher priority. For this reason, only one of the best candidates of this analysis, HS 0007+1917, was re-observed at the NOT, but it was found to be not variable. HS 0143+2139 and HS 1607+1436 have been found by the two-colour photometry that was subsequently obtained at the Calar Alto 2.2 m telescope (see the next chapters) not to be situated near the ZZ Ceti instability strip.

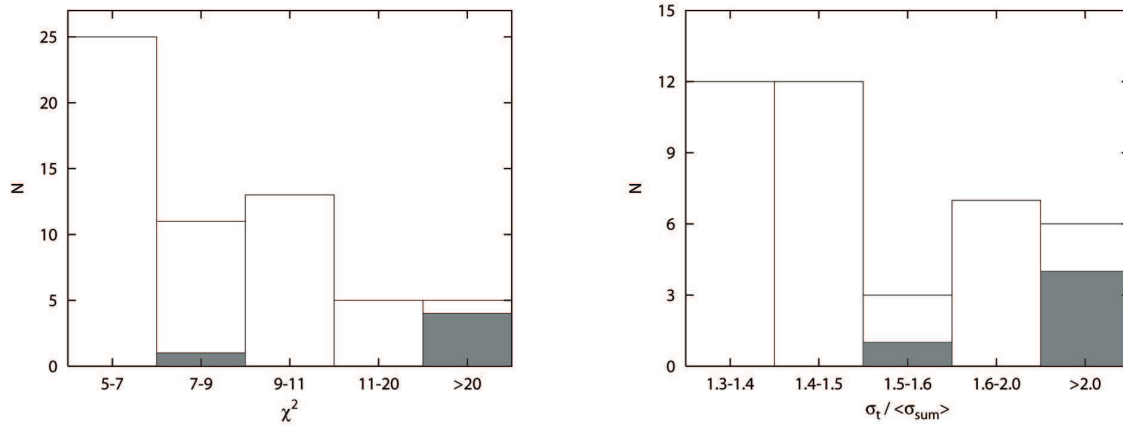


Figure 9.2: The distributions of the variability indicator values of the observed objects. The left panel shows the distribution of the number of objects with respect to χ^2 , and the right with respect to $\sigma_t / \langle \sigma_s \rangle$. The filled parts of each bin show the known variables. The majority of objects with $\chi^2 < 5$ or $\sigma_t / \langle \sigma_s \rangle < 1.3$ is not shown.

The other candidates remain to be investigated.

About half of the known ZZ Ceti stars are of the sub-type that shows long periods and high amplitudes. Thus, it would also be expected to find at least a few of these high-amplitude variables in a sample of 100 of Homeier's cool objects. Such high-amplitude variables would have been clearly detected by these observations, even under unfavourable observing conditions, and without the need of further confirmation by re-observations. However no such object was found, and there is thus a discrepancy of the expectations and the results. The photometric accuracy was low for some of the observations and would not have allowed the detection of the weakest kind of ZZ Ceti pulsations, but this is of no concern for the detection of higher amplitude ZZ Ceti variables. However, the higher-amplitude pulsators often show a multitude of pulsation modes that superimpose and can cause beating effects in some ZZ Ceti, due to which a pulsating star can appear to be not variable for up to one hour, i.e., longer than the duration of the time series that were recorded. This effect reduces the number of expected detections, since not all observed variables will exhibit their full amplitudes when they are observed. A further decrease of the expected number of high-amplitude variables is due to the fact that not all stars in Homeier's catalogue are white dwarfs; there are some (e.g., HS 1607+1436) which were later found to be stars of a different type.

More probable, though, is that the lack of a clear detection is due to the involved small number statistics: The number of expected high-amplitude detections is not as high as not to allow for some probability of no such detections to be made even from a sample of 100 stars.

Chapter 10

Observations with BUSCA at the Calar Alto 2.2m Telescope

After it became clear that the 1.23 m telescope would be inoperative for an indefinite time, an alternative way to continue the project of re-observing Homeier's objects and create a sample of probable new ZZ Ceti stars had to be found. While a large amount of guaranteed observing time had been available at the 1.23 m telescope, time at another telescope would have to be competitively applied for, and a much smaller amount of such observing time would have to suffice. On the other hand, the chance of possibly using a telescope with a larger aperture and a different instrumentation offered the opportunity of selecting or de-selecting a given number of Homeier's stars as ZZ Ceti candidates in a much shorter time than with the 1.23 m telescope.

10.1 Photometry versus Spectroscopy

As explained earlier, the surface gravity and, more importantly, the temperature of an object can be used to determine whether it is placed within or without the region of the ZZ Ceti instability strip. This method was already used in chapter 4 to identify some objects as probable new pulsators based on their SPY analysis results. Thus, atmosphere parameters that are more precise than those derived from the HQS spectra need to be determined for Homeier's stars. This could either be done by recording and analysing higher-resolution spectra than those of the HQS, or by an analysis of photometric data that would have to be acquired using certain filters.

The temperature of a star can be determined from such photometric measurements because the difference of the fluxes measured through two filters with different central wavelengths is a measure of the slope of the continuum, and thus of the temperature. The most commonly employed systems of such standardized filters are that of Johnson, Morgan, and Cousins (Johnson & Morgan 1953, Bessell 1979) with filter bandwidths of about 1000 Å, and that of Strömgren and Crawford (Strömgren 1963, Crawford & Mander 1966) with bandwidths of about 200 Å. The difference of the flux measured through two filters is designated as a "colour" which is named after the abbreviations of the two filters, e.g., $B - V$ which is composed of the filters B and V of the Johnson system. While this colour, and its analogue $b - y$ in the Strömgren system, is a direct measure of the stellar

temperature, the colours $U - B$ (Johnson) or $u - b$ (Strömgren) are also sensitive to the surface gravity since they not only measure the continuum slope but also the strength of the Balmer jump. Thus, if the colours $u - b$ and $b - y$ are plotted against each other, stars with different temperature but the same surface gravity are distributed along an S-shaped curve, where the dependency on temperature is monotonous along the $b - y$ axis but not on the $u - b$ axis. If stars of different surface gravities are considered, a spread along the $u - b$ axis is found. This can be seen in Fig. 10.1 where a grid of DA atmosphere models of different temperatures and gravities is plotted in a $u - b$ vs. $b - y$ diagram.

This grid was calculated by convolving the transmission curves of the Strömgren u , b , and y filters with DA model spectra for different effective temperatures and surface gravities. The convolutions result in a set of synthetic photometry points, that are arranged along lines of constant gravity (shown as solid lines in the figure) and lines of constant temperature (shown as dotted lines). The circle symbols depict the measured colors of known ZZ Ceti variables, taken from McCook & Sion (1999). It can be seen that the combination of the Strömgren $u - b$ versus $b - y$ colors is well suited to identify white dwarfs in the ZZ Ceti instability strip, i.e., in the region in which the known variables are found, because the dependency of the colours on the atmosphere parameters is especially strong in the region of the instability strip. A photometric accuracy of ± 0.02 mag should be sufficient to attain a temperature resolution of ± 500 K and thus allow a separation of probable pulsators from expected non-pulsating stars.

The spectroscopic method for the determination of temperatures is most commonly used today, and most recent ZZ Ceti discoveries were based on a spectroscopic target selection. However the photometric method which involves the observation of a star in three filters, e.g., Strömgren u , b , and y , is as useful in principle and has been made extensive use of earlier (e.g., Koester et al. 1979). This method has only come out of common use because, with the availability of CCDs, the recording of a spectrum became faster and easier than that of three photometric measurements. Besides the longer required observation time, a major drawback of photometric measurements is that they require very stable atmospheric conditions to yield good results. This can be seen from equation 9.2: Here we do not deal with differential but with absolute photometry, and thus all the coefficients in the equation have to be determined, independently for each filter through which the observations are made. These coefficients are determined from the observation of “standard stars” of precisely known magnitudes and colours, but the results are valid only as long as there is no change of the atmospheric conditions. Thus, thin clouds that would hardly be noticeable in differential photometry can easily render observations of the kind that is needed here useless. Another drawback of this multi-color photometry is that large uncertainties can be introduced to the final result due to the multitude of contributing error sources.

However, the photometric method can be useful under certain circumstances: If all measurements of one target, i.e., the photometry through all three filters, can be obtained at the same time with the same instrument, and if one is not interested in the individual measurements but only in their differences, i.e., the colors, then the situation is similar to that of differential photometry: The problem of possibly variable atmospheric conditions is removed as much as it is for differential photometry.

Using such a setup in which the colours are recorded simultaneously, the photometric method is as feasible as the spectroscopic one. If the instrument that records the photom-

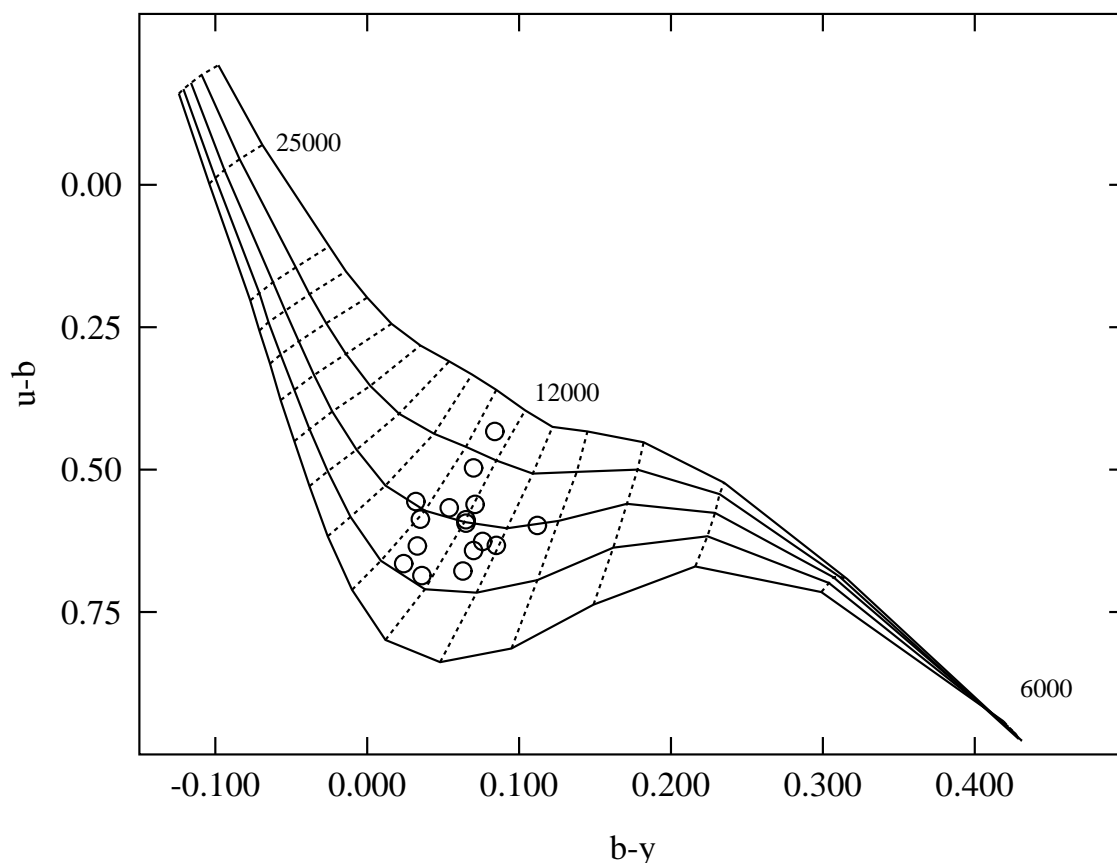


Figure 10.1: The position of known variables (circles) in the Strömgen $u - b$ vs. $b - y$ two-colour diagram. Overplotted is a grid of DA model atmospheres, computed from a convolution of the Strömgen filter curves with the model spectra. Solid lines are lines of constant gravity from $\log g = 7.0$ to 9.0 (bottom to top, in steps of 0.5 dex), and dotted lines have constant temperature, from $T_{\text{eff}} = 6000$ K (lower right) in steps of 1000 K up to $20\,000$ K, followed by $T_{\text{eff}} = 25\,000$ K and $30\,000$ K models in the upper left.

etry is sensitive enough, the multicolor photometry of one target might even be accomplished faster than the recording of a spectrum, and therefore be the preferred method.

10.2 BUSCA

The instrument BUSCA (Bonn University Simultaneous Camera)¹ at the Calar Alto 2.2 m telescope offers all of these advantages, and therefore observations with this instrument were applied for. BUSCA is a four-channel CCD camera, comprised of four independent CCD cameras which are fed with different spectral parts of the stellar flux by a beam splitter system. This beam splitter consists of a setup of three dichroics which separate the light beam from the telescope according to its wavelengths, and each wavelength range is then imaged by one of the CCDs. Due to this setup, not every filter can be used in every spectral channel, and some filter combinations are excluded by this (unless they

¹see <http://www.caha.es/guijarro/BUSCA/busca.html> for more details about the instrument

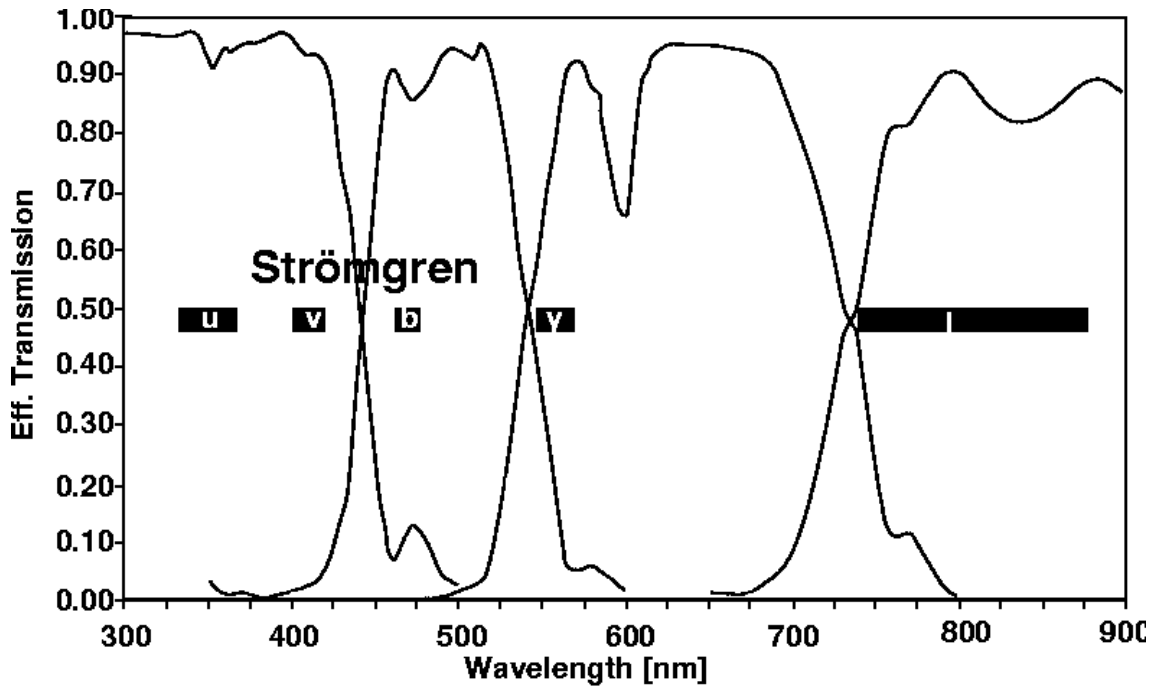


Figure 10.2: The transmission curves of the four BUSCA dichroics, from left to right: The channels a, b, c, and d. Overplotted are the wavelength ranges of the filters of the Strömrgren system, *u* and *v* within the spectral range of the a channel, *b* in the b channel and *y* in the c channel, as well as the much wider *I* filter of the Johnson/Cousins system in the d channel. (Adapted from the BUSCA documentation)

are recorded sequentially). Fig. 10.2 shows the spectral ranges of each channel, and also the wavelength intervals that are covered by the filters of Strömrgren filter system.

The CCDs in each of the four channels have 4096×4096 pixels, which correspond to $0.176''$ on the sky. However for these observations the CCDs were read out with a 2×2 binning, because under usual seeing conditions with stellar images that are never smaller than $0.7''$ and mostly larger than $1''$, the full image scale offers no advantages over the chosen binning, while the noise as well as the readout times are reduced if binning is used. Furthermore not the entire resulting array of 2048×2048 binned pixels was read out, but only the central 512×512 section plus the pixels in the readout direction as seen from that central square. This setup was chosen because only one star, the target, is of interest in each image, and the readout of the extension of the central square towards the chip edge is necessary because the BUSCA controller electronics are not able to skip pixels during the readout of the chip. Both the limited area and the binning serve to decrease the time that is needed to observe one target.

In summary, BUSCA in combination with the large aperture of the 2.2 m telescope seemed to be the ideal instrument for the aim of a photometric determination of stellar parameters. The expected exposure times were as short as to make such observations more feasible than spectroscopy.

10.3 The Observations

The necessary exposure times were determined from information received from O. Cordes (priv. comm.); $t_{\text{exposure}} = 600$ s was predicted for a target with $V = 16$ mag. Based on this, the observations were laid out so that all 250 cool HQS targets with $B < 16$ mag would be observed within two times six nights, separated by half a year, since the targets are distributed equally over the sky. About 20 targets would be observed each night, with some overhead time left for the necessary observations of standard stars that are needed to correct the data for atmospheric effects. Two types of such calibration stars were observed, spectrophotometric standards and Strömgren standard stars. Furthermore, some known variables were included in the observations as a check of the calibration methods.

To attain useful results from which the stellar parameters can be derived with the needed accuracy, sufficiently low shot noise uncertainty and thus a sufficiently high count level is necessary. This demands a certain minimum exposure time, which also depends on the count levels of the sky background. Therefore the photometric uncertainties were monitored throughout the observations and the exposure times were adjusted, if necessary.

The weather in the two observation runs, conducted in August 2003 and March 2004, was such that only a part of the expected data could be obtained. Thus, two more observing runs were applied for. Finally four observation runs comprising a total of 27 nights were carried out with BUSCA from 2003 to 2005. One of the runs, in September 2004, was conducted as a service-mode observation and received additional ‘‘Service Buffer’’ observation time in October 2004, which can be counted as a fifth run from a calibration point of view. The observing times, the fraction of useful nights and the numbers of observed objects are given in table 10.1. 289 objects were observed, a larger than expected total number. The fraction of useful time was especially low in the winter (February/March) runs. Therefore not all objects of the $B < 16$ mag subsample could be observed in the corresponding range of right ascensions. On the other hand more useful time than necessary was available in the summer (August and September) runs, supplemented by the Service buffer time, and thus full coverage of the subsample was reached here, and several secondary targets with $B > 16$ were observed.

Table 10.1: Log of the BUSCA observation runs

Run	Number of Nights	Useful Time [%]	Observed Objects	Remarks
2003-08	6	50	66	
2004-03	6	15	25	
2004-09	6	75	107	Service mode
2004-10	(2.5)	(100)	47	Service buffer
2005-02	4 + 6×0.5	33	44	
Total	27.5	43	289	

10.4 Reduction of the BUSCA Data

The imaging data were reduced with IRAF. Bias and flat field correction images were assembled from multiple bias and flat field exposures, separately for each night, and applied to the data images. Then aperture photometry was carried out.

The aperture size that yields the lowest uncertainty is determined by two factors: an aperture that is as large as possible maximizes the fraction of the stellar flux that is taken into account, i.e., increases the signal and thus the S/N . On the other hand, an increase of the aperture area also increases the amount of total counts that need to be subtracted to take the sky level into account. Thus, for apertures larger than a certain threshold radius the noise will be dominated by the sky level shotnoise, because its contribution to the measurement uncertainty increases linearly with the aperture area. This threshold radius was determined empirically and it was found that the aperture radius is best chosen as 20 pixels, corresponding to 7'' on the sky.

The sky level was determined from circular regions around the aperture. In some images, cosmics (i.e., single pixels with a very high count level, mostly caused by natural radioactivity) had to be removed when they would have been within the aperture. This was done using the program “fitstools”². In a few cases, the target star has a neighbouring star whose image is placed at least partially within the aperture. Such neighbouring stars were removed from the image using some tools that are provided by IRAF: First, a model of the PSF of the stars in the image was created from several bright, isolated stars in the frame. This model was then scaled to fit the star that is to be removed, and the scaled model was centered on that star and subtracted from the image. In this way, the flux contribution of the unwanted star is removed properly even from those pixels on which the removed star and the target star overlap, i.e., were both contribute a non-negligible fraction of the counts of that pixel.

²written by C. A. Goessl, <http://www.usm.lmu.de:81/people/cag/fitstools.html>

Chapter 11

Analysis of the BUSCA Photometry: Identifying the Probable Pulsators

11.1 Correction for Effects of the Atmosphere

The photometry data need to be corrected for atmospheric and instrumental effects, in a way similar to that which is described in equation 9.2.

This correction does not become simple as in the transition from equation 9.2 to 9.3, because the differences that are used here are those of the fluxes of one star seen through different filters, and not those of two stars in the same filter. Therefore the coefficients w_1 and w_2 can not be omitted here, because they are normally different for two filters. Thus the transformation that is needed here to correct the measurements for atmospheric and instrumental effects is similar to equation 9.2:

$$(u - b)_{\text{corr}} = (u - b) + w_1 + w_2 \cdot X + w_3 \cdot (u - b) + w_4 \cdot (u - b) \cdot X \quad (11.1)$$

for the colour $u - b$, and analogously for any other colour. The coefficients are the differences of those that are found for the contributing magnitudes, e.g., $w_1 = w_{1,u} - w_{1,b}$.

The coefficients of the correction have to be determined from the observations of reference stars. A first step is the determination of w_2 , the extinction coefficient. It is derived from observations of a star at different airmasses, i.e., from repeated measurements of a star at different elevations, as it sets or rises in the night. Such data were obtained for several stars to increase the accuracy of the resulting coefficient. In principle any star could serve this purpose, but the other coefficients w_3 and w_4 can only be determined if stars of different colours are observed. Therefore it is best to use stars that cover a broad range of colours, including some of which the colours are similar to those of the targets, i.e., cool white dwarfs. The w_4 and w_3 terms are normally small compared to that of w_2 and so equation 11.1 can be written as

$$(u - b) = w_2 \cdot X + C((u - b), X) \quad (11.2)$$

Thus, although C is not constant, a least-squares fit of a linear function to the $((u - b); X)$ points yields a value of w_2 , and any departures of the $((u - b); X)$ data from the fitted linear relation may be due to the uncertainty of the measurements, as well as to the w_3

and w_4 terms. Both of these terms might be more complex than a simple linear relation. However no significant w_4 dependency is found, and therefore $w_4 = 0$ is assumed for these observations.

11.2 Correction for Instrumental Effects

If the w_4 term is negligible and if w_2 is known and has been corrected for, equation 11.1 becomes

$$(u - b)_{\text{corr}} = (u - b)_{X0} + w_1 + w_3 \cdot (u - b) \quad (11.3)$$

where $(u - b)_{X0}$ is the measured colour that has been corrected for the extinction, i.e., $(u - b)_{X0} = (u - b) - w_2 \cdot X$. Thus, an offset with a possible dependency on the colour can be derived by fitting a function to the $((u - b)_{\text{corr}}; (u - b)_{X0})$ data. This function might be described as a constant, if $w_3 = 0$, or a linear relation, or a higher order polynomial.

For this calibration step there are two different possibilities how the $(u - b)_{\text{corr}}$ values can be obtained; either as literature values of the colours of certain stars, or indirectly from flux distribution data. In the latter case, the $(u - b)_{\text{corr}}$ value of a star is calculated from its literature flux distribution by convolving it with the u and b filter transmission functions. The first method is more straightforward and easier applied, while the second method offers more freedom, because also non-standard transmission functions can be used in the convolution.

The purpose of this last calibration step is to make the final result comparable to other data; either to those of other observers or to theoretical models like the synthetic colours of the model grid in Fig. 10.1. If a comparability of the colours to those of other studies is the aim, the data need to be transformed to one of the standardized photometric systems, in this case that of Strömgren/Crawford, and the result are colours $(u - b)_{\text{corr,Strömgren}}$. That normally involves a potentially complex (non-linear) w_3 correction, because the filters that are actually employed in an observation might have transmission functions that do not exactly match those of the standardised filters that define the photometric system. If the transmission functions differ, a star does not have the same colour in observations through these filters, and the w_3 correction serves to take this into account.

If on the other hand not the comparability to the data of other studies, but the comparability to synthetic colors of model atmospheres is the aim, then there is no need to care about the standard system and its transmission functions. In this case, it is possible to eliminate any need of a w_3 correction and to limit the calibration to the w_1 term, by employing the same transmission functions in the calculation of $(u - b)_{\text{corr}}$ as in the observation of $(u - b)_{X0}$. In this case, the calibration does not use the Strömgren standard system as the reference, but the so-called instrumental system, and the result will be colours $(u - b)_{\text{corr,instrumental}}$.

For this, the transmission functions of the actually employed filters have to be known, and can then be convolved with the flux distribution of the reference stars to create “ w_3 -free” instrumental $(u - b)_{\text{corr}}$ data. If these data are compared to the observed $(u - b)_{X0}$ data there should only be a constant offset, w_1 , provided that the transmission functions that were used in the convolution are actually an exact description of the filter properties. In practice, not only the filter transmission has to be taken into account, but also the

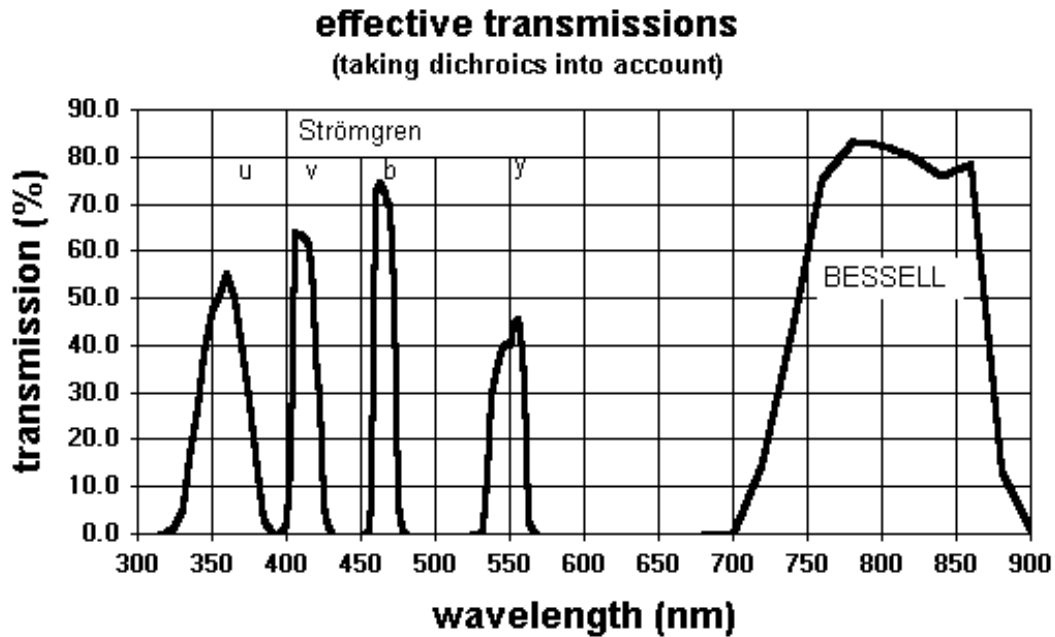


Figure 11.1: The effective transmission curves of the combination of the BUSCA dichroics plus the BUSCA Strömngren filters. (Adapted from the BUSCA documentation)

transmission functions of any other optical elements that are employed besides the filters. Thus, for the BUSCA observations, a convolution of four functions is necessary to attain useful $(u - b)_{\text{corr}}$ data:

- The stellar flux distribution or the model spectrum
- The filter transmission function (Fig. 11.1, shown already convolved with the dichroics transmission)
- The dichroics' transmission function (Fig. 10.2)
- The wavelength-dependent CCD quantum efficiency (Fig. 11.2)

11.3 $u - b$ vs. $b - y$ Analysis

In the analysis of the BUSCA data, both methods have been tried. First, several stars for which Strömngren colours are found in the literature were observed, and it was attempted to derive w_3 and w_1 from a fit of the observed to the literature values. It was found that, as expected, a constant offset is not sufficient and that the relation of $(u - b)_{X0}$ and $(u - b)_{\text{corr,Strömngren}}$ is a complex function. A multitude of $((u - b)_{X0}; (u - b)_{\text{corr,Strömngren}})$ data points would be necessary to derive a proper transformation, but it is not feasible to observe a huge number of reference stars. Instead, synthetic colours were used: A large number of such data points could be employed if $(u - b)_{\text{corr,Strömngren}}$ and also $(u - b)_{X0}$ could

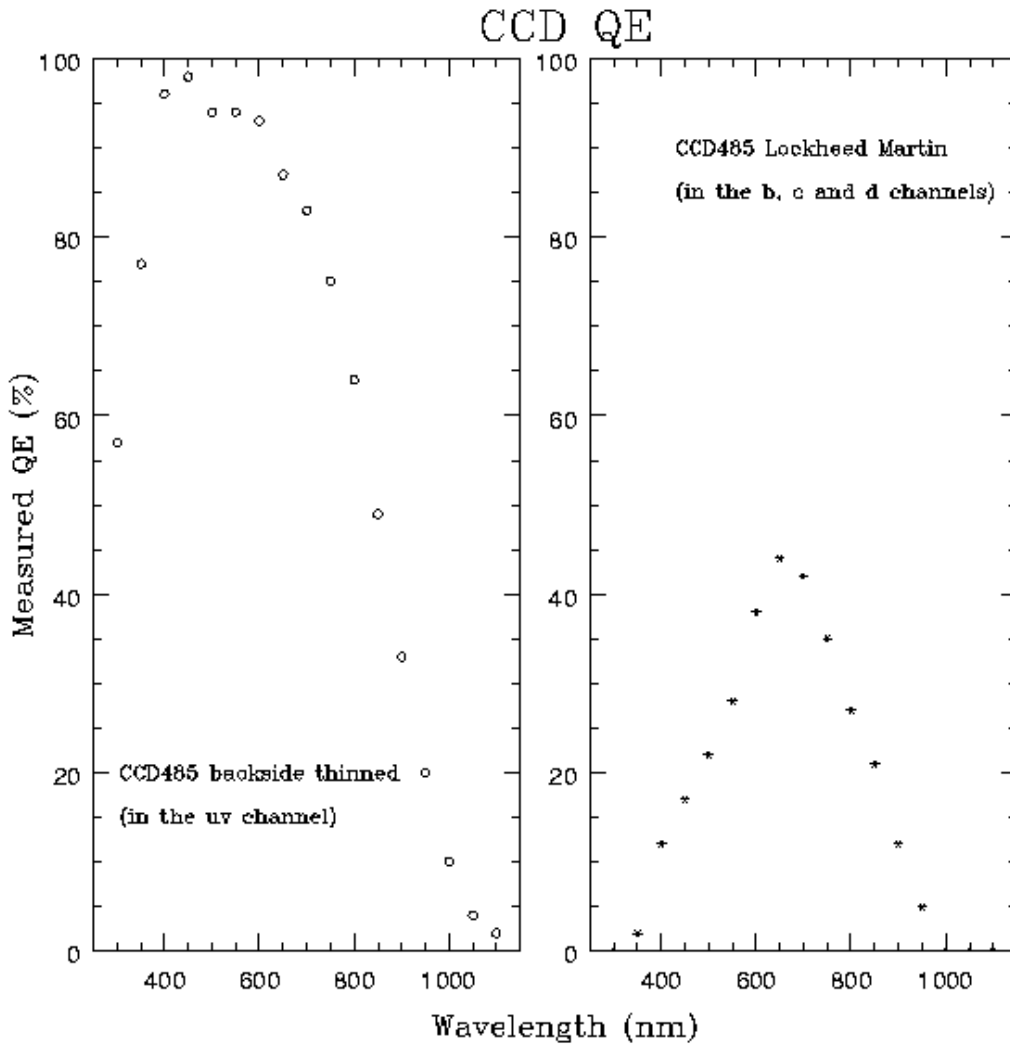


Figure 11.2: The quantum efficiency of the BUSCA CCDs. The left plot shows the efficiency of the CCD in the a channel, the right plot that of the CCDs in the channels b, c, and d. (Adapted from the BUSCA documentation)

be calculated from model spectra. That is not possible for $(u - b)_{X0}$, but the transformation from $(u - b)_{X0}$ to $(u - b)_{\text{corr,Stromgren}}$ can be separated into two steps: the w_1 and the w_3 correction. If the w_1 step is applied first, the intermediate result can be called $(u - b)_{X0,w1}$. This quantity can be calculated; it is equivalent to $(u - b)_{\text{corr,instrumental}}$.

The second step, the w_3 correction, is thus equivalent to a transformation from $(u - b)_{\text{corr,instrumental}}$ to $(u - b)_{\text{corr,Stromgren}}$. These are quantities which can both be calculated; $(u - b)_{\text{corr,instrumental}}$ as a convolution of model spectra and the BUSCA filter transmissions, and $(u - b)_{\text{corr,Stromgren}}$ as a convolution of the same model spectrum with the Strömren system standard transmissions. A number of pairs of colour values ($(u - b)_{\text{corr,Stromgren}}$; $(u - b)_{\text{corr,instrumental}}$) is the result, one for each point of the model atmosphere grid. The w_3 transformation can now be derived by fitting a function to these pairs of values. This was done for both $u - b$ and $b - y$; higher-order polynomials can be employed since the

grid provides a large number of data points for the fit. Of course the fit improves with an increase of the order of the fitted polynomial, but only at the expense of the validity of the resulting transformation outside of the model grid: A polynomial of very high order will yield a good transformation within the parameter space that is covered by the model grid but will not be useful beyond its edges. As a compromise, a polynomial relation of 6th order was chosen. In the resulting transformations $(b - y)_{\text{corr,Strömrgren}}((b - y)_{\text{corr,instrumental}})$ and $(u - b)_{\text{corr,Strömrgren}}((u - b)_{\text{corr,instrumental}}, (b - y)_{\text{corr,instrumental}})$, the dependency on $(b - y)_{\text{corr,instrumental}}$ is of 6th order in both cases and the dependency on $(u - b)_{\text{corr,instrumental}}$ is linear. The coefficients of these transformations are listed in table 11.1, and the fits from which the coefficients were derived are shown in Fig. 11.3. The two grids of the Strömrgren and instrumental model colours are shown in Fig. 11.4.

Table 11.1: Coefficients of the transformations from the instrumental to the Strömrgren system, the “grid transformation”.

Dependency of	Dependency on	Order	Coefficient
$(b - y)_{\text{corr,Strömrgren}}$	$(b - y)_{\text{corr,instrumental}}$	0	0.477
		1	0.395
		2	-3.806
		3	-9.142
		4	-0.972
		5	19.159
		6	15.454
$(u - b)_{\text{corr,Strömrgren}}$	$(u - b)_{\text{corr,instrumental}}$	0	0.867
		1	1.084
$(u - b)_{\text{corr,Strömrgren}}$	$(b - y)_{\text{corr,instrumental}}$	1	1.497
		2	9.477
		3	24.72
		4	12.212
		5	-30.564
		6	-28.238

With this “grid transformation” in place, a three-step approach was used to transform $(u - b)_{X0}$ to the Strömrgren system:

- First, a w_1 calibration is done, i.e., a transformation of $(u - b)_{X0}$ to $(u - b)_{\text{corr,instrumental}}$. This is a constant offset that is derived from a comparison of the observed to the calculated colours of spectrophotometric reference stars. These are those reference stars for which detailed flux distributions are available in the literature that can be used to calculate synthetic colours, in the same way as it is done with the model spectra to calculate the model grid. These data have been taken from the ESO website¹.
- Second, the w_3 correction is applied, i.e., the “grid transformation” from $(u - b)_{\text{corr,instrumental}}$ to $(u - b)_{\text{corr,Strömrgren}}$

¹<http://www.eso.org/observing/standards/spectra/>

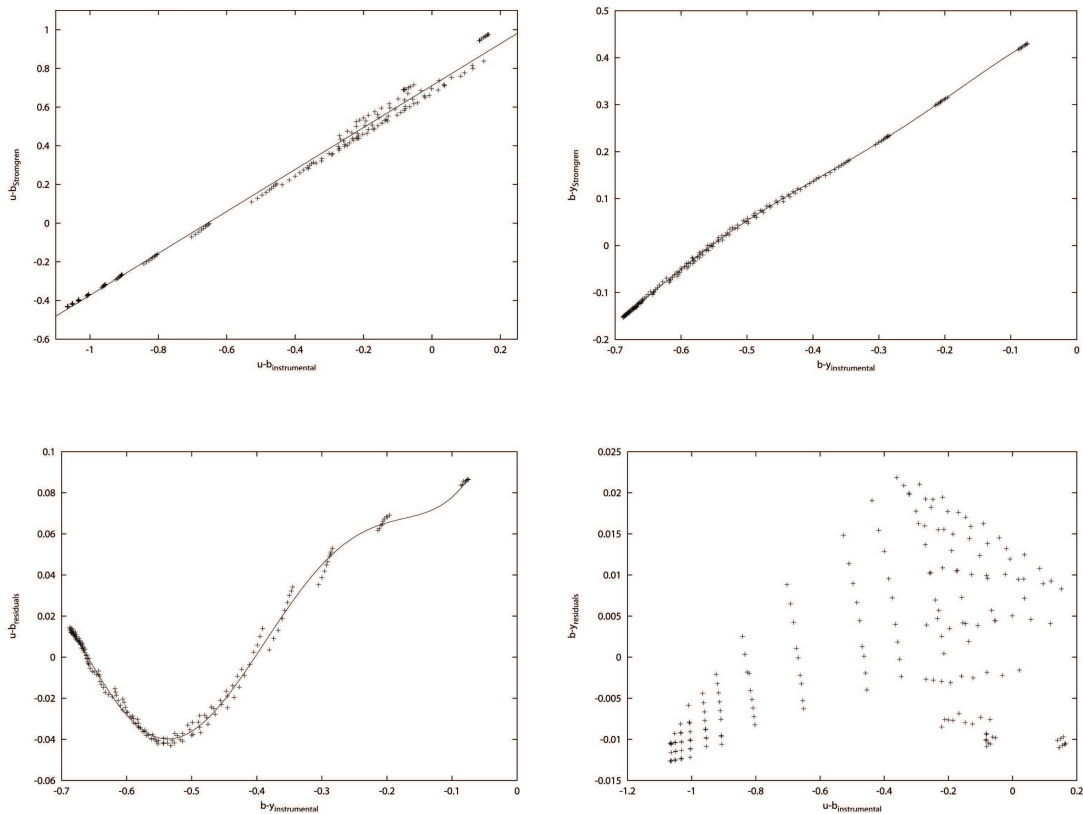


Figure 11.3: The fits of the BUSCA to the Strömrgren data points. In the upper left panel $(u - b)_{\text{corr,Strömrgren}}$ is plotted against $(u - b)_{\text{corr,instrumental}}$ for the model atmospheres, and the linear fit that relates both is shown as a line. The upper right panel depicts the same for $b - y$, and the lower panels display plots of the residuals of each fit against the other colour. A dependency of the $u - b$ residuals on $b - y$ can be fitted, as shown by the line in the lower left panel, but no such “cross-dependency” exists for $b - y$ (lower right).

- Third, another constant offset is applied to the data. This second offset is derived from a comparison of the literature Strömrgren colours of reference stars to observed colours of these stars that have been corrected by the first two steps. This third step is the proper w_1 correction for the Strömrgren system. The Strömrgren literature references have been taken from Wegner (1983).

The resulting colours are not as accurate as expected. The uncertainties can be estimated empirically from the scatter of the different transformed measurements of each reference star. The resulting uncertainties are 0.04 mag for $b - y$ and 0.03 mag for $u - b$, which is larger than the aimed at accuracy of ± 0.02 mag which would have been necessary to allow a discrimination of probable new variables and non-variables. In Fig. 11.5 the results of the first run are shown; there are several stars in the area of the instability strip that have earlier been found not to be variable while the known variables that were included in the observations are placed outside the instability strip. This is another indication of larger than expected uncertainties. As a further indication of large uncertainties, the colours of second observations that were made for some targets as a check of the uncertainties differ by up to 0.05 mag in $b - y$.

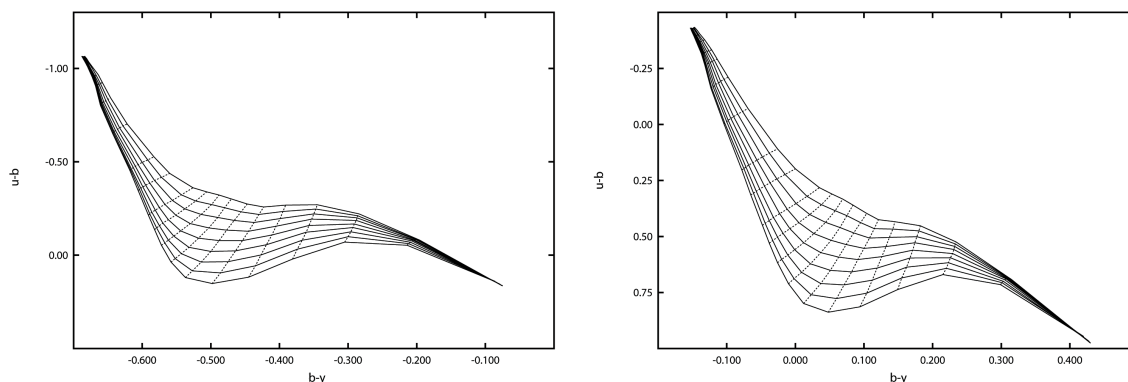


Figure 11.4: The model atmosphere grids that were computed as convolution of the model spectra with the Strömgen standard filter curves (right) and with the BUSCA filter curves (left). It can be seen that a higher-order transformation is necessary to transform the BUSCA data to the standard system, since the grids differ not only by an offset but also appear warped with respect to each other.

The y filter was identified as a reason of these larger than expected uncertainties. It transmits in a wavelength range in which the spectral channel c which is used to record the y data is not fully transparent, but only by 60-70%. The y flux is therefore significantly reduced. This low effective transmission of the BUSCA y filter can be seen in Fig. 11.1. The exposure times for all four spectral channels are the same, and thus one of the channels will be the limiting one with the lowest count rates that determines the exposure time for all channels. Normally this would be the a channel with the u filter, if the instrumental transmissions were the same in all channels and filters. For BUSCA, however, the c channel with the y filter turns out to be the limiting one that achieves the lowest count rates.

Furthermore, the y filter is placed in a spectral region with a highly variable transmission of the dichroic, due to the strong transmission slope at the edge of the dichroic's transmission range. This causes a very distorted effective transmission function of the dichroic + y filter combination as compared to the standard Strömgen y filter function. Therefore the y filter is most probably also the cause of the need of high-order transformations to derive the colours in the Strömgen standard system.

In addition to these disadvantages of the y filter, an unstable zeropoint (i.e., w_1 term) was reported to occur for the BUSCA c channel by Cordes (2005).

11.4 $u - b$ vs. $b - I$ Analysis

As an alternative to the problematic y filter and thus inaccurate $b - y$ colour, the possibility of using the fourth channel of BUSCA exists. There is no filter of the Strömgen system in the wavelength range of the D channel, only the I filter of the Johnson/Cousins system. One would normally not create a “mixed” colour from filters of the Strömgen and Johnson systems because there would not be any references in the literature that the resulting data could be compared to.

However, as mentioned before, there is no need to transform the data to any of the stan-

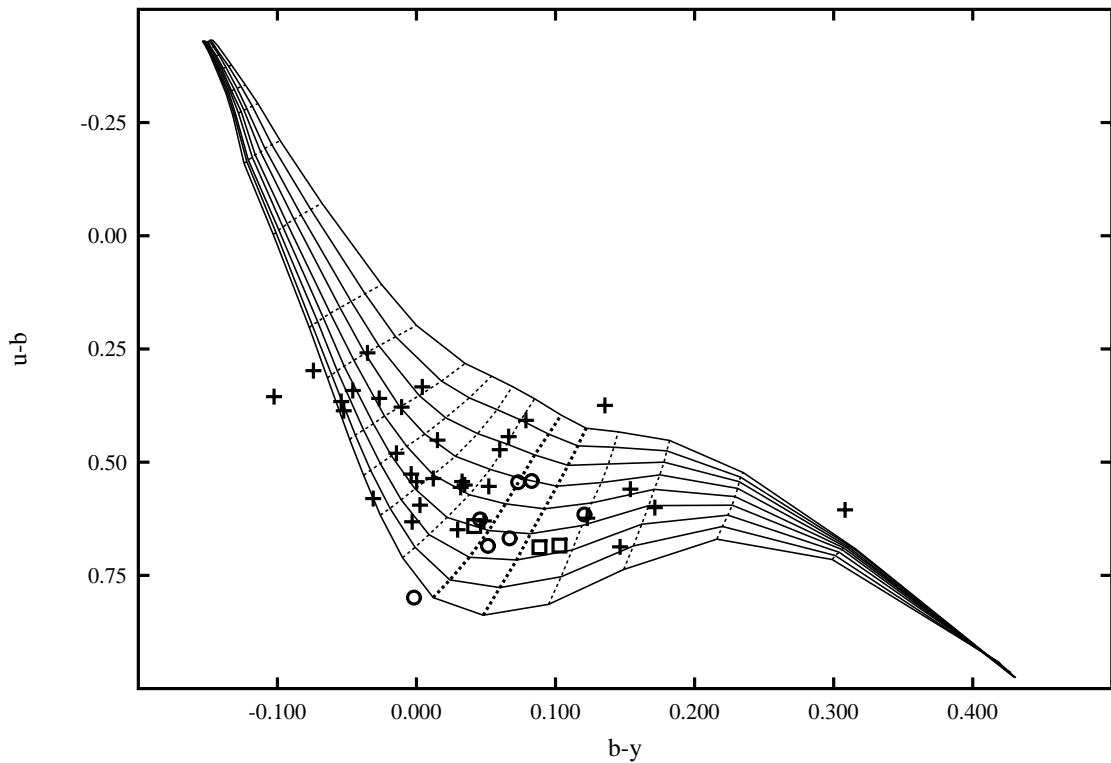


Figure 11.5: The $u - b$ vs. $b - y$ data of the first run, transformed to the Strömgen system and plotted together with the model atmosphere grid. The two thick grid lines of constant temperature are those for $T_{\text{eff}} = 11\,000\text{ K}$ and $T_{\text{eff}} = 12\,000\text{ K}$, which mark the region of the diagram where the instability strip is found. Circles are objects which are not variable, squares are ZZ Ceti stars and crosses denote objects without any knowledge about the presence of pulsations.

standard photometric systems because the aim is a comparison to the model spectra colours which can be calculated even for uncommon filter combinations like Strömgen b and Johnson I . The I data had been recorded together with the Strömgen measurements for all objects, because otherwise the d channel would have been unused without any advantage gained from that.

Therefore, an analysis of $u - b$ vs. $b - I$ data was possible, and the attempt yielded much better results than the $u - b$ vs. $b - y$ analysis. As it was expected, only the first step of the three-part transformation that is described above was necessary; i.e., a simple constant offset is sufficient to transform $(b - I)_{X0}$ to $(b - I)_{\text{corr, instrumental}}$. It was checked whether a non-constant offset, e.g., a linear transformation yields better results than a constant offset, which is not the case. Also, it was ascertained that there is no residual w_3 dependency of the results on the stellar colour.

Furthermore the use of $b - I$ instead of $b - y$ offers the advantage that the parts of the continuum that are sampled by both filters are further apart and thus the temperature sensitivity is even higher than that of $b - y$. Expressed differently, the range of $b - I$ values in a certain temperature interval, e.g., 1000 K , is much larger than the range of $b - y$ values in the same temperature interval. At the same time, the numerical values of the uncertainties are similar for both colours, and thus a finer temperature discrimination

can be achieved using $b - I$. This can be seen in plots of the $u - b$ vs. $b - I$ diagram, like Fig. 11.6. The dependency of the colours on temperatures and especially gravities is low for very hot and for very cool temperatures, but is very strong in the region of the ZZ Ceti instability strip, stronger than for $b - y$.

The advantages of the $b - I$ colour as compared to $b - y$ are thus manifold, a higher temperature sensitivity is reached with shorter exposure times; and more targets can be observed in a given time. Thus for all following runs, only $u - b$ vs. $b - I$ data were analysed, and accordingly no Strömgren reference stars were observed in the later runs but only spectrophotometric references. A relatively large number of 7-9 such stars were observed in each night to cover a wide range of colours and to allow a reliable estimation of the uncertainties. Figs. 11.6 to 11.10 show the calibration results for individual nights of each run, i.e., the calculated colours of the reference stars, derived from their spectrophotometric data, compared to the transformed observed colours. The results for the other, not shown nights of each run are similar to that which are shown.

In the first run, only two hot spectrophotometric references were observed, and thus a possible w_3 dependency could not be investigated here but only in the following runs. Only the data of the 2004/09 and 2004/10 runs show any dependency of the (theoretical – transformed observations) colour residuals on the colours. As it can be seen in Fig. 11.8, the theoretical colours (crosses) of the hot as well as of the cold reference stars appear bluer than the corresponding observations (circles), and vice versa the theoretical colours are redder than the observations for the references at intermediate colours. This could be interpreted as a w_3 term of quadratic form, but such a fit gave results that were only marginally improved over a constant offset.

It can be seen that the calibration results are very good for the second run (Fig. 11.7). For each of the later (third-fifth) runs, there are one or two reference stars with much larger differences of calibrated observations and theory than for the other references. The empirical uncertainties, derived from the residuals of (calibrated observations – reference colours), are especially large in the third run, where even the w_2 correction seems to be inaccurate since the individual observations of one object which differ mostly by their airmasses should be transformed to one calibrated colour value, which is not the case. Furthermore, as already mentioned there seems to be a systematic effect by which the observed colours of the hot and cold references are placed systematically different from the colours of the references at intermediate temperatures, which as mentioned above can however not be well reproduced as a colour-dependent effect. Another possibility might be a dependency on the stellar flux, since the hot and cold references have an on average higher flux than those at intermediate temperatures, but there is no physical reason to assume such a dependency. The b data might be the cause of a systematic effect since the systematic differences are similar in size but are of different sign in $u - b$ and $b - I$. Problems with the charge transfer efficiency of the BUSCA b channel CCD might be an explanation for this (O. Cordes, priv. comm.). The magnitude of such an effect would however be dependent on the position of the star on the chip, and no such dependency could be found. Thus, the reason for the systematic uncertainty remains undetermined, but the effect of any present systematic uncertainty should be similar for the targets and for the reference stars at intermediate temperatures, since they and the targets have similar colours. Therefore the data of the third and fourth runs are calibrated based only on the intermediate temperature references.

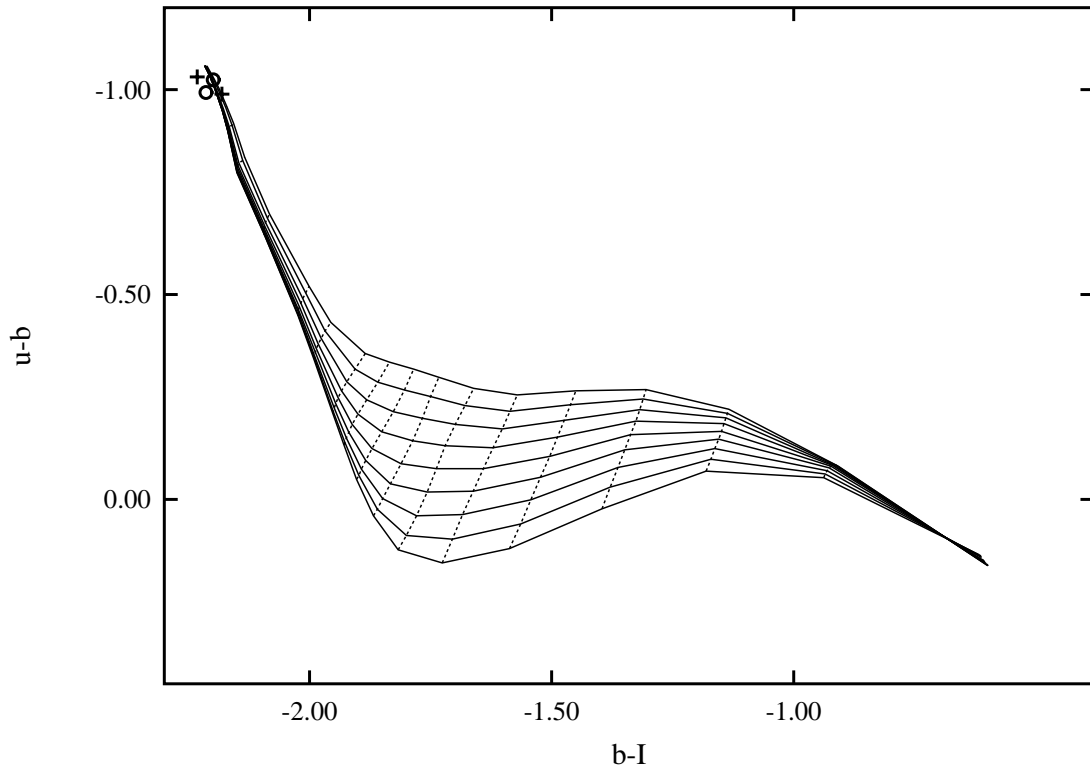


Figure 11.6: The calibration of the first run data; crosses show the calculated colours and circles the observations of the first night of the run. Only two spectrophotometric references of similar temperature were observed because it was originally planned to calibrate the data with Strömgen literature reference stars which can not be employed in the $b - I$ analysis.

The calibrated data are shown in Figs. 11.11 to 11.15 for the five runs; it can be noticed that the data cluster around the $\log g = 8$ line of constant gravity in the first two and the last run but are found at on average lower gravities in the third and fourth run plots. This is an additional indication of a higher uncertainty for the data of these runs. Nevertheless, the identification of new variables was as successful from the two problematic runs as from the other three; in each plot the new and previously known ZZ Ceti stars are plotted, as well as the non-variables. The positioning of both types of stars can be considered as a further measure of the uncertainty. The distributions of variables and non-variables are consistent with a maximal uncertainty of 0.05 mag.

The uncertainties that are derived from the calibration residuals are about 0.05 mag for the more problematic calibrations and better than that for the remaining runs, e.g., 0.03 mag for both colours in the second run.

Such a $b - I$ difference corresponds to a temperature difference of 500 K in the region of the instability strip, which fulfils the original temperature resolution aim. Figure 11.16 shows that although several non-variables are found within the instability strip according to their colours and some variables are placed outside, the selection of possible variables is well possible if also those candidates that are placed near the instability strip are considered as possible variables. If an overall uncertainty of 0.05 mag is taken into account, the “success rate” should be close to 50%, i.e., half of the stars that were selected as probable

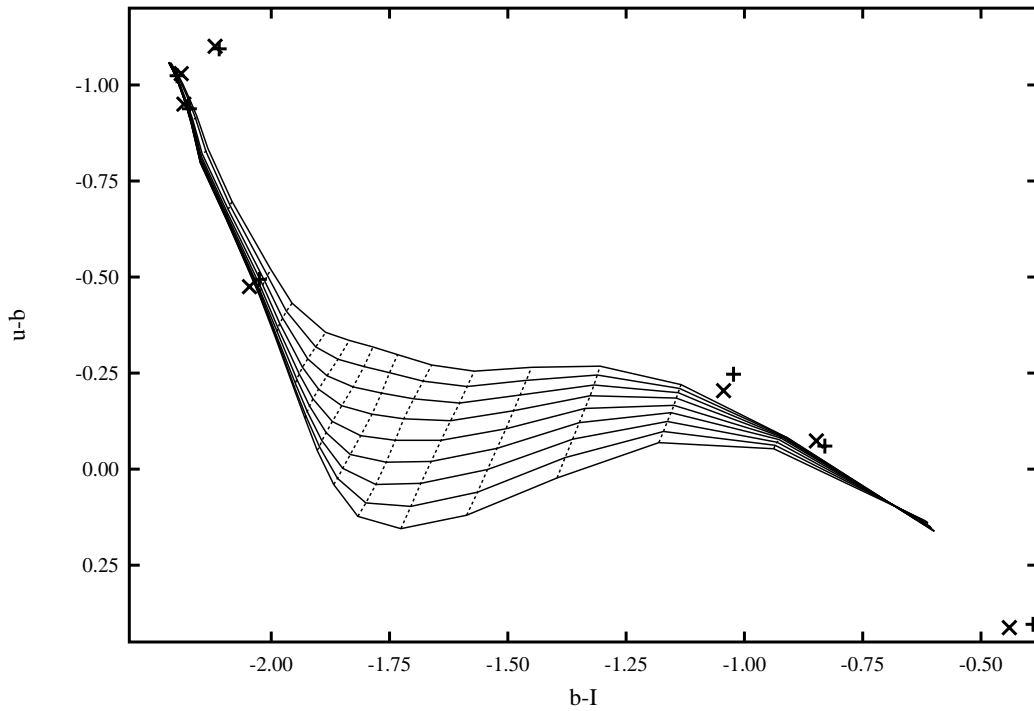


Figure 11.7: The same as Fig. 11.6, for the second run. \times symbols depict the observations and crosses the reference colours that are calculated from spectrophotometric data.

variables should indeed be ZZ Ceti stars.

Temperatures and gravities have been derived from the colours using a fitting routine developed by D. Koester which, similar to the algorithm described in chapter 3, minimizes the differences between observed colours and those of the model grids by calculating χ^2 for each grid point and interpolating to a χ^2 minimum in between the grid points. The temperature results that are derived in this way are listed in the appendix in table F.1. Two observations are available for 24 objects, from which an average temperature difference of $\langle \Delta T_{\text{eff}} \rangle = 345$ K and an average $\log g$ difference of $\langle \Delta \log g \rangle = 0.39$ can be derived.

The BUSCA results can be compared to the SPY results that are available for some common objects. The SPY and BUSCA temperatures of five such objects that were compared agree within 350 K in all cases, the average temperature difference is 140 K. The agreement of the $\log g$ data is not as good, the average difference is 0.28 dex. Nevertheless the temperature, which is more important for the ZZ Ceti candidate selection, is less uncertain according to the comparison with SPY temperatures than it would have been expected from the overall 0.05 mag $b - I$ uncertainty.

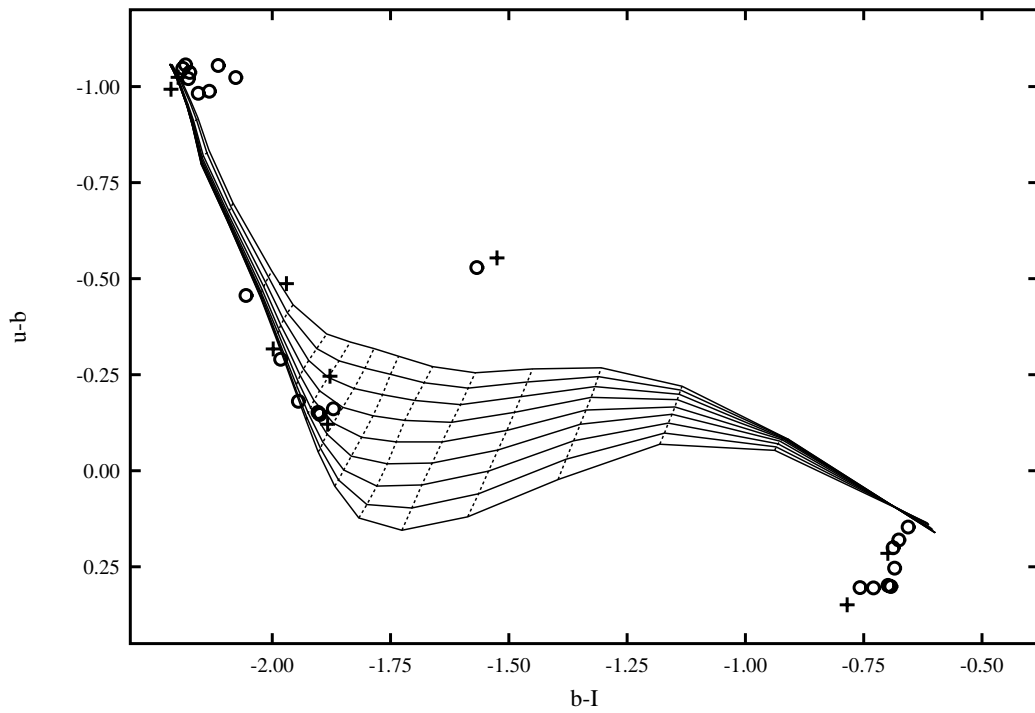


Figure 11.8: The same as Fig. 11.6, for the fifth night of the third run. Multiple observations of one target are shown for those that were observed repeatedly at different airmasses.

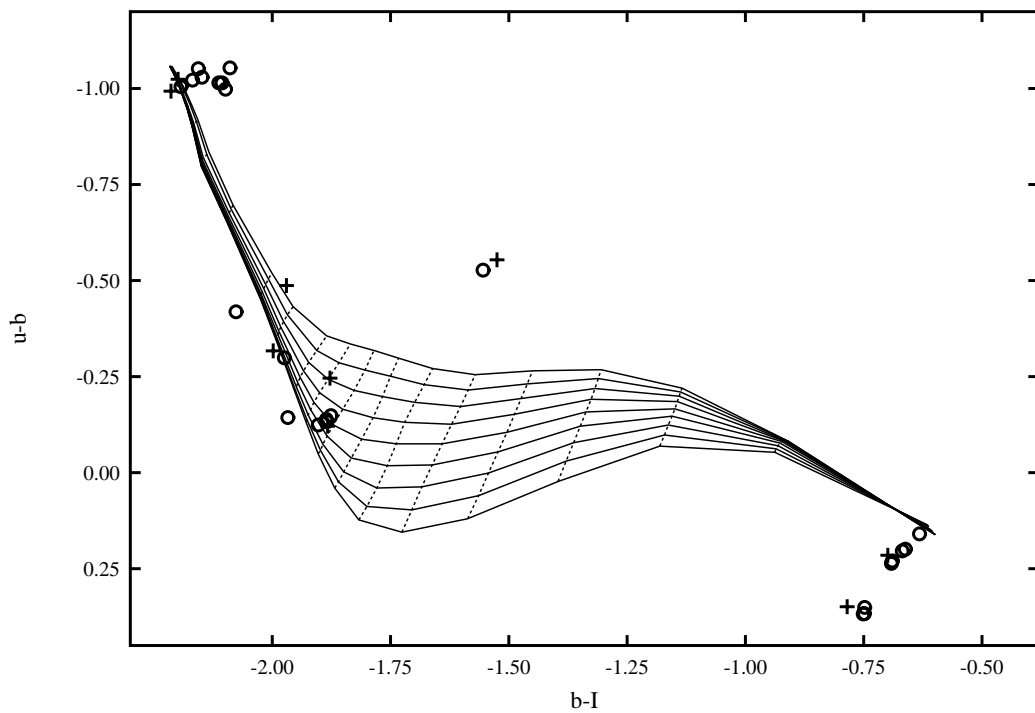


Figure 11.9: The same as Fig. 11.8, for the second night of the fourth run, i.e., for the service buffer observations.

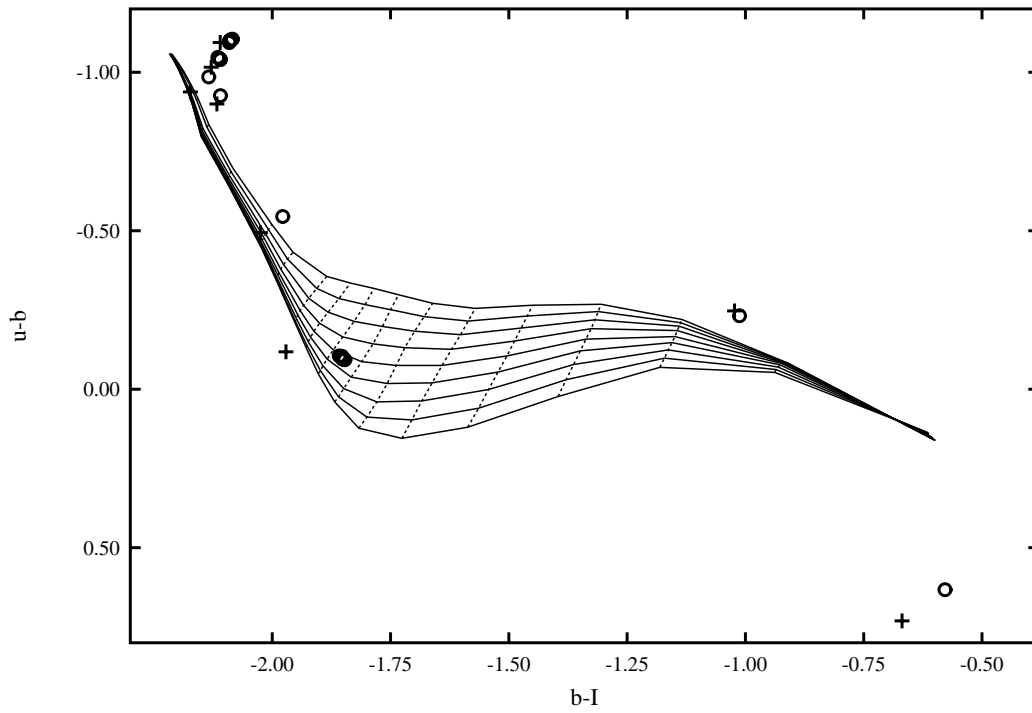


Figure 11.10: The same as Fig. 11.8, for the last night of the fifth run.

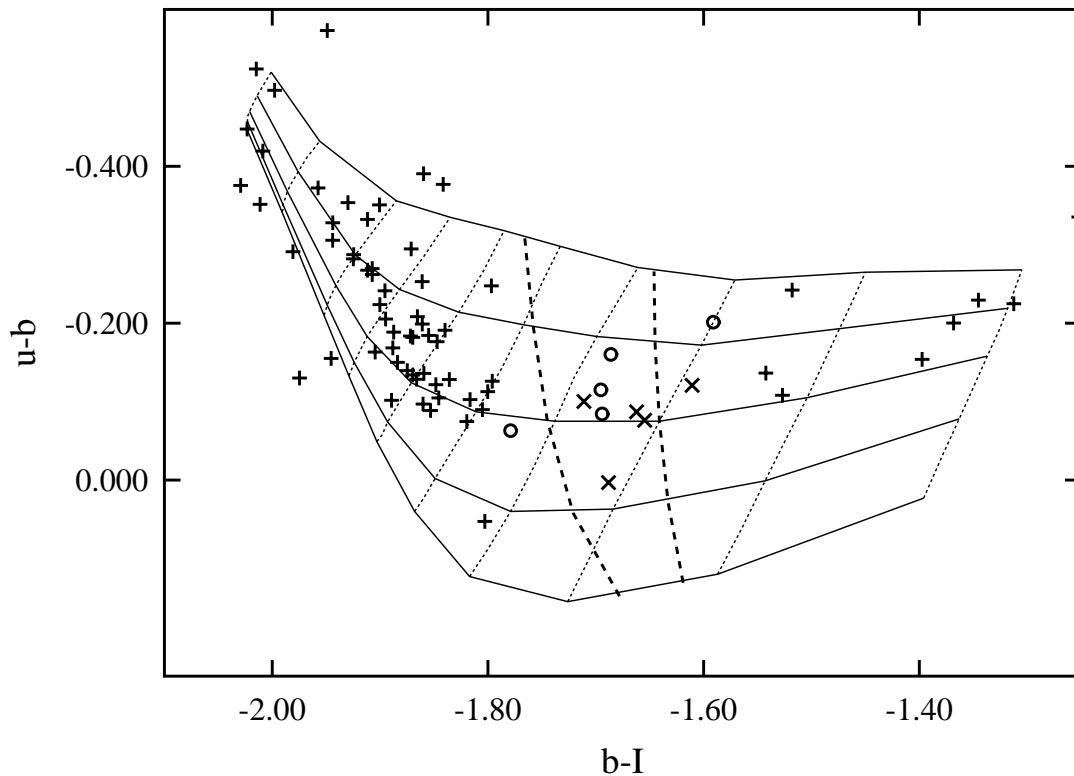


Figure 11.11: The calibrated observation results of the first run. ZZ Ceti stars are shown as \times symbols, non-variables as circles and objects without lightcurve observations as crosses. Only a part of the model atmosphere grid is shown, from temperatures of 9000 K (right) to 20 000 K (left).

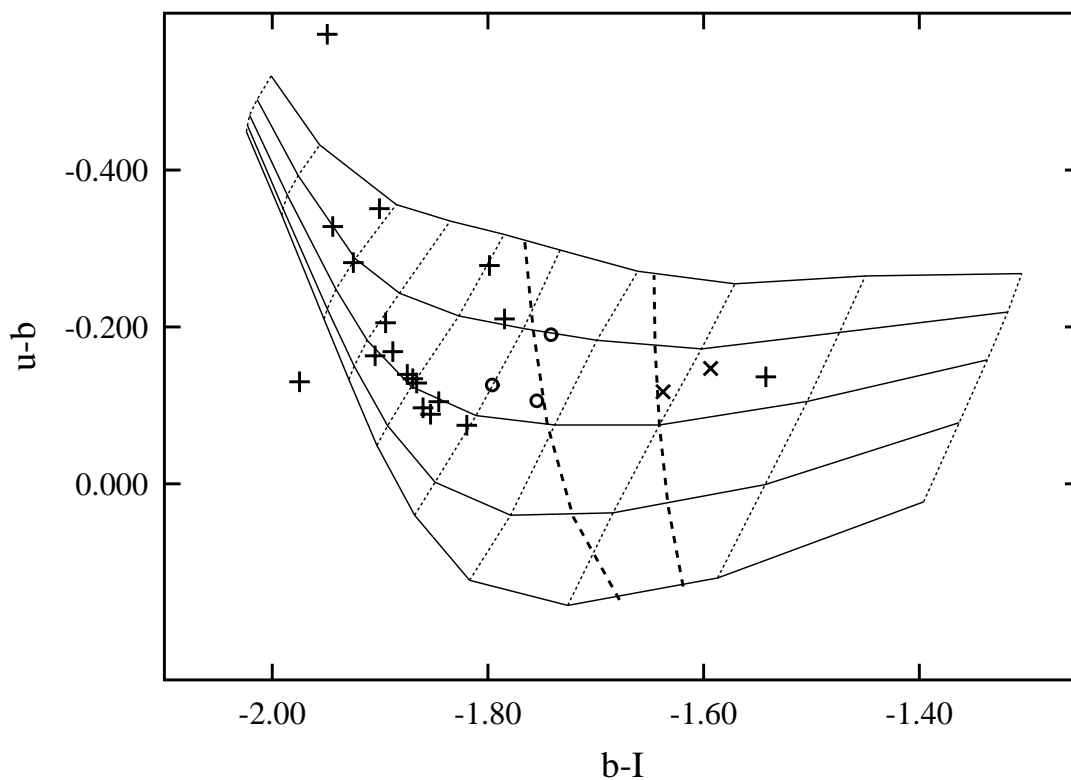


Figure 11.12: The same as Fig. 11.11, for the second run.

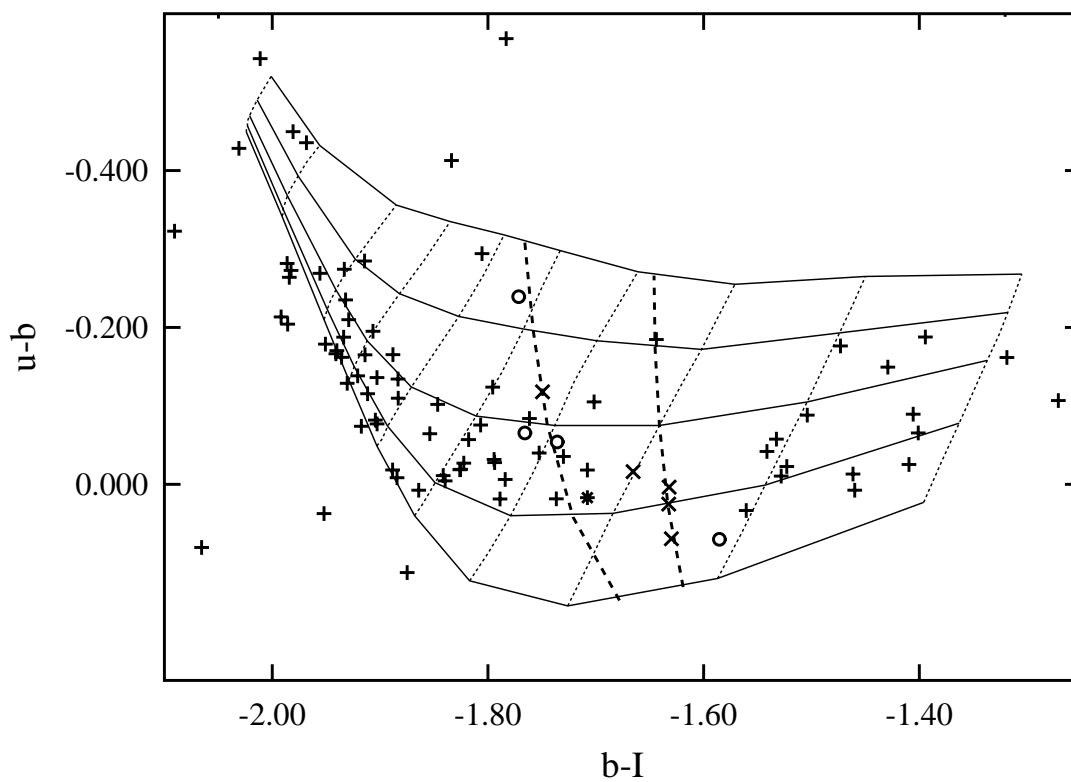


Figure 11.13: The same as Fig. 11.11, for the third run. An object for which ambiguous lightcurve observations were obtained and that is possibly variable is marked as an asterisk.

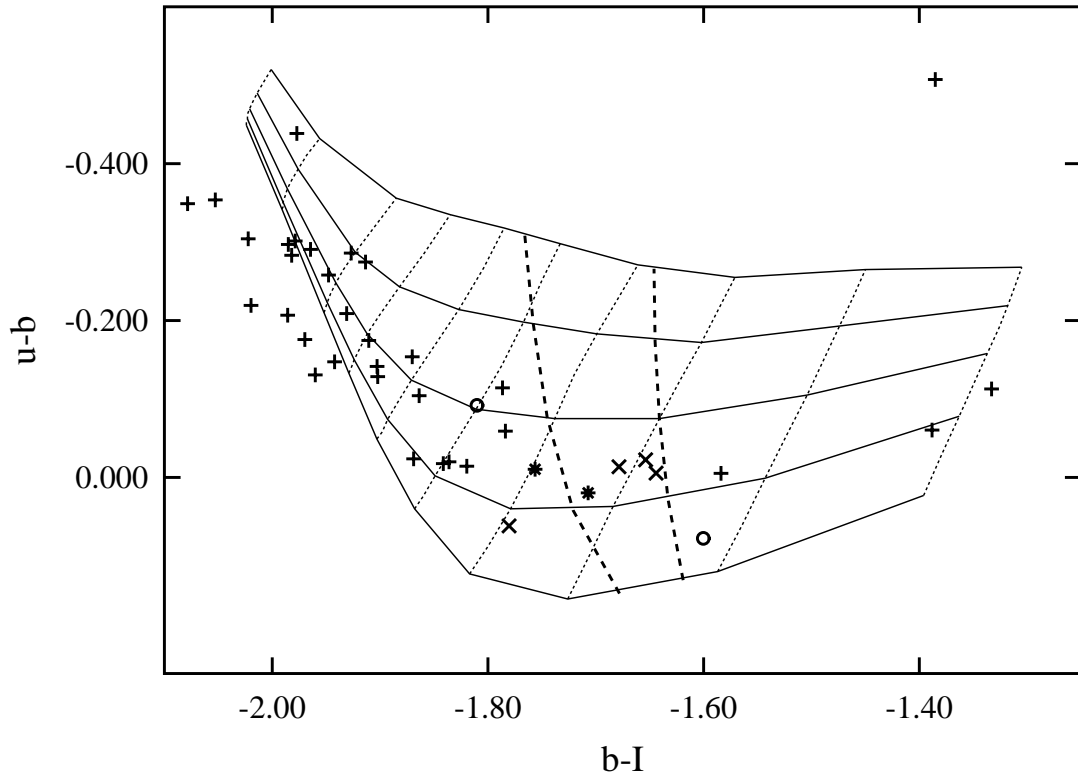


Figure 11.14: The same as Fig. 11.13, for the fourth run.

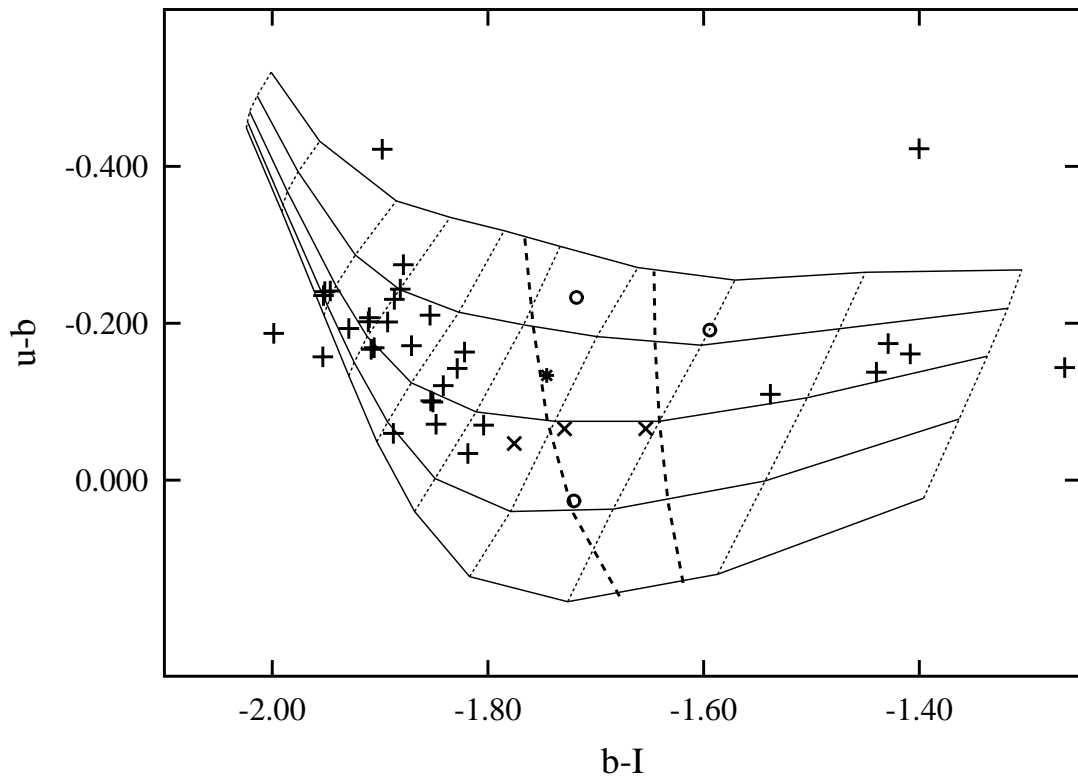


Figure 11.15: The same as Fig. 11.13, for the fifth run.

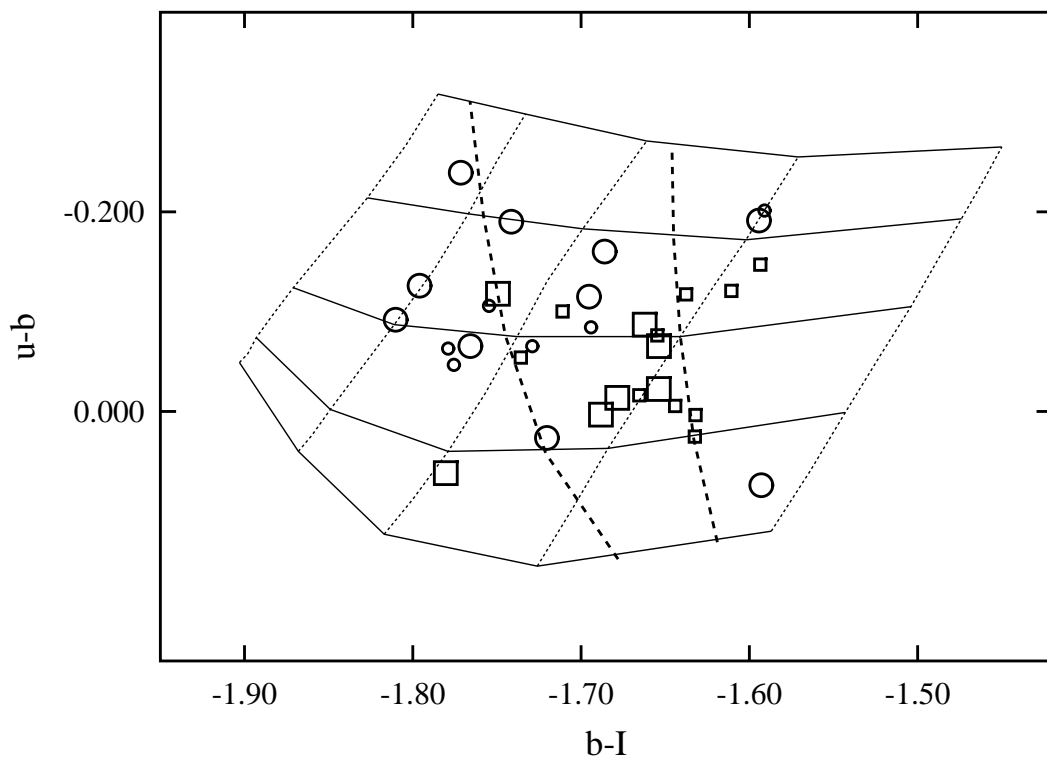


Figure 11.16: The observed ZZ Ceti and nonvariable stars of all runs, plotted as circles (non-variables) and squares (variables). Small symbols show previously known variables or non-variables, and large symbols display those for which lightcurve observations were obtained based on these photometry results. Only a part of the model atmosphere grid is shown, from temperatures of 10000 K to 14000 K.

Part IV

**Lightcurve Observations of New ZZ
Ceti Stars**

Chapter 12

Early Lightcurve Observation Attempts

12.1 Three New Variables from Observations by Collaborators

After candidate ZZ Ceti stars had been selected from the analysis of SPY spectra, the BUSCA photometry, and the observations at the Calar Alto 1.23 m telescope, these probable variables needed to be confirmed as pulsators by lightcurve observations. Such observations require a relatively high temporal resolution of less than half of the shortest known periods of the ZZ Ceti pulsations, i.e., ~ 30 s, and at the same time the recorded flux has to be sufficiently high to allow to detect the weakest known ZZ Ceti pulsations which have amplitudes of $\sim 0.1\%$. To achieve this goal, a special instrumentation of the employed telescope is necessary, either using a photoelectric photometer or a CCD camera with a specialized controller hardware that allows a fast readout of the CCD chip. Only these types of instruments allow lightcurve observations of the relatively faint targets. However, at the observatories that can normally be accessed by german astronomers, i.e., that at Calar Alto and those of ESO, such an instrumentation is not available.

Therefore some of the candidate ZZ Ceti stars were forwarded to other observers with access to such instruments, namely R. Silvotti with access to Loiano observatory, Italy, and B. G. Castanheira with access to such instrumentation at different telescopes in Brazil. They discovered three new variables, HS 1039+4112, HE 1429–0343, and WD 0016–258, among the BUSCA and SPY candidates and found five further candidates to be non-variable. The new variables were published in Silvotti et al. (2005) and Castanheira et al. (2006). These eight observed candidates are contained in the comprehensive plot of SPY- and BUSCA-based ZZ Ceti discoveries in Figs. 14.8 and 14.9.

12.2 Observations at Observatoire Haute-Provence

At the same time, it was attempted to gain direct access to a fast-photometry-equipped telescope, without having to hand over the observations to collaborators. This became possible after the EU-financed OPTICON project offered access to a multitude of european observatories to observers from all european countries. These observatories include the Observatoire Haute-Provence (OHP), France, and the Nordic Optical Telescope

Table 12.1: Properties of the ZZ Ceti candidate stars that were observed at OHP, according to the SPY analysis and the two-colour photometry.

Object	RA (J2000)	DE	B [mag]	T_{eff} [K]	$\log g$	method
HE 0043–0318	00 46 18.4	-03 02 01	15.5	12010	7.94	spectroscopy
WD 0318-021	03 20 58.8	-02 00 00	16.0	11923	8.10	spectroscopy
HS 1612+5528	16 13 16.6	+55 21 26	15.9	11706	8.19	photometry
HS 1701+5039	17 02 19.0	+50 34 59	16.4	11586	8.05	photometry
WD 1959+059	20 02 12.9	+06 07 35	16.4	11033	8.23	spectroscopy
HS 2354+1929	23 56 38.3	+19 45 52	16.0	12479	7.92	photometry

(NOT) at Observatorio Roque de Los Muchachos, Spain. At OHP, a photoelectric photometer can be employed at a 1.93 m telescope, and the NOT offers the possibility of lightcurve observations using a specialised CCD camera. Observation time was applied for at both observatories, first at OHP.

The OHP observations were planned and carried out in collaboration with G. Vauclair (Observatoire Midi-Pyrénées) and M. Chevreton (Observatoire Paris-Meudon), of which the latter is the developer and owner of the employed instrument. An observation time of five nights in September 2004 was granted, and the observations were carried out with the help of M. Chevreton. Due to the weather conditions, only a small fraction of the observation time could be used and only six candidates were observed for two hours each, all of which were found to be non-variable.

Table 12.1 lists the properties of the observed candidates. Three were selected from the SPY spectra analysis and three from the BUSCA photometry. One of the SPY candidates, WD 1959+059, was later re-observed at the NOT and found to be indeed variable with a long period and low amplitude. For another SPY target, WD 0318-021, signs of possible variations could be found in parts of the lightcurve, but the weather situation prevented a confirmation of pulsations.

Chapter 13

The NOT Observations

13.1 Setup of the Observations

The Nordic Optical Telescope (NOT) is located at the Roque de los Muchachos Observatory on the Island of La Palma (Spain). Due to its low latitude location of $28^{\circ} 45'$, it is even more suitable for observations of the ZZ Ceti candidates with low declinations that are selected from the SPY sample than the OHP 1.93 m telescope. The NOT has a main mirror with a diameter of 2.5 m, and therefore fainter targets can be observed than at OHP. It should be possible to obtain useful data for targets that are fainter than $B = 17$ mag, but all ZZ Ceti candidate stars that were identified from the SPY sample and in the BUSCA observations are brighter than that.

The instrument that was used, ALFOSC (Andalucia Faint Object Spectrograph and Camera, see <http://www.not.iac.es/instruments/alfosc/>), is a multi-purpose instrument with which photometric as well as spectroscopic observations can be carried out. It can be equipped with a special camera controller that allows a fast readout of the chip and thus facilitates “fast photometry” observations such as the recording of ZZ Ceti pulsation lightcurves. This controller and the software with which the fast photometry observations are carried out are described in Østensen & Solheim (2000).

The camera uses an E2V back-illuminated 2048×2048 CCD chip, and the fast photometry controller permits a multi-windowed readout mode in which only the data from multiple small areas of the chip is read, which typically takes about 5 s, compared to 90 s for the full frame. Windows with a size of 64×64 pixels were used, corresponding to about $12''$ on the sky. In addition to the target star window, at least five additional windows were read from the CCD, at least three of them centered on the brightest comparison stars that are available in the field of view, and two on empty sky fields. Similar to the earlier observations at OHP and at the Calar Alto 1.23 m telescope, a broad spectral range was covered, this time using a sky contrast filter “W” (NOT # 92) with a bandwidth of 2750 \AA , centered on 5500 \AA . The integration times were between 9.9 s and 50 s, leading to cycle times between 15 s and 56 s, depending on the target magnitude. More details about the sequence lengths and cycle times are given in the NOT observation journal in Table 13.2. Two separate runs of lightcurve observations were carried out at the NOT, one in May 2005 and another in December 2005. Table 13.1 lists the properties of the targets that were observed in these runs.

Four of the observed SPY objects are in common with the sample of photometrically

selected candidates, i.e., for these four stars parameters were derived from both types of data. The values of the effective temperatures are in very good agreement for all four objects, but the values of $\log g$ are quite different in two cases.

13.2 Data Reduction and Analysis

The reduction of the NOT data was done by a combination of the program packages IRAF and RTP (Østensen & Solheim 2000)¹. IRAF was used to assemble a combined bias frame and flat field from several individual bias and flat exposures. These combined correction images were then applied to the imaging data by RTP. The photometric data were obtained from the images by RTP, as well. For that, the program determines the background sky level either from one of the recorded empty sky fields, or from an annulus surrounding each star within its 64×64 -pixel image region. Taking this sky level into account, the counts within a circular aperture are determined, and a weighed sum of (target - reference star) magnitudes is computed. The position of the center of the aperture is recomputed individually for the stars in each frame.

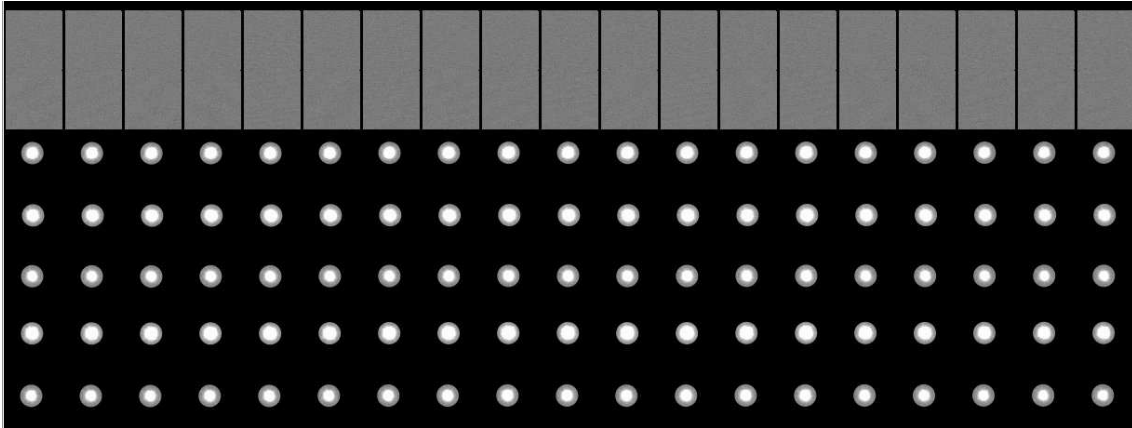


Figure 13.1: This example shows a part of the imaging data of one target. Each column corresponds to one frame of data, and each line shows the data of one window at different times. The upper two lines show the empty sky regions, the third line displays the target window and below that the reference star windows are shown. For the target and reference star windows, only the circular segment within the photometry aperture is shown.

Different fixed apertures were used, i.e., the entire reduction was repeated several times with different aperture radii, as well as with the different methods of determining the sky level. The resulting lightcurves were corrected for atmospheric extinction, assuming an average extinction coefficient for the W filter $k_W = 0.18$ that had been determined by R. Østensen during earlier observations with the same setup. Finally, the lightcurves were corrected for any remaining linear trend.

The fourier transform (FT) of each lightcurve was then computed using another program of the RTP package, RTFT, and the noise in the FT is determined by computing $\langle A \rangle$, the mean amplitude in those parts of the FT where no signal is present. Ideally the

¹also see <http://www.not.iac.es/instruments/alfosc/fastphot/>

Table 13.1: Properties of the observed ZZ Ceti candidate stars, according to the SPY analysis and the two-colour photometry. Results from both methods are available for four objects, and for two objects there are two independent sets of photometric data. The last column gives the type of the objects, where NOV_x describes an object for which no variations with an amplitude higher than x mma were present.

Object	Alias	RA (J2000)	DE	B [mag]	T_{eff} [K]	$\log g$	Source	Type
HS 0210+3302		02 13 06.2	+33 16 10	15.8	11924	7.39	BUSCA	hDAV
HS 0213+0359	PB 6785	02 15 36.7	+04 13 38	16.6	13035	8.01	BUSCA	NOV2
WD 0235+069	HS 0235+0655	02 38 33.1	+07 08 10	16.6	10950	7.75	BUSCA	cDAV
WD0344+073	HS 0344+0718, KUV	03 46 51.4	+07 28 02	16.2	10470	7.77	SPY	NOV2
					10136	7.23	BUSCA	
					10234	7.21	BUSCA	
HE 0344-1207		03 47 06.7	-11 58 09	15.8	11466	8.28	SPY	cDAV
HS 0401+1454		04 04 35.0	+15 02 27	16.2	12375	8.10	SPY	NOV2
					12329	7.93	BUSCA	
WD0710+216	GD 83, EGGR 214	07 13 21.6	+21 34 07	15.3	10222	7.97	SPY	NOV1
HS 0733+4119		07 37 07.9	+41 12 28	15.9	11162	7.72	BUSCA ¹	cDAV
WD0946+488	HS 0946+4848, SDSS	09 49 35.4	+48 34 05	17.5			²	NOV2
WD 1126-222	EC 1126-2217	11 29 11.6	-22 33 44	16.5	12077	8.08	SPY	hDAV
WD 1149+057	PG 1149+058	11 51 54.3	+05 28 38	15.1 ¹	10994	7.98	SPY	cDAV
					11105	7.95	BUSCA	
WD 1150-153	EC 11507-1519	11 53 15.4	-15 36 36	16.0	12453	8.03	SPY	hDAV
HS 1249+0426	PB 4304	12 52 15.2	+04 10 43	15.8	11494	8.05	SPY	hDAV
WD 1300-098	PG 1300-099	13 03 16.8	-10 09 13	16.3 ¹	13299	8.27	SPY	NOV1
HS 1308+1646		13 11 06.1	+16 31 03	15.5	10957	8.33	SPY	NOV1
					11004	8.62	BUSCA	
WD 1342-237	EC 13429-2342	13 45 46.6	-23 57 11	16.1	11124	8.21	SPY	cDAV
HS 1441+3219	CBS 391, WD 1441+323	14 43 17.5	+32 06 57	16.4	12390	8.24	BUSCA	NOV2
HS 1531+7436		15 30 35.4	+74 26 04	16.2	12357	8.17	BUSCA	hDAV
HS 1544+3800		15 46 05.6	+37 51 27	14.4	13042	8.17	BUSCA	NOV1
HS 1556+1634		15 58 40.3	+16 25 55	15.8	11439	7.55	BUSCA	NOV1
HS 1612+5528	SDSS 1612+555	16 13 16.6	+55 21 26	15.9	11707	8.18	BUSCA	NOV2
HS 1625+1231		16 28 13.8	+12 24 56	16.1	11272	8.06	BUSCA	cDAV
HS 1824+6000		18 24 44.3	+60 01 58	15.7	11192	7.65	BUSCA	hDAV
HS 1951+7147		19 50 45.6	+71 55 39	16.8	11789	8.40	BUSCA	NOV2
HS 2217+2454		22 20 15.7	+25 09 09	16.1	11971	7.72	BUSCA	NOV3
					11490	7.75	BUSCA	
WD 2333-049	G 157-82	23 35 54.0	-04 42 15	15.7	10506	8.00	SPY	NOV2
HS 2351+3554		23 53 55.0	+36 11 27	16.6	11325	7.58	BUSCA	NOV2

¹ Homeier (1998) gives $T_{\text{eff}} = 11420$ K, $\log g = 7.63$ for HS 0733+4119.

² This object was selected based on the parameters $T_{\text{eff}} = 11700$ K, $\log g = 8.69$ that are given in Homeier (1998). However, a later analysis, carried out together with D. Homeier, of a now available SDSS spectrum of that object revealed that it has a late-type main sequence companion, and that the white dwarf itself is probably hotter, with $T_{\text{eff}} = 16015$ K, $\log g = 7.72$.

Table 13.2: Journal of observations with the NOT, ordered by starting date & time.

Object	Date	Starting Time [UTC]	Integration & Cycle Times [s]	Length [s]	Observing Conditions
WD 1126–222	2005-05-13	21:07:20	25.1	30	3630
WD 1300–098	2005-05-13	22:51:24	29.1	30	1830
WD 1342–237	2005-05-13	23:35:22	26.1	30	1950
HS 1544+3800	2005-05-14	00:34:34	9.9	15	1275
HS 1531+7436	2005-05-14	01:08:10	33.3	40	3800
HS 1612+5528	2005-05-14	02:59:55	24.1	30	2280
HS 1824+6000	2005-05-14	03:47:07	22.7	30	1290
HS 1441+3219	2005-05-15	00:21:42	38.5	45	1620
HS 1625+1231	2005-05-15	01:00:04	28.5	35	5005
HS 1824+6000	2005-05-15	03:03:11	22.6	30	2400
WD 1126–222	2005-05-16	21:43:44	50.0	56	2432
WD 1149+057	2005-05-16	23:25:41	35.1	40	2480
HS 1249+0426	2005-05-18	01:12:20	40.0	45	1890
HS 1441+3219	2005-05-18	02:40:18	38.1	45	1845
HS 1556+1634	2005-05-18	03:20:28	29.5	35	2555
HS 1531+7436	2005-05-18	04:10:30	23.4	30	1710
HS 1824+6000	2005-05-18	04:47:31	22.4	30	1170
HS 1951+7147	2005-12-07	19:18:19	24.1	30	5700
HS 0213+0359	2005-12-07	22:23:43	40.0	45	6075
HE 0344–1207	2005-12-07	00:13:15	38.9	45	5625
HS 0733+4119	2005-12-08	01:59:43	24.1	30	5820
WD 0946+488	2005-12-08	03:45:11	44.0	50	5300
HS 1951+7147	2005-12-08	19:06:31	44.0	50	4900
HS 2351+3554	2005-12-08	20:42:39	44.5	50	7150
WD 0235+069	2005-12-08	22:53:41	34.1	40	7600
HE 0344–1207	2005-12-09	02:03:19	35.0	40	3280
HS 0733+4119	2005-12-09	03:05:35	33.0	40	3720
HS 0401+1454	2005-12-09	04:14:48	35.0	40	4400
HS 1951+7147	2005-12-09	19:21:56	34.1	40	5680
HS 2217+2454	2005-12-09	21:45:14	44.0	50	2950
HS 2351+3554	2005-12-09	23:11:52	39.4	45	3015
HS 0210+3302	2005-12-10	00:10:22	30.0	35	5355
WD 0235+069	2005-12-10	01:55:56	39.1	45	4320
WD 0344+073	2005-12-10	03:20:17	38.2	45	3465
HS 1308+1646	2005-12-10	04:35:03	24.0	30	4230
WD 1150–153	2005-12-10	06:02:06	23.4	30	2970
HS 1951+7147	2005-12-10	19:28:38	43.1	50	2900
WD 2333–049	2005-12-10	20:29:22	28.2	35	4165
HS 2217+2454	2005-12-10	21:44:53	53.9	60	2580
HS 0210+3302	2005-12-10	22:52:47	54.0	60	3960
WD 0710+216	2005-12-11	04:10:26	29.0	35	3710

noise would be determined locally in the FT, and not for the entire frequency range at once. However, since on the order of 200 data points were normally obtained, the FTs do not have a resolution that would be sufficient to derive a frequency-resolved value of the noise. Therefore only the overall noise is determined, and for that wide regions in the FT that cover most of the spectrum are used, only avoiding the very low frequencies and the peaks in the FT. If clouds are present during the observation, they can induce low-frequency variations due to differential extinction. This happens because, as mentioned before, the colours of the blue white dwarf target star and the comparison stars which are average field stars, and thus rather red, are very different. Thus, differential extinction may affect the lightcurves, and when this is the case, it leads to an increased noise in the low frequency region of the FT. Such effects of differential extinction are normally important at frequencies below 2 mHz, and an overall estimate of the noise is thus not useful in this region of the FT if clouds are present.

This is important because the noise level is employed to identify the significant peaks in the FT; those with an amplitude that is at least three times higher than $\langle A \rangle$ are interpreted as significant. Only if such a peak is present the target is interpreted as a new variable. Besides this formal criterion, the identification of significant peaks can often be facilitated by comparing the FTs of individual differential magnitudes as opposed to only that of the weighted sum. If all FTs of the individual (target - reference) lightcurves peak at the same frequency but are uncorrelated at other frequencies, that peak is probably a real feature. Furthermore a comparison of the (target - reference) FT to the FTs of (reference - reference) lightcurves, for two different reference stars, allows to identify significant features since the latter are expected to be featureless.

Besides identifying the significant features in the FT, the noise is also employed to determine which lightcurve of those that were derived with different settings for the aperture radius and the sky level determination produces the lowest noise in the corresponding FT. This lightcurve and its FT are selected as the final reduction result.

For some observations it was furthermore necessary to discard certain parts of the lightcurve since strong variations of even the differential magnitude, caused by the presence of thick clouds, prevented a useful analysis of the entire data set. However, a fraction of the data could often be used and still give meaningful results, as in the cases of WD 1149+057 and HS 1249+0426.

13.3 Observing Conditions

In the first run, the conditions were partially clouded in all of the nights, and thus only 12 objects could be observed, which was less than half of the planned number. For the same reason, the lightcurves of some objects are rather short and thus the resulting frequency resolutions are rather low. For two of the new variables, HS 1249+0426 and WD 1149+057, only a very short lightcurve barely covering one pulsation cycle could be obtained. However, the variability is unambiguously present even in these ill-observed stars. For three of the new variables that were discovered in this run, data from more than one night exists. These lightcurves are, due to the cloudy conditions, mostly rather short and are separated by more than one night. Therefore a combined FT would produce alias patterns that would prevent any effective gain of the frequency resolution, because

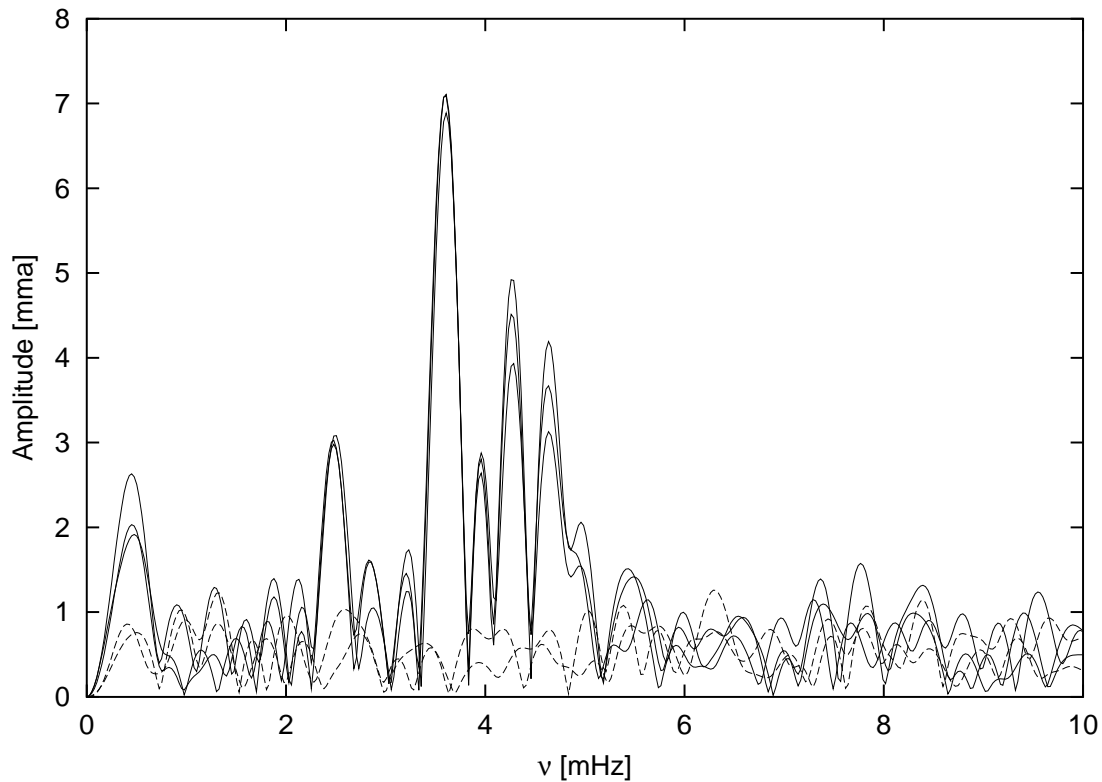


Figure 13.2: An example of a comparison of the FTs of different target-reference star combinations for one object. The solid lines show the three FTs of the differential (target-reference) lightcurves of WD 1126–222, i.e., for the three different reference stars. The dashed lines show the same for two (reference-reference) combinations. It can be noticed that all five curves are seen at a common noise level at most frequencies but separate where a real pulsation feature is present.

the alias pattern would be so severe that it can not be determined which of the several peaks is the strongest peak that corresponds to the target's pulsation frequency. Thus, a combined FT of all data of one object does not provide an advantage compared to the FT of a single data set, and so only the separate lightcurves and the corresponding separate FTs are analysed.

The second run, on the other hand, was more successful; all but one of the variables could be observed for at least two hours, distributed over two adjacent nights. Thus, it is feasible to compute FTs of the combined two-night data for these variables. Only for one variable that was found in the third night of observations, WD 1150–153, no second observation was possible because the observing conditions were prohibitive in the corresponding part of the following fourth, last night of the run. Some of the observations from the second half of the run are of a limited quality because of interfering clouds, but most of the data are of much higher quality than that from the first run.

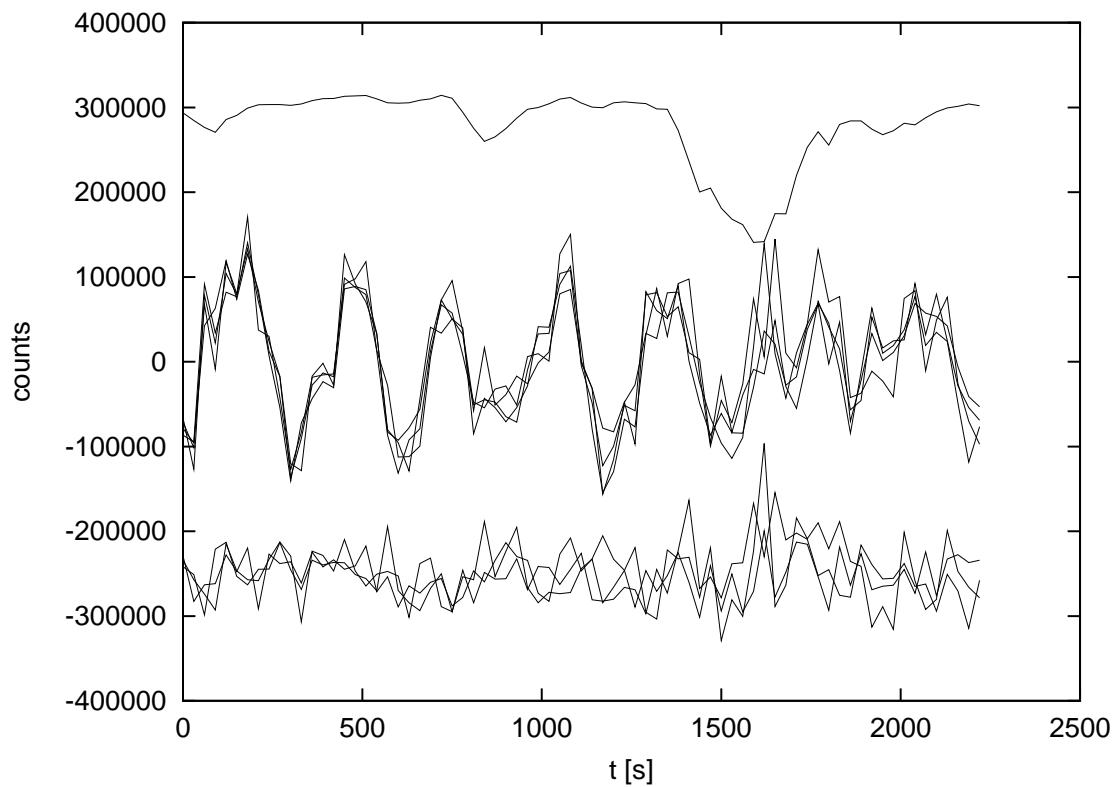


Figure 13.3: An example of how the presence of thin clouds affects the differential photometry: In this observation of HS 1844+6000, the absolute counts of the target (upper line) drop to about 50% near 1500 s. The differential magnitudes of target-reference star, plotted for 4 different reference stars in the middle of the figure, is only modestly affected. The change of absolute counts manifests itself through an enhanced noise and thus the pulsations are less clearly visible after $t = 1500$ s, but there is no drop as it is found for the absolute counts. The differences of the counts of two reference stars are plotted for three combinations of reference stars at the bottom of the figure; here the increased noise after $t = 1500$ s is also visible. All the differential photometry curves are plotted in units of magnitudes and are scaled by 10^7 , and the bottom curves are displaced downward by 2.5×10^5 .

Chapter 14

The NOT Results: 12 New ZZ Ceti Variables

14.1 Overview of the New Variables

The results on seven of the twelve new variables, those that were discovered in the first run, have already been published in Voss et al. (2006).

Four of the new variables show multiple periods; in the cases of WD 1126–222, HE 0344–0712, and HS 0733+4119 there is evidence for a variation of the amplitudes in between different nights. HS 1824+6000 also shows some differences in the measured amplitudes, but these observations are too short to judge whether this is a real effect, or just a consequence of beating between closely spaced modes.

Six of the new ZZ Ceti stars are long-period pulsators, the remaining six have periods below 400 s. Among the hDAV stars is HS 1531+7436 which shows a period of only 112 s, i.e., one of the shortest periods of ZZ Ceti stars known to date. On the other hand, the new ZZ Ceti WD 0235+069 has a very long period that counts among the longest periods of ZZ Ceti stars.

The lightcurves and their FTs are shown in Figs. 14.7 and 14.6, and the pulsation frequencies and amplitudes that are derived from the FTs are listed in Table 14.1.

14.2 NOV Objects

Besides the twelve new variables, there are fifteen objects for which no clear variations were detected. However, these objects are not necessarily non-variables, as it is quite possible that weak variations are present below the noise level of the present observations. Even more importantly, strong variations may be present but temporarily hidden from view due to beating effects that are known to cause almost flat lightcurves for over one hour in many ZZ Ceti stars. Therefore these objects should be referred to as “not observed to vary” (NOV) rather than “not variable”. The level above which variations can be excluded in the individual lightcurves, that is the amplitude of the strongest peak in the corresponding FT, is given in Table 14.2.

For both WD 0344+073 and HS 1308+1646, a significant low-frequency peak is found in the FTs, but it is not a sign of intrinsic pulsations of these objects but caused by a vari-

Table 14.1: Observed periods and amplitudes. In the second column, “all” refers to the results from the combined FT of both lightcurves. For HE 0344-1207, the ‘.1’ and ‘.2’ extensions denote the first and second halves of each lightcurve. The amplitude is given in “mma” units; 1 mma corresponds to a change of the intensity of 0.1%.

Object	Date	$\langle A \rangle$ [mma]	Amplitude [mma]	Freq. [mHz]	Period [s]		
HS 0210+3302	2005-12-09	0.64	3.84	4.81	207.8		
			4.38	5.28	189.4		
			1.93	9.16	109.2		
	2005-12-10	1.34	5.59	5.27	189.8		
			All	0.64	3.68	4.82	207.5
				4.74	5.28	189.4	
WD 0235+069	2005-12-08	0.56	3.66	0.78	1287.0		
	2005-12-09	0.50	5.33	0.80	1257.9		
	All	0.38	4.21	0.78	1283.7		
HE 0344-0712	2005-12-07.1	2.50	13.19	1.33	754.7		
			9.88	1.88	533.3		
			33.48	2.52	397.1		
			8.17	3.20	312.1		
			9.69	3.76	266.3		
	2005-12-07.2	1.82	22.89	1.37	732.6		
			10.34	1.84	544.4		
			10.80	2.26	441.7		
			11.96	2.66	375.5		
	2005-12-08.1	2.60	17.86	1.44	695.9		
			28.93	2.41	415.8		
			8.81	3.85	260.1		
	2005-12-08.2	2.44	14.89	1.42	705.2		
			14.67	2.42	414.1		
			9.50	3.87	258.6		
			All	1.23	18.92	1.31	762.2
			7.18	1.72	581.1		
				8.22	1.95	513.1	
				11.37	2.17	461.0	
				21.14	2.55	392.9	
				5.22	2.86	350.1	
			6.32	3.80	263.1		
HS 0733+4119	2005-12-07	3.13	11.21	0.67	1497.0		
			23.86	1.09	919.1		
			51.61	1.55	645.6		
			22.07	2.14	467.3		
	2005-12-08	1.35	8.30	0.98	1018.3		
			32.12	1.37	729.4		
			15.00	1.74	573.4		
			15.05	2.09	479.6		
			All	2.30	8.85	0.68	1479.3
				8.54	0.88	1142.9	
				17.44	1.07	932.8	
				20.30	1.34	747.4	
				38.73	1.52	656.2	
				19.39	2.13	468.8	
			7.39	3.02	331.1		

continued on the next page

Table 14.1 continued

Object	Date	$\langle A \rangle$ [mma]	Amplitude [mma]	Freq. [mHz]	Period [s]
WD 1126–222	2005-05-13	0.28	3.01	2.48	402.7
			7.04	3.60	277.6
			4.49	4.27	234.1
	2005-05-16	0.41	3.68	4.64	215.7
			4.01	2.59	386.4
			7.69	3.63	275.7
			8.13	4.58	218.3
WD 1149+057	2005-05-16	0.40	10.47	0.98	1023.5
WD 1150–153	2005-12-10	0.58	2.44	3.25	307.3
			4.73	4.01	249.4
			3.59	5.22	191.7
HS 1249+0426	2005-05-18	0.53	7.55	3.46	288.9
WD 1342–237	2005-06-08	0.13	6.17	0.85	1177.0
			5.17	1.02	982.0
HS 1531+7436	2005-05-14	0.26	4.23	8.89	112.5
	2005-05-18	0.59	3.38	8.97	111.5
HS 1625+1231	2005-05-15	0.20	48.87	1.16	862.9
			23.60	1.87	533.6
			16.99	2.60	385.2
HS 1824+6000	2005-05-14	0.78	8.84	3.40	294.3
	2005-05-15	0.42	3.30	2.60	384.4
	2005-05-18	0.86	7.66	3.29	304.4
			13.56	3.03	329.6

able level of the sky background. These periodic sky transparency variations caused a periodically varying differential extinction that mimicked ZZ Ceti pulsations. In Table 14.2, the amplitudes of the resulting main peaks at low frequencies in the FTs of these two objects are not given, but the amplitudes of the second highest peaks, since the main peaks can clearly be attributed to the changing observing conditions.

14.3 Individual Discussion of the New ZZ Ceti Stars

WD 1149+057 and HS 1249+0426 Only scarce NOT data exists for these new ZZ Ceti stars, again due to the unfavourable weather conditions. In spite of the shortness of the lightcurves and thus rather inaccurate determination of their pulsation frequencies, these objects are clearly variable. Further observations are however needed to derive precise pulsational parameters. Only the main peak in the FT of HS 1249+0426 is significant, all other features in that FT are not.

WD 1149+057 has a very long period, and this agrees well with the result of the spectral analysis that places it on the cool edge of the instability strip.

WD 1342–237 As in the case of WD 1159+057 and HS 1249+0426, the NOT lightcurve of this object is short and covers only one pulsational cycle. These data do not allow a derivation of precise parameters for this object, but fast photometry of WD 1342–237 was also obtained by S. O. Kepler at the SOAR telescope, Chile. This lightcurve is of

Table 14.2: Objects not observed to vary. Given are the square root of the average power in the FT of the object's lightcurve ($\langle A \rangle$), and the amplitude of the highest peak in the FT. Most of the peaks are close to 2σ in these observations, which can be considered as insignificant. One exception is HS 2351+3554, where the amplitude of the highest peak is marginally larger than $3\langle A \rangle$, but there are other reasons not to interpret this feature in the FT as a certain sign of an intrinsic pulsation.

Object	$\langle A \rangle$ [mma]	Highest Peak [mma]
HS 0213+0359	0.82	2.10
WD 0344+073	0.59	1.31
HS 0401+1454	0.88	2.10
WD 0710+216	0.49	1.03
WD 0946+488	1.11	2.49
WD 1300-098	0.60	1.09
HS 1308+1646	0.36	0.72
HS 1441+3219	0.91	2.02
HS 1544+3800	0.38	0.70
HS 1556+1634	0.51	0.94
HS 1612+5528	0.66	1.33
HS 1951+7147	0.84	2.14
HS 2217+2454	1.17	2.80
WD 2333-049	0.66	1.85
HS 2351+3554	0.70	2.11

much higher quality, and was published together with the NOT observations in Voss et al. (2006). It is displayed along with its FT in Fig.14.1; in Table 4.1 only the frequencies and amplitudes of WD 1342-237 that have been derived from these SOAR data are listed, not the more inaccurate ones that were derived from the NOT lightcurve. The high-resolution data allows to resolve the main peak into two components that are separated by 0.17 mHz. According to the spectral analysis, this object should be a cDAV, which is consistent with the long periods of its pulsations.

HS 1441+3219 This object shows a peak at 5.6 mHz which seems fairly pronounced. This peak can be considered as an indication of uncertain possible variations. The feature is only found in the FT of the second of two lightcurves, but its absence in the FT of the first lightcurve is easily explained by the much higher noise of more than 3 mma in that first FT. The square root of the average power in the second FT is 0.91 mma, so the peak, which has an amplitude of 2.02 mma, is in fact below the significance level. Therefore it is included in the list of NOV objects, Table 14.2. However if one regards Fig. 14.2, where the FTs of the differential photometry of the target and the individual comparison stars are plotted together with the FTs of the differential photometry of two comparison stars, it can be seen that only the FTs in which the target star is included show a peak above twice the mean FT level. This gives some support to the interpretation of the peak at 5.6 mHz as a possibly real peak. Thus, although there is no solid evidence for pulsations of HS 1441+3219, it may be variable, and follow-up observations of this candidate are therefore desirable.

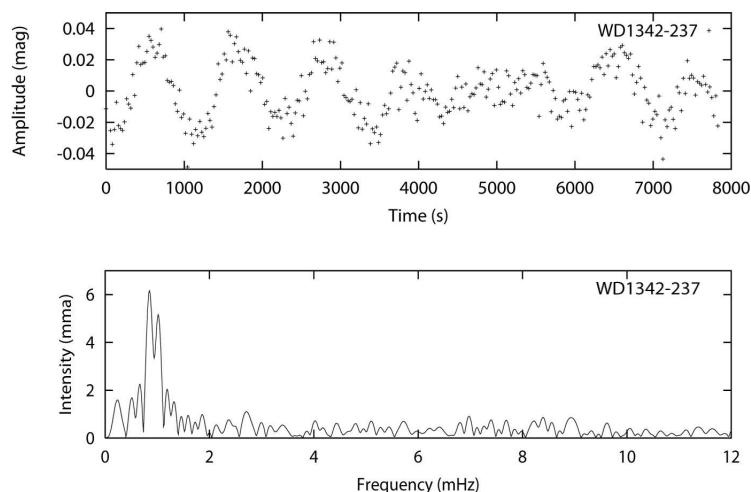


Figure 14.1: SOAR photometry of WD 1342–237 (top) and the fourier transform of the lightcurve (bottom).

HS 1531+7436 Two lightcurves were obtained for HS 1531+7436, but only the first one (2005-05-14) is of good quality. The long-period peak at 0.3 mHz in the FT of the first lightcurve is, like that in the FT of WD 1126–222, probably due to a long-term atmospheric trend in the data that was not properly removed by a linear correction. According to the two-colour photometry, this object should be an extreme hDAV, which is indeed consistent with the exceptionally short period of only 112 s.

HS 1625+1231 Five consecutive points of the lightcurve of HS 1625+1231 are outliers with respect to the otherwise undisturbed lightcurve. These points have been rejected and a linear interpolation was used to replace them.

The FT shows a high number of at least 13 seemingly significant peaks. If the FT is compared to the spectral window, as shown in Fig.14.3, one finds that the peaks at 0.7, 0.9, 1.4, and possibly also that at 0.4 mHz are probably alias peaks, as they coincide with peaks in the spectral window. Still, these peaks would be strangely high above the noise level.

As mentioned earlier, that can be explained by the fact that clouds were disturbing the observation of this lightcurve, causing low-frequency variations which also affect the differential lightcurves and increase the low-frequency noise. Therefore, in the case of this object, the true noise at low frequencies has to be higher than the overall estimate, and thus the above mentioned peaks are probably insignificant.

Furthermore, most peaks in the differential FT correspond to features in the FT of the absolute photometry of the reference stars, which is also shown in Fig.14.3. These coincidental peaks could as well be reflections of cloud interference. The only peaks that one can expect to be real pulsation features of the target star are, besides the main peak, those at 1.8 and possibly that at 2.7 mHz.

HS 1824+6000 Data of HS 1824+6000 has been obtained on three nights, although two of the three lightcurves are too brief to yield meaningful frequencies. The shift of the

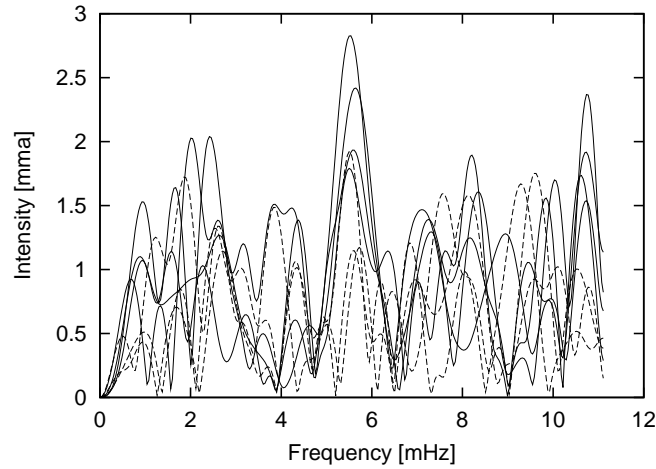


Figure 14.2: The FTs of the differential photometry of HS1441+3219 (target - reference; solid lines) and those of the differential photometry of two comparison stars (reference - reference; dashed lines). It can be noticed that the peak at 5.6 mHz appears at the same frequency in all the FTs that involve the target star.

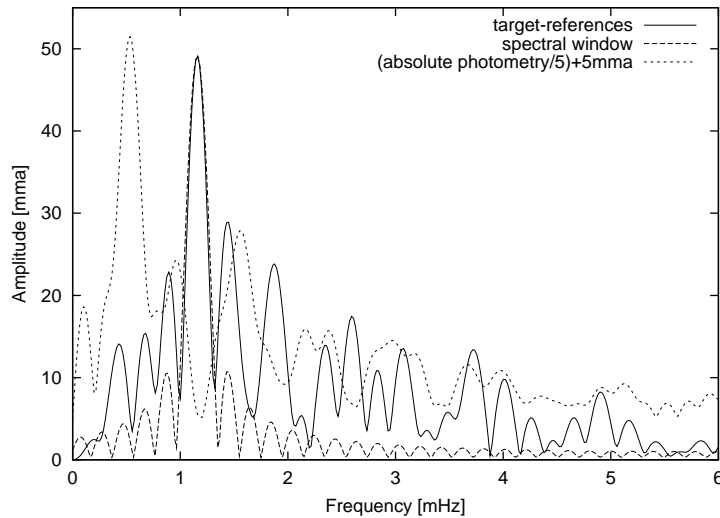


Figure 14.3: Comparison of the FT of the differential lightcurve of HS 1625+1231 to the spectral window, and to the FT of the absolute (non-differential) photometry of a reference star. The absolute photometry shows atmospheric variations. It has been scaled to a fifth of its amplitude and shifted up by 5 mma for better visibility in this plot. The spectral window curve has been scaled to match the peak amplitude of the main peak in the FT. One can see that many of the peaks in the FT of HS 1625+1231 are due to aliases or to variations that are also present in the absolute FT, and thus are probably not real features but caused by cloud interference.

frequency of the main peak, especially from the second to the third lightcurve, is large but less than a third of the peak width in the 2005-05-18 FT. Thus this shift is not significant. Also, the length of the runs is too short to be able to regard the change in amplitude as a real change.

HS 2351+3554 and HS 1951+7147 These two stars show weak, ambiguous signs of possible pulsations:

The FT of the lightcurve of HS 2351+3554 shows a high-frequency peak, near 10 mHz, in its FT that would formally be a significant feature. However, other peaks at similar but marginally insignificant amplitudes are present, and if the FTs of the individual (target - reference star) lightcurves are considered, this 10 mHz peak is not the strongest feature in most of the individual FTs. Therefore it is not certain that it corresponds to a real pulsation, and thus this target is classified as an NOV object.

The same conclusion can be drawn considering a formally significant peak that is present in the FT of one lightcurve of HS 1951+7147, because this feature appears in the FT of only one out of four individual lightcurves that were obtained.

Both stars are placed within the instability strip, according to their atmospheric parameters. Therefore, it is quite probable that weak pulsations are present at or below the amplitude level at which they can now be excluded. The mentioned uncertain features in the FTs of both objects might be indicative of that.

HS 0733+4119 and HE 0344–1207 Similar to HS 1625+1231, the determination of the noise in the FT is problematic for these two cDAV variables. Especially for HS 0733+4119, the noise level is considerably lower for frequencies larger than 5 mHz than it is below that frequency. Ideally the noise should not depend on the frequency, but as mentioned above, it is possible that changes in the observing conditions are affecting the low frequencies in the FT through differential extinction. Such an effect should be recognizable when the absolute, non-differential photometry lightcurves of both the target and the reference stars are considered. In both cases, however, an FT of these absolute lightcurves does not reveal any dichotomy of high- and low-frequency noise, like the differential lightcurve does, and thus the reason for the high noise below 5 mHz remains uncertain.

The noise was thus estimated from the frequency region 2.5-6 mHz, which gives a reasonable average of the overall noise in the FT while excluding the main peaks below 2.5 mHz. For HE 0344–1207, where the main peaks are found at higher frequencies, an interval from 4 to 10 mHz was used.

In the FT of HS 0733+4119, it can be noticed that the peaks at 3.02 and 2.13 mHz appear at about twice the frequencies of those at 1.52 and 1.07 mHz, and thus might be their first harmonics. Furthermore, the frequencies and the amplitudes changed considerably; while in the first lightcurve the 1.52 mHz and 1.07 mHz pulsations are dominant, the main peak in the second lightcurve is found at 1.37 mHz and a secondary at 1.74 mHz. A comparison of both individual FTs is shown in Fig.14.4. The combined FT is dominated by that of the first lightcurve, because there the peak amplitudes are almost twice as high as those of the second lightcurve.

Similarly, the pulsation properties that are found for HE 0344–1207 are changing in between the two different lightcurves, as well as within both lightcurves. In Fig.14.5,

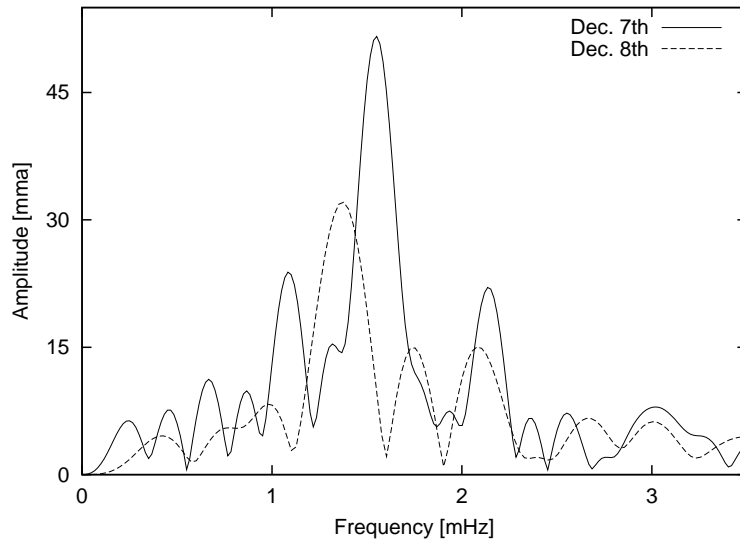


Figure 14.4: A comparison of the FTs of the two individual lightcurves of HS 0733+4119. It can be seen that the amplitudes are much higher in the 2005-12-07 lightcurve, while the frequencies of two of the main peaks are lower in the 2005-12-08 lightcurve than in that of 2005-12-07.

it is shown how the pulsation spectrum evolved during the first lightcurve observation. The amplitudes are changing by factors of up to three, but the main frequencies remain constant and are visible throughout the observations. Several minor peaks in that FT are probably alias peaks as they coincide with peaks in the window function, and are not listed in Table 14.1. As in the case of HS 0733+4119, the first harmonics of some pulsation frequencies might be present in the FT; especially the frequencies of the peaks at 2.55 and 3.80 mHz are close to multiples of the frequency of the peak at 1.31 mHz.

WD 0235+069 The secondary peak that appears at 0.69 mHz in the combined FT of both lightcurves is probably an alias peak and is thus not listed in Table 14.1; the window function has a peak at 0.64 mHz, which is not significantly different from the frequency of the questionable peak in the data, since the spectral resolution (i.e., the inverse of the length of the lightcurve) is only 0.131 mHz.

HS 0210+3302 Two secondary peaks that appear in the FT of HS 0210+3302, each at a frequency approximately 0.25 mHz higher than that of the two main peaks, are probably alias peaks since the frequency difference of the main and secondary peaks of the window function is 0.26 mHz. These secondary peaks are thus not listed in Table 14.1.

WD 1150–153 In addition to the pulsations that are listed for WD 1150–153 in Table 14.1, a peak at twice the frequency of the main peak is found in the FT of that object but is marginally insignificant. It might be the first harmonic of the main peak.

This white dwarf shows the CaII K line in its spectrum, and it is thus a DAZ WD and only the third ZZ Ceti WD of this type, in addition to WD 2326+049 which is a well studied variable and WD 1116+026 for which pulsations have recently been discovered

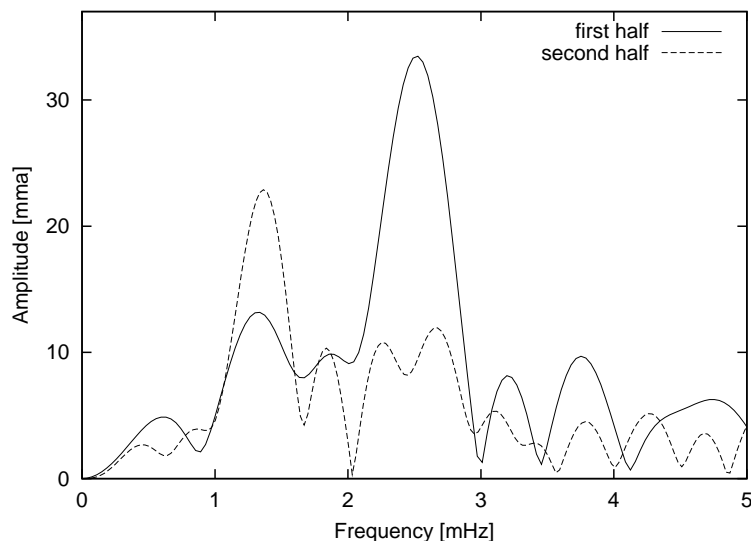


Figure 14.5: A comparison of the FTs of the first half, from $t = 0$ s to $t = 2867$ s, and the second half, from $t = 3047$ s to $t = 6422$ s, of the 2005-12-07 lightcurve of HE 0344–1207. The pulsation spectrum of the 2005-12-08 observation is similar to that of the first half of the 2005-12-07 lightcurve.

by Silvotti and were published by Gianninas et al. (2005). Koester et al. (2005a) first reported WD 1150–153 as a DAZ.

This is of some interest as it has long been found that the shapes of the $H\alpha$ line cores in the spectra of ZZ Ceti stars are too shallow to be fit by model spectra of non-rotating model atmospheres. Thus, ZZ Ceti stars seem to be relatively fast rotators, but the opposite is found from asteroseismology, where the rotational splitting of pulsation modes provides independent values of the rotation speeds that are close to zero (e.g., Koester et al. 1998 & Karl et al. 2005, and references therein). Horizontal surface motions of the ZZ Ceti oscillations have been suggested as an alternative explanation, but it is still uncertain if they are strong enough to account for the width of the ZZ Ceti line core broadening.

Berger et al. (2005) have presented the first white dwarf rotation velocities that are derived from the broadening of the CaII line, and they found that this, compared to an analysis of the $H\alpha$ line broadening, yields more precise results at lower rotation speeds. WD 1150–153 is one of very few objects for which they determine a significant rotation velocity of $9.5 \pm 5.4 \text{ km s}^{-1}$. They suggest, however, that the line profile is probably not caused by rotation but by the same effect that is responsible for the peculiar $H\alpha$ line shapes in the ZZ Ceti stars.

14.4 Results and Discussion

Ten candidates that were selected from spectroscopy are placed in the instability strip or nearer to its empirical edges, according to Bergeron et al. (2004), than the extent of their error bars. An uncertainty of 2% of the temperature, corresponding to 230 K in the instability strip region, was assumed. Of these 10 candidates, 8 were found to be variable. The fraction of variables is thus 0.8, similar to values that have been found by other studies (e.g., Mukadam 2004a). This number is lower for the photometrically

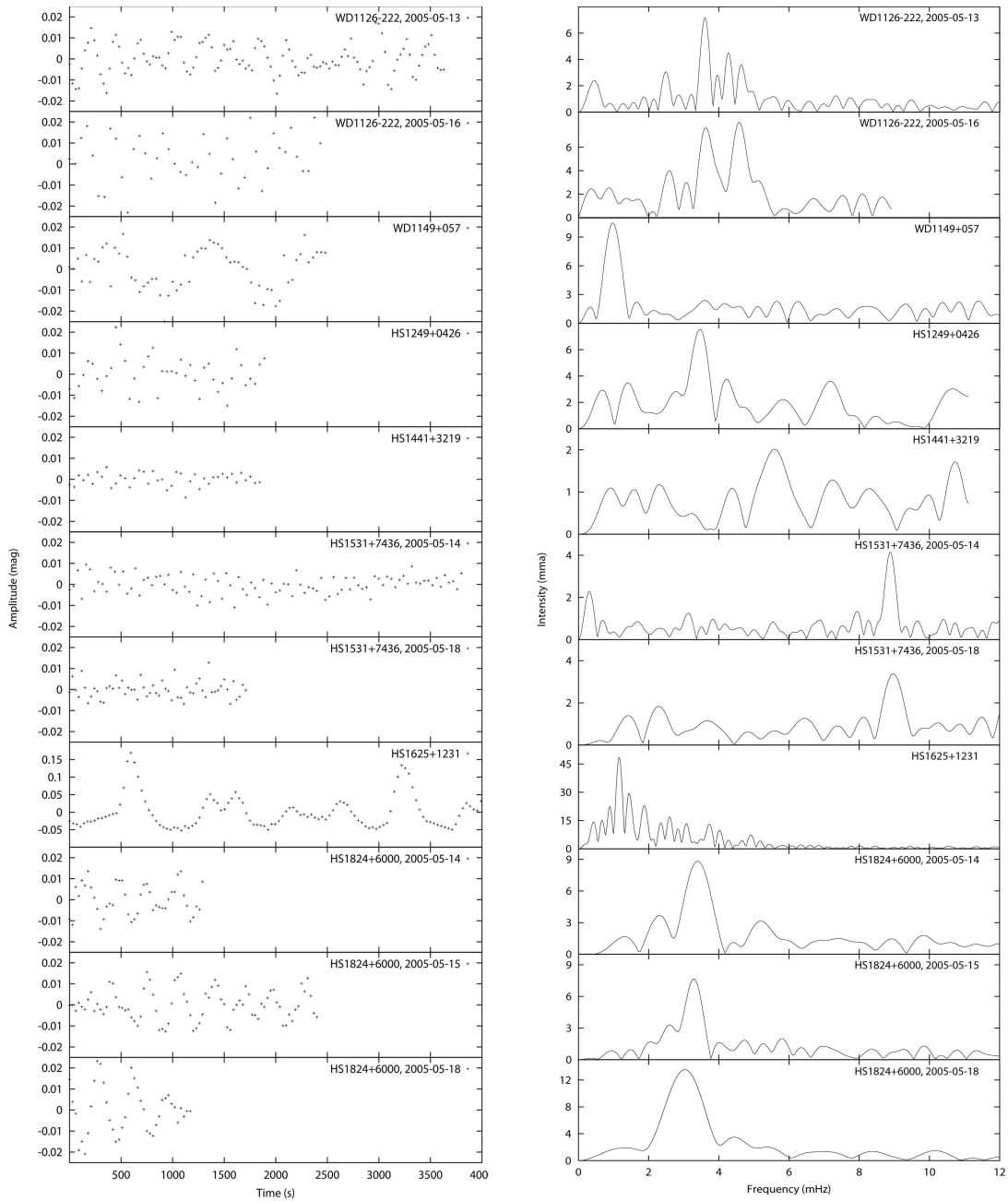


Figure 14.6: Differential NOT photometry (left) and the fourier transforms of the lightcurves (right) of the seven new ZZ Ceti variables of the first run, and of the ambiguous object HS 1441+3219. For the targets for which data was obtained on more than one night, these individual lightcurves are shown separately. The scaling of the intensity axes is not the same for all objects.

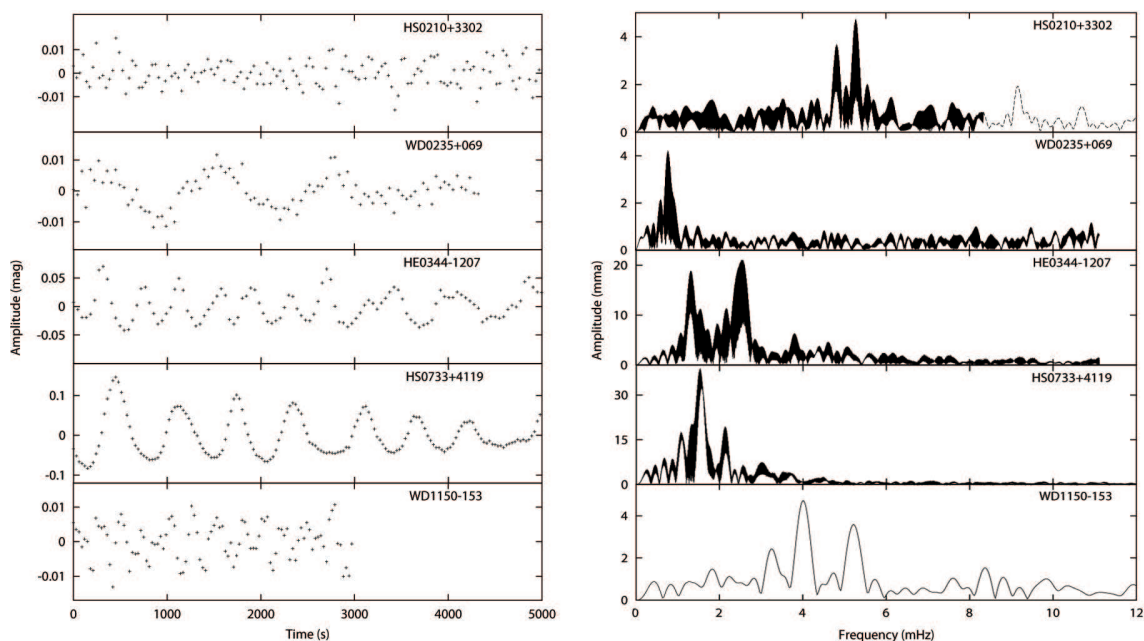


Figure 14.7: Differential photometry (left) and the fourier transforms of the lightcurves (right) of the five new ZZ Ceti variables of the second run. For the targets for which data was obtained on more than one night, only one of the lightcurves is shown together with the combined FT of both curves. In the case of HS 0210+3302, where a high-frequency peak is visible in one of the individual lightcurve FTs but not in the combined FT which has a rather low nyquist frequency, the combined FT has been extended with data of the individual FT. The scaling of the intensity axes is not the same for all objects.

derived candidates. Seventeen of these are placed inside or very close to the instability strip, of which eight are found to be variable, leading to a “success fraction” of 0.5 for this method. These numbers include the observations that were made by Silvotti et al. (2005) and Castanheira et al. (2006b), see chapter 12.

Compared to the typical magnitude of the numerous ZZ Ceti stars from the SDSS ($B \approx 18$) that have recently been published, the new ZZ Ceti stars from the SPY and HQS surveys are relatively bright, with $B \approx 16$, which makes them more suitable candidates for detailed asteroseismological analyses. Almost all ZZ Ceti stars with $B < 16$ mag that were known before this work have already been investigated in such detailed studies by the Whole Earth Telescope collaboration, and thus future studies of this kind of further ZZ Ceti stars will have to either target increasingly faint variables, or one of the objects that are published here.

In Fig.14.8 the results of the observations are plotted in the $T_{\text{eff}} / \log g$ -plane, together with the empirical instability strip edges from Bergeron et al. (2004) and Mukadam et al. (2004b). The NOV objects do not contribute well to any decision about which edges are a better match to the distribution of these new variables. The cool variables are much better constrained by the Bergeron edge than by that from Mukadam et al. (2004b). On the hot edge the decision is less clear but the Bergeron edge is favored as well: There is one variable with a low gravity and high temperature whose position is better reproduced by the Mukadam edge, but three hot variables at high gravity are positioned in favor of the

Bergeron edge. This sample of 15 new variables is too small to justify a fitting of a new set of empirical strip edges. However, if the variable at low gravity and high temperature, HS 0210+3302, is considered as an outlier, a fit of empirical edges to the remaining 14 ZZ Ceti stars would yield results that are very similar to those of Bergeron et al. (2004). The only difference might be that such a new blue edge might show a smaller slope, placing the three BUSCA NOV objects at low gravities outside such a strip.

A pure instability strip is found if only the objects with spectroscopic parameters are taken into account; but no firm statement can be made for the entire sample, because the uncertainties of the BUSCA photometry are as big as half the width of the instability strip. Therefore the BUSCA NOV objects which are placed in the middle of the strip but show no signs of variations might have a true effective temperature that in fact places them outside of the strip. On the other hand, because the lightcurves of one of these targets is not very long, it is also well possible that this object is indeed a variable, with pulsations that were temporarily hidden due to beating effects. This possibility is supported by the fact that both of the NOV objects in the centre of the strip have a relatively high noise in the FT and are therefore among the less well constrained of the NOV stars. Therefore, and also because the number of NOV objects that are found is too small, it can merely be said that the results are consistent with a pure instability strip.

Another conclusion is that the pulsational properties of the new variables are in agreement with the atmospheric parameters that were determined, as can be seen from Fig. 14.9: The six variables that are placed near the red edge of the instability strip show cDAV pulsations, and the four new ZZ Ceti stars with $T_{\text{eff}} > 11800$ K are hDAV variables. Near the middle of the strip, a mixed population of five cDAV or hDAV stars is found. This is consistent with the assumption of cDAV and hDAV populations that are in fact separated near the middle of the strip but scattered due to the assumed temperature uncertainties, 500 K for the BUSCA observations and half as much for the SPY data.

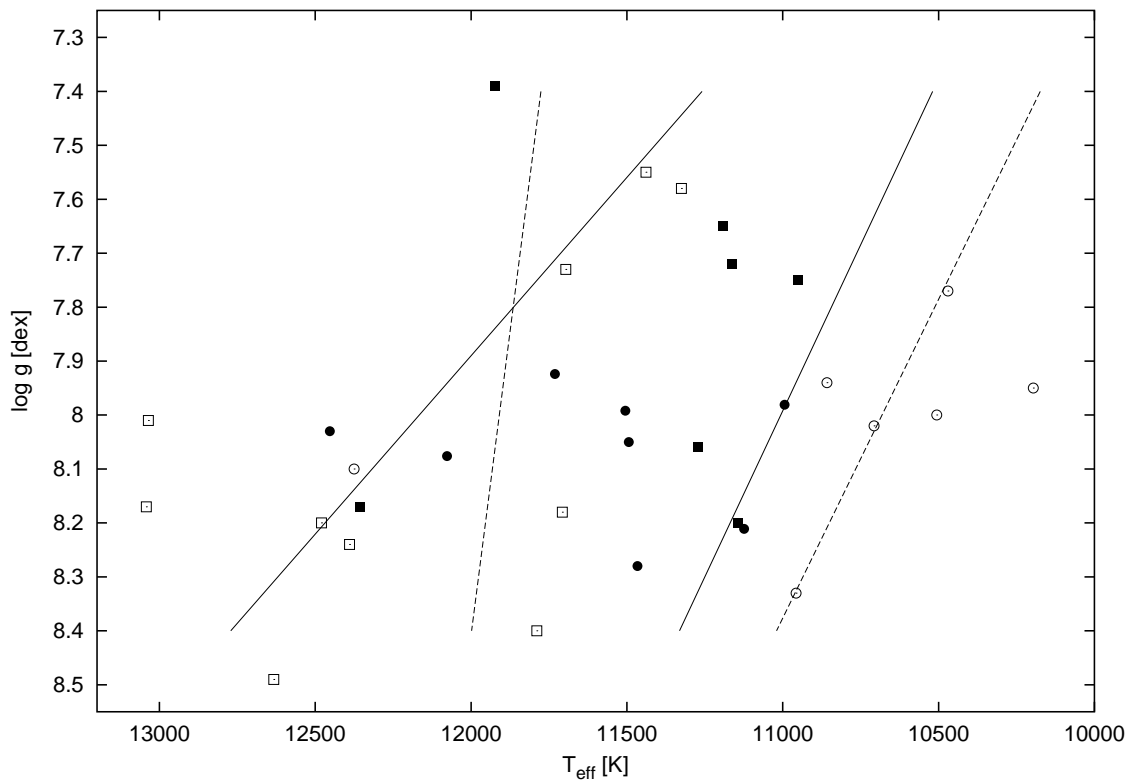


Figure 14.8: The temperatures and gravities of the new variables and NOV objects, plotted together with the empirical instability strip edges from Bergeron et al. (2004, solid lines) and Mukadam et al. (2004, dashed lines). Open symbols show NOV stars, filled symbols are ZZ Ceti variables. Circles represent objects with SPY parameters and squares those with BUSCA data. The overall uncertainties of these data are ± 500 K and ± 0.25 dex for BUSCA data as well as ± 250 K and ± 0.07 dex for SPY parameters.

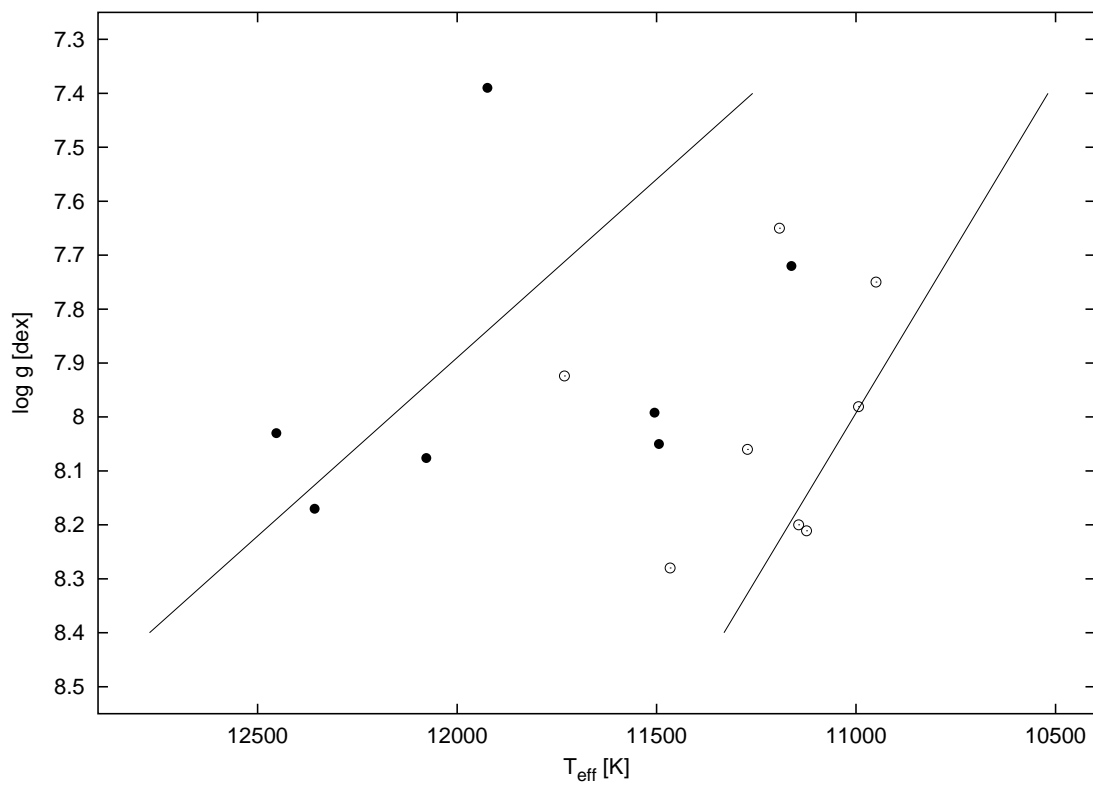


Figure 14.9: The temperatures and gravities of the cDAV (open symbols) and hDAV (filled symbols) variables, plotted together with the empirical instability strip edges from Bergeron et al. (2004).

Chapter 15

Summary and Outlook

In this work, the large amount of data on white dwarfs from two surveys, SPY and HQS, were studied. These two analyses are different in their natures, methods, and their aims: The SPY analysis yields a diversity of results about white dwarfs of different kinds, based on spectra of the objects which were already available in reduced form. The analysis of the HQS stars of Homeier's cool objects subsample (Homeier 2001), on the other hand, involved photometric observations and the subsequent data reduction, and was targeted at a more specific aim: The identification of new ZZ Ceti stars. The selection of candidate variable white dwarfs connects both studies, since also the SPY analysis provided probable new ZZ Ceti stars.

15 new variables of this kind were finally identified; 12 from observations at the NOT telescope and 3 from observations by collaborators. The selection methods, i.e., the atmosphere temperatures that were derived from the SPY spectra and the BUSCA photometry, proved successful, although the uncertainties of the BUSCA temperatures are too large to allow these data to provide constraints on the questioned purity of the instability strip. The SPY temperatures of the new ZZ Ceti stars, however, clearly support the assumption of a pure instability strip within which all DA stars are pulsating.

Besides leading to the discovery of half of the new ZZ Ceti stars, the BUSCA observations also yielded a catalog of atmosphere parameters of 220 new DA White Dwarfs. Together with the SPY results for 170 objects that were not published before, 390 new white dwarfs are presented in this thesis.

Besides atmosphere data, masses and radii of 700 DA and 60 DB white dwarfs, the SPY analysis yielded a variety of results on several other types of white dwarfs, e.g., on those with magnetic fields, on the DBA stars, and on the question whether any helium-atmosphere white dwarfs are found in the temperature region of the DB gap: One such object is found in the SPY sample and is one of only two DO stars with temperatures below 40 000 K that are currently known.

Based on these results, several future studies of the SPY and HQS data that are beyond the scope of this work remain to be carried out. The DA+dM composite spectra have been analyzed only preliminarily, and a fit that takes the main sequence component into account will provide further results on these systems. The field geometry of the new magnetic DA stars, especially that of HS 1031+0343, remains to be investigated, as well as the detailed properties of some peculiar objects like the DAB star HE 2149–0516 and the DA+DBA system WD 0453–295. Furthermore there are several types of white dwarfs in the SPY

sample that were not fitted with model atmospheres, e.g., the very cool DA and helium-atmosphere stars as well as the hot DO white dwarfs. Finally, lightcurves still need to be obtained for some of the candidate ZZ Ceti stars.

Appendix A

Hydrogen Atmosphere Fit Results

The table on the following pages lists the fit results for hydrogen-rich spectra that were fitted with the DA model atmospheres, except for the DA+dM systems. The objects that are listed in this table are mainly single DA stars, but also include DD, DAH, and subdwarf stars as well as some peculiar objects.

- The type of each object which is not a single, non-magnetic DA star is given in the last column of the table.
- Aliases that are given in parentheses indicate earlier detections of the star as a blue object, but not as a white dwarf.
- Not all digits of the parameter values are significant; as explained above, the formal uncertainties do not include systematic effects and the true uncertainties are similar to 2% for the temperatures, 0.07 dex for the surface gravities and $0.05 M_{\odot}$ for the masses.
- For a few objects no decision was possible for either the solution which has a hotter or for the one which has a cooler temperature than that of the maximum strength of the Balmer lines. Both solutions are given for these objects.
- The column “spectra” indicates if the given fit results are those of one spectrum or an average of those of two spectra.
- Masses and radii are only given for single DA stars, not for DD systems or peculiar objects.
- Several objects in the temperature region of the ZZ Ceti instability strip show shallow cores of the Balmer lines, a feature that resembles rotational broadening and is believed to be connected to horizontal pulsation motions of the stellar surface; if this feature is present in the spectra this is indicated as “shallow cores”.
- Objects with low temperatures for which the fit seems inaccurate (see section 4) are labeled as “cool”; sometimes accompanied by “linear fit”, which indicates cases where a quadratic interpolation of the continuum levels did not produce a good fit but only a linear interpolation.

Table A.1: Fit results for hydrogen atmosphere stars

Object	RA	DE	mag	Aliases	T_{eff} [K]	$\sigma(T_{\text{eff}})$ [K]	log g	$\sigma(\log g)$	Spectra	M [M_{\odot}]	R [R_{\odot}]	Comments
WD 2359-434	00:02:10.73	-43:09:55.3	13.05	L362-81, LHS1005	8794	10	8.555	0.009	1	0.938	0.00846	DAH; kGauss-DAP; Cool, bad fit
WD 2359-324	00:02:32.36	-32:11:50.7	15.87	MCT2359-3228	22390	73	7.83	0.011	1	0.513	0.01441	
WD 0000-186	00:03:11.21	-18:21:57.6	16.29	MCT0000-1838, GD575	14951	22	7.967	0.006	2			
					12347	56	8.049	0.010	1			
HS 0002+1635	00:04:43.34	+16:52:16.7	15.3	(PHL647)	25824	33	7.895	0.005	2	0.553	0.01388	
WD 0005-163	00:07:34.80	-16:05:31.8	16.29	G158-132, GR509	11763	31	7.849	0.007	1	0.495	0.01385	Shallow cores; NOV (Gianninas 2005)
WD 0011+000	00:13:39.19	+00:19:23.1	15.31	G031-035, WOLF1	9612	8	8.063	0.01	1	0.613	0.01205	
WD 0013-241	00:16:12.63	-23:50:06.4	15.36	MCT0013-2406, GR458	18121	31	7.87	0.006	1	0.523	0.01390	
WD 0016-258	00:18:44.49	-25:36:42.2	16.07	MCT0016-2553	10707	11	8.017	0.011	1	0.587	0.01243	Shallow cores; NOV1.8
WD 0016-220	00:19:28.23	-21:49:04.9	15.31	GD597, PHL2856	13005	48	7.81	0.004	2	0.478	0.01424	
WD 0017+061	00:19:40.99	+06:24:06.2	14.55	PG0017+061, PHL790	28174	43	7.742	0.008	1	0.484	0.01550	
WD 0018-339	00:21:12.90	-33:42:27.4	14.7	GD603, BPM46232	20256	21	7.8	0.004	2	0.493	0.01463	
WD 0024-556	00:26:41.08	-55:24:44.9	15.21	L170-27, BPM16115	10201	7	8.655	0.007	1	1.003	0.00780	
PG 0026+136	00:28:52.33	+13:54:45.8	15.74	WD0026+136, PHL810	35078	155	5.407	0.015	1			sdO
WD 0027-636	00:29:56.79	-63:24:58.3	15.29	RE0029-632, EUVEJ0030-634	61820	391	8.021	0.017	1	0.674	0.01326	
WD 0028-474	00:30:47.16	-47:12:36.9	15.24	HE0028-4729, JL192	16706	29	7.629	0.006	1			
WD 0029-181	00:32:30.33	-17:53:23.3	16.05	HE0029-1809, KUV00300-1810	12909	60	7.788	0.009	1	0.467	0.01443	
HE 0031-5525	00:33:36.03	-55:08:37.5	15.94	(JL197)	11505	31	7.992	0.008	1	0.574	0.01266	ZZ Ceti; Shallow cores
MCT 0031-3107	00:34:24.85	-30:51:25.6	16.43		40061	188	7.796	0.021	2	0.533	0.01527	
HE 0032-2744	00:34:37.91	-27:28:20.0	16.28		24011	59	7.816	0.008	2	0.509	0.01460	
WD 0032-317	00:34:49.82	-31:29:54.3	15.62	MCT0032-3146	36878	99	7.161	0.012	2	0.295	0.02351	
WD 0032-175	00:35:17.47	-17:18:51.1	14.94	MCT0032-1735, EGGR 511	9786	7	8.051	0.009	1	0.606	0.01214	
WD 0032-177	00:35:25.20	-17:30:40.4	15.7	KUV00329-1747	16601	58	7.795	0.011	1	0.480	0.01452	
WD 0033+016	00:35:35.93	+01:53:06.5	15.52	L1011-71, G001-007	10824	8	8.781	0.006	2	1.078	0.00699	Shallow cores; NOV3.7 (Kepler 1995)
MCT 0033-3440	00:36:13.89	-34:23:35.7	16.42	HBQS0033-3440	14999	73	8.095	0.004	1	0.644	0.01190	
WD 0037-006	00:40:22.94	-00:21:31.1	14.85	PG0037-006, PB6089	15840	0	7.841	0.007	1			
HE 0043-0318	00:46:18.38	-03:02:00.8	15.48		12010	22	7.939	0.006	1	0.545	0.01310	
WD 0047-524	00:50:03.74	-52:08:17.1	14.2	BPM16274, L219-048	17969	18	7.64	0.004	2	0.415	0.01614	
HS 0047+1903	00:50:12.43	+19:19:49.3	15.5		16497	37	7.84	0.007	1	0.503	0.01411	
WD 0048-202	00:51:03.97	-20:00:00.3	14.85	GD656, PHL861	29836	50	5.636	0.008	2			sdB; binary
WD 0048-544	00:51:08.87	-54:11:21.2	15.29	HE0048-5427, L220-145	17385	18	7.981	0.003	2	0.581	0.01290	
WD 0048+202	00:51:11.00	+20:31:22.3	15.36	PG0048+202	20024	22	7.881	0.004	2	0.534	0.01386	
HE 0049-0940	00:52:15.30	-09:24:20.3	16	(PHL3044)	12995	34	7.735	0.004	1	0.441	0.01491	
WD 0050-332	00:53:17.43	-32:59:56.8	13.36	MCT0050-3316, SB 360	36642	38	7.872	0.005	1	0.561	0.01437	
HS 0051+1145	00:54:18.25	+12:01:59.9	15.6	(PHL886)	20389	31	7.812	0.006	1	0.499	0.01452	DAH; New magnetic
WD 0052-147	00:54:55.86	-14:26:09.1	15.12	MCT0052-1442, GD662	26076	35	8.221	0.005	1	0.742	0.01104	
WD 0053-117	00:55:50.33	-11:27:31.3	15.26	L796-10, LP706-065	7549	11	8.586	0.022	1	0.958	0.00825	Cool DA, bad fit, Zuckerman 2003: 7054 K, log $g = 7.93$
WD 0058-044	01:01:02.25	-04:11:11.2	15.38	GD9, GR407	16531	37	7.952	0.007	1	0.563	0.01312	DAH
WD 0101+048	01:03:50.01	+05:04:29.2	13.96	G002-017, G001-045	8638	3	8.179	0.007	2	0.686	0.01115	DD
WD 0102-185	01:04:53.10	-18:19:50.2	16.4	MCT0102-1835, KUV 01024-183	22613	154	7.671	0.023	1	0.441	0.01605	
WD 0102-142	01:05:22.16	-13:59:12.8	15.93	MCT0102-1414, PHL980	19660	26	7.89	0.005	2	0.538	0.01377	
HE 0103-3253	01:05:30.77	-32:37:54.3	16.12		12613	35	7.961	0.007	2	0.559	0.01294	
WD 0103-278	01:05:53.52	-27:36:56.8	15.45	G269-093, LIT0615	13509	9	7.859	0.004	1	0.505	0.01383	
MCT 0105-1634	01:08:09.81	-16:18:44.5	16.44	PHL997	28066	133	7.753	0.027	1	0.489	0.01537	
WD 0106-358	01:08:20.75	-35:34:43.0	14.74	MCT0106-3550, GD683	29082	32	7.827	0.006	2	0.525	0.01463	
HE 0106-3253	01:08:36.07	-32:37:43.5	15.34	(TonS193, SGPA234)	16544	28	7.894	0.005	1	0.531	0.01363	Bad fit around $H\alpha$ / $H\beta$ cores
WD 0107-192	01:09:33.13	-19:01:19.2	16.18	GD685, GR563	12982	70	7.82	0.015	1	0.483	0.01415	
WD 0108+143	01:10:55.14	+14:39:21.3	16.4	G033-045, LP467-027	9341	21	8.566	0.032	1	0.946	0.00839	
WD 0110-139	01:13:09.85	-13:39:35.8	15.68	MCT0110-1355	24046	62	7.994	0.008	1	0.602	0.01293	
MCT 0110-1617	01:13:14.12	-16:01:45.6	16.37		35182	161	7.885	0.019	1	0.565	0.01420	
MCT 0111-3806	01:14:03.23	-37:50:41.9	15.48		76857	746	7.367	0.025	1	0.466	0.02339	
WD 0112-195	01:15:05.62	-19:15:20.0	16.2	MCT0112-1931	36153	284	7.599	0.036	1	0.446	0.01753	
WD 0114-605	01:16:19.55	-60:16:07.6	14.9	HK22953-18	24671	52	7.792	0.007	1	0.499	0.01485	
WD 0114-034	01:16:58.80	-03:10:55.7	16.2	GD821, GR515	18874	102	7.869	0.019	1	0.525	0.01394	
WD 0124-257	01:26:55.90	-25:30:53.7	15.66	MCT0124-2546, GD1352	21995	51	7.713	0.012	1	0.457	0.01557	
WD 0126+101	01:29:24.38	+10:22:59.7	14.38	G002-040, WOLF72	8726	4	7.712	0.009	2	0.414	0.01483	
WD 0127-050	01:30:23.06	-04:47:57.8	13.6	HE0127-0503, G271-081	15942	4	7.766	0.005	1	0.464	0.01476	
WD 0128-387	01:30:28.02	-38:30:38.8	15.32	HE0128-3846, MCT0128-3846	27615	64	8.45	0.01	1			DA+DB
WD 0129-205	01:31:39.21	-20:19:59.1	14.64	MCT0129-2035	19088	48	7.815	0.008	1	0.498	0.01445	
HS 0129+1041	01:31:45.54	+10:56:59.1	15.6		16375	14	7.921	0.008	1	0.545	0.01338	
HS 0130+0156	01:32:57.38	+02:11:32.6	16	PHL1026	41590	194	7.94	0.017	1	0.603	0.01377	
HE 0130-2721	01:33:09.08	-27:05:45.0	16.08	GD1372, KUV01308-2721	21398	47	7.893	0.007	2	0.543	0.01379	
HE 0131+0149	01:34:28.46	+02:04:21.4	14.69	(PHL1040)	15563	15	7.827	0.005	2	0.493	0.01418	
WD 0133-116	01:36:13.39	-11:20:31.3	14.1	G271-106, ZZ CETI	12093	18	7.987	0.004	1	0.573	0.01271	ZZ Ceti; Shallow cores

Table A.1 continued

Object	RA	DE	mag	Aliases	T_{eff} [K]	$\sigma(T_{\text{eff}})$ [K]	log g	$\sigma(\log g)$	Spectra	M [M_{\odot}]	R [R_{\odot}]	Comments
WD 0135-052	01:37:59.40	-04:59:44.9	12.84	G271-115, LHS1270	7741	7	8.397	0.017	1			DD, double-lined; Cool, bad fit
MCT 0136-2010	01:38:31.67	-19:54:50.6	16.49	PHL3537	8752	9	8.622	0.012	1			DD, single-lined
HE 0138-4014	01:40:10.98	-39:59:24.6	16.37	MCT0138-40	21309	43	7.901	0.007	2	0.547	0.01371	
WD 0137-291	01:40:16.79	-28:52:53.7	16.04	MCT0137-2908, GD1384	20457	55	7.73	0.009	1	0.461	0.01534	
WD 0138-236	01:40:28.15	-23:21:22.8	16.1	MCT0138-2336, PHL1100	36270	387	7.809	0.045	1	0.531	0.01502	
WD 0140-392	01:42:50.99	-38:59:06.9	14.37	MCT0140-03914, SB702	21391	26	7.89	0.004	2	0.541	0.01382	
WD 0143+216	01:46:41.34	+21:54:48.1	15.05	G94-9, WOLF82	9391	8	8.567	0.01	1	0.947	0.00838	
WD 0145-221	01:47:21.76	-21:56:51.4	15.3	MCT0145-2211, GD1400	11663	29	8.078	0.008	1	0.627	0.01198	ZZ Ceti; Shallow cores
WD 0148-255j	01:48:08.18	-25:32:44.1	14.3		25982	42	7.878	0.006	1	0.544	0.01405	
HS 0145+1737	01:48:21.51	+17:52:13.5	15.7		17958	30	7.933	0.006	1	0.556	0.01333	
HE 0145-0610	01:48:22.27	-05:55:36.5	16.45	(PHL1166,BPSC22962-0027)	8871	11	8.199	0.015	1	0.699	0.01100	
HE 0150+0045	01:52:59.22	+01:00:20.2	16.4	WD0152+0100, PHL3911, GD18	12480	73	7.996	0.018	1	0.579	0.01265	NOV (Mukadam et al. 2004a)
WD 0151+017	01:54:13.88	+02:01:23.5	15	G073-004, G159-012	12646	57	7.762	0.012	1	0.453	0.01465	Shallow cores; NOV2.0 (Kepler et al. 1995)
HE 0152-5009	01:54:35.98	-49:55:01.9	16.32	(CSI-50-01527JL265)	12241	25	7.858	0.005	2	0.501	0.01379	
WD 0155+069	01:57:41.33	+07:12:03.8	15.34	GD20, FEIGE17	21092	38	7.621	0.01	1	0.416	0.01652	
WD 0158-227	02:00:53.41	-22:27:35.7	16	HE0158-224, PHL1251	75758	1128	7.386	0.038	1	0.470	0.02298	
HE 0201-0513	02:03:37.60	-04:59:12.8	15.94	(PB9009,G159-31)	24406	98	7.626	0.013	1	0.427	0.01663	
HS 0200+2449	02:03:45.80	+25:04:09.1	15.6		23161	61	7.9	0.008	1	0.550	0.01377	
WD 0205-136j	02:05:49.05	-13:38:27.4	15.7		48265	291	7.935	0.021	1	0.611	0.01394	
WD 0204-233	02:06:45.10	-23:16:14.0	15.6	G274-150, LP829-017	13299	105	7.896	0.009	1	0.524	0.01350	
HE 0204-3821	02:06:47.55	-38:07:04.0	15.6		13666	12	7.833	0.005	1	0.491	0.01406	
HE 0204-4213	02:06:49.89	-41:59:25.8	16.43		22178	72	7.876	0.011	1	0.536	0.01397	
WD 0205-365	02:07:25.46	-36:20:49.4	16.1	MCT0205-3635	62499	601	7.694	0.029	1	0.538	0.01725	
WD 0205-304	02:07:40.86	-30:10:59.6	15.67	GD1442	16711	33	7.731	0.007	1	0.451	0.01514	
HE 0205-2945	02:08:08.00	-29:31:38.8	16.06		10595	16	7.775	0.011	1	0.453	0.01443	
WD 0208-263	02:10:58.63	-26:07:01.3	15.8	HE0208-2621	34313	53	7.865	0.012	2	0.554	0.01438	
WD 0209+085	02:12:04.90	+08:46:50.1	13.9	HS0209+0832	36911	44	7.913	0.006	2			DAB
HE 0210-2012	02:13:01.93	-19:58:35.2	16.29		17027	28	7.819	0.006	2	0.494	0.01432	
HE 0211-2824	02:13:56.66	-28:10:17.8	15.27		13977	59	7.842	0.007	1	0.497	0.01399	
WD 0212-231	02:14:21.26	-22:54:49.1	16.4	HE0212-2308, GR286	26717	86	7.951	0.008	2	0.584	0.01338	
HS 0213+1145	02:16:07.61	+11:59:18.9	15.5		17073	74	7.9	0.014	1	0.536	0.01359	NOV
WD 0216+143	02:18:48.27	+14:36:03.2	14.58	PG0216+144, RXJ	26888	33	7.809	0.005	1	0.512	0.01475	
HE 0219-4049	02:21:19.69	-40:35:29.7	16.2		12402	29	8.08	0.006	2			
					14886	67	7.790	0.008	1			
HE 0221-2642	02:23:29.40	-26:29:19.7	15.63		32600	57	7.657	0.015	1	0.459	0.01664	
WD 0220+222	02:23:36.07	+22:27:28.4	15.83	G94-B5B, EG18	14945	66	7.882	0.01	1	0.521	0.01368	
HE 0221-0535	02:23:59.88	-05:21:45.9	15.59	(PHL1276)	24413	53	7.948	0.007	1	0.578	0.01336	
HE 0222-2336	02:24:19.89	-23:23:15.6	16.48		32240	90	7.807	0.017	1	0.522	0.01493	
HE 0222-2630	02:24:36.06	-26:16:52.2	15.59		22965	42	7.877	0.007	1	0.538	0.01398	
HS 0223+1211	02:26:29.98	+12:25:22.8	16		14106	70	7.288	0.011	1			
HE 0225-1912	02:27:41.43	-18:59:24.5	16.14	(PHL1295)	16900	43	7.53	0.01	1			
HS 0225+0010	02:27:55.50	+00:23:39.1	15.9		12949	32	7.888	0.007	2	0.519	0.01356	
WD 0226-329	02:28:27.70	-32:42:35.9	13.73	HE0226-3255	22129	31	7.832	0.005	1	0.513	0.01438	
WD 0227+050	02:30:16.66	+05:15:50.7	12.65	Feige22, EG19	18506	11	7.651	0.003	1	0.422	0.01606	
WD 0229-481	02:30:53.31	-47:55:25.9	14.53	LB1628, RE0230-475	58984	383	7.908	0.021	1	0.616	0.01444	
WD 0231-054	02:34:07.73	-05:11:39.6	14.24	GD31, PHL1358	13705	35	8.499	0.005	1	0.906	0.00887	
HS 0237+1034	02:40:35.57	+10:47:01.5	16		17385	40	7.959	0.014	1	0.569	0.01309	
WD 0239+109	02:42:08.54	+11:12:31.8	16.18	G004-034, LTT10886	45148	485	7.836	0.036	1	0.560	0.01495	DAH
HS 0241+1411	02:44:00.75	+14:24:29.6	16.2		13419	145	7.807	0.016	1	0.477	0.01428	
WD 0242-174	02:45:02.35	-17:12:20.6	15.33	HK22189-19	20159	34	7.816	0.006	1	0.501	0.01448	
WD 0243+155	02:46:24.06	+15:45:01.9	16.46	PG0243+155	17450	56	8.018	0.01	1	0.603	0.01258	
HE 0245-0008	02:47:46.45	+00:03:30.4	16.45	(GD34,HBQS,PB6885)	17411	91	7.994	0.016	1	0.589	0.01279	
HE 0246-5449	02:48:07.16	-54:36:44.9	16.39		15447	55	7.965	0.007	1	0.568	0.01298	
WD 0250-026	02:52:51.05	-02:25:17.4	14.73	HE0250-0237, KUV02503-0238	14667	42	7.814	0.008	1	0.484	0.01427	
WD 0250-007	02:53:32.29	-00:33:45.3	16.4	BD-1 407, LP591-117	8260	13	8.192	0.023	1	0.694	0.01105	Cool, bad fit
WD 0252-350	02:54:37.25	-34:49:56.6	15.89	HE0252-3501	16717	30	7.429	0.006	2	0.314	0.01811	
WD 0255-705	02:56:16.90	-70:22:17.7	14.08	L54-5, LFT245	10424	7	8.029	0.006	1	0.594	0.01233	NOV (Gianninas et al. 2005)
HE 0255-1100	02:58:21.72	-10:48:25.7	15.99		20827	132	7.836	0.02	1	0.512	0.01431	
HE 0256-1802	02:58:59.54	-17:50:20.3	16.41		26012	62	7.824	0.009	2	0.517	0.01458	
HE 0257-2104	02:59:52.65	-20:52:49.6	16.3		17059	46	7.718	0.01	1	0.446	0.01529	
WD 0257+080	02:59:59.24	+08:11:55.3	15.9	LHS5064, G76-48	7334	17	8.833	0.026	1	1.107	0.00667	DAH; Cool: 6680 K / log $g = 7.96$ (Bergeron et al. 2001)
WD 0258+184	03:01:12.87	+18:40:54.0	15.26	PG0258+185	28147	101	5.372	0.014	1			sdB
HE 0300-2313	03:02:36.69	-23:01:52.0	15.35		21966	58	8.176	0.01	1	0.707	0.01136	
WD 0302+027	03:04:37.40	+02:56:56.6	14.97	GD41, FEIGE31	35219	45	7.797	0.008	2	0.524	0.01513	

Table A.1 continued

Object	RA	DE	mag	Aliases	T_{eff} [K]	$\sigma(T_{\text{eff}})$ [K]	log g	$\sigma(\log g)$	Spectra	M [M_{\odot}]	R [R_{\odot}]	Comments
HE 0303–2041	03:06:04.96	–20:29:31.1	16.26	(PHL1467)	10073	14	8.134	0.012	1	0.659	0.01151	
HE 0305–1145	03:08:10.25	–11:33:45.7	15.4	(PHL8567)	26538	100	7.685	0.015	1	0.456	0.01606	
HE 0306–0309	03:08:40.80	–02:58:02.8	16.11		25555	163	5.753	0.015	1			sdB
WD 0307+149	03:09:53.95	+15:05:22.1	15.1	HS037+1454, PG0307+149	20976	31	7.887	0.005	1	0.539	0.01383	
HS 0307+0746	03:10:09.13	+07:57:32.6	16.3		10155	16	8.012	0.015	1	0.583	0.01246	
WD 0310–688	03:10:30.99	–68:36:03.3	11.4	CPD–69 177, LB3303	15847	12	7.928	0.002	1	0.548	0.01331	
HE 0308–2305	03:11:07.24	–22:54:05.6	15.16		24717	86	8.57	0.01	1	0.961	0.00841	
WD 0308+188	03:11:49.22	+19:00:55.5	13.86	PG0308+188	18096	17	7.734	0.004	2	0.457	0.01519	
HS 0309+1001	03:12:34.96	+10:12:27.2	15.6		18763	33	7.795	0.006	1	0.487	0.01463	
WD 0315–332	03:17:26.05	–33:03:05.4	16.53	HE0315–3314	50579	393	7.578	0.026	2	0.471	0.01845	
HS 0315+0858	03:17:43.18	+09:09:55.2	15.9		18111	43	7.811	0.008	1	0.493	0.01445	
HE0315–0118	03:18:13.31	–01:07:13.1	14.71		12413	36	7.841	0.009	1			
HE 0317–2120	03:19:27.22	–21:09:13.2	15.8		9754	16	8.086	0.018	1	0.628	0.01187	
WD 0317+196	03:20:04.07	+19:47:35.4	15.58	PG0317+196	16864	44	7.757	0.009	1	0.463	0.01490	
WD 0318–021	03:20:58.77	–01:59:59.5	16.01	HE0318–0210, KUV03184–0211	11923	28	8.104	0.008	1	0.644	0.01178	Shallow cores
WD 0320–539	03:22:14.81	–53:45:16.3	14.99	LB1663, REJ0322–534	33045	30	7.806	0.007	2	0.523	0.01497	
HE 0320–1917	03:22:31.91	–19:06:47.8	16	(PHL4402)	11853	0	7.227	0.029	1			DD, single-lined (Nelemans et al. 2005)
					12755	89	7.120	0.023				
HE 0324–2234	03:26:26.88	–22:24:15.0	16.39	(PHL1537, LEHPM3322)	16239	48	7.868	0.01	1	0.516	0.01384	
HE 0324–0646	03:26:39.97	–06:36:05.2	15.95	(PHL1535)	15275	70	7.901	0.014	1	0.532	0.01352	
HE 0324–1942	03:27:05.02	–19:32:23.8	16.25	(PHL1541)	20494	63	8.093	0.011	1	0.654	0.01202	
HE 0325–4033	03:27:43.92	–40:23:26.1	16.38		16021	22	7.94	0.005	2	0.555	0.01321	
HS 0325+2142	03:28:25.24	+21:53:08.4	15.3		13326	60	8.058	0.01	1	0.618	0.01217	
WD 0326–273	03:28:48.81	–27:19:01.7	14	LP888–064, L0587–077A	9286	4	7.702	0.007	1			DD, single-lined, DA+DC? (Nelemans et al. 2005)
WD 0328+008	03:31:33.93	+01:03:26.5	16.14	HE0328+0053, KUV03290+0053	34417	108	7.947	0.024	1	0.595	0.01356	
HE 0330–4736	03:32:03.98	–47:25:57.7	16.03		12868	36	8.019	0.006	2	0.593	0.01247	
HS 0329+1121	03:32:35.92	+11:31:31.9	15.8		17007	77	7.938	0.014	1	0.556	0.01326	
WD 0330–009	03:32:36.90	–00:49:36.6	15.74	HE0330–0059, KUV03301–0100	34251	49	7.772	0.011	2	0.510	0.01537	
HS 0331+2240	03:34:53.26	+22:50:07.8	15		20974	38	7.781	0.004	1	0.486	0.01484	
HE 0333–2201	03:36:02.77	–21:51:21.5	15.46	(PHL4465)	15286	52	8.09	0.007	1	0.641	0.01195	
HE 0336–0741	03:38:26.79	–07:31:54.6	16.33		14749	78	7.834	0.014	1	0.495	0.01409	
WD 0336+040	03:38:56.21	+04:09:43.0	15.9	KUV03363+0400	8947	16	7.948	0.026	1	0.542	0.01293	
HS 0337+0939	03:39:58.55	+09:49:11.3	16.2		12213	79	8.108	0.016	1	0.647	0.01175	
HE 0338–3025	03:40:18.33	–30:15:36.0	16.25	(PHL8735)	9952	7	8.094	0.008	2	0.633	0.01181	
WD 0339–035	03:41:54.49	–03:22:40.9	15.2	GD47, LP653–026	12033	14	8.012	0.004	2	0.587	0.01251	Shallow cores; NOV (Gianninas et al. 2005)
WD 0341+021	03:44:10.77	+02:15:29.9	15.3	HE0341+0206, KUV03416+0206	21914	49	7.355	0.008	2	0.306	0.01942	
WD 0343–007	03:46:25.21	–00:38:39.4	14.91	KUV0898–06	59686	585	7.641	0.033	1	0.514	0.01793	
WD 0344+073	03:46:51.42	+07:28:01.9	16.1	KUV03442+0719	10470	23	7.774	0.02	1	0.452	0.01443	NOV1.3
HS 0344+0944	03:46:52.31	+09:53:56.1	16.5		12740	111	7.93	0.024	1	0.542	0.01320	
HE 0344–1207	03:47:06.71	–11:58:08.5	15.8		11466	38	8.283	0.019	1	0.761	0.01041	ZZ Ceti
HS 0345+1324	03:48:39.58	+13:33:29.3	15.9		25321	83	8.143	0.01	1	0.692	0.01167	
HS 0346+0755	03:49:15.29	+08:04:53.6	16.3		15831	28	7.802	0.015	1	0.481	0.01442	
HE 0348–4445	03:49:59.27	–44:36:27.4	16.22		19337	49	7.942	0.009	1	0.565	0.01329	
HE 0348–2404	03:50:38.82	–23:55:45.2	16.2		13168	21	7.805	0.006	2	0.476	0.01429	
HE 0349–2537	03:51:41.37	–25:28:16.6	15.74		20461	28	7.821	0.005	2	0.504	0.01444	
WD 0352+049	03:54:40.21	+05:08:45.5	16.2	KUV03520+0500	36559	134	8.707	0.016	1	1.051	0.00752	
WD 0352+052	03:54:41.09	+05:23:19.4	15.9	KUV03520+0515	10056	17	7.819	0.016	1	0.474	0.01403	
WD 0352+018	03:54:43.47	+01:58:41.4	15.63	HE0352+0149, KUV03521+0150	21479	53	7.742	0.008	2	0.469	0.01525	
WD 0352+096	03:55:22.02	+09:47:17.5	14.47	HS0352+0938, HZ4	14887	30	8.118	0.002	1	0.658	0.01172	
HE 0358–5127	03:59:38.30	–51:18:41.5	15.6		22915	44	7.933	0.006	2	0.567	0.01346	
HS 0400+1451	04:03:42.08	+14:59:28.9	15.1		14521	77	8.174	0.006	1	0.692	0.01127	
HS 0401+1454	04:04:35.02	+15:02:26.7	16.2		12375	46	8.1	0.009	1	0.642	0.01182	NOV
HE 0403–4129	04:05:30.11	–41:21:10.2	16.13		22069	110	7.77	0.017	1	0.483	0.01499	
HE 0404–1852	04:07:11.18	–18:44:33.5	16	(PPM710547)	18562	55	7.636	0.011	1	0.416	0.01622	
WD 0406+169	04:09:28.89	+17:07:54.0	15.35	GH7–112, LP414–101	14687	82	8.297	0.006	1	0.774	0.01033	
WD 0407+179	04:10:10.33	+18:02:24.0	14.14	HZ10, HS0407+1754	12381	15	8.005	0.003	2	0.584	0.01257	NOV (Gianninas et al. (2005)
WD 0408–041	04:11:02.17	–03:58:22.2	15.5	GD56, GR571	14568	49	7.834	0.01	1	0.494	0.01408	
HE 0409–5154	04:11:10.33	–51:46:50.8	15.48		25541	80	7.764	0.011	1	0.488	0.01517	
HE 0410–1137	04:12:28.99	–11:30:08.3	16.13	(GD57)	17385	53	7.565	0.012	1			
WD 0410+117	04:12:43.60	+11:51:48.5	13.86	HS0409+1144, HZ2	20643	29	7.843	0.004	1	0.516	0.01424	
HS 0412+0632	04:14:58.36	+06:40:07.0	15.5	GD59	13229	77	7.952	0.01	1	0.555	0.01303	
HE 0414–4039	04:16:02.87	–40:32:11.7	15.88		20484	75	7.848	0.014	1	0.518	0.01418	
WD 0416–550	04:17:11.51	–54:57:47.9	15.11	HE0416–5505	30283	53	7.172	0.011	1	0.270	0.02251	

Table A.1 continued

Object	RA	DE	mag	Aliases	T_{eff} [K]	$\sigma(T_{\text{eff}})$ [K]	log g	$\sigma(\log g)$	Spectra	M [M_{\odot}]	R [R_{\odot}]	Comments
HE 0416-3852	04:18:04.14	-38:45:20.6	16.01		18859	59	7.853	0.012	1	0.517	0.01409	
HE 0416-1034	04:18:47.84	-10:27:09.6	15.83		24464	52	7.77	0.008	1	0.488	0.01507	
HE 0417-3033	04:19:22.07	-30:26:44.0	16.51		18679	54	7.87	0.01	1	0.525	0.01392	
HE 0418-5326	04:19:24.83	-53:19:17.4	16.38	FAUST545, FD30	26155	81	7.778	0.013	1	0.496	0.01505	
HE 0418-1021	04:21:12.03	-10:14:09.0	16.21		23463	43	8.3	0.006	1	0.789	0.01039	
WD 0421+162	04:23:55.81	+16:21:13.9	14.29	GH7-191, VR7	19823	39	8.041	0.007	1	0.622	0.01245	
HE 0423-2822	04:25:20.85	-28:15:19.9	16.54		10858	15	7.942	0.012	2	0.544	0.01304	Shallow cores; NOV2.1
HS 0424+0141	04:26:52.45	+01:47:47.7	15.6		46264	404	7.657	0.03	1	0.489	0.01718	
HE 0425-2015	04:27:39.77	-20:09:15.2	16.49		19561	45	8.036	0.008	2	0.618	0.01248	
WD 0425+168	04:28:39.48	+16:58:10.4	14.01	GH7-233, VR16	23991	26	8.026	0.003	2	0.621	0.01265	
HE 0426-1011	04:28:42.32	-10:04:48.9	16.07		17651	27	7.819	0.005	1	0.496	0.01435	
WD 0426+106	04:28:58.29	+10:44:48.7	16.3	KUV04262+1038	10224	28	8.362	0.023	1	0.812	0.00982	
HE 0426-0455	04:29:26.32	-04:48:46.7	14.89		13536	49	8.005	0.003	2	0.586	0.01260	
WD 0431+126	04:33:45.08	+12:42:40.4	14.18	HS0430+1236, HZ7	21112	42	7.991	0.007	1	0.595	0.01290	
HE 0436-1633	04:38:47.33	-16:27:21.4	16.22		13432	34	8.018	0.005	2	0.594	0.01249	
WD 0437+152	04:39:52.97	+15:19:44.0	15.83	KUV04370+1514	17166	43	7.105	0.009	1	0.170	0.02136	
WD 0443-037j	04:43:07.07	-03:46:49.5	16.00		71545	805	8.538	0.033	1	0.975	0.00879	Linear fit, no quadratic termination
WD 0446-789	04:43:46.67	-78:51:50.2	13.47	BPM3523	23222	28	7.692	0.004	1	0.451	0.01585	
HE 0452-3429	04:54:05.85	-34:25:05.9	16.49		12619	43	7.944	0.009	1	0.549	0.01308	
HE 0452-3444	04:54:23.69	-34:39:48.7	15.86		20640	48	7.763	0.008	1	0.477	0.01501	
WD 0453-295	04:55:35.98	-29:29:01.3	15.12	HE0453-2933, MCT0453-2933	27186	81	7.393	0.012	1			DA+DBA
HE 0455-5315	04:56:58.35	-53:10:26.6	16.2		24516	109	7.706	0.016	1	0.460	0.01575	
WD 0455-282	04:57:13.38	-28:07:53.6	13.95	RE0457-280, EUVEJ0457-281	54101	162	7.704	0.01	1	0.524	0.01683	
HE 0456-2347	04:58:51.47	-23:42:55.7	16.42		23107	80	7.777	0.011	1	0.489	0.01496	
PN 2155-308	05:03:07.52	-15:36:22.7	15.6	WD0500-156	94488	112	7.214	0.036	1			DAO
HS 0503+0154	05:05:39.24	+01:58:28.2	15.2	WD0503+019, RXP, RXS	62556	1011	7.691	0.051	1	0.537	0.01730	
HE 0507-1855	05:09:20.47	-18:51:17.3	16.38		20129	46	8.213	0.008	2	0.728	0.01104	
WD 0507+045.2	05:10:13.59	+04:38:54.0	15.6		11537	25	8.124	0.007	1	0.656	0.01161	ZZ Ceti; Shallow cores
WD 0507+045.1	05:10:14.01	+04:38:37.4	14.3		20534	22	7.858	0.004	1	0.523	0.01409	
HE 0508-2343	05:10:39.43	-23:40:10.1	16.24		16493	73	7.777	0.014	1	0.471	0.01469	
WD 0509-007	05:12:06.51	-00:42:07.2	13.9	RE0512-004, EUVEJ0512-007	32152	31	7.298	0.007	2	0.326	0.02119	
WD 0512-417j	05:12:23.03	-41:45:26.3	16.50		51120	489	7.919	0.028	1	0.608	0.01417	
HE 0516-1804	05:19:04.27	-18:01:29.1	16.14		12579	81	7.755	0.016	1	0.450	0.01471	
WD 0518-105	05:21:18.95	-10:29:17.4	15.89	RE0521-102, EUVEJ0521-104	32474	67	8.747	0.014	1	1.070	0.00725	
HE 0532-5605	05:33:06.70	-56:03:53.3	16.12	EC0532-5605	11347	15	8.451	0.007	2	0.872	0.00919	ZZ Ceti; Shallow cores
WD 0548+000	05:50:37.62	+00:05:50.4	14.79	GD257, GR289	45422	186	7.708	0.013	1	0.507	0.01649	
WD 0549+158	05:52:27.63	+15:53:13.1	13.06	GD71, LTT11733	33034	23	7.798	0.005	1	0.520	0.01505	
WD 0556+172	05:59:44.95	+17:12:03.9	15.79	KPD0556+1712	17963	39	8.076	0.007	1	0.638	0.01211	
WD 0558+165	06:01:17.67	+16:31:37.2	15.69	KPD0558+1631	16499	41	8.165	0.007	1	0.690	0.01137	
WD 0605-483j	06:05:02.75	-48:19:59.8	16.00		34882	61	7.851	0.013	1	0.548	0.01454	
WD 0612+177	06:15:18.67	+17:43:40.1	13.39	G104-27, LTT11818	25722	37	7.896	0.005	1	0.553	0.01387	
WD 0621-376	06:23:12.71	-37:41:30.8	12.09	RE0623-374, EUVEJ0623-376	60864	180	7.357	0.007	1	0.424	0.02257	
WD 0625-253	06:27:02.07	-25:22:50.8	16.16	Abell15, GR903	70054	2385	5.556	0.073	1			sdO; McCarthy et al. (1997): 110000 K, log $g = 5.7$
WD 0628-020	06:30:38.59	-02:05:51.0	15.3	LP600-42	7291	15	8.599	0.025	1	0.967	0.00816	Cool, linear fit; Svestri et al. (2001): 5161 K, 0.62 M_{\odot}
WD 0630-050	06:32:57.79	-05:05:49.8	15.54	RE0632-050, EUVEJ0632-050	41810	184	8.324	0.015	1	0.824	0.01034	
WD 0642-285	06:44:28.77	-28:32:38.6	15.2	LP895-041	9325	13	7.99	0.021	1	0.568	0.01261	
WD 0648-253j	06:48:56.20	-25:23:48.2	13.80		27664	27	7.822	0.004	1	0.520	0.01465	
WD 0710+216	07:13:21.61	+21:34:06.8	15.29	GD83 EG214	10243	11	7.963	0.01	1	0.554	0.01285	Shallow cores; NOV1.0
WD 0715-704j	07:15:17.00	-70:25:06.5	14.00		46210	305	7.866	0.022	1	0.575	0.01464	
WD 0723-277j	07:23:20.06	-27:47:22.8	14.80		37044	97	7.756	0.011	1	0.509	0.01564	
WD 0732-427	07:33:37.84	-42:53:58.8	14.16	L384-24, BPM33039	14596	84	8.108	0.007	1	0.651	0.01179	
WD 0810-728	08:09:31.99	-72:59:17.2	15.15	RE0809-725, EUVEJ0809-729	31037	47	7.942	0.009	1	0.586	0.01355	
HS 0820+2503	08:23:46.21	+24:53:45.9	15	(Ton316,RXS)	33817	81	7.919	0.018	1	0.579	0.01383	
WD 0830-535	08:31:52.02	-53:40:33.7	14.46	RE0831-534, EUVE0831-536	30007	31	7.823	0.006	1	0.525	0.01470	
WD 0841+035j	08:41:03.90	+03:21:16.1	15.20		38922	51	7.735	0.007	1	0.504	0.01594	Linear fit, no good quadratic fit
WD 0839-327	08:41:32.62	-32:56:34.8	11.9	L532-81, CD-32 5613	9244	4	7.649	0.008	1	0.384	0.01539	
WD 0839+231	08:42:53.06	+23:00:25.8	14.42	PG0839+232	25785	55	7.733	0.007	1	0.475	0.01551	
WD 0852+192	08:55:30.73	+19:04:37.8	15.7	LB8888, HS0852+1916	14060	84	7.874	0.012	1	0.514	0.01372	
WD 0858+160	09:01:33.46	+15:51:43.3	15.83	HS0858+1603	15709	11	7.85	0.005	2	0.505	0.01398	
WD 0902-041j	09:02:17.34	-04:06:56.3	12.40		23601	21	7.768	0.003	1	0.486	0.01506	
WD 0908+171	09:11:24.05	+16:54:11.5	16.06	PG0908+171	16915	35	7.813	0.007	1	0.490	0.01437	
WD 0911-076	09:14:22.39	-07:51:25.6	16.16	EC09119-0738	17682	49	7.902	0.009	1	0.539	0.01360	
WD 0916+064	09:18:41.87	+06:17:02.2	15.66	PG0916+065	44537	249	7.347	0.026	1	0.384	0.02170	Linear fit, no reasonable quadratic fit

Table A.1 continued

Object	RA	DE	mag	Aliases	T_{eff} [K]	$\sigma(T_{\text{eff}})$ [K]	$\log g$	$\sigma(\log g)$	Spectra	M [M_{\odot}]	R [R_{\odot}]	Comments
WD 0922+162b	09:25:13.22	+16:01:45.6	16.14		23674	67	8.272	0.009	1	0.771	0.01061	
WD 0922+162a	09:25:13.55	+16:01:44.7	16.14		24198	73	8.264	0.009	1	0.767	0.01068	
WD 0922+183	09:25:18.37	+18:05:34.3	16.46	PG0922+183	24123	67	8.24	0.008	1	0.751	0.01087	
WD 0928-713	09:29:08.65	-71:34:02.8	15.44	L64-40, BPM05639	8646	5	8.294	0.01	2	0.764	0.01030	
HS 0926+0828	09:29:36.53	+08:15:46.8	16.2		11643	47	8.058	0.012	1	0.614	0.01213	Shallow cores; NOV6 (Mukadam et al. 2004a)
HS 0929+0839	09:32:29.85	+08:26:37.5	16.1		13012	108	8.076	0.015	1	0.629	0.01202	
HS 0931+0712	09:34:32.67	+06:58:48.2	16.5		39513	244	7.744	0.034	1	0.509	0.01585	
HS 0933+0028	09:36:07.96	+00:14:35.9	16		32891	90	8.172	0.019	1	0.721	0.01152	
HS 0937+0130	09:39:58.67	+01:16:38.2	16.5		18805	55	8.312	0.009	1	0.790	0.01026	
WD 0937-103	09:40:11.96	-10:34:25.1	15.97	EC09377-1020	17818	27	8.437	0.007	1	0.869	0.00933	
WD 0939-153	09:41:56.22	-15:32:14.6	15.92	EC09395-1518	13002	41	7.847	0.006	2	0.497	0.01391	
HS 0940+1129	09:43:14.38	+11:16:11.4	16.1		14475	115	7.815	0.012	1			
					13031	128	7.878	0.014	1			
HS 0943+1401	09:46:31.60	+13:47:35.8	16.4		16918	101	8.364	0.015	1	0.821	0.00985	
WD 0944-090	09:47:03.39	-09:19:50.5	15.95	EC09445-0905	69208	1016	5.89	0.045	1			sdO
HS 0944+1913	09:47:31.67	+18:59:12.7	15.3		17044	18	7.883	0.004	1	0.527	0.01374	
WD 0945+245	09:48:46.66	+24:21:26.1	14.32	PG0945+246, LB11146	35709	77	8.661	0.011	1			DA+DAXP (Liebert et al. 1993)
HS 0949+0935	09:51:48.94	+09:21:12.6	16.3		17958	78	7.733	0.016	1	0.456	0.01519	
HS 0949+0823	09:51:56.17	+08:09:33.7	16.1		14298	162	7.926	0.007	1	0.543	0.01328	NOV (Mukadam et al. 2004a)
WD 0950+077	09:52:59.15	+07:31:08.3	16.12	PG0950+078	15652	38	7.904	0.006	1	0.534	0.01351	
WD 0951-155	09:53:40.36	-15:48:56.6	16.09	EC09512-1534	17834	39	7.784	0.008	1	0.479	0.01469	
WD 0954+134	09:57:18.99	+13:12:57.0	16.41	PG0954+135	16285	79	7.816	0.015	1	0.490	0.01432	
WD 0955+247	09:57:48.37	+24:32:55.5	15.07	G49-33, LTT12661	8707	5	8.122	0.009	2	0.649	0.01158	
WD 0956+045	09:58:37.24	+04:21:31.0	15.8	PG0956+046	18403	49	7.754	0.009	2	0.467	0.01501	
WD 0956+020	09:58:50.49	+01:47:23.5	15.61	HE0956+0201, PG0956+021	15973	12	7.819	0.007	1	0.490	0.01427	
HE 0959-0828	10:01:33.43	-08:42:51.7	16.13	EC09590-0828, PG0959-085	78791	2317	6.747	0.088	1			sdO
WD 1000-001	10:03:16.34	-00:23:36.9	16.08	PG1000-002, LB564	19797	50	7.846	0.008	1	0.515	0.01418	
WD 1003-023	10:05:51.54	-02:34:19.5	15.43	PG1003-023	19983	30	7.835	0.005	2	0.510	0.01429	
HS 1003+0726	10:06:23.08	+07:12:12.6	15.3		9578	14	8.065	0.015	1	0.614	0.01203	
WD 1008-179	10:10:33.50	-18:11:48.6	15.19	EC10081-1757, HE1008-1757	71540	816	6.343	0.025	1			sdO
WD 1010+043	10:13:12.78	+04:05:12.8	16.34	PG1010+043	28836	64	7.964	0.012	1	0.594	0.01330	
HE 1012-0049	10:15:11.75	-01:04:17.1	15.57		22797	50	8.015	0.007	1	0.612	0.01273	
HS 1013+0321	10:15:48.15	+03:06:46.8	15.6	WDJ1015+0306, SDSS	11366	15	7.938	0.009	1	0.543	0.01309	ZZ Ceti; Shallow cores
WD 1013-010	10:16:07.01	-01:19:18.7	15.33	G053-038, EG253	8311	0	7.668	0.012	2			DD, single-lined (Nelemans et al. 2005)
WD 1013-050	10:16:28.76	-05:20:33.5	14.3	RE1016-052, EUVEJ1016-053	59577	334	7.685	0.075	1			DAO
WD 1015-216	10:17:26.67	-21:53:43.4	15.66	EC10150-2138	31588	52	7.875	0.01	1	0.553	0.01422	
WD 1015+076	10:18:01.69	+07:21:22.4	15.37	PG1015+076	25623	137	7.664	0.019	1	0.445	0.01626	
WD 1015+161	10:18:03.84	+15:51:58.3	15.57	PG1015+161	19855	74	8.009	0.015	1	0.603	0.01272	
WD 1017-138	10:19:52.45	-14:07:35.5	14.56	EC10174-1352, REJ1019-140	31942	36	7.872	0.007	1	0.553	0.01425	
WD 1017+125	10:19:56.02	+12:16:29.9	15.75	PG1017+125	21066	67	7.886	0.01	1	0.539	0.01385	
WD 1019+129	10:22:28.77	+12:41:59.4	15.6	PG1019+129	17909	38	7.871	0.007	1	0.523	0.01388	
WD 1020-207	10:22:43.83	-21:00:02.1	15.09	EC10203-2044	19281	51	7.862	0.009	1	0.522	0.01402	
WD 1022+050	10:24:59.90	+04:46:09.0	14.18	PG1022+050, LP550-52	11280	0	7.914	0.009	1			DD, single-lined (Morales-Rueda et al. 2005); NOV1.4 (Kepler et al. 1995)
WD 1023+009	10:25:49.77	+00:39:04.4	16.4	PG1023+009	39787	163	7.894	0.023	1	0.577	0.01421	
WD 1026+023	10:29:09.87	+02:05:49.7	14.2	PG1026+024, LP550-292	11679	18	8.063	0.005	1	0.618	0.01209	NOV3.0 (Kepler et al. 1995)
WD 1031-114	10:33:42.79	-11:41:40.4	13	EC10312-1126, L0825-014	25230	25	7.831	0.003	1	0.519	0.01449	
WD 1031+063	10:34:05.43	+06:02:45.6	16.26	PG1031+063	20588	54	7.779	0.005	2	0.484	0.01485	
WD 1036+085	10:39:07.48	+08:18:39.1	16.07	PG1036+086	21460	96	7.249	0.016	1	0.258	0.02050	
HS 1043+0258	10:46:23.34	+02:42:35.6	15.6		13192	119	7.858	0.012	1	0.503	0.01383	
WD 1049-158	10:52:20.69	-16:08:05.9	14.36	EC10498-1552	19514	21	8.268	0.004	1	0.763	0.01060	
WD 1053-550	10:55:13.77	-55:19:05.8	14.32	L250-52, BPM20383	12705	16	8.026	0.004	2	0.597	0.01241	NOV (Gianninas et al. 2005)
WD 1053-290	10:55:40.04	-29:19:53.4	15.38	EC10532-2903	10619	12	8.1	0.006	1	0.638	0.01178	Shallow cores
HE 1053-0914	10:55:45.41	-09:30:59.1	16.38	WD1053-092, PG1053-092	21430	32	7.629	0.008	2	0.421	0.01645	
HS 1053+0844	10:55:51.54	+08:28:46.6	16.5		16177	78	8	0.007	1	0.589	0.01270	
WD 1056-384	10:58:20.19	-38:44:26.5	14.08	RE1058-384, EUVEJ1058-387	27665	23	7.936	0.004	1	0.577	0.01354	
WD 1058-129	11:01:12.28	-13:14:42.7	14.93	EC10587-1258, PG1058-129	24800	78	8.618	0.01	1	0.990	0.00808	
HS 1102+0934	11:04:36.76	+09:18:22.7	16.4		16087	51	7.224	0.012	2	0.216	0.01999	
WD 1102-183	11:04:47.08	-18:37:15.2	15.99	EC11023-1821	8442	8	8.185	0.013	2	0.689	0.01110	
HS 1102+0032	11:05:15.33	+00:16:26.3	14.8	WDJ1105+0016, SDSS, GD127	12786	74	8.214	0.01	1	0.716	0.01094	NOV2 (Mukadam et al. 2004a)
WD 1105-048	11:07:59.98	-05:09:27.3	12.92	LP672-001, G163-050	15488	12	7.72	0.002	1	0.441	0.01517	
HE 1106-0942	11:09:08.22	-09:58:48.6	16.34	PG1106-097	76156	1755	6.446	0.07	1			sdO
HS 1115+0321	11:17:46.18	+03:04:51.3	15.4	GD131, GEN#	12558	36	7.841	0.006	1	0.493	0.01395	
WD 1115+166	11:17:55.21	+16:21:27.9	15.1	PG1115+166	35378	93	8.029	0.012	1			DA+DB

Table A.1 continued

Object	RA	DE	mag	Aliases	T_{eff} [K]	$\sigma(T_{\text{eff}})$ [K]	log g	$\sigma(\log g)$	Spectra	M [M_{\odot}]	R [R_{\odot}]	Comments
HE 1115-0631	11:18:11.69	-06:47:33.2	14.7	PG1115-065	37208	99	5.884	0.011	2			sdO
WD 1116+026	11:19:12.55	+02:20:30.9	14.57	GD133, PG1116+026	11625	12	8.097	0.004	2	0.639	0.01183	ZZ Ceti; Shallow cores
HE 1117-0222	11:19:34.66	-02:39:06.3	14.25	WD1117-024, GD135	13254	34	8.031	0.005	1	0.601	0.01238	
WD 1121+216	11:24:13.08	+21:21:34.8	14.23	G120-45, LHS304	7771	5	8.365	0.006	2	0.811	0.00978	Cool, bad fit; Zuckerman et al. 2003: 7495 K, log $g = 8.19$
WD 1122-324	11:24:35.62	-32:46:25.7	15.86	EC11221-3229	20875	28	7.804	0.005	2	0.497	0.01462	
WD 1123+189	11:26:19.11	+18:39:17.2	14.01	PG1123+189, REJ1126+183	59566	272	7.553	0.014	1	0.484	0.01926	
HE 1124+0144	11:26:49.74	+01:27:56.4	16.49	PG1130-063	15824	14	7.802	0.008	1	0.481	0.01442	
WD 1124-293	11:27:09.32	-29:40:11.8	15.02	EC11246-2923, ESO0439-080	9532	6	8.074	0.007	1	0.619	0.01196	
WD 1124-018	11:27:21.33	-02:08:37.7	16.47	PG1124-019	24255	80	7.537	0.011	1	0.392	0.01766	
WD 1125-025	11:28:14.50	-02:50:27.3	15.32	PG1125-026, REJ1128-025	31825	65	8.279	0.011	1	0.786	0.01063	
WD 1125+175	11:28:15.68	+17:14:06.9	15.95	PG1125+175	64538	636	7.618	0.034	1	0.517	0.01846	
WD 1126-222	11:29:11.64	-22:33:44.4	16.17	EC11266-2217	12077	60	8.076	0.012	1	0.627	0.01200	ZZ Ceti; Shallow cores
WD 1129+071	11:32:03.58	+06:55:07.9	14.9	PG1129-072	12740	34	7.934	0.007	1	0.544	0.01317	
WD 1129+155	11:32:27.46	+15:17:29.1	14.04	PG1129+156	17367	20	8.057	0.004	1	0.626	0.01226	
HE 1130-0620	11:32:41.60	-06:36:54.4	15.79	PG1130-063	44696	552	5.53	0.035	1			sdO
WD 1130-125	11:33:19.50	-12:49:01.2	15.5	EC11307-1232	13935	53	8.269	0.007	1	0.755	0.01054	
HS 1136+1359	11:39:25.42	+13:43:11.0	16	(A1 117)	24213	203	7.807	0.026	1	0.505	0.01469	
HS 1136+0326	11:39:26.64	+03:10:19.7	16.2		13633	159	7.701	0.015	1	0.427	0.01525	
WD 1141+077	11:43:59.45	+07:29:04.7	14.11	PG1141+078	62137	357	7.329	0.016	1	0.418	0.02315	
WD 1144-246	11:47:20.13	-24:54:56.7	15.71	EC11448-2438	30698	52	7.216	0.01	1	0.289	0.02203	
HS 1144+1517	11:47:25.13	+15:00:38.7	16.3		14844	104	7.826	0.013	1	0.491	0.01417	
WD 1145+187	11:48:03.18	+18:30:46.6	14.22	PG1145+188, REJ1148+183	27067	33	7.839	0.005	1	0.528	0.01448	
WD 1147+255	11:50:20.18	+25:18:32.6	15.55	G121-022, HS 1406+2229	10001	12	8.152	0.01	2	0.670	0.01137	NOV (Gianninas et al. 2005)
WD 1148-230	11:50:38.85	-23:20:34.3	11.76	EC11481-2303	43407	160	5.615	0.007	1			sdOB; Stys et al. (2000): Binary?
WD 1149+057	11:51:54.29	+05:28:38.3	14.91	PG1149+058	10994	22	7.981	0.014	1	0.567	0.01273	ZZ Ceti; Shallow cores
WD 1150-153	11:53:15.37	-15:36:36.8	16	EC11507-1519	12453	47	8.028	0.009	1	0.598	0.01239	ZZ Ceti
HE 1152-1244	11:54:34.91	-13:01:16.8	15.81		13034	87	7.643	0.009	1	0.399	0.01576	
WD 1152-287	11:54:45.82	-29:00:40.7	16.38	EC11522-2843	19443	59	7.609	0.011	1	0.407	0.01656	
HS 1153+1416	11:55:59.76	+14:00:13.3	15.8	(PB3724)	15086	95	7.852	0.017	1	0.505	0.01394	
WD 1155-243	11:57:33.65	-24:39:27.9	16.48	EC11550-2422	12975	58	7.845	0.008	2	0.496	0.01393	
WD 1159-098	12:02:07.71	-10:04:40.8	15.97	HE1159-0947, LP734-006	9442	6	8.523	0.008	2	0.918	0.00868	
WD 1201-001	12:03:47.53	-00:23:11.8	15.12	HE1201-006, PG1201-001	19382	27	8.233	0.005	2	0.740	0.01087	
WD 1201-049	12:04:21.65	-05:13:26.5	16.34	PG1201-049	74798	944	7.475	0.035	1	0.497	0.02135	"Balmer line problem"
WD 1202-232	12:05:26.80	-23:33:13.6	12.79	EC12028-2316	8852	3	8.139	0.006	1	0.660	0.01145	
WD 1204-322	12:06:47.63	-32:34:33.8	15.68	EC12042-3217, HE1204-3217	20098	38	7.861	0.006	1	0.524	0.01405	
WD 1204-136	12:06:56.43	-13:53:53.6	15.52	EC12043-1337	11096	17	8.342	0.002	1	0.800	0.00997	Shallow cores; NOV2 (Bergeron et al. 2004)
HS 1204+0159	12:07:29.51	+01:42:50.6	16.5		24648	104	7.83	0.014	1	0.518	0.01448	
WD 1207-157	12:10:09.34	-16:00:40.4	16.32	EC12075-1543, HE1207-1543	16390	54	7.824	0.01	1	0.494	0.01425	
WD 1210+140	12:12:33.89	+13:46:25.1	14.67		32640	48	6.997	0.012	1			DD, single-lined (Nelemans et al. 2005)
WD 1214+032	12:16:51.84	+02:58:04.3	15.32	LP544-063	7397	15	8.549	0.03	1	0.934	0.00850	Cool object, bad fit
HE 1215+0227	12:17:56.20	+02:10:45.8	16.35		57798	957	7.686	0.054	1	0.525	0.01721	
WD 1216+036	12:18:41.15	+03:20:21.7	15.94	PG1216+036	12750	39	7.845	0.008	2	0.495	0.01392	
WD 1218-198	12:21:07.35	-20:07:05.1	16.35	EC12185-1950	35907	208	7.813	0.025	1	0.532	0.01497	
WD 1220-292	12:23:05.17	-29:32:28.9	15.79	EC12204-2915	17370	32	7.809	0.006	1	0.490	0.01443	
HE 1225+0038	12:28:07.72	+00:22:19.6	15.09		9519	4	8.102	0.005	2	0.637	0.01174	
WD 1229-012	12:31:34.46	-01:32:08.5	14.24	HE 1229-0115, PG1229-013	19311	28	7.468	0.005	1	0.345	0.01801	
WD 1230-308	12:33:00.67	-31:08:36.4	15.81	EC12303-3052	22984	52	8.29	0.007	1	0.782	0.01047	
WD 1231-141	12:33:36.89	-14:25:08.6	16.12	EC12310-1408	17453	47	7.992	0.005	1	0.588	0.01280	
HE 1233-0519	12:35:37.58	-05:35:36.7	16.48		15763	0	8.285	0.01	2	0.768	0.01043	DAH
WD 1233-164	12:36:14.02	-16:41:53.5	15.1	EC12336-1625	24896	44	8.23	0.006	2	0.746	0.01096	
WD 1236-495	12:38:50.02	-49:48:01.1	13.96	L327-186, LTT4816	11374	8	8.712	0.002	2	1.038	0.00743	ZZ Ceti; Shallow cores
WD 1237-028	12:40:09.66	-03:10:14.8	15.97	PG1237-029, LP615-183	10042	14	8.373	0.013	1	0.819	0.00974	
WD 1241+235	12:44:16.57	+23:14:10.8	15.18	PG1241+235, LB16	27453	62	7.914	0.01	1	0.565	0.01374	
WD 1241-010	12:44:28.66	-01:18:59.6	14	PG1241-010	23034	20	7.326	0.004	1	0.298	0.01985	DD, double lined
HS 1243+0132	12:45:38.74	+01:16:16.1	15.6	(UM517, LEDA43016)	21057	70	7.75	0.005	1	0.472	0.01516	
WD 1244-125	12:47:26.88	-12:48:42.0	14.7	EC12448-1232	13057	49	7.937	0.005	1	0.546	0.01315	
HE 1247-1130	12:49:54.26	-11:47:00.2	14.74		27813	83	7.774	0.013	1	0.497	0.01514	
EC12489-2750	12:51:41.1	-28:06:49	16.22		64080	632	7.867	0.029	1	0.606	0.01502	
HS 1249+0426	12:52:15.19	+04:10:43.0	15.8	(PB4304)	11494	12	8.05	0.006	2	0.609	0.01219	ZZ Ceti; Shallow cores
WD 1249+160	12:52:17.15	+15:44:43.4	14.63	GD150	25583	61	7.188	0.008	1	0.253	0.02168	
WD 1249+182	12:52:23.34	+17:56:53.9	15.48	GD151	19519	23	7.754	0.004	2	0.470	0.01506	Linear fit, no good quadratic fit
HE 1252-0202	12:54:58.10	-02:18:36.7	16.5		15489	85	7.946	0.011	1	0.557	0.01314	
WD 1254+223	12:57:02.33	+22:01:52.7	13.33	GD153 BPM88611	40016	67	7.822	0.003	1	0.544	0.01498	

Table A.1 continued

Object	RA	DE	mag	Aliases	T_{eff} [K]	$\sigma(T_{\text{eff}})$ [K]	log g	$\sigma(\log g)$	Spectra	M [M_{\odot}]	R [R_{\odot}]	Comments
WD 1257+047	12:59:50.35	+04:31:26.6	14.99	GD267, LP556-035	22417	49	7.953	0.007	1	0.577	0.01327	
WD 1257+032	12:59:56.69	+02:55:56.2	15.6	PG1257+032, PB4421	17376	39	7.866	0.007	1	0.519	0.01391	
HE 1258+0123	13:01:10.50	+01:07:39.9	16.42	WD 1258+013, SDSS	11264	22	8.112	0.007	1	0.648	0.01170	ZZ Ceti; Bergeron 2004; Shallow cores
WD 1300-098	13:03:16.77	-10:09:12.5	16.25	PG1300-099	13299	57	8.274	0.009	1	0.757	0.01049	NOV1.0
WD 1305-017	13:08:15.22	-01:59:04.2	16.28	PG1305-017	85773	992	7.8	0.091	1			DAO
HS 1305+0029	13:08:20.87	+00:13:30.5	16.2		12524	39	8.028	0.008	2	0.598	0.01239	
HE 1307-0059	13:09:41.67	-01:15:05.9	15.72		17574	59	7.825	0.013	1	0.498	0.01429	
HS 1308+1646	13:11:06.06	+16:31:03.4	15.5		10957	15	8.331	0.003	1	0.792	0.01005	NOV0.7
WD 1308-301	13:11:17.52	-30:25:57.6	15.11	EC13085-3010	14001	31	7.861	0.004	1	0.507	0.01383	
HE 1310-0337	13:13:28.35	-03:53:19.7	16.31		18541	63	7.826	0.011	1	0.502	0.01432	
WD 1310-305	13:13:41.59	-30:51:33.7	14.48	EC13109-3035	20216	22	7.811	0.004	2	0.499	0.01453	
EC 13123-2523	13:15:03.9	-25:39:01	15.69		75463	825	7.682	0.027	1	0.559	0.01784	
WD 1314-153	13:16:43.59	-15:35:58.7	14.86	EC13140-1520, LHS 2712	15887	12	7.809	0.005	2	0.485	0.01436	
WD 1314-067	13:17:18.46	-06:59:28.1	15.87	PG1314-067	16700	100	7.831	0.019	1	0.499	0.01420	
HE 1315-1105	13:17:47.29	-11:21:06.2	15.76		9169	8	8.099	0.011	1	0.635	0.01176	
HE 1318-2111	13:21:15.66	-21:27:18.5	14.6	EC13185-2111	37149	172	5.452	0.02	1			sdO
WD 1323-514	13:26:09.62	-51:41:37.9	14.6	L258-46, L257-47	18745	18	7.744	0.004	2	0.463	0.01512	
HE 1325-0854	13:28:23.90	-09:09:53.0	15.14		16578	24	7.703	0.006	1	0.437	0.01540	
HE 1326-0041	13:29:24.69	-00:56:43.9	16.27		18193	71	7.83	0.013	1	0.503	0.01427	
WD 1326-236	13:29:24.92	-23:52:18.1	15.97	EC13266-2336	13519	97	7.909	0.008	1	0.532	0.01340	
WD 1327-083	13:30:13.58	-08:34:30.2	12.31	G014-058, BD-07D3632	13890	37	7.847	0.002	1	0.499	0.01394	
HE 1328-0535	13:31:20.03	-05:50:52.4	16.34		36181	206	7.872	0.025	1	0.560	0.01435	
WD 1328-152	13:31:34.82	-15:30:48.0	15.49	EC13288-1515, HE 1328-1515	59406	331	7.667	0.018	1	0.522	0.01754	
WD 1330+036	13:33:17.80	+03:21:00.2	15.86	GD269, BPM89123	17394	11	7.835	0.007	1	0.503	0.01419	
WD 1332-229	13:35:10.47	-23:10:38.3	16.3	EC13324-2255	19657	42	7.878	0.007	1	0.531	0.01388	
HS 1334+0701	13:36:33.67	+06:46:26.8	15		15319	45	7.075	0.01	1	0.140	0.02127	
WD 1334-160	13:36:59.29	-16:19:44.1	15.32	EC13342-1604, L0762-021	18077	31	8.221	0.005	1	0.729	0.01095	
WD 1334-678	13:38:08.11	-68:04:37.4	15.57	L106-73, LHS 2769	8970	8	8.069	0.015	1	0.615	0.01199	
HE 1335-0332	13:38:22.72	-03:47:19.5	16.47		19806	93	8.4	0.015	1	0.848	0.00961	
HS 1338+0807	13:41:27.63	+07:52:29.5	16		24189	164	7.731	0.021	1	0.470	0.01547	
HE 1340-0530	13:43:17.88	-05:45:35.8	16.4		33379	163	7.885	0.036	1	0.562	0.01416	
WD 1342-237	13:45:46.58	-23:57:11.0	16.06	EC13429-2342	11124	25	8.211	0.009	1	0.711	0.01094	ZZ Ceti; Shallow cores
WD 1344+106	13:47:24.45	+10:21:36.6	15.08	G063-054, LHS 2800	7617	9	8.678	0.018	2	1.016	0.00764	Cool, bad fit; Zuckerman et al. 2003: 6945 K, log g = 7.99
WD 1348-273	13:51:22.84	-27:33:59.1	15	LP846-53, LTT5382	9853	11	7.831	0.015	1	0.480	0.01392	
WD 1349+144	13:51:54.06	+14:09:44.2	15.34	PG1349+114, PB4117	17425	28	7.828	0.003	1			DD, double-lined
WD 1350-090	13:53:15.56	-09:16:33.3	14.55	PG1350-090, LP907-037	22902	0	7.501	0.008	1	0.372	0.01795	DAH
WD 1356-233	13:59:07.97	-23:33:28.7	14.96	EC13563-2318	9651	5	8.109	0.007	2	0.642	0.01169	
WD 1401-147	14:03:57.16	-15:01:10.4	15.67	EC14012-1446	11680	19	8.114	0.006	2	0.650	0.01170	ZZ Ceti; Shallow cores
WD 1403-077	14:06:04.86	-07:58:31.0	15.82	PG1403-077, EUVEJ1406-07.	47500	261	7.919	0.017	1	0.602	0.01410	
HE 1407+0033	14:10:20.73	+00:18:54.6	15.55	PG	35006	82	5.541	0.012	2			sdB
WD 1410+168	14:12:27.89	+16:35:40.5	15.7	LP439-387	20258	49	7.655	0.009	1	0.428	0.01611	
HS 1410+0809	14:13:06.56	+07:55:23.5	15.5		15114	156	8.393	0.015	1	0.838	0.00963	
WD 1411+135	14:13:58.22	+13:19:19.3	16.2	US9369	18291	50	8.215	0.009	2	0.726	0.01100	
WD 1412-109	14:15:07.75	-11:09:24.2	15.86		25760	50	7.82	0.007	2	0.515	0.01461	
HE 1413+0021	14:16:00.21	+00:07:59.3	16.03		13817	83	8.072	0.008	2	0.628	0.01206	
HE 1414-0848	14:16:52.07	-09:02:03.8	16.15		9823	7	7.867	0.01	2			DD, double-lined
HE 1415-1942	14:18:20.93	-03:22:54.1	16.32		29913	227	5.611	0.035	1			sdB
WD 1418-088	14:20:54.82	-09:05:08.7	15.36	G124-026	8319	8	8.165	0.013	2	0.676	0.01125	
WD 1420-244	14:23:26.25	-24:43:29.4	16.24	EC14205-2429	21381	59	8.101	0.01	1	0.660	0.01197	
WD 1422+095	14:24:39.24	+09:17:12.7	14.32	GD165, L1124-010	12446	25	7.959	0.005	1	0.558	0.01295	ZZ Ceti; Shallow cores
HE 1423-0119	14:25:51.29	-01:33:17.4	16.36	PG1423-013	42415	589	5.516	0.032	1			sdO
WD 1426-276	14:29:27.38	-27:51:01.3	15.92	EC14265-2737	17466	35	7.623	0.007	1	0.406	0.01628	
HE 1429-0343	14:32:03.15	-03:56:37.8	15.84		11731	53	7.924	0.014	1	0.536	0.01322	ZZ Ceti
HS 1430+1339	14:33:05.47	+13:26:32.4	16.1		10165	16	8.331	0.016	2	0.791	0.01004	
WD 1425-811	14:33:08.92	-81:20:12.6	13.75	L19-2, BPM00784	12466	25	8.188	0.004	1	0.698	0.01114	ZZ Ceti; Shallow cores
WD 1431+153	14:34:06.80	+15:08:17.9	15.8	HS 1431+1521, PG1431+153	12634	28	7.969	0.007	2	0.564	0.01287	NOV (Gianninas et al. 2005)
HS 1432+1441	14:35:20.85	+14:28:41.3	16	GD167, GEN#	16176	51	7.841	0.01	1	0.502	0.01408	
WD 1434-223	14:37:14.74	-22:31:16.0	16.37	EC14343-2218	27418	135	7.346	0.021	1	0.325	0.02009	
HE 1441-0047	14:44:33.85	-00:59:59.5	16.4	WDJ1444-0059, SDSS	12658	81	8.123	0.016	2	0.657	0.01164	NOV (Mukadam et al. 2004a)
HS 1447+0454	14:50:09.91	+04:41:45.7	15.6		12631	28	8.014	0.006	1	0.590	0.01251	
WD 1448+077	14:50:49.46	+07:33:32.9	15.46	G136-022, LP561-013	15003	20	7.806	0.006	1	0.481	0.01435	
HE 1448-0510	14:51:13.13	-05:23:16.9	14.42	PG	34244	78	5.572	0.017	1			sdB

Table A.1 continued

Object	RA	DE	mag	Aliases	T_{eff} [K]	$\sigma(T_{\text{eff}})$ [K]	log g	$\sigma(\log g)$	Spectra	M [M_{\odot}]	R [R_{\odot}]	Comments
WD 1449+168	14:52:11.37	+16:38:03.5	15.44	PG1449+168	21658	54	7.789	0.009	1	0.491	0.01479	
WD 1451+006	14:53:50.48	+00:25:29.3	15.19	GD173, GR297	26114	44	7.902	0.006	1	0.557	0.01382	
WD 1457-086	14:59:52.99	-08:49:29.5	15.77	EC14572-0837, PG1457-086	20703	38	7.868	0.007	2	0.528	0.01400	
WD 1500-170	15:03:14.45	-17:11:56.7	15.27	EC15004-1700	31737	25	7.909	0.004	2	0.571	0.01388	
WD 1501+032	15:04:23.92	+03:02:30.5	15.43	PG1501+032	13154	52	8.043	0.007	1	0.608	0.01228	
WD 1503-093	15:06:19.44	-09:30:20.9	15.15	EC15036-0918	12721	20	8.054	0.004	2	0.614	0.01219	
WD 1507+220	15:09:39.99	+21:50:15.5	15	PG1507+220	19656	27	7.797	0.005	2	0.491	0.01464	
WD 1507+021	15:09:56.98	+01:56:07.5	16.49	PG1507+021	19602	56	7.778	0.01	1	0.481	0.01483	
WD 1507-105	15:10:29.08	-10:45:19.8	15.42	GD176	10147	8	7.568	0.008	1	0.348	0.01617	NOV (Gianninas et al. 2005)
HE 1511-0448	15:14:12.97	-04:59:33.9	15.41	PG1511-048	49888	160	7.585	0.011	2			DD, single-lined (Nelemans et al. 2005)
WD 1511+009	15:14:21.31	+00:47:52.3	15.87	PG1511+009, LB769	27541	79	7.741	0.013	1	0.482	0.01549	
HE 1512-0331	15:14:50.13	-03:42:50.6	16.13	WD 1512-035, PG1512-035	86621	1246	6.931	0.043	2			sdO
HE 1513-0432	15:16:19.17	-04:43:58.0	15.69	PG1513-045	41428	306	6.068	0.021	1			sdO
WD 1515-164	15:18:35.07	-16:37:29.2	16.03	EC15157-1626	13483	45	7.933	0.005	2	0.545	0.01320	
HS 1517+0814	15:20:06.00	+08:03:27.4	15.9		12463	34	7.832	0.009	1	0.488	0.01402	
HE 1518-0344	15:20:46.03	-03:54:52.2	16.03		28591	68	7.726	0.014	1	0.478	0.01569	
HE 1518-0020	15:21:30.87	-00:30:54.7	15.25		15455	32	7.95	0.004	1	0.559	0.01311	
HE 1522-0410	15:25:12.26	-04:21:29.3	16.36		10398	15	8.063	0.014	1	0.615	0.01206	
HS 1527+0614	15:29:41.47	+06:04:01.9	15.9		14326	58	7.776	0.009	1	0.465	0.01460	
WD 1527+090	15:29:50.41	+08:55:46.6	14.29	PG1527+091	20502	15	7.823	0.003	2	0.505	0.01442	
WD 1524-749	15:30:36.64	-75:05:24.2	15.93	L72-91, BPM9518	22709	61	7.6	215.38	1	0.412	0.01684	
WD 1531+184	15:33:49.31	+18:18:55.4	16.2	GD186	12752	50	7.866	0.01	1	0.506	0.01374	NOV (Gianninas et al. 2005)
WD 1531-022	15:34:06.08	-02:27:07.3	14.03	GD185, BPM77964	18774	18	8.292	0.004	2	0.777	0.01041	
WD 1532+033	15:35:09.96	+03:11:13.9	16.02	PG1532+034	65691	543	7.823	0.023	1	0.591	0.01560	
WD 1537-152	15:40:23.77	-15:23:43.2	15.9	EC15375-1514	17040	13	7.905	0.009	1	0.539	0.01355	
WD 1539-035	15:42:14.15	-03:41:31.4	15.2	GD189, PG1539-035	9964	7	8.1	0.01	1	0.637	0.01177	
WD 1543-366	15:46:58.23	-36:46:44.1	15.81	RE1546-364, EUVEJ1546-367	41903	116	8.916	0.01	2	1.169	0.00614	
WD 1544-377	15:47:30.00	-37:55:08.8	12.72	CD-37D6571B, L481-060	10402	6	8.05	0.005	1	0.606	0.01217	NOV (Gianninas et al. 2005)
WD 1547+057	15:49:34.93	+05:35:15.9	15.92	PG1547+057	24099	51	8.295	0.006	2	0.786	0.01044	
WD 1547+015	15:49:44.93	+01:25:55.1	15.9	PG1547+016	75585	561	7.612	0.021	2	0.538	0.01895	
WD 1548+149	15:51:15.52	+14:46:58.3	15.06	PG1548+149	20838	57	7.865	0.009	1	0.527	0.01404	
WD 1550+183	15:52:26.38	+18:10:18.8	14.83	GD194, LTT14705	13666	108	8.415	0.017	1	0.851	0.00946	NOV (Gianninas et al. 2005)
WD 1555-089	15:58:04.83	-09:08:06.9	14.8	G152-B4B, EG174	13143	60	7.929	0.007	1	0.542	0.01322	NOV (Gianninas et al. 2005)
WD 1609+135	16:11:25.67	+13:22:17.1	15.1	G138-008, LHS 3163	9418	6	8.571	0.009	1	0.949	0.00835	
WD 1609+044	16:11:49.11	+04:19:38.0	15.22	PG1609+045	29567	21	7.763	0.005	2	0.496	0.01532	
HS 1609+1426	16:12:06.51	+14:19:05.8	16.1		12483	46	7.955	0.011	1	0.555	0.01299	
WD 1614+136	16:16:52.31	+13:34:21.5	15.24	PG1614+137	21495	34	7.201	0.006	1	0.238	0.02101	
WD 1614+160	16:17:08.79	+15:54:37.8	16.08	PG1614+160	17567	23	7.85	0.004	2	0.511	0.01406	
HS 1614+1136	16:17:09.44	+11:29:01.8	16.4		13659	130	8.151	0.015	1	0.677	0.01144	
WD 1614-128	16:17:28.02	-12:57:45.6	15	G153-040, LTT6494	15997	6	7.754	0.006	1	0.459	0.01488	
WD 1615-154	16:17:55.24	-15:35:52.7	13.4	G153-041, LP744-040	29381	14	8.007	0.003	2	0.619	0.01291	
HS 1616+0247	16:19:18.91	+02:40:14.1	16		18059	44	8.05	0.008	1	0.623	0.01233	
WD 1619+123	16:22:03.92	+12:13:32.0	14.57	PG1619+123	16308	33	7.689	0.007	1	0.430	0.01552	
WD 1620-391	16:23:33.87	-39:13:47.9	10.97	CD-38D10980	24645	14	7.936	0.002	1	0.572	0.01347	
WD 1636+057	16:38:54.53	+05:40:40.1	15.76	G138-049, LHS 3230	8799	11	8.552	0.015	1	0.937	0.00848	Cool object, bad fit
WD 1640+113	16:42:54.87	+11:16:40.6	16.03	PG1640+114	19330	14	7.897	0.008	1	0.541	0.01370	
HS 1641+1124	16:43:54.12	+11:18:50.2	16.1		12209	33	7.962	0.007	2	0.559	0.01292	
HS 1646+1059	16:48:40.74	+10:53:52.8	16.1		19430	40	7.756	0.007	2	0.471	0.01504	
HS 1648+1300	16:51:02.78	+12:55:12.7	15.6		17650	23	7.719	0.005	1	0.448	0.01531	
WD 1655+215	16:57:09.84	+21:26:48.4	14.04	G169-34, LHS 3524	9304	4	8.067	0.007	2	0.615	0.01201	
HS 1705+2228	17:07:08.03	+22:24:30.0	14.4		15861	13	7.864	0.007	1	0.513	0.01386	
WD 1716+020	17:18:35.27	+01:56:51.4	14.26	WOLF672A, G019-020	12637	32	7.767	0.005	1			NOV3.4 (Kepler et al. 1995)
WD 1736+052	17:38:41.72	+05:16:06.3	15.89	GR140-002, GR371	9101	7	8.175	0.011	2	0.684	0.01118	
WD 1755+194	17:57:38.92	+19:24:18.5	15.91	GD370, GR548	24490	49	7.855	0.007	2	0.530	0.01423	
WD 1802+213	18:04:23.53	+21:21:02.5	15.77	GD372, GR496	16339	41	7.667	0.008	2	0.420	0.01574	
WD 1824+040	18:27:13.13	+04:03:45.9	13.9	G021-015, ROSS137	14187	17	7.39	0.003	1			DD, single-lined (Morales-Rueda et al. 2005)
WD 1826-045	18:29:09.87	-04:29:36.5	14.57	G021-016, L0993-018	9204	6	8.098	0.01	1	0.634	0.01177	
WD 1827-106	18:30:39.60	-10:37:00.9	14.25	G155-019, EG177	13371	15	7.707	0.002	2			NOV (Gianninas et al. 2005)
					12697	13	7.683	0.006				
WD 1834-781	18:42:25.50	-78:05:06.4	15.45	L44-95, BPM11593	17272	22	7.781	0.004	2	0.476	0.01469	
WD 1840+042	18:43:25.83	+04:20:20.6	14.92	GD215, EG225	8911	5	8.06	0.009	2	0.609	0.01206	
WD 1847-223j	18:47:56.57	-22:19:37.9	13.90		32411	39	8.115	0.007	1	0.685	0.01200	
WD 1857+119	18:59:49.27	+11:58:39.8	15.52	G141-054, EG128	9868	13	7.981	0.014	1	0.564	0.01270	
WD 1911+135	19:13:38.77	+13:36:26.3	14	G142-B2A, EG130	13395	48	7.968	0.006	1	0.565	0.01290	NOV (Gianninas et al. 2005)

Table A.1 continued

Object	RA	DE	mag	Aliases	T_{eff} [K]	$\sigma(T_{\text{eff}})$ [K]	$\log g$	$\sigma(\log g)$	Spectra	M [M_{\odot}]	R [R_{\odot}]	Comments
WD 1914+094	19:16:50.53	+09:34:46.5	15.43	KPD1914+0929	32945	61	7.731	0.014	1	0.490	0.01578	
WD 1914-598	19:18:44.85	-59:46:33.5	14.39	HK22891-122	19161	36	7.752	0.006	1	0.468	0.01506	
WD 1918+110	19:20:35.29	+11:10:43.3	16.23	GD218	19392	54	7.834	0.01	1	0.508	0.01428	
WD 1919+145	19:21:40.51	+14:40:40.5	12.94	GD219, BPM94172	15108	12	8.078	0.001	1	0.634	0.01204	
WD 1932-136	19:35:42.05	-13:30:07.8	15.95	L852-037, LP753-005	16580	41	7.736	0.009	1	0.452	0.01508	
WD 1943+163	19:45:31.73	+16:27:38.8	13.99	G142-50, LTT15765	19495	24	7.86	0.004	1	0.522	0.01404	
WD 1948-389	19:52:19.69	-38:46:13.6	14.63	HK22964-60	38050	87	8.06	0.013	1	0.662	0.01256	
WD 1950-432	19:53:47.72	-43:07:13.6	14.86	MCT	40571	280	7.585	0.025	1	0.451	0.01791	
WD 1952-206	19:55:46.99	-20:31:02.9	15	L709-20, LTT7873	13409	41	7.88	0.004	2	0.516	0.01364	NOV (Gianninas et al. 2005)
WD 1952-584	19:56:12.99	-58:20:49.0	16.06	HK22873-42	33539	49	7.735	0.011	2	0.493	0.01576	
WD 1953-011	19:56:29.21	-01:02:32.2	13.69	G092-040, L0997-021	8166	10	8.618	0.022	1	0.979	0.00804	DAH; Cool, bad fit
WD 1953-715	19:58:38.64	-71:23:43.6	15.15	L80-56, LTT7875	18942	26	7.896	0.005	1	0.539	0.01370	
WD 1959+059	20:02:12.92	+06:07:35.4	16.41	GD226	11033	20	8.231	0.009	1	0.725	0.01079	ZZ Ceti
WD 2004-605	20:09:05.83	-60:25:43.9	13.33	RE2009-602, EUVEJ2009-604	41460	77	8.214	0.007	1	0.757	0.01124	
WD 2007-219	20:10:17.48	-21:46:46.0	14.4	L710-30, LTT7983	9858	4	8.032	0.005	2	0.594	0.01229	
WD 2007-303	20:10:56.82	-30:13:06.7	12.18	LTT7987	15275	14	7.899	0.001	1	0.531	0.01354	
WD 2014-575	20:18:54.88	-57:21:33.8	13	RE2018-572, EUVEJ2018-573	26209	30	7.849	0.004	1	0.530	0.01434	
WD 2018-233	20:21:28.71	-23:08:30.4	14.4	HK22955-37	15380	28	7.895	0.003	2	0.529	0.01358	
WD 2020-425	20:23:59.57	-42:24:26.7	14.87	RE2023-422, EUVEJ2024-424	28412	26	8.145	0.005	2			DD, double-lined
WD 2021-128	20:24:42.94	-12:41:48.4	14.2	HK22950-122	20564	45	7.812	0.009	1	0.500	0.01453	
WD 2029+183	20:32:02.91	+18:31:15.1	16.31	GD230	12950	37	7.814	0.007	2	0.480	0.01420	NOV (Gianninas et al. 2005)
WD 2032+188	20:35:13.84	+18:59:21.8	15.34	GD231, BPM95701	17299	30	7.25	0.007	1			DD, single-lined (Morales-Rueda et al. 2005)
WD 2039-202	20:42:34.64	-20:04:35.6	12.33	LTT8189, L711-010	18784	16	7.674	0.003	1	0.432	0.01584	
WD 2039-682	20:44:21.35	-68:05:21.4	13.25	L116-79, LTT8190	16697	22	8.359	0.003	1	0.818	0.00989	
HS 2046+0044	20:48:38.26	+00:56:00.8	15.9		27026	75	7.797	0.011	1	0.507	0.01488	
WD 2046-220	20:49:46.18	-21:54:43.1	15.48	HK22880-124	22917	45	7.841	0.007	1	0.519	0.01432	
WD 2051+095	20:53:43.18	+09:41:14.5	16.2	LP516-013, HS 2051+0929	15464	49	7.881	0.002	1	0.521	0.01370	
WD 2051-208	20:54:42.76	-20:39:25.9	15.06	HK22880-134	20413	0	8.979	0.004	1	1.197	0.00574	DAH; New magnetic; Linear fit, no quadratic termination
HS 2056+0721	20:58:45.03	+07:33:37.5	15.3		27130	28	8.346	0.004	2	0.822	0.01007	
WD 2056+033	20:58:46.84	+03:31:49.4	16.26	PG2056+033	51542	211	7.711	0.015	2	0.521	0.01666	
HS 2058+0823	21:01:13.36	+08:35:09.1	14.7	RXS	36936	83	7.871	0.01	1	0.561	0.01438	
WD 2058+181	21:01:16.50	+18:20:55.4	15	GD232, GR279	16880	24	7.769	0.005	2	0.469	0.01478	
HS 2059+0208	21:01:47.77	+02:20:27.6	16.5		18124	70	7.785	0.013	1	0.481	0.01469	
WD 2059+190	21:02:02.68	+19:12:57.5	16.36	G144-51, GR377	7470	22	8.881	0.047	1	1.136	0.00637	Cool, bad fit; Linear fit; Bergeron et al. (2001): 6840 K, $\log g = 7.86$
HS 2108+1734	21:10:59.52	+17:46:32.8	15.2	(RXS)	28898	40	8.424	0.008	1	0.873	0.00949	
WD 2105-820	21:13:16.52	-81:49:14.3	13.5	L24-52, LTT8381	10206	9	8.071	0.007	1	0.619	0.01200	DAH
WD 2115+010	21:17:33.58	+01:15:47.1	15.6	PG2115+011	25393	37	7.746	0.005	2	0.480	0.01536	
WD 2115-560	21:19:36.60	-55:50:15.6	14.28	L212-19, BPM27273	9659	8	8.035	0.009	1	0.595	0.01226	
WD 2120+054	21:22:34.98	+05:42:38.8	16.38	PG2120+055	36069	84	7.743	0.011	2	0.501	0.01575	
WD 2122-467	21:25:30.19	-46:30:36.8	16.13	HE 2122-4643, MCT	16071	52	8.015	0.011	1	0.598	0.01257	
WD 2127-221j	21:27:43.21	-22:11:48.9	14.70		47411	129	7.757	0.009	2	0.531	0.01594	
HS 2130+1215	21:33:01.47	+12:28:30.4	16.3		33786	106	7.844	0.024	1	0.543	0.01459	
HS 2132+0941	21:34:50.91	+09:55:19.0	15.8		12963	71	7.627	0.011	1	0.391	0.01591	
HE 2133-1332	21:36:16.18	-13:18:33.0	13.94		9836	4	7.493	0.007	2	0.308	0.01676	
WD 2134+218	21:36:36.15	+22:04:32.8	14.45	GD234, EG227	17179	20	7.821	0.004	2	0.495	0.01431	
WD 2136+229	21:38:46.21	+23:09:20.9	15.25	G126-18, GR582	10062	7	7.937	0.006	1	0.539	0.01306	NOV (Gianninas et al. 2005)
HE 2135-4055	21:38:49.70	-40:41:28.9	13.43		19004	20	7.957	0.004	1	0.572	0.01315	
WD 2137-379	21:40:18.48	-37:42:46.7	16.03	HE 2137-3756	21180	79	7.781	0.013	1	0.486	0.01485	
HS 2138+0910	21:41:03.02	+09:23:45.4	15.9		9339	6	7.682	0.011	2	0.402	0.01513	
WD 2139+115	21:41:28.37	+11:46:22.1	15.8	GD235, GR280	15526	15	7.969	0.003	2	0.570	0.01295	
HE 2140-1825	21:43:42.73	-18:11:32.6	16.04		13153	21	7.677	0.003	1	0.415	0.01545	
WD 2146-433	21:49:38.96	-43:06:14.4	15.81	HK22951-67, MCT	81638	1245	7.994	0.038	1	0.689	0.01383	
HS 2148+1631	21:51:14.54	+16:45:23.1	15.9		15845	11	7.767	0.001	2	0.465	0.01475	
HE 2148-3857	21:51:19.23	-38:43:04.5	16.27		26895	90	7.876	0.014	1	0.545	0.01409	
WD 2149+021	21:52:25.43	+02:23:17.8	12.72	G093-048, EG150	17243	12	7.833	0.003	1	0.501	0.01420	
WD 2150+021	21:53:30.29	+02:23:11.6	16.4	PG2150+021	41597	164	7.767	0.014	2	0.523	0.01565	
WD 2152-045	21:54:41.18	-04:18:18.0	15	HK22965-20	19777	45	7.423	0.009	1	0.327	0.01851	
WD 2151-307	21:54:53.38	-30:29:19.6	14.82	RE2154-302, EUVEJ2154-304	28485	23	8.234	0.004	2	0.754	0.01096	
WD 2156-546j	21:56:21.32	-54:38:24.1	14.50		44401	107	7.8	0.01	1	0.543	0.01535	
WD 2153-419	21:56:35.32	-41:42:17.0	15.89	HE 2153-4156, REJ2156-414	47240	234	8.038	0.016	1	0.663	0.01289	
WD 2154-061	21:57:29.92	-05:51:54.8	15.1	HK22965-8, PB7026	36465	104	7.753	0.012	1	0.507	0.01565	
HE 2155-3150	21:58:46.08	-31:36:06.5	16.06		15971	51	8.058	0.006	2	0.623	0.01222	

Table A.1 continued

Object	RA	DE	mag	Aliases	T_{eff} [K]	$\sigma(T_{\text{eff}})$ [K]	log g	$\sigma(\log g)$	Spectra	M [M_{\odot}]	R [R_{\odot}]	Comments
WD 2157+161	21:59:34.35	+16:25:39.0	16.2	GD272, GR282	18639	37	7.913	0.007	1	0.547	0.01353	
HE 2159-1649	22:02:20.82	-16:34:38.3	15.9		18820	36	7.787	0.007	1	0.484	0.01471	
WD 2159-414	22:02:28.57	-41:14:30.6	15.88	HE 2159-4129, EUVEJ2202-41.	56186	248	7.741	0.013	2	0.542	0.01641	
WD 2200-136	22:03:35.63	-13:26:49.9	15.36	HE 2200-1341	25141	56	7.637	0.008	1	0.433	0.01654	
HE 2200-1341	22:03:35.63	-13:26:50.0	15.31	BPSCS22892-0017	24305	0	7.616	0.006	0 2			
WD 2159-754	22:04:21.27	-75:13:25.9	15.06	LHS 3572, BPM14525	9194	4	8.78	0.007	2	1.077	0.00700	
HE 2203-0101	22:06:02.44	-00:46:33.5	15.82	(PB5070)	17299	28	7.813	0.006	2	0.492	0.01439	
WD 2204+071	22:07:16.20	+07:18:36.0	15.86	PG2204+071	24290	66	7.936	0.009	1	0.571	0.01346	
WD 2205-139	22:08:29.60	-13:41:13.2	15.08	HE 2205-1355	24965	42	8.246	0.005	1	0.756	0.01083	
HE 2205-1355	22:08:29.60	-13:41:13.2	14.71	BPSCS22892-0038	25226	59	8.206	0.008	1	0.731	0.01115	
WD 2207+142	22:09:47.19	+14:29:46.6	15.61	G018-034, LTT16482	8001	21	8.507	0.037	1	0.906	0.00879	Cool, bad fit; Zuckerman et al. (2003): 7899 K, log g = 8.34
HE 2208+0126	22:10:45.47	+01:41:35.4	15.26	(PB5096)	24025	78	5.552	0.008	1			sdB
HE 2209-1444	22:12:18.05	-14:29:48.0	15.32	WD 2209-147, NLTT53177, ...	8290	0	8.191	0.03	1			DD, double-lined (Karl et al. 2003)
HS 2210+2323	22:12:53.48	+23:38:00.4	15.7		23015	42	8.291	0.006	2	0.782	0.01046	
WD 2211-495	22:14:11.93	-49:19:27.1	11.7	RE2214-491, EUVEJ2214-493	63321	195	7.521	0.008	1	0.483	0.01996	
HS 2216+1551	22:18:57.15	+16:06:56.9	15.7		15963	6	7.829	0.005	2			
HE 2218-2706	22:21:23.91	-26:50:55.2	14.89		14299	70	7.804	0.005	1	0.478	0.01434	
HE 2220-0633	22:22:44.44	-06:17:54.9	15.97	(PHL243)	15502	13	7.979	0.004	2			
					12423	29	8.014	0.006	2			
HS 2220+2146b	22:23:01.64	+22:01:31.0	15		18234	39	8.257	0.007	2	0.753	0.01067	
HS 2220+2146	22:23:01.74	+22:01:25.0	15		14601	32	8.08	0.012	1	0.634	0.01201	
WD 2220+133	22:23:13.95	+13:38:55.5	15.6	PG2220+134	22418	36	8.304	0.005	1	0.790	0.01035	
HE 2221-1630	22:24:17.51	-16:15:47.0	16.18	(PHL5103)	9975	8	8.183	0.009	1	0.690	0.01114	
HS 2225+2158	22:28:11.47	+22:14:15.1	15.3		25892	59	7.851	0.008	1	0.531	0.01431	
WD 2226+061	22:29:08.66	+06:22:46.3	14.7	GD236, LP580-021	16100	26	7.714	0.005	1	0.441	0.01527	
WD 2226-449	22:29:19.47	-44:41:39.4	15.5	HK22960-99	12801	14	7.793	0.002	2	0.469	0.01438	
HS 2229+2335	22:31:45.45	+23:51:23.9	15.6		19135	46	7.953	0.008	1	0.570	0.01319	
HE 2230-1230	22:33:38.69	-12:15:30.4	16.08	PHL315, GD237	20421	37	7.788	0.006	2	0.488	0.01476	
HE 2231-2647	22:34:02.59	-26:32:21.1	14.96		21052	42	7.704	0.009	1	0.451	0.01563	
HS 2233+0008	22:36:03.20	+00:07:23.9	13.9	(PHL329,RX,EUVE)	24501	20	7.993	0.003	2	0.603	0.01295	
WD 2235+082	22:37:35.56	+08:28:48.5	15.42	PG2235+082	36840	71	7.826	0.008	2	0.540	0.01486	
HE 2238-0433	22:41:04.90	-04:18:09.1	14.3	(PHL372)	16916	89	8.213	0.023	1	0.722	0.01100	very noisy spectra
WD 2240+125.2	22:42:30.33	+12:50:02.2	16.2		13759	101	7.976	0.008	2	0.570	0.01284	
WD 2240+125.1	22:42:31.14	+12:50:04.7	16.5		15293	22	8.001	0.006	1	0.588	0.01267	
WD 2240-045	22:42:44.62	-04:14:15.1	15.21	GD240, FEIGE106	43839	106	7.745	0.011	1	0.518	0.01598	
WD 2240-017	22:43:04.76	-01:27:53.6	16.17	G028-013, PHL386	9215	12	8.098	0.022	1	0.634	0.01177	
HE 2241-3235	22:44:43.23	-32:19:43.7	15.97	WD 2241-325,PHL396,Tons72,EUVE	33135	43	7.934	0.009	1	0.586	0.01367	
HS 2244+2103	22:46:45.28	+21:19:47.7	15.7		24001	55	7.937	0.007	2	0.571	0.01345	
HS 2244+0305	22:47:22.35	+03:21:45.8	16.2	PB5160	59690	540	7.866	0.03	1	0.598	0.01493	
HE 2246-0658	22:48:40.05	-06:42:44.2	14.14	(PB7225)	11371	50	8.186	0.02	1	0.695	0.01114	very noisy spectra
WD 2248-504	22:51:02.02	-50:11:31.8	14.96	L285-14, BPM28016	16235	51	7.898	0.005	1	0.532	0.01358	
HE 2251-6218	22:54:59.62	-62:02:10.2	15.89		17540	48	7.884	0.009	1	0.529	0.01375	
WD 2253-081	22:55:49.49	-07:50:03.3	16.5	G156-064, BD-08D5980B	7552	19	8.909	0.033	1	1.152	0.00619	Cool, bad fit; Bergeron et al. (2001): 6770 K, log g = 8.41
WD 2254+126	22:56:46.26	+12:52:49.9	16	GD244, LP521-049	11678	24	8.099	0.007	2	0.640	0.01181	ZZ Ceti; Shallow cores
HS 2259+1419	23:01:55.18	+14:36:00.	15.8		12278	28	7.993	0.006	2	0.577	0.01267	
WD 2303+017	23:06:13.09	+01:58:51.6	15.76	PG2303+017, PHL400	42013	128	7.812	0.011	2	0.544	0.01515	ZZ Ceti; Shallow cores
WD 2303+242	23:06:17.70	+24:32:07.5	15.29	PG2303+243, KR Peg	11305	18	8.058	0.006	1	0.614	0.01213	ZZ Ceti
WD 2306+130	23:08:30.58	+13:19:22.7	15.1	PG2306+131, KUV23060+1303	12746	25	7.964	0.005	1	0.561	0.01292	NOV (Gianninas et al. 2005)
WD 2306+124	23:08:35.07	+12:45:39.0	15.23	PG2306+125, KUV23061+1229	19857	39	7.959	0.006	1	0.575	0.01316	
WD 2308+050	23:11:18.05	+05:19:27.9	16.02	PG2308+050, PB5280	36592	102	7.759	0.013	1	0.509	0.01559	
WD 2309+105	23:12:21.71	+10:47:02.8	13	GD246, BPM97895	55593	165	7.859	0.008	1	0.588	0.01493	
WD 2311-260	23:13:53.20	-25:48:49.0	16.05	GD1636, TONS094	47598	375	7.82	0.029	1	0.557	0.01520	
WD 2312-356	23:15:34.95	-35:24:51.8	15.2	HK22888-32	14085	38	7.803	0.006	1	0.477	0.01434	
WD 2314+064	23:16:50.36	+06:41:27.6	15.93	PG2314+064, PB5312	17281	26	7.792	0.005	1	0.481	0.01459	
HE 2315-0511	23:18:04.31	-04:54:45.7	15.37	(PHL444)	33316	92	7.74	0.02	1	0.494	0.01570	
WD 2318+126	23:20:31.30	+12:58:14.5	16.1	HS 2318+1241, LP582-41	12323	53	8.003	0.009	1	0.583	0.01259	
WD 2318-226	23:21:26.43	-22:20:22.5	16.05	GD1648, PHL475	29779	59	7.832	0.012	1	0.529	0.01460	
WD 2321-549	23:24:30.85	-54:41:35.5	15.2	HE 2321-5458, RE J2324-544	44773	96	7.923	0.01	1	0.600	0.01400	
WD 2322+206	23:24:35.22	+20:56:33.9	15.59	PG2322+207	12598	27	7.932	0.005	1	0.543	0.01318	NOV (Gianninas et al. 2005)
WD 2322-181	23:25:18.40	-17:51:57.8	15.38	G273-040, LP822-081	20579	37	7.8	0.006	1	0.494	0.01464	
WD 2324+060	23:26:44.55	+06:17:41.4	15.38	PG2324+060, PB5379	15892	7	7.877	0.004	1	0.520	0.01375	
WD 2326+049	23:28:47.74	+05:14:53.5	13.1	G029-038, LTT16907	11641	8	8.141	0.003	1	0.667	0.01149	ZZ Ceti; Shallow cores
WD 2328+107	23:30:41.79	+11:02:05.0	15.53	PG2328+108, KUV23282+1046	21863	25	7.743	0.005	1	0.470	0.01526	

Table A.1 continued

Object	RA	DE	mag	Aliases	T_{eff} [K]	$\sigma(T_{\text{eff}})$ [K]	$\log g$	$\sigma(\log g)$	Spectra	M [M_{\odot}]	R [R_{\odot}]	Comments
WD 2329–332	23:32:10.90	–33:01:08.1	16.26	HE 2329–3317, GD1670	20162	67	7.883	0.011	2	0.535	0.01385	
WD 2330–212	23:32:59.48	–20:57:12.1	16.25	HE 2330–2113, PHL559	26631	67	7.461	0.01	2	0.369	0.01870	
WD 2331–475	23:34:02.32	–47:14:27.6	13.42	RE2334–471, EUVEJ2334–472	50360	99	7.877	0.006	2	0.587	0.01461	
WD 2333–165	23:35:36.59	–16:17:42.5	13.8	GD1192, BPM82758	13268	24	7.917	0.002	2	0.536	0.01332	
WD 2333–049	23:35:53.96	–04:42:14.8	15.65	G157–082	10509	8	7.997	0.008	2	0.575	0.01259	Shallow cores; NOV1.9
HE 2334–1355	23:37:30.38	–13:38:33.4	15.64	GD1207, PB7713	30694	29	7.331	0.006	2	0.333	0.02062	
WD 2336–187	23:38:52.78	–18:26:11.9	15.6	G273–097, GR557	8222	8	7.978	0.016	1			
WD 2336+063	23:38:58.25	+06:35:28.6	15.6	PG2336+063, PB5486	16477	14	8.081	0.003	2	0.638	0.01204	
MCT 2343–1740	23:46:25.63	–17:24:10.2	16.12	GD1324	21410	131	7.868	0.02	1	0.530	0.01402	
HE 2345–4810	23:47:46.16	–47:53:42.8	15.99		29485	45	7.262	0.01	1	0.301	0.02132	
MCT 2345–3940	23:48:26.42	–39:23:47.4	16.06		18665	39	7.845	0.007	2	0.512	0.01415	
WD 2347+128	23:49:53.51	+13:06:12.5	16.05	G030–020, GR405	11130	21	8.175	0.006	1	0.687	0.01122	ZZ Ceti; Shallow cores
WD 2347–192	23:50:02.96	–18:59:21.9	16.03	MCT2347–1916, GD1248	26031	54	7.844	0.008	1	0.527	0.01438	
HE 2347–4608	23:50:32.90	–45:51:34.8	16.2		17399	36	7.32	0.008	1	0.269	0.01928	
WD 2348–244	23:51:22.10	–24:08:17.0	15.33	EC23487–2424	11437	14	8.118	0.006	1	0.652	0.01166	ZZ Ceti; Shallow cores
MCT 2349–3627	23:52:08.16	–36:10:40.1	16.41		44777	334	7.515	0.034	1	0.437	0.01911	
WD 2349–283	23:52:23.18	–28:03:15.9	15.54	MCT2349–2819, PHL578	17157	20	7.724	0.004	2	0.449	0.01523	
WD 2350–248	23:53:03.79	–24:32:03.1	15.21	MCT2350–2448, PHL580	28812	23	8.308	0.005	2	0.801	0.01038	
WD 2350–083	23:53:27.63	–08:04:39.5	16.18	G273–B1B, GR558	18315	49	7.818	0.01	1	0.497	0.01439	
WD 2351–368	23:54:18.82	–36:33:55.1	15.1	L505–42, LP936–025	13089	24	7.939	0.004	2	0.548	0.01314	
MCT 2352–1249	23:55:13.68	–12:32:55.1	16.49	PHL584, PB8098	39366	345	7.882	0.045	1	0.571	0.01432	
WD 2353+026	23:56:27.70	+02:57:06.0	15.83	PG2353+027, PB5617	65216	440	7.948	0.018	1	0.644	0.01410	
WD 2354–151	23:57:33.44	–14:54:09.1	15.02	MCT2354–1510, PHL599	35030	37	7.154	0.007	2	0.285	0.02336	
HE 2356–4513	23:58:57.83	–44:57:13.5	15.38		16056	5	7.768	0.004	2	0.466	0.01475	

Appendix B

Fit Results for DA+dM Composite Spectra

The table on the following pages lists the fit results for composite spectra of a DA and a late main-sequence star. In the last column, (a) stands for a negligible degree of contamination of the higher Balmer lines by the companion flux, (b) for a modest and (c) for a strong contamination.

Object names that are printed in boldface indicate new objects without earlier spectroscopy in the literature. Aliases that are given in parentheses indicate earlier detections as blue objects, but not as white dwarfs. The given magnitude is Johnson *V*, unless noted otherwise.

Table B.1: Fit results for DA+dM binaries

Object	RA	DE	V [mag]	Aliases	T_{eff} [K]	$\sigma(T_{\text{eff}})$ [K]	$\log g$	$\sigma(\log g)$	χ^2	Type
HE 0016–4340	00:19:06.10	–43:24:18.5	15.62 B		22878	90	7.546	0.014	0.817	a
WD 0034–211	00:37:24.99	–20:53:43.6	14.53	MCT 0034–2110, LP 852–559	15515	36	7.984	0.013	1.794	b
HE 0105–0232	01:08:06.33	–02:16:53.1	15.77 B	(PB6272)	26389	96	7.944	0.015	0.849	a
WD 0131–163	01:34:24.08	–16:07:08.2	13.98	MCT 0131–1622, PHL 1043	46152	197	7.694	0.014	0.904	b
WD 0137–349	01:39:42.88	–34:42:39.1	15.33	HK 29504–36	16582	28	7.333	0.007	1.196	a
WD 0205+133	02:08:03.59	+13:36:23.9	14.73 mc	PG 0205+134	54535	429	7.497	0.029	0.792	a
WD 0232+035	02:35:07.67	+03:43:55.6	12.25	Feige 24	67086	404	7.377	0.019	4.7164	b ¹
WD 0303–007	03:06:07.21	–00:31:14.3	16.21	HE 0303–0042, KUV 03036–0043	20989	187	7.636	0.033	1.004	b
WD 0308+096	03:10:54.90	+09:49:31.6	15.23 y	PG 0308+096	26419	124	7.915	0.018	2.511	c
HE 0331–3541	03:33:52.53	–35:31:18.9	14.79 B		25391	177	7.543	0.027	1.020	b
WD 0347–137	03:50:14.55	–13:35:13.5	14.0	GD 51, LP 713–034	15493	57	7.965	0.006	0.684	a
HE 0409–3233	04:11:21.14	–32:26:14.9	16.03 B		18203	86	7.753	0.016	0.725	a
WD 0429+176	04:32:23.76	+17:45:02.4	13.93	GH 7–255, HZ9B	18046	60	8.112	0.011	4.051	b
WD 0430+136	04:33:10.59	+13:45:12.4	16.5	KUV 04304+1339	36248	393	7.756	0.045	0.898	a
HE 0523–3856	05:25:28.11	–38:54:12.5	16.07 B		18374	122	7.812	0.021	0.815	b
WD 0718–316	07:20:47.92	–31:47:04.6	15.1	RE 0720–314, EUVE J 0720–317	57568	617	7.940	0.038	2.033	c ²
WD 0933+025	09:35:40.69	+02:21:59.6	15.99 mc	PG 0933+026	21314	110	7.961	0.018	1.841	b
WD 0950+185	09:52:45.80	+18:21:02.9	15.3 mc	PG 0950+186	31168	88	7.644	0.016	0.822	c
WD 1001+203	10:04:04.30	+20:09:22.5	15.35	TON 1150, HS 1001+2023	20823	79	7.733	0.014	0.952	b
WD 1026+002	10:28:34.88	–00:00:29.6	13.83 mc	PG 1026+002, HE 1026+014	17454	62	7.922	0.010	0.737	a
WD 1042–690	10:44:10.63	–69:18:22.9	13.09	BPM 06502, L 101–080	20687	65	7.694	0.010	5.251	a
WD 1049+103	10:52:27.82	+10:03:36.5	15.65 mc	PG 1049+103	19913	57	7.708	0.011	0.728	a
HE 1103–0049	11:06:27.66	–01:05:14.9	16.3 B		18374	122	7.812	0.021	0.815	c
HE 1208–0736	12:11:01.08	–07:52:42.9	15.67 B		26985	118	7.350	0.019	0.415	b
WD 1247–176	12:50:22.13	–17:54:48.2	16.19	EC 12477–1738, HE 1247–1738	19860	93	8.198	0.019	1.064	b
WD 1319–288	13:22:40.46	–29:05:35.0	15.99	EC 13198–2849	10774	18	8.208	0.015	1.210	b
HE 1333–0622	13:36:19.64	–06:37:58.9	16.11 B		21897	88	7.750	0.015	17.506	b
EC 13349–323	13:37:50.77	–32:52:22.5	16.34		39426	262	7.347	0.041	0.858	c
HE 1346–0632	13:48:48.34	–06:47:21.0	16.27 B		21838	238	7.507	0.029	0.851	a
EC 13471–125	13:49:51.95	–13:13:37.5	14.80	WD 1347–129, RXS	17047	11	8.553	0.016	0.817	c
WD 1415+132	14:17:40.22	+13:01:48.6	15.29	US 3974, Feige 93	34006	81	7.277	0.020	5.507	b
EC 14329–162	14:35:45.7	–16:38:17.0	14.89	WD 1432–164, HE 1432–1625	15781	20	8.150	0.007	1.691	b
WD 1436–216	14:39:12.70	–21:50:14.6	15.94	EC 14363–2137, HE 1436–2137	23399	127	7.698	0.021	1.235	c
WD 1458+171	15:00:19.36	+16:59:14.7	16.12 B	PG 1458+172	10138	11	8.271	0.015	4.399	c

Table B.1 continued

Object	RA	DE	V [mag]	Aliases	T_{eff} [K]	$\sigma(T_{\text{eff}})$ [K]	$\log g$	$\sigma(\log g)$	χ^2	type
WD 1541–381	15:45:10.97	–38:18:51.3	14.9	LDS 539B, L 480–085	12083	82	7.830	0.014	0.875	c
HS 1606+0153	16:08:55.22	+01:45:48.6	15.0 B		14574	52	7.743	0.009	0.698	c
WD 1643+143	16:45:39.05	+14:17:42.0	15.38	PG 1643+144	24818	111	7.764	0.017	1.293	b
WD 1646+062	16:49:07.83	+06:08:43.6	15.98 mc	PG 1646+062	28367	81	7.981	0.015	0.821	b
WD 1845+019	18:47:39.09	+01:57:33.5	12.95	LAN 18, KPD 1845+0154	29497	28	7.837	0.006	1.090	a
WD 1844–654	18:49:02.00	–65:25:14.2	15.8 B	HK 22959–81	43162	327	7.724	0.033	1.476	b
HS 2120+0356	21:23:09.53	+04:09:28.3	16.2 B		15657	29	7.888	0.010	0.755	b
HE 2123–4446	21:26:41.88	–44:33:38.8	15.97 B		16300	18	7.801	0.012	0.839	b
HE 2147–1405	21:50:03.69	–13:51:45.9	15.94 B	(PHL 167)	22514	87	7.584	0.015	1.089	b
WD 2151–015	21:54:06.53	–01:17:10.9	14.41	G 093–053, L 1003–016	29497	28	7.837	0.006	1.090	a
HE 2217–0433	22:20:05.80	–04:18:44.5	16.28 B		17232	89	8.055	0.006	1.322	c
WD 2313–330	23:16:02.90	–32:46:41.4	15.74 B	HK 22888–45, MCT	41069	540	7.017	0.040	2.998	b

¹ WD 0232+035 is classified as DAZQO in McCook & Sion (1999) but is a DA+dM binary (Benedict et al. 2000)

² WD 0718–316 is a DAO+dM binary, which was treated like the other binaries.

Appendix C

Helium Atmosphere Fit Results

The table on the following pages lists the fit results for stars with helium-rich model atmosphere fits. As it is described in chapter 5, DBA stars for which two sets of fit results are given have H abundances y that are, according to χ^2 and to a visual inspection, in between two of the employed fixed values of y . The more probable solution (that with slightly lower χ^2) is given first.

There are several spectra in which the H α line is even less pronounced than in the $\log y = 5$ models. A fit for a lower limit hydrogen abundance was derived for these spectra, too, using the models for pure helium atmospheres. These fits are indicated by an entry “*” in the $\log y$ column. It should be noticed that these are nevertheless spectra in which hydrogen is *unambiguously present*.

For DB stars that do not show H in their spectra but have effective temperatures larger than 20 000 K, a fit with $\log y = 5$ models was also carried out, to check the influence that an invisibly small admixture of hydrogen might have on the fit result. These fits are marked by the entry “(5)” in the $\log y$ column.

Aliases that are given in parentheses indicate earlier detections as blue objects, but not as white dwarfs. The given magnitude is Johnson B , unless noted otherwise.

Table C.1: Fit results for stars with He atmosphere fits

Object	RA	DE	B [mag]	Aliases	Type	$\log y$	T_{eff} [K]	$\sigma(T_{\text{eff}})$ [K]	$\log g$	$\sigma(\log g)$	χ^2	M [M_{\odot}]	Comments
HE 0025–0317	00:27:41.71	–03:00:58.3	15.69		DBA	3	18947	29	8.34	0.014	1.276	0.808	
HE 0110–5630	01:12:21.16	–56:14:27.3	15.86		DBAZ	4	18881	38	8.196	0.01	1.3613	0.715	
WD 0119–004	01:21:48.27	–00:10:54.4	16.0 V	G 271–047A, LP 587–044	DB		16205	68	7.791	0.034	1.015	0.477	
WD 0125–236	01:27:44.57	–23:24:49.3	15.42 y	G 274–039, MCT	DBA	5	16796	25	8.081	0.011	1.0073	0.639	3
MCT 0149–2518	01:51:59.62	–25:03:15.1	15.91	PHL 1201	DB		16834	62	7.94	0.025	1.572	0.557	
WD 0158–160	02:00:56.69	–15:46:09.7	14.38	G 272–B2B, MCT	DB		25518	178	7.875	0.012	1.14	0.542	
						(5)	25259	218	7.891	0.012	1.2143		2
HE 0215–0225	02:17:32.67	–02:11:15.0	16.13	(PB6822)	DBA	*	16882	46	7.897	0.019	1.2987	0.601	4
						5	16778	44	8.018	0.02	1.3205		
WD 0249–052	02:52:15.55	–05:02:32.5	16.1	HE 0245–0514, KUV	DB		17908	34	7.992	0.01	0.984	0.589	
WD 0300–013	03:02:53.20	–01:08:34.6	15.56 V	GD 40, GR 384	DBZA	*	15503	43	8.062	0.025	2.5465	0.625	
						5	15806	42	8.378	0.022	2.6173		
HE 0308–5635	03:09:47.84	–56:23:49.6	14.02	WD 0308–565, BPM 17088	DB		18915	25	7.92	0.006	1.305	0.552	
WD 0349+015	03:51:51.65	+01:39:47.6	16.3	KUV 03493+0131	DB		18741	153	7.889	0.04	0.9996	0.535	
HE 0413–3306	04:15:20.63	–32:59:10.0	15.9		DBA	5	17333	62	8.113	0.023	14.5013	0.660	3
						4	18461	72	8.392	0.020	14.5766		
HE 0417–5357	04:19:10.04	–53:50:45.7	15.12	BPM 17731	DB		18733	36	7.942	0.009	0.962	0.563	
HE 0420–4748	04:22:11.38	–47:41:42.3	14.7		DB		27288	212	7.808	0.011	2.284	0.512	
						(5)	27245	219	7.809	0.011	2.3809		2
HE 0423–1434	04:25:51.72	–14:27:52.0	16.21		DB		16904	59	7.794	0.026	0.696	0.481	4
HE 0429–1651	04:32:13.81	–16:45:08.5	15.82		DB+dM		15659	68	7.659	0.028	1.57		4
WD 0503+147	05:06:15.83	+14:48:31.1	13.8 V	KUV 05034+1445	DBA	5	15996	25	8.043	0.013	1.6753	0.614	3
WD 0615–591	06:16:14.48	–59:12:28.1	14.09 V	L 182–61, BPM 18164	DB		16714	33	8.017	0.012	2.28	0.600	
WD 0845–188	08:47:29.52	–18:59:50.7	15.55 V	LP 786–006, L 0748–070	DB		17566	61	7.969	0.02	2.401	0.575	
WD 0853+163	08:56:19.01	+16:11:03.9	15.83 mc	PG 0853+164, LB 8827	DBAH	3	26128	310	8.396	0.014	1.5244	0.853	6
						4	35053	187	8.381	0.017	1.5481		6
WD 0900+142	09:03:31.31	+14:00:49.2	16.48	PG 0900+142	DB		16142	51	8.215	0.024	4.539	0.722	
WD 0921+091	09:23:55.27	+08:57:17.5	16.19 V	PG 0921+092	DBA	5	18691	65	7.951	0.014	2.4443	0.568	3
						4	21294	127	7.939	0.016	2.4632		
WD 0948+013	09:51:02.21	+01:04:32.1	15.89	PG 0948+013	DBA	5	17022	36	7.999	0.013	1.3296	0.591	3
WD 1004–178	10:07:07.91	–18:05:25.8	15.6 V	EC 10047–1750	DB+dM		16357	100	7.7	0.041	1.264		
WD 1046–017	10:48:32.65	–02:01:11.3	15.81 V	GD 124, GR 387	DB		15671	35	8.438	0.034	2.204	0.868	
WD 1115+158	11:18:22.77	+15:33:33.3	16.12	PG 1115+158, DT Leo	DBA	4	21990	145	7.76	0.019	1.4082	0.478	3.5
						5	18593	81	7.842	0.019	1.4308		
WD 1134+073	11:36:54.31	+07:03:35.7	16.32	PG 1134+073	DBAZ	5	18227	81	8.331	0.021	2.8584	0.801	3.8
						*	18379	77	8.249	0.022	2.8691		

Table C.1 continued

Object	RA	DE	B [mag]	Aliases	Type	$\log y$	T_{eff} [K]	$\sigma(T_{\text{eff}})$ [K]	$\log g$	$\sigma(\log g)$	χ^2	M [M_{\odot}]	Comments
WD 1144–084	11:46:54.07	–08:45:48.5	15.95	PG 1144–085	DB		16385	33	7.952	0.015	3.866	0.562	
WD 1149–133	11:51:50.61	–13:37:15.1	16.29 V	EC 11492–1320, PG	DBA	4	18977	65	8.195	0.017	1.88	0.714	
						5	18224	88	8.074	0.020	1.8853		
HE 1207–2349	12:09:36.56	–24:06:19.4	15.79		DBA	5	17415	43	7.928	0.016	2.626	0.552	4
						*	17488	42	7.839	0.017	2.6262		
EC 12438–1346	12:46:30.42	–14:02:40.8	16.39 V		DBA	5	16960	42	7.954	0.021	5.7148	0.565	3
						4	17952	43	8.239	0.020	5.7922		
WD 1252–289	12:54:55.30	–29:11:54.6	15.85 V	EC 12522–2855	DBA	5	19802	79	7.994	0.011	1.1884	0.595	3
						*	21029	135	7.970	0.011	1.1976		
WD 1311+129	13:13:51.35	+12:40:09.4	16.26 mc	PG 1311+129, LP497–114	DBA	3	18823	36	8.068	0.017	1.6212	0.636	
WD 1326–037	13:29:16.37	–03:58:51.8	15.6 V	PG 1326–037	DB		22645	129	7.999	0.012	2.448	0.603	7
						(5)	22192	147	7.995	0.013	2.2931		2
WD 1336+123	13:39:13.63	+12:08:29.6	13.9	LP 498–026	DB		16345	31	7.884	0.015	1.199	0.525	
WD 1338–220	13:41:17.29	–22:19:43.7	16.2	HE 1338–2204, EC 13385–2204	DBA	5	14924	115	8.716	0.063	2.4275		1
HE 1349–2305	13:52:44.26	–23:20:06.5	16.36		DBAZ	5	17875	77	8.09	0.028	2.1106	0.647	
						4	19490	117	8.339	0.023	2.1302		
WD 1352+004	13:55:32.38	+00:11:24.1	15.72	PG 1352+004	DBAZ	5	15348	61	8.644	0.038	136.532		1
WD 1403–010	14:06:19.96	–01:19:32.6	15.9 V	G 064–043, GR 272	DBA	*	16023	37	8.063	0.018	2.5927	0.626	3
						5	18656	71	8.121	0.018	2.6631		
HE 1409–1821	14:11:48.67	–18:35:05.6	15.6		DBA	5	18656	71	8.121	0.018	2.6631	0.617	3
						*	18632	70	8.037	0.02	2.6632		
WD 1421–011	14:24:29.21	–01:22:16.7	15.97	PG 1421–011	DBAZ	4	16884	41	8.048	0.022	4.1279	0.619	3,8
						3	21319	61	8.260	0.020	4.1648		
WD 1428–125	14:31:39.64	–12:48:55.5	715.98 V	EC 14289–1235	DB		21586	129	8.167	0.01	1.174	0.701	
						(5)	21657	135	8.179	0.011	1.1303		2
WD 1444–096	14:47:37.02	–09:50:05.5	14.98 V	EC 14449–0937, PG1444–096	DBA	*	16777	32	7.929	0.014	1.4635	0.551	3
						5	16692	31	8.064	0.015	1.5122	0.515	
WD 1445+152	14:48:14.37	+15:04:49.6	15.55	PG 1445+153	DB		18638	59	7.852	0.015	1.582		
WD 1456+103	14:58:32.74	+10:08:17.6	15.89	PG 1456+103, CW Boo	DBA	3	23237	239	7.852	0.027	1.0474	0.526	5
						4	20680	208	8.125	0.022	1.066		
WD 1542+182	15:44:19.46	+18:06:43.6	14.72 V	GD 190, EG 193	DB		18959	37	7.882	0.01	1.136	0.532	
WD 1557+192	15:59:21.08	+19:04:09.0	15.4 V	KUV 15571+1913	DBA	5	18724	110	8.1	0.026	2.9605	0.655	3
						4	19846	123	8.202	0.023	2.9630		
WD 1612–111	16:15:23.96	–11:18:29.5	15.53 V	GD 198, EG 194	DB		22143	63	8.073	0.005	1.474	0.645	
						(5)	22338	97	8.076	0.008	1.4537		2

Table C.1 continued

Object	RA	DE	B [mag]	Aliases	Type	$\log y$	T_{eff} [K]	$\sigma(T_{\text{eff}})$ [K]	$\log g$	$\sigma(\log g)$	χ^2	$M [M_{\odot}]$	Comments
WD 1654+160	16:56:57.56	+15:56:26.6	16.15	PG 1654+160, V 824 Her	DB	(5)	25447	205	7.846	0.014	8.333	0.527	5
						4	25501	253	7.839	0.014	16.0569		2
WD 1709+230	17:11:55.68	+23:01:01.5	14.9 V	GD 205, BPM 92077	DBAZ	5	19296	68	8.192	0.011	1.2741	0.713	
						5	18468	55	8.084	0.013	1.2975		
WD 2130-047	21:33:34.86	-04:32:24.9	14.5 V	GD 233, L 1002-062	DBA	*	17658	26	7.872	0.009	1.2897	0.523	3
						5	17666	26	7.983	0.009	1.3415		
WD 2142-169	21:45:27.60	-16:43:08.0	14.6	HK 22944-44	DOZ	2	39138	241	7.737	0.019	1.234	0.505	9
WD 2144-079	21:47:37.34	-07:44:13.1	14.82 V	G 026-031, LTT 8702	DBZ		16518	33	7.895	0.014	7.558	0.532	
WD 2154-437	21:58:01.55	-43:28:00.8	15.04 V	L 427-060, BPM 44275	DBA	5	17213	26	8.021	0.01	1.328	0.604	3
WD 2229+139	22:31:45.50	+14:11:13.1	15.99 mc	PG 2229+139, GR 906	DBAZ	5	15390	40	8.186	0.027	3.18		1
WD 2234+064	22:36:42.06	+06:40:16.4	16.26 y	PG 2234+064, GR 907	DB	(5)	20890	132	8.035	0.011	1.4	0.620	2
						4	19864	87	8.028	0.012	1.3442		
WD 2253-062	22:55:47.43	-06:00:51.4	15.06 y	GD 243, EG 230	DBA	5	17598	21	8.051	0.009	1.1407	0.623	
						5	17359	26	7.981	0.010	1.3561		
HE 2334-4127	23:37:38.74	-41:10:32.7	15.61	(LTT 9631)	DBA	*	18364	30	7.957	0.007	1.6203	0.618	4
						5	18275	33	8.041	0.008	1.6208		
WD 2354+159	23:56:34.74	+16:15:39.8	15.78	PG 2354+159	DBZ		18832	40	8.058	0.01	1.32	0.630	
WD 2354-305	23:56:37.07	-30:16:25.4	16.26		DB		18006	87	7.883	0.025	1.03	0.530	

¹ Cool DBA star; the object probably has a lower temperature than given and $\log y > 5$, but only the $\log y = 5$ fit of which the results are given here terminates.

² Fit with $\log y = 5$ models to check the influence of possible admixtures of invisibly small amounts of hydrogen.

³ First reported as a DBA here; previously listed as DB.

⁴ New object or an object which has not been observed spectroscopically before.

⁵ Pulsating DB star

⁶ WD 0853+163 is a magnetic DBA, and thus this is an uncertain fit since the Zeeman-split lines were fitted with a non-magnetic model.

⁷ Beauchamp et al. (1999) list WD 1326-037 as a DAB; however no H is visible in the SPY spectra. A $\log y = 5$ fit has a higher χ^2 than a fit with a pure He model, but Beauchamp assumed $\log y = 2$.

⁸ WD 1134+073 and WD 1421-011 show CaII lines but are not mentioned among the SPY DBZ/DBAZ objects of Koester et al. (2005).

⁹ WD 2142-169 shows a HeI-dominated spectrum with Balmer and HeII 4686 Å lines. It is thus a cool DO star inside the DB gap, see section 7.2. It probably has $\log y > 2$.

Appendix D

List of Objects without a Fit

The table on the following pages lists the objects for which neither a hydrogen nor a helium atmosphere fit was achieved.

The labels 'hot' and 'cool' describe why no fit was obtained for the regarding object; 'hot' objects have temperatures outside of the model grid, and for 'cool' objects, the same might be the case, or they show line broadening that is too strong compared to that of the employed stark-broadening-only models to allow the fit to converge.

An object name printed in bold face indicates an object that has not been observed spectroscopically before or one for which previously unknown spectral features are detected. The given magnitude is Johnson V , unless otherwise noted.

The column " $T_{\text{eff}} (\log g = 8)$ " lists effective temperatures that were obtained from fits in which $\log g = 8$ was kept fixed, and for which only the lines that are visible in the spectra were used, e.g., in some cases only $H\alpha$. Therefore, these are inaccurate results.

Table D.1: Individual listing of objects without a fit

Object	RA	DE	V [mag]	Aliases	Type	Comments	T_{eff} (log $g = 8$)	Literature
HS 0146+1847	01:48:56.76	+19:02:27.4	15.6 B	GD16, LTT10628, Wolf88	DAZB	Peculiar		Koester et al. (2005b)
HE 0309–2105	03:09:47.84	–56:23:49.6	14.02 B		Cool DA	Only weak H α	<5000	Friedrich et al. (2000): DC; Sefako et al. (1999): Weak H β
HE 0414–0434	04:16:52.65	–04:27:23.6	15.7		Cool DBA	log $y \sim 5$	13700	New object
HE 0442–3027	04:44:29.39	–30:21:40.4	16.2 B		DQ			Friedrich et al. (2000): DC or DQ
HE 0449–2554	04:51:53.72	–25:49:14.4	16.5		Cool DZA	Weak H α and CaII only	6100	Koester et al. (2005a): 12200 K ²
HE 1257–2021	13:00:27.33	–20:37:27.5	16.51 B		hot DO			Christlieb et al. (2001): DO or PG1159
HE 1314+0018	13:17:24.74	+00:02:37.1	15.62 B		hot DO			Werner et al. (2004): DO
HE 1349–2320	13:52:15.00	–23:34:58.7	15.14 B		hot He-sdO	HeII lines only		
HE 2149–0516	21:51:43.31	–05:02:45.9	15.3		DAB		5400?	New object
HE 2237–0509	22:39:40.75	–04:54:17.2	14.0		Cool DBA		13100	Friedrich et al. (2000): DB or DBA
HS1031+0343	10:34:30.14	+03:27:36.0	16.5 B		DAH	$B=6.1$ MG	25000	New object
PN 0276+169	17:41:41.00	+03:06:56.1	14.95	DeHt2	hot DO			
PN 0361–571	22:29:38.51	–20:50:13.6	13.58	NGC 7293, WD 2226–210	hot DAO			
PN 2191+312	08:54:13.16	+08:53:53.1	15.6	A31	hot DAO			Napiwotzki et al. (1995): DA or DAO
PN 2580–157	07:14:49.37	–46:57:39.3	17.0	Longmore 3	PG1159			
MCT 0026–2150	00:29:26.14	–21:33:41.7	16.39 B		D+dM	Only dM features: CaI, CaII, MgI, NaI		Schmidt et al. (2001): DA+dM
WD 0000–170	00:03:31.64	–16:43:58.6	14.67	G 266–032, L 0793–018	Cool DBA	First detection of H: Weak H α , log $y < 5$	13800	Wegner & Welan (1987): 11000K; Oke, Weidemann & Koester (1984): 12110K
WD 0000–345	00:02:40.12	–34:13:39.5	14.90		DC			
WD 0038–226	00:41:26.12	–22:21:04.1	14.50	G 268–027, G 266–157	DQ			
WD 0041–102	00:43:45.98	–10:00:26.3	14.47 mc	G 270–048, Feige 7	Peculiar	DABP		
WD 0046+051	00:49:09.97	+05:23:18.0	12.40	G 001–027, WOLF 28	DZ			
WD 0046+077	00:48:37.94	+08:02:44.4	15.59 y	PG 0046+078	hot DO			
WD 0101–182	01:04:15.04	–18:01:45.1	15.87	MCT 0101–1817, PHL 970	hot DO			
WD 0122–753j	01:22:53.26	–75:21:14.3	15.4	RXJ 0122–7521, WD 0121–756	PG1159			Werner et al. (1996): $T_{\text{eff}} = 180000$ K
WD 0123–262	01:25:24.47	–26:00:45.2	14.95	G 269–160, LTT 0784	DC			
WD 0127–311	01:29:56.11	–30:55:09.6	14.51	HE 0127–3110, GD 1363	Cool DB	HeI 5876Å only	14500	Reimers et al. (1996): DAH, Friedrich et al. (2000): DB, 13800 K
WD 0156+155	01:59:39.37	+15:48:47.3	15.80 mc	PG 0156+156	DC			
WD 0200–127	02:03:04.36	–12:29:01.4	14.55	GD 1072	Cool DA	First detection of H, weak H α only	<5000	McCook & Sion (1999): DC; Fey & Bues (1995): Helium-rich, $T_{\text{eff}} \sim 10000$ K
WD 0203–181	02:05:23.98	–17:53:25.8	16.0	HE 0203–1807, G 272–152	Cool DB	Weak lines		McCook & Sion (1999): DC; Putney et al. (1997): DB4
WD 0204–306	02:07:02.28	–30:23:32.2	16.0	LP 885–22	Cool DA	Only H α , H β	6900	Silvestri et al. (2001): 5709 K
WD 0230–144	02:32:37.89	–14:11:50.5	15.76	LHS 1415, LP 710–047	Cool DA	Weak H α & H β only	6600	McCook & Sion (1999): DC; Putney et al. (1997): DA9
WD 0237+115	02:40:06.73	+11:48:27.2	15.76 mc	PG 0237+116	hot DO			
WD 0243–026	02:46:30.80	–02:27:24.7	15.54	LHS 1442, GR 565	Cool DA		7200	Zuckerman et al. (2003): 6798 K, log $g = 8.15$
WD 0322–019	03:25:11.14	–01:49:16.5	16.12	G 077–050, LHS 1547	Cool DZA	Weak H α only	6700	Zuckerman et al. (2003): 5204 K, log $g=8.00$; DD
WD 0341+182	03:44:34.87	+18:26:10.0	15.18	G 6–30, LHS 179	DQ			
WD 0346–011	03:48:50.24	–00:58:33.2	13.99	GD 50, GR 288	DAB	log > 9.0 , outside grid		e.g., Aznar Cuardrado et al. (2004): log $g=9.08$, Napiwotzki et al. (1999): log $g=9.07$
WD 0357+081	04:00:26.67	+08:14:07.0	15.87	G 007–016, LHS 1617	Cool DA	H α only	6800	Zuckerman et al. (2003): 5490 K, log $g = 8.03$
WD 0423+120	04:25:53.83	+12:11:47.0	15.42	G 083–010, LB 1320	DC			
WD 0435–088	04:37:47.47	–08:49:12.8	13.75	LHS 194, LP 655–42	DQ			
WD 0443–275.1	04:45:17.37	–27:26:25.0	15.9	LP 891–013	DQ			1
WD 0504–241	05:06:18.09	–24:04:01.0	15.2 B	HE 0504–2408	hot DO			
WD 0511+079	05:14:03.61	+08:00:14.5	15.89	G 084–041	Cool DA		7100	Zuckerman et al. (2003): 6915 K, log $g = 8.0$
WD 0548–001	05:51:19.58	–00:10:23.6	14.56	G 099–037, LTT 17876	DQ			
WD 0552–041	05:55:09.57	–04:10:07.7	14.45	G 099–044, LP 658–002	DZ			
WD 0553+053	05:56:25.52	+05:21:47.4	14.12	G 099–047, LTT 17891	DAH			Liebert et al. (2003): $T_{\text{eff}} = 5790$ K, $B=20$ MG
WD 0659–063	07:01:55.00	–06:27:48.7	15.27	LHS 1892, LP 661–003	Cool DA		7100	Zuckerman et al. (2003): 6499 K, log $g = 8.6$
WD 0752–676	07:53:07.76	–67:47:32.6	14.08	L 97–12, BPM 04729	Cool DAZ	Weak CaII, stronger H	6600	McCook&Sion (1999): DQ; Bergeron et al. (1997): DZA, 5730 K, log $g=8.21$
WD 0806–661	08:06:53.77	–66:18:18.6	13.71	L 97–3, LTT 3059	DQ			
WD 0913+103	09:16:02.70	+10:11:10.7	15.77 mc	PG 0913+104, LB 3013	DQZ	First detection of CaII		Putney et al. (1997): DQ
WD 0950+139	09:52:59.05	+13:44:33.0	16.05	PG 0950+139	hot DAO			
WD 0959+149	10:01:49.44	+14:41:22.6	15.37	G 042–033, LTT1 2680	DC			
WD 1015+014	10:18:05.09	+01:11:22.7	16.26 mc	PG 1015+014	DAH			Liebert et al. (2003): $T_{\text{eff}} = 14000$ K, $B=90$ MG
WD 1034+001	10:37:03.83	–00:08:19.8	13.19 mc	PG 1034+001	hot DOZ			
WD 1055–072	10:57:35.22	–07:31:24.6	14.33	G 163–027, LTT 4020	DC			
WD 1115–029	11:18:15.10	–03:14:07.3	15.40	G 010–011, L9 71–014	DC			
WD 1142–645	11:45:42.03	–64:50:29.6	11.50	L 145–141, BPM 7108	DQ			
WD 1154+186	11:56:43.87	+18:22:19.7	15.54	G 57–29, LP 434–97	DZ			
WD 1225–079	12:27:47.42	–08:14:37.7	14.84 mc	HE 1225–0758, PG 1225–079	DZAB			Kilkenny et al. (1986): DZA, Christlieb et al. (2001): DBA
WD 1237–230	12:40:24.33	–23:17:44.6	16.5	LHS 339, LP 853–015	Cool DA	Only H α , H β	6600	
WD 1257+037	13:00:09.08	+03:28:41.0	15.9	G 060–054, WOLF 457	Cool DA	Only H α , H β	6900	Zuckerman et al. (2003): 5800 K, log $g = 8.19$
WD 1334+039	13:36:31.99	+03:40:44.6	14.7	G 062–053, WOLF 489	Cool DA	H α only	6500	Zuckerman et al. (2003): 5050 K, log $g = 7.96$
WD 1345+238	13:48:03.05	+23:34:46.5	15.63	LHS 361, LP 380–5	Cool DA	Weak, broad H α only	<5000	McCook & Sion (1999): DC, Bergeron et al. (2001): 4590 K, log $g=7.77$
WD 1503–070	15:05:49.33	–07:14:41.8	15.91	GD 175, EG 190	DAH		6700	Liebert et al. (2003): $T_{\text{eff}} = 6990$ K, $B=2.3$ MG

Table D.1 continued

WD 1520–340	15:23:16.62	–34:12:08.4	14.7 B	LAWD 57, L 551–74	DC	First spectroscopic observation		
WD 1533–057	15:36:34.93	–05:52:40.1	15.33	PG 1533–057	DAH			Liebert et al. (1985): $B=31$ MG
WD 1542–275	15:45:22.57	–27:40:06.4	15.5	LP 916–027	Cool DBA	Weak lines; first observation of H	11000	McCook & Sion (1999): DB
WD 1625+093	16:27:53.57	+09:12:14.8	16.14	G 138–031, GR 327	Cool DA		7300	Bergeron et al. (2001): 6870 K, $\log g = 8.44$
WD 1632+222	16:34:16.09	+22:11:40.9	15.28 B	PG 1632+223	He-sdO	Strong HeI, weak HeII, no hydrogen		McCook & Sion (1999): DB3; Bergeron et al. (2000): sdO
WD 1705+030	17:08:08.01	+02:57:35.5	15.17	G 139–013, GR 494	DZ			
WD 1708–147	17:11:26.81	–14:47:54.4	14.30	L 845–70, LTT 6847	DQZ	First detection of CaII		Weidemann & Koester (1995): DQ
WD 1712+215	17:14:30.50	+21:27:11.1	16.51	G 170–27	DC			
WD 1733–544	17:37:00.76	–54:25:56.9	15.8	L 270–37, LTT 6999	Cool DA		7200	Bergeron et al. (2001): 6520 K, $\log g = 8.13$
WD 1750+098	17:52:55.78	+09:47:51.8	15.72	G 140–B1B, EG 124	DC			
WD 1818+126	18:20:30.95	+12:39:17.0	15.89	G 141–002, LTT 15423	Cool DA	Weak, broad H α only	<5000	Zuckerman et al. (2003): 6340 K, $\log g = 7.29$
WD 1821–131	18:24:04.67	–13:08:42.6	15.6	G 155–015, LHS 3384	Cool DA		6700	Zuckerman et al. (2003): 7029 K, $\log g = 8.38$
WD 1831+197	18:33:58.36	+19:45:53.1	16.45	G184–12	DQ			
WD 1837–619	18:42:28.71	–61:51:54.7	14.90	L 158–53, LTT 7406	DQ	First optical detection of C ₂		McCook & Sion (1999): DC; Wegner (1983): 8500 K, C/He=10 ^{–5} from UV CI lines
WD 1917–077	19:20:34.96	–07:40:00.8	12.28	L 923–021, LTT 7658	Cool DBA	Only H α & HeI 5876Å, 4471Å	<10000	Oswalt et al. (1991): DBQA5, but no C ₂ visible in the SPY spectra
WD 2011+065	20:13:55.72	+06:42:43.8	15.67	G 024–009, LTT 15921	DC			Greenstein (1984): DQ7, Putney (1997): DC
WD 2049–222	20:52:16.86	–22:06:34.2	15.00	HK 22880–126, LP 872–48	DC			
WD 2129+000	21:32:16.39	+00:15:13.3	14.73	LP 638–4, PHL 028	Cool DB		14600	Wegner & Nelan (1987): $T_{\text{eff}} \approx 13000$ K
WD 2140+207	21:42:41.02	+20:59:58.3	13.23	G 126–27, LHS 3703	DQ			
WD 2148–294	21:51:19.17	–29:14:43.4	16.20 B	MCT 2148–294	Hot DO			
WD 2154–512	21:57:38.35	–51:00:31.9	14.68	L 283–7, BPM 27606	DQ			
WD 2207–625	22:11:21.75	–62:17:19.3	15.7 B	HK 22956–84	Hot DOZ	First detection of HeI, HeII, CaII		McCook & Sion (1999): DC
WD 2216–657	22:19:48.29	–65:29:18.4	14.43	L 119–34, LHS 3794	DZ			
WD 2251–070	22:53:53.51	–06:46:56.4	15.65	LHS 69, LP 701–29	DZ			
WD 2253+054	22:55:55.83	+05:45:21.3	15.8	LP581–035, G028–024	Cool DA	Weak Balmer lines	6600	McCook & Sion (1999): DA or DB; no atmosphere parameters in the literature
WD 2253–081	22:55:55.83	+05:45:21.3	15.8	LP 581–035, G 028–024	Cool DA		7200	Bergeron et al. (2001): 6770 K, $\log g = 8.41$
WD 2258+155	23:00:57.75	+15:48:39.8	15.3	PG 2258+155, KUV 22585+1533	He-sdO	HeII and HeI of about equal strength; no hydrogen		Wegner & Dupuis (1993): DB; Kilkenny et al. (1988): sdO
WD 2311–068	23:14:25.23	–06:32:48.7	15.37	G 157–034, PHL 2142	DC			
WD 2312–024	23:15:18.96	–02:09:42.7	16.29	G 157–035, LHS 3917	DZ			
WD 2316–173	23:19:35.39	–17:05:28.8	14.04	G 273–013, L 0791–040	Cool DBA			Weidemann & Koester (1995): 10800 K
WD 2316+123	23:18:45.21	+12:36:01.6	15.29	KUV 0813–14	DAH			Liebert et al. (1985): 10400 K, $B=29$ MG
WD 2322+118	23:24:58.07	+12:07:38.5	16.0	PG 2322+119, KUV 23224+1151	Cool DZA		6600	
WD 2323+157	23:26:06.59	+16:00:18.8	15.11	GD 248, GR 335	Cool DA	Weak, broad H α only	<5000	McCook & Sion (1999): DC; Putney (1997): DA5

¹ WD 0443–275.1 is a DB, but both spectra clearly show carbon band heads and no He lines. Thus, the DQ WD 0443–275.2 must have been observed, although the observation coordinates are that of the DB and not those of the DQ. The most probable explanation is an error in the input coordinates of the SPY observations. The coordinates that are given in the table are that that were observed and are those of the DB according to the SPY input catalog. The alias and magnitude is that of the DQ; the DB is also known as LP891–012 and has $V=15.6$.

² HE 0449–2554 is listed as a DBAZ in Friedrich et al. (1001), but no Helium lines are visible in the SPY spectra; thus this object is classified as a cool DAZ here.

Appendix E

CA 1.23m observation log

The following table lists the log of the observations at the Calar Alto 1.23 m telescope in 2002. The first column gives the starting date of the observation night, and the second and third columns, labeled 'u' and 'l', tabulate the number of used and lost hours of each night, respectively. The reason for the loss of time is listed in the fourth column, where 'CA net' indicates time loss due to connection problems occurring at the observatory, 'Hamburg' and 'software' stand for a connection that was not possible because of net failures at Hamburg observatory or software problems in Kiel, and 'telescope' describes technical problems with the telescope itself. The column 'obs' lists the observers, where 'BV' is Björn Voss, 'DK' is Detlev Koester, 'DS' is Danica Schemionek (now Danica Kröger), and 'MH' is Matthias Hünsch. The last column lists the objects that were observed in each night; those for which no prefix is given are HQS objects. Only objects that were observed for this project are listed, not those that were observed in the same nights for other projects.

Table E.1: CA 1.23 m Observation Log

Date	u [h]	l [h]	Reason	Obs	Observed Objects
08-15	7	2	CA net	BV	G29-38, ZZ Ceti
08-16	9	0.5	CA net	BV	PG2303+242, G226-29
08-17	6	3	CA net	BV	
08-18	9	-		BV	2101+0622,2051+0929,2124+0751,0115+1905
08-19	9	-		DK	
08-20	9	-		DK	0116+0449,2132+0941,2145+2231,2145+2231, 2212+0320,2317+0012
08-21	5	4	Weather	BV	2147+2151,2344+2144
08-22	8	1	Weather	BV	0120+0014,2155+0759,2216+1551,2229+2327 2240+1438,2303+2120,
08-23	-	9	Weather	BV	
08-24	9	-		MH	0125+1335,1606+0153,2105+0943,2226+1738, 2238+1816,2301+0127,2346+1006,2354+1929
08-25	7	2	Weather/net	DK	0148+0013,1607+1436,1711+1716,2117+1514, 2156+0103,2245+0420,2306+1229
08-26	5	4	Hamburg	BV	0103+2253,0132+2214
08-27	3	6	Weather	BV	2206+2248
08-28	6	3	Weather	BV	2316+1250,2346+1303
08-29	9	-		MH	2123+0013,2202+0204,2244+0237
08-30	9	-		BV	0131+0149,2147+0536,2148+1631,2222+2300 2232+2109,2242+1947,2347+1321
08-31	9	-		BV	0145+0950,0157+0855,0201+0712,1641+1124, 2201+1435,2250+0146,2255-0006,2303+0255, 2312+1653,2347+1754
09-01	5	4	Weather	BV	0106+1459,0156+2313,0207+1229,0223+1211, 0246+0607,0325+2142
09-02	9	-		DS	0119+2307,0141+1734,0307+0746,1654+1927, 2303+2106,2327+1837,2354+1126
09-03	8	1.5	CA net	MH	0225+0010,0309+1001,2220+0045,2241+1950
09-04	9	-		BV	0329+1930,0337+0939,0355+1337,1602+1156, 1621+2021,2054+0610,2138+0910
09-05	9	-		BV	0123+2146,0128+0753,0135+0906,0145+1820, 0338+1858,0400+1451,0401+1454,0412+0632, 1610+0533
09-19	5	5	Weather	BV	
09-20	9	1	Weather	BV	
12-23	-	14	Weather	DS	
12-24	-	14	Weather	DK	
12-25	-	14	Software	DS	
12-26	3	11	Weather	DS	
12-27	-	14	Weather	DS	
12-28	12	2	Telescope	BV	0929+0839,0940+1129,1102+0934
12-29	6	6	Weather	DS	0237+1034
12-30	-	14	Weather	BV	
12-31	-	14	Weather	DK	
01-01	-	14	Weather	BV	

Appendix F

Results of the BUSCA Observations: Parameters for 223 New WD

The following table lists the fitted effective temperatures and surface gravities that were derived from the BUSCA $u - b$ vs. $b - I$ photometry data. Several objects are placed outside the model atmosphere grid and are labeled “no white dwarf”. Some of these are found at only slightly redder $u - b$ colours than the $\log g = 7.0$ model atmospheres, and thus at only slightly lower surface gravities. These objects might either be white dwarfs which are only placed at such low gravities due to high $\log g$ uncertainties, or objects with low gravities similar to $\log g = 6.0$, e.g., subdwarf stars; these stars are labeled as “subdwarf?”. No parameters are given for such objects outside the model atmosphere grid, except for some cool objects that are placed near the cool end of the grid (i.e., around $T_{\text{eff}} = 6000$ K) which might be cool white dwarfs. For some cool and hot object exceedingly high uncertainty values are derived by the fit routine and are not given in the table. Thus, parameters for which no uncertainty is given have formal uncertainties of several 1000 K or several dex.

Two independent observations are available for several objects.

Table F.1: BUSCA observations results

Object	RA	DE	B [mag]	T_{eff} [K]	$\sigma(T_{\text{eff}})$ [K]	$\log g$	$\sigma(\log g)$
HS 0002+0507	00 05 20.2	+05 24 10	16.2	7242		8.92	
HS 0005+1934	00 07 47.5	+19 51 24	16.2	11348	10	7.59	0.01
HS 0005+0803	00 08 06.6	+08 20 05	16.1	15571	214	7.55	0.57
HS 0007+0928	00 10 29.0	+09 45 34	16.0	16924	416	7.54	1.22
HS 0014+1642	00 16 51.5	+16 58 42	16.1	6932		8.75	
HS 0017+2623	00 20 22.3	+26 40 09	16.3	13932	13	8.09	0.01
HS 0021+4422	00 23 59.9	+44 38 39	16.5	12277	13	7.67	0.01
HS 0023+3852	00 26 33.0	+39 09 05	15.8	No white dwarf			
HS 0026+1406	00 29 20.5	+14 22 50	16.5	6239		8.25	
HS 0027+4402	00 29 52.5	+44 19 04	16.2	14341	140	7.25	0.40
HS 0030+4427	00 33 02.5	+44 44 13	16.4	10043	19	7.39	0.02
HS 0033+0136	00 35 36.1	+01 53 15	15.4	11008	18	8.67	0.02
HS 0034+1844	00 36 43.6	+19 01 29	15.9	8934	412	8.92	1.02
HS 0036+3115	00 39 03.6	+31 31 37	16.2	11648	19	7.59	0.01
HS 0037+4213	00 39 56.7	+42 29 29	16.2	9499	60	7.46	0.09
HS 0037+4115	00 40 36.7	+41 31 37	15.9	12726	11	7.64	0.01
				12518	11	7.77	0.01
HS 0038+0312	00 41 27.6	+03 29 08	16.9	8902	6	7.69	0.01
HS 0045+0217	00 48 13.3	+02 33 50	16.3	16999		7.54	
HS 0051+1145	00 54 18.2	+12 02 01	15.6	19666	528	7.69	1.68
HS 0052+2239	00 54 46.0	+22 56 06	16.4	9457	6	8.35	0.01
HS 0052+1900	00 54 49.3	+19 16 60	16.1	Hot white dwarf			
HS 0052+3253	00 55 17.8	+33 09 49	16.2	14559	19	7.77	0.04
HS 0057+1617	01 00 29.7	+16 33 50	16.2	14177	99	7.57	0.19
HS 0101+0559	01 03 48.9	+06 15 07	16.0	14026	16	8.38	0.01
HS 0101+3800	01 04 19.4	+38 16 54	14.3	15769	15	8.04	0.03
HS 0102+0933	01 04 41.3	+09 49 42	14.4	22732	24	8.75	0.03
HS 0104+0128	01 06 37.4	+01 45 01	16.4	11789	12	7.83	0.01
HS 0104+3914	01 06 53.8	+39 30 56	14.8	9603	6	8.14	0.01
HS 0108+1428	01 10 42.7	+14 44 36	16.4	6516	1259	7.63	
HS 0108+1045	01 10 47.4	+11 01 13	16.1	5763	724	8.48	
HS 0123+2146	01 25 57.8	+22 02 33	16.5	13426	18	7.76	0.02
HS 0125+1335	01 28 33.9	+13 51 21	14.1	12826	4	7.70	0.01
HS 0126+0335	01 28 53.3	+03 50 59	16.3	16482	59	7.92	0.13
HS 0127+2623	01 30 01.5	+26 38 58	15.1	14361	28	8.05	0.03
HS 0129+0511	01 32 13.2	+05 26 35	15.9	14697	25	8.22	0.03
HS 0131+0149	01 34 28.4	+02 04 22	14.4	11465	15	8.54	0.02
HS 0132+2214	01 35 05.4	+22 29 35	16.8	15590	1030	7.54	2.74
HS 0136+2845	01 39 14.4	+29 00 58	16.0	74516		8.97	
HS 0137+2642	01 40 25.6	+26 57 32	16.1	12488	14	7.75	0.01
HS 0142+3117	01 45 11.0	+31 32 44	14.9	8560	3	7.57	0.01
HS 0144+0850	01 46 40.7	+09 05 36	16.2	No white dwarf			
HS 0143+2139	01 46 41.3	+21 54 48	15.2	9305	6	8.41	0.01
HS 0150+0045	01 52 59.2	+01 00 19	16.3	12172	118	7.48	0.10
HS 0151+0146	01 54 13.7	+02 01 23	14.9	11906	10	7.91	0.01
HS 0153+2940	01 56 30.0	+29 55 32	14.7	14545	7	8.07	0.01
HS 0155+0657	01 57 41.3	+07 12 06	14.7	20734	101	8.87	0.13
HS 0156+2601	01 59 13.0	+26 16 15	16.1	13792	16	7.91	0.02
				13947	27	8.02	0.03
HS 0157+0855	01 59 44.1	+09 09 42	16.3	15356	170	7.55	0.42
HS 0159+0429	02 02 15.1	+04 43 29	16.2	9224	10	7.54	0.02
HS 0201+0712	02 04 13.8	+07 26 28	15.9	18856	723	7.99	1.78
HS 0204+3232	02 07 03.3	+32 46 46	16.0	15632	21	8.49	0.02
HS 0210+1629	02 13 05.3	+16 43 12	16.3	No white dwarf (subdwarf?)			
HS 0210+3302	02 13 06.2	+33 16 10	16.9	11919	15	7.40	0.02

Table F.1 continued

Object	RA	DE	B [mag]	T_{eff} [K]	$\sigma(T_{\text{eff}})$ [K]	$\log g$	$\sigma(\log g)$
HS 0213+0359	02 15 36.7	+04 13 38	16.7	13030	22	8.02	0.02
HS 0213+3937	02 16 16.5	+39 51 25	14.7	8910	2	8.03	0.01
				9217	28	8.57	0.07
HS 0220+2213	02 23 36.0	+22 27 29	15.9	No white dwarf			
HS 0223+1211	02 26 30.0	+12 25 23	16.0	12892	22	7.95	0.02
HS 0225+0010	02 27 55.5	+00 23 38	15.9	12222	11	7.55	0.01
HS 0230+3420	02 33 39.7	+34 33 22	16.2	14867	168	7.56	0.38
HS 0235+0655	02 38 33.1	+07 08 10	16.7	10942	11	7.75	0.01
HS 0237+1034	02 40 35.6	+10 47 01	16.0	16270	56	8.72	0.06
HS 0241+1411	02 44 00.8	+14 24 30	16.2	12919	18	7.54	0.02
HS 0243+1532	02 46 24.1	+15 45 02	15.7	12015	23	7.68	0.02
HS 0246+3238	02 49 27.6	+32 51 13	16.1	10819	8	7.66	0.01
				10697	6	7.60	0.01
HS 0307+0746	03 10 09.2	+07 57 35	16.3	9999	10	7.83	0.01
HS 0308+1656	03 11 38.1	+17 07 42	16.6	No white dwarf			
HS 0309+1001	03 12 34.9	+10 12 28	15.7	15587	924	8.94	0.52
HS 0315+1552	03 18 17.5	+16 03 22	16.6	No white dwarf			
HS 0325+2518	03 28 17.0	+25 28 52	15.9	12919	22	7.86	0.02
HS 0327+2756	03 30 40.9	+28 06 55	15.8	16879	3011	8.91	2.83
HS 0329+1121	03 32 35.8	+11 31 32	15.8	17125	163	7.75	0.43
HS 0337+0939	03 39 58.5	+09 49 11	16.2	12832	17	7.65	0.02
HS 0338+1858	03 41 10.5	+19 07 59	16.1	9399	6	8.11	0.01
HS 0344+0718	03 46 51.4	+07 28 01	16.2	10231	16	7.23	0.02
				10133	14	7.24	0.01
HS 0352+0514	03 54 40.9	+05 23 22	16.4	10115	85	7.71	0.09
HS 0352+0938	03 55 21.9	+09 47 17	14.5	13113	31	8.74	0.02
HS 0355+1337	03 58 09.4	+13 45 41	16.8	19006		7.52	
HS 0400+1451	04 03 42.1	+14 59 28	15.1	14386	11	8.35	0.01
HS 0401+1454	04 04 35.0	+15 02 27	16.2	12171	22	8.01	0.01
HS 0407+1754	04 10 10.3	+18 02 24	14.2	12697	13	7.75	0.01
HS 0412+0632	04 14 58.2	+06 40 10	15.5	No white dwarf (subdwarf?)			
HS 0513+7538	05 20 14.1	+75 41 46	16.0	No white dwarf (subdwarf?)			
HS 0524+8521	05 40 17.5	+85 23 19	15.8	13574	20	7.87	0.02
HS 0604+6538	06 09 11.4	+65 38 08	15.6	17185	433	7.53	1.35
HS 0637+7838	06 45 33.7	+78 35 04	16.3	25312		7.90	
HS 0658+6227	07 03 26.3	+62 22 53	15.7	No white dwarf (subdwarf?)			
HS 0707+3035	07 10 11.4	+30 30 41	16.6	16069	28	8.44	0.04
HS 0726+4119	07 30 18.4	+41 13 20	16.6	13335	85	7.57	0.13
HS 0726+7248	07 32 33.6	+72 41 40	15.1	15772	15	8.46	0.02
				16244	14	8.89	0.01
HS 0729+4211	07 32 37.9	+42 04 54	16.3	17207	105	7.75	0.30
HS 0730+4847	07 34 27.6	+48 41 15	14.9	14210	9	8.12	0.01
				14003	19	8.80	0.01
HS 0733+4119	07 37 07.9	+41 12 28	15.8	11155	8	7.73	0.01
HS 0736+7702	07 43 31.9	+76 55 51	16.4	18965	2081	8.52	4.17
HS 0743+4416	07 47 26.0	+44 08 48	15.0	15922	20	4.57	0.08
HS 0744+4414	07 48 04.9	+44 06 32	16.8	14512	26	7.71	0.05
HS 0751+4808	07 55 19.5	+48 00 33	16.5	17112	307	7.54	0.94
HS 0756+3228	07 59 19.5	+32 19 48	16.0	5897	314	7.21	
HS 0811+6427	08 15 34.4	+64 18 18	15.0	13712	7	7.88	0.01
HS 0821+6316	08 25 35.6	+63 06 52	15.8	16801	21	8.49	0.03
HS 0839+2311	08 42 53.1	+23 00 24	14.3	26131	1124	7.71	2.53
HS 0838+7510	08 44 17.6	+75 00 06	16.4	12351	23	8.02	0.02

Table F.1 continued

Object	RA	DE	B [mag]	T_{eff} [K]	$\sigma(T_{\text{eff}})$ [K]	$\log g$	$\sigma(\log g)$
HS 0945+2435	09 48 46.7	+24 21 25	0.0	19926	6197	8.93	2.76
HS 1039+4112	10 42 33.5	+40 57 16	15.9	11143	10	8.21	0.01
HS 1043+0258	10 46 23.5	+02 42 34	15.6	13825	69	7.57	0.12
HS 1103+0153	11 06 51.8	+62 50 23	17.1	5681		8.25	
HS 1108+4015	11 10 56.6	+39 59 16	15.4	10285	21	8.07	0.03
HS 1121+5050	11 24 31.5	+50 33 31	15.2	14807	32	8.00	0.04
HS 1135+2701	11 38 11.4	+26 44 42	15.6	16012	15	8.44	0.02
HS 1145+4052	11 48 28.2	+40 35 57	15.9	6995		7.63	
HS 1149+0545	11 51 54.2	+05 28 50	15.1	11097	17	7.96	0.02
HS 1149+4103	11 51 42.2	+40 47 12	15.9	14832	47	7.97	0.07
HS 1158+4316	12 01 09.5	+42 59 46	16.2	12813	22	7.75	0.02
HS 1225+0038	12 28 07.8	+00 22 16	15.4	9491	8	8.18	0.02
HS 1246+1232	12 49 02.3	+12 16 14	15.5	12590	234	8.55	0.18
HS 1253+1033	12 56 28.5	+10 17 09	14.4	12633	34	8.49	0.02
HS 1258+5920	13 00 35.2	+59 04 14	15.1	15008	35	8.48	0.03
HS 1300+3808	13 02 48.9	+37 51 54	16.1	13644	73	7.94	0.08
HS 1301+0103	13 03 57.5	+00 47 27	13.9	5876		8.88	
HS 1307+3525	13 09 57.8	+35 09 45	14.8	10852	8	8.35	0.01
HS 1308+1646	13 11 06.1	+16 31 03	15.5	11009	38	8.58	0.04
HS 1310+5821	13 12 57.7	+58 05 11	13.9	10405	3	8.23	0.01
HS 1317+4520	13 19 14.2	+45 05 06	14.3	13403	7	7.81	0.01
HS 1319+4639	13 21 15.3	+46 23 22	14.4	15179	11	8.13	0.02
HS 1334+0701	13 36 33.7	+06 46 28	15.0	13357	13	8.53	0.01
HS 1335+4007	13 37 25.0	+39 52 39	16.3	8589	8	7.85	0.02
HS 1339+3601	13 41 15.4	+35 45 55	16.0	15394	328	7.55	0.83
HS 1348+2449	13 50 32.4	+24 34 14	16.0	13600	44	8.08	0.04
HS 1349+5512	13 51 19.8	+54 57 41	15.7	11882	15	7.96	0.01
HS 1350+6539	13 52 11.5	+65 24 55	15.5	12357	15	7.85	0.01
HS 1351+1845	13 53 47.6	+18 30 59	15.9	14929	22	8.26	0.02
HS 1405+7453	14 05 40.2	+74 39 01	15.7	9188	52	7.38	0.08
HS 1406+2229	14 09 18.6	+22 15 30	15.8	14068	11	8.04	0.01
HS 1407+4230	14 09 45.1	+42 16 00	14.8	9644	3	8.08	0.01
HS 1410+4230	14 12 07.7	+42 16 27	15.3	16056	165	7.93	0.34
HS 1414+3129	14 16 26.0	+31 16 01	15.5	13058	9	7.92	0.01
HS 1423+1434	14 25 28.9	+14 21 01	16.3	17078	517	8.91	0.50
HS 1428+3723	14 30 42.6	+37 10 15	15.0	13613	23	7.93	0.02
HS 1432+1441	14 35 20.8	+14 28 48	16.0	16276	1007	7.51	2.70
HS 1441+3219	14 43 17.5	+32 06 57	16.4	12376	26	8.25	0.02
HS 1442+4729	14 44 18.3	+47 17 03	16.3	9656	8	8.31	0.01
HS 1443+2934	14 45 28.5	+29 21 31	14.5	12380	8	8.12	0.01
HS 1444+3505	14 47 00.0	+34 53 07	16.1	26541		7.42	
HS 1447+0454	14 50 10.2	+04 41 45	15.6	13572	10	7.97	0.01
HS 1448+4107	14 50 06.7	+40 55 35	15.8	13557	37	8.20	0.03
HS 1453+5707	14 55 21.5	+56 55 43	14.7	15220	10	8.64	0.01
HS 1501+0314	15 04 23.5	+03 02 21	15.5	14782	12	7.91	0.02
				15374	55	7.85	0.12
HS 1503+1402	15 05 52.9	+13 50 57	16.2	12831	54	7.93	0.04
HS 1508+6343	15 09 39.0	+63 32 26	15.0	9919	27	7.60	0.03
HS 1512+7705	15 11 03.5	+76 53 48	15.1	15442	94	7.64	0.25
HS 1509+5337	15 11 26.7	+53 26 05	16.0	14541	58	7.57	0.13
HS 1515+6653	15 15 52.9	+66 42 40	15.4	9953	8	7.90	0.01
HS 1518+1451	15 20 57.5	+14 41 01	16.3	16110	92	7.86	0.22
HS 1518+7213	15 18 12.7	+72 02 10	16.7	No white dwarf (subdwarf?)			

Table F.1 continued

Object	RA	DE	B [mag]	T_{eff} [K]	$\sigma(T_{\text{eff}})$ [K]	$\log g$	$\sigma(\log g)$
HS 1517+0814	15 20 06.0	+08 03 29	15.9	14174	11	8.03	0.01
HS 1527+0814	15 30 06.4	+08 04 53	17.0	14569	17	8.10	0.02
HS 1531+7436	15 30 35.4	+74 26 04	16.2	12355	45	8.18	0.03
HS 1538+2353	15 40 26.6	+23 43 34	16.4	15859	334	8.45	0.39
HS 1541+6503	15 41 44.7	+64 53 53	15.8	11026	12	7.73	0.01
HS 1544+3800	15 46 05.6	+37 51 27	14.4	13042	7	8.17	0.01
HS 1545+1708	15 47 52.7	+16 58 59	14.3	No white dwarf			
HS 1545+3443	15 47 42.0	+34 33 57	16.4	10299	853	8.91	1.23
HS 1547+2541	15 49 10.6	+25 32 50	15.2	14326	26	8.21	0.02
HS 1550+1819	15 52 26.4	+18 10 18	14.7	14979	16	8.42	0.01
HS 1556+1634	15 58 40.3	+16 25 55	15.8	11426	59	7.59	0.05
HS 1605+0853	16 08 05.1	+08 45 18	16.7	10184	14	8.05	0.02
HS 1607+1436	16 10 17.3	+14 28 17	16.8	No white dwarf			
HS 1609+1330	16 11 25.6	+13 22 44	15.4	8981	5	8.56	0.01
HS 1610+6149	16 11 37.8	+61 41 30	16.6	10769	15	7.53	0.02
HS 1610+1639	16 13 02.4	+16 31 56	14.2	14520	17	8.38	0.02
HS 1612+5528	16 13 16.6	+55 21 26	15.9	11706	11	8.19	0.01
HS 1611+2637	16 13 18.6	+26 30 08	16.3	14391	20	8.26	0.02
HS 1611+3203	16 13 51.6	+31 56 14	16.1	14035	27	8.30	0.02
HS 1614+0537	16 17 10.5	+05 30 38	14.7	No white dwarf			
HS 1622+6708	16 22 47.2	+67 02 03	16.8	6168	1333	7.76	
HS 1625+1231	16 28 13.8	+12 24 56	16.1	11271	14	8.06	0.01
HS 1640+4545	16 41 42.2	+45 40 03	16.3	19003	175	8.24	0.38
HS 1646+1059	16 48 40.8	+10 53 53	16.1	19822	153	7.74	0.41
HS 1651+1848	16 53 35.1	+18 43 33	16.2	No white dwarf			
HS 1654+6344	16 54 29.2	+63 39 22	15.7	15018	14	8.11	0.02
HS 1656+2005	16 58 53.1	+20 01 10	16.5	17479	58	8.55	0.09
HS 1659+3019	17 01 08.0	+30 15 37	14.4	13650	20	7.09	0.06
				13972	34	8.05	0.03
HS 1701+5039	17 02 19.0	+50 34 59	16.4	11586	17	8.05	0.01
HS 1701+6247	17 01 44.8	+62 43 03	16.9	8549	145	8.92	0.56
HS 1704+2759	17 06 46.4	+27 55 25	16.3	14434	22	8.26	0.02
HS 1710+6843	17 10 42.4	+68 40 06	16.6	16093	1015	7.55	2.69
HS 1711+1408	17 13 41.6	+14 05 16	16.5	No white dwarf			
HS 1720+3605	17 22 06.7	+36 02 29	15.1	12041	12	7.84	0.01
HS 1720+2648	17 22 30.0	+26 45 26	15.3	14125	106	7.56	0.19
				15398	660	7.56	1.62
HS 1722+3901	17 23 47.5	+38 58 57	16.4	No white dwarf (subdwarf?)			
HS 1729+7735	17 26 38.8	+77 33 34	16.0	12962	16	7.58	0.02
HS 1728+6940	17 28 01.2	+69 38 38	15.3	14258	32	7.96	0.04
HS 1728+5012	17 29 46.3	+50 10 04	15.9	13560	10	7.96	0.01
				13761	18	8.68	0.01
HS 1735+6104	17 36 08.4	+61 02 25	15.5	14936	15	7.81	0.03
HS 1746+6322	17 46 35.4	+63 21 41	16.9	5934	702	8.82	
HS 1824+6000	18 24 44.3	+60 01 58	15.7	10486	17	7.30	0.02
				11192	12	7.65	0.01
HS 1858+7147	18 58 16.2	+71 51 34	16.4	15086	21	7.81	0.04
HS 1938+6902	19 38 19.4	+69 09 11	16.3	12835	22	8.13	0.02
				12427	7	8.27	0.01
HS 1951+7147	19 50 45.6	+71 55 39	16.8	11789	21	8.40	0.02
HS 2051+0929	20 53 43.1	+09 41 13	16.2	15562	45	8.45	0.05
HS 2054+0610	20 56 50.6	+06 21 49	16.9	9164	4	7.22	0.01

Table F.1 continued

Object	RA	DE	B [mag]	T_{eff} [K]	$\sigma(T_{\text{eff}})$ [K]	$\log g$	$\sigma(\log g)$
HS 2109+0212	21 11 40.4	+02 24 53	16.3	14592	21	7.80	0.04
				14216	30	8.13	0.03
HS 2111+0954	21 13 39.5	+10 06 42	16.5	10559	1592	8.93	2.05
				10138	2655	8.93	3.27
HS 2112+0106	21 14 59.6	+01 18 57	16.1	No white dwarf			
HS 2117+1514	21 20 02.7	+15 26 52	16.3	9861	6	7.57	0.01
HS 2118+0355	21 21 08.6	+04 08 45	16.9	6246		8.25	
HS 2120+0213	21 23 18.0	+02 25 59	14.8	No white dwarf			
HS 2123+0013	21 26 23.2	+00 26 40	16.6	17806		7.53	
HS 2132+0941	21 34 50.8	+09 55 20	15.9	13021	13	7.52	0.02
HS 2138+0910	21 41 03.0	+09 23 46	15.9	9129	5	7.46	0.01
				9015	4	7.67	0.01
HS 2139+1132	21 41 28.1	+11 46 22	15.6	14935	15	7.94	0.03
				14737	12	8.16	0.02
HS 2148+1631	21 51 14.6	+16 45 24	15.9	15277	23	8.75	0.02
HS 2159+2904	22 02 05.6	+29 19 06	14.9	15207	30	8.42	0.03
HS 2201+1435	22 04 16.2	+14 50 30	16.8	17859	933	7.53	2.83
HS 2206+2248	22 08 37.7	+23 03 27	16.2	15509	34	7.94	0.07
HS 2216+1551	22 18 57.1	+16 06 57	15.7	16059	528	8.91	0.44
HS 2217+2454	22 20 15.7	+25 09 09	16.1	11714	492	8.07	0.39
				11935	42	7.68	0.03
HS 2226+1738	22 28 27.8	+17 54 04	16.0	14207	35	8.31	0.03
HS 2232+2941	22 34 35.9	+29 56 45	16.0	15415	1260	8.94	0.89
HS 2232+2109	22 35 17.8	+21 25 15	16.5	15866	30	8.52	0.03
HS 2239+1729	22 41 35.8	+17 45 05	16.2	No white dwarf			
HS 2244+0237	22 46 46.7	+02 53 43	16.5	12953	18	7.63	0.02
HS 2246+2220	22 49 05.3	+22 36 31	14.2	9963	3	8.39	0.00
HS 2254+1236	22 56 46.1	+12 52 50	15.5	11815	20	8.12	0.02
HS 2259+1419	23 01 55.2	+14 35 60	15.8	12956	21	8.02	0.02
HS 2303+2120	23 06 05.0	+21 36 25	16.3	15754	441	7.55	1.18
				15450	40	8.66	0.04
HS 2303+2415	23 06 17.6	+24 32 08	15.1	11147	13	8.01	0.01
HS 2304+2809	23 06 36.1	+28 25 30	16.3	12512	16	7.90	0.01
				11731	15	8.14	0.01
HS 2306+1303	23 08 30.5	+13 19 23	15.2	13705	21	8.05	0.02
HS 2306+1229	23 08 35.1	+12 45 39	14.8	18785	38	8.75	0.05
				20535	48	8.73	0.07
HS 2314+1407	23 17 23.6	+14 23 55	16.7	16832	106	8.00	0.22
HS 2318+1241	23 20 31.2	+12 58 14	16.1	14139	29	7.72	0.05
HS 2321+3358	23 23 38.0	+34 15 26	14.7	18571	12	8.77	0.02
				18339	17	8.86	0.02
HS 2322+0952	23 24 32.8	+10 08 53	16.6	19350		7.51	
HS 2336+0618	23 38 58.0	+06 35 30	15.5	16239	31	7.95	0.06
				16366	436	7.54	1.18
HS 2341+1042	23 43 56.1	+10 59 20	16.7	25318	1449	8.66	2.28
HS 2346+1303	23 48 57.3	+13 20 33	16.7	18257	447	7.87	1.24
HS 2346+1006	23 49 29.6	+10 22 57	16.3	13016	29	8.12	0.02
HS 2347+1249	23 49 53.2	+13 06 12	16.1	10635	7	7.50	0.01
				10901	12	8.22	0.01
HS 2351+3554	23 53 55.0	+36 11 27	16.6	11316	29	7.59	0.02
HS 2353+3504	23 55 42.3	+35 21 34	16.3	14281	136	8.78	0.08
HS 2354+1126	23 56 37.2	+11 43 31	16.3	12479	28	7.92	0.02
HS 2354+1929	23 56 38.3	+19 45 52	16.0	13370	205	7.55	0.30
				13570	12	8.11	0.01

Appendix G

Graphical Representation of the SPY Spectra Fits

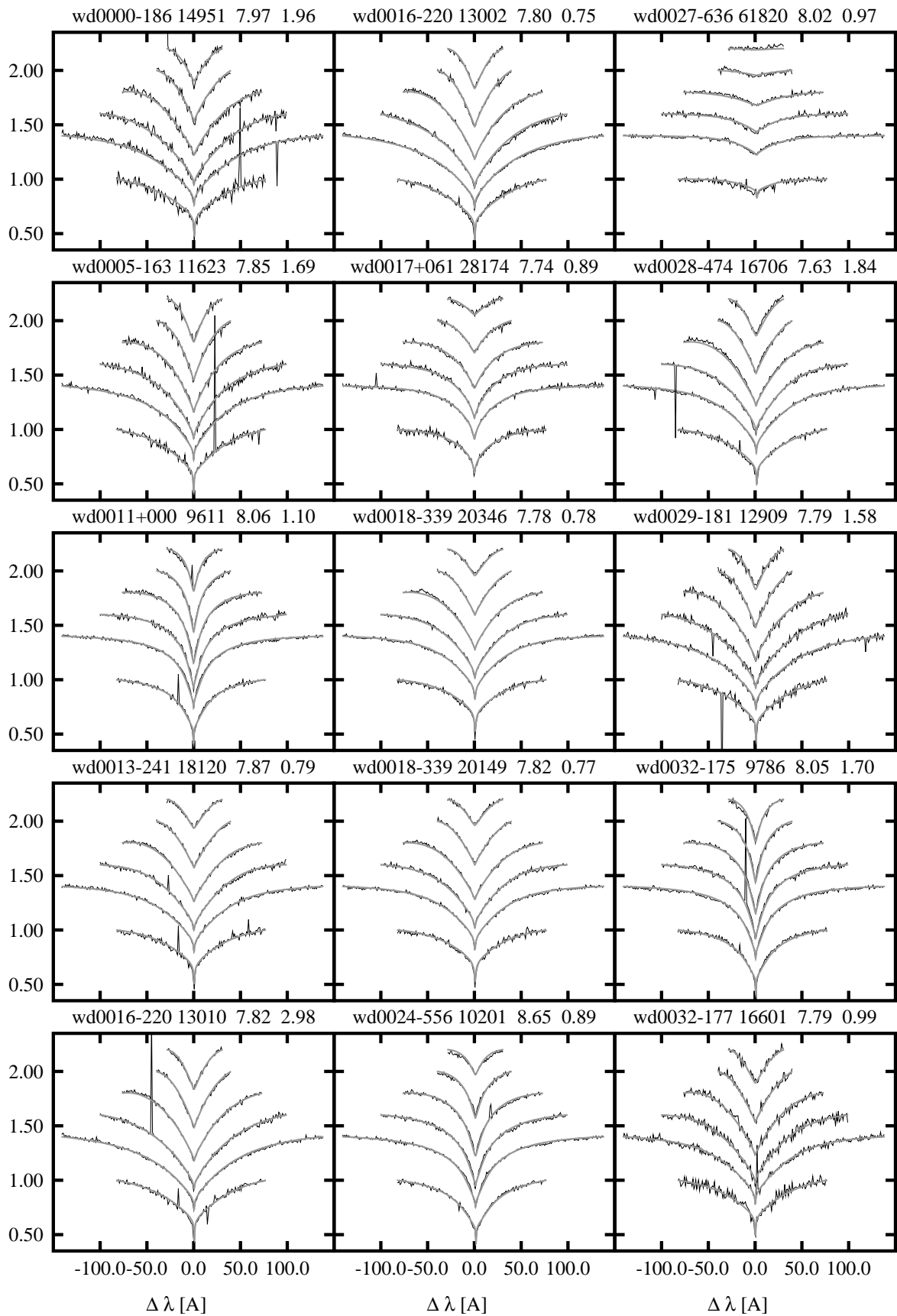
G.1 DA Stars

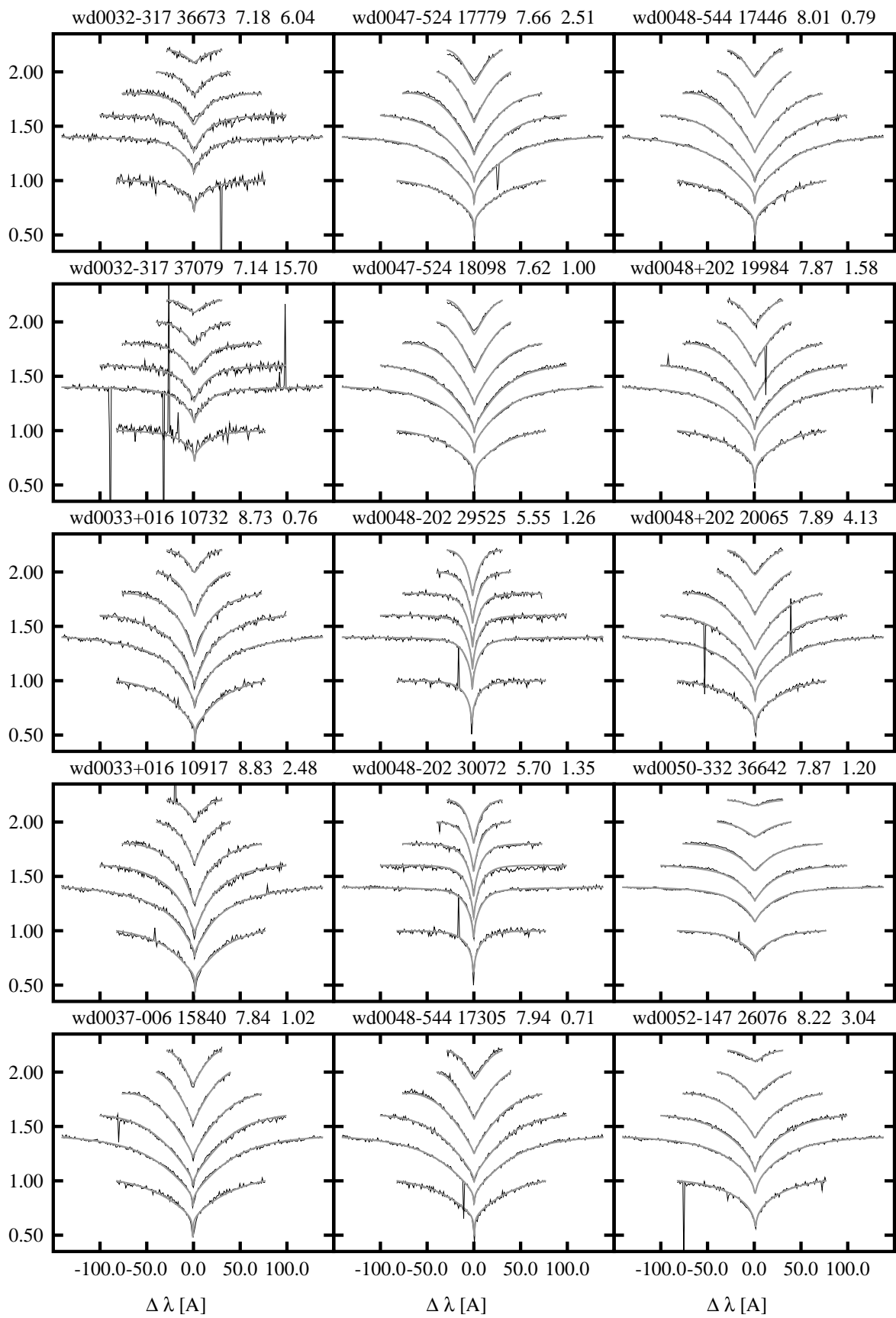
On the following pages the fit results for all DA model fits is displayed, in the stacked fashion plots that were used before, i.e., with H8 on top down to H α . The relative intensity scale is correct for H α and has been shifted for each higher line. The spectra are shown rebinned to a stepwidth of 1 Å, plotted as back lines, and the fit is plotted as thick grey line. On top of each panel, the object name, fit result (T_{eff} , $\log g$) and the χ^2 of the fit is given.

For some objects the fit is not good; these are mostly objects which are not DA stars, see table A.1. In one case (HE 0959–0828, see chapter 7) only the lines H α through H γ were fitted and are displayed.

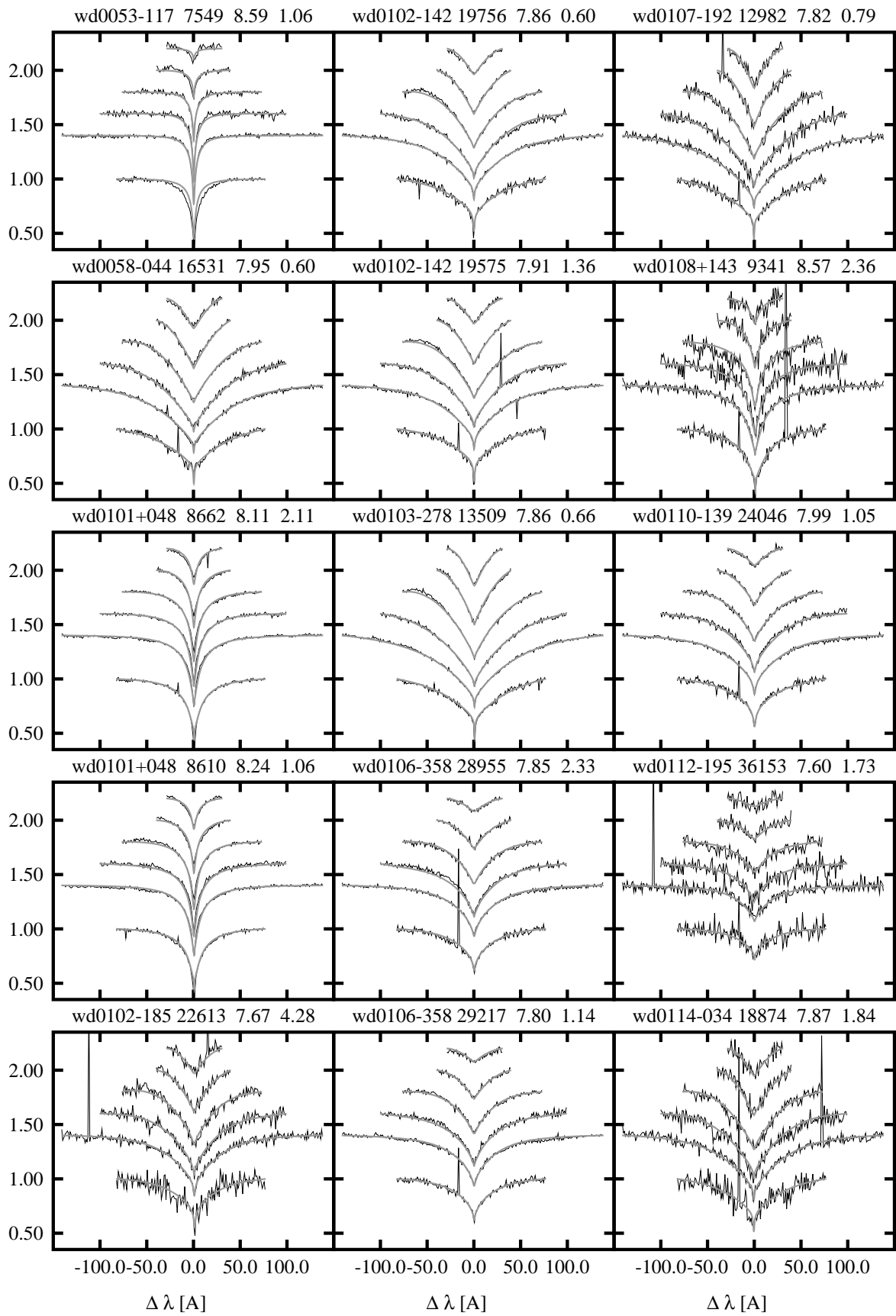
For objects for which two spectra were averaged to yield the objects' final result, the fits of both spectra are shown.

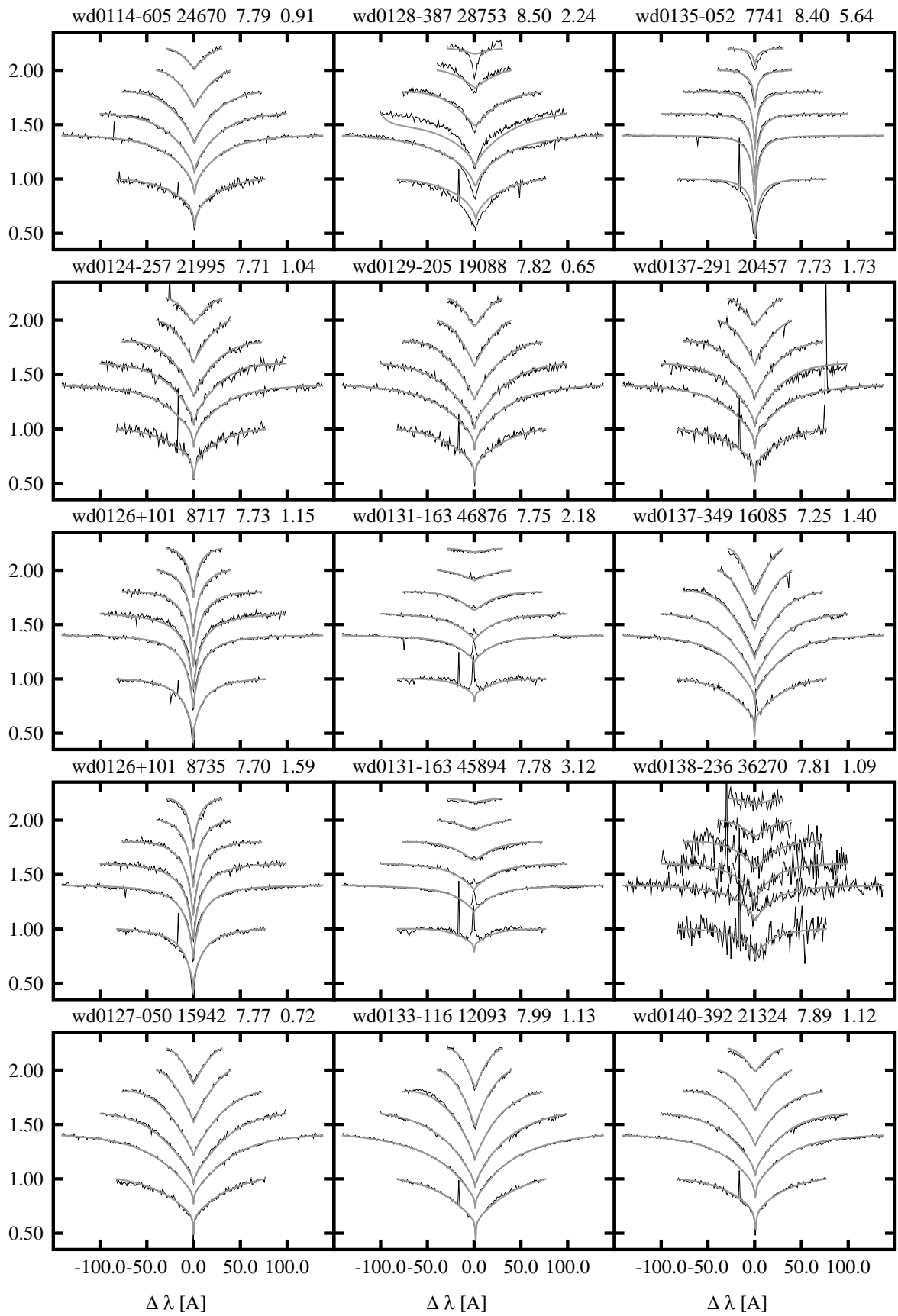
162 APPENDIX G. GRAPHICAL REPRESENTATION OF THE SPY SPECTRA FITS



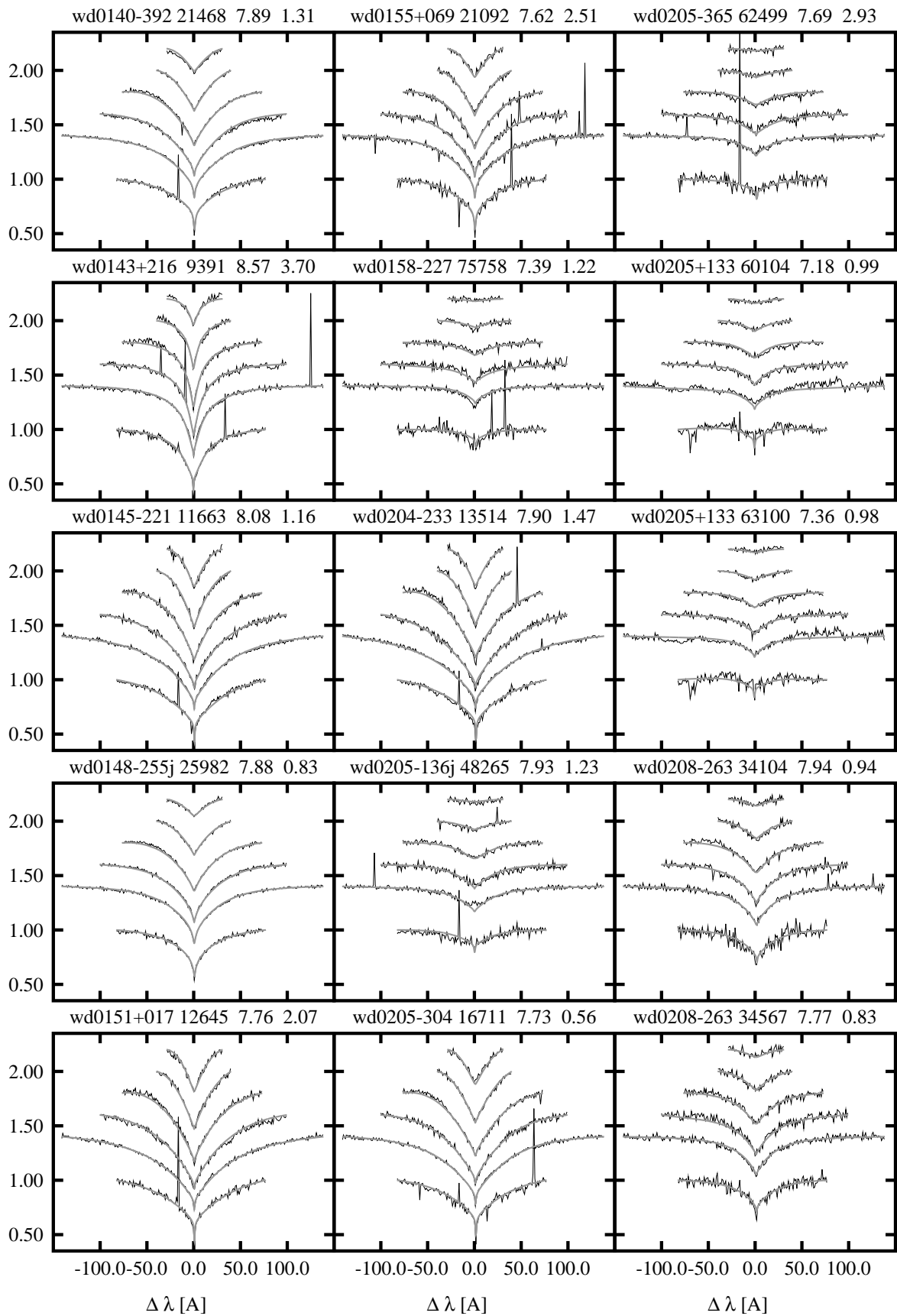


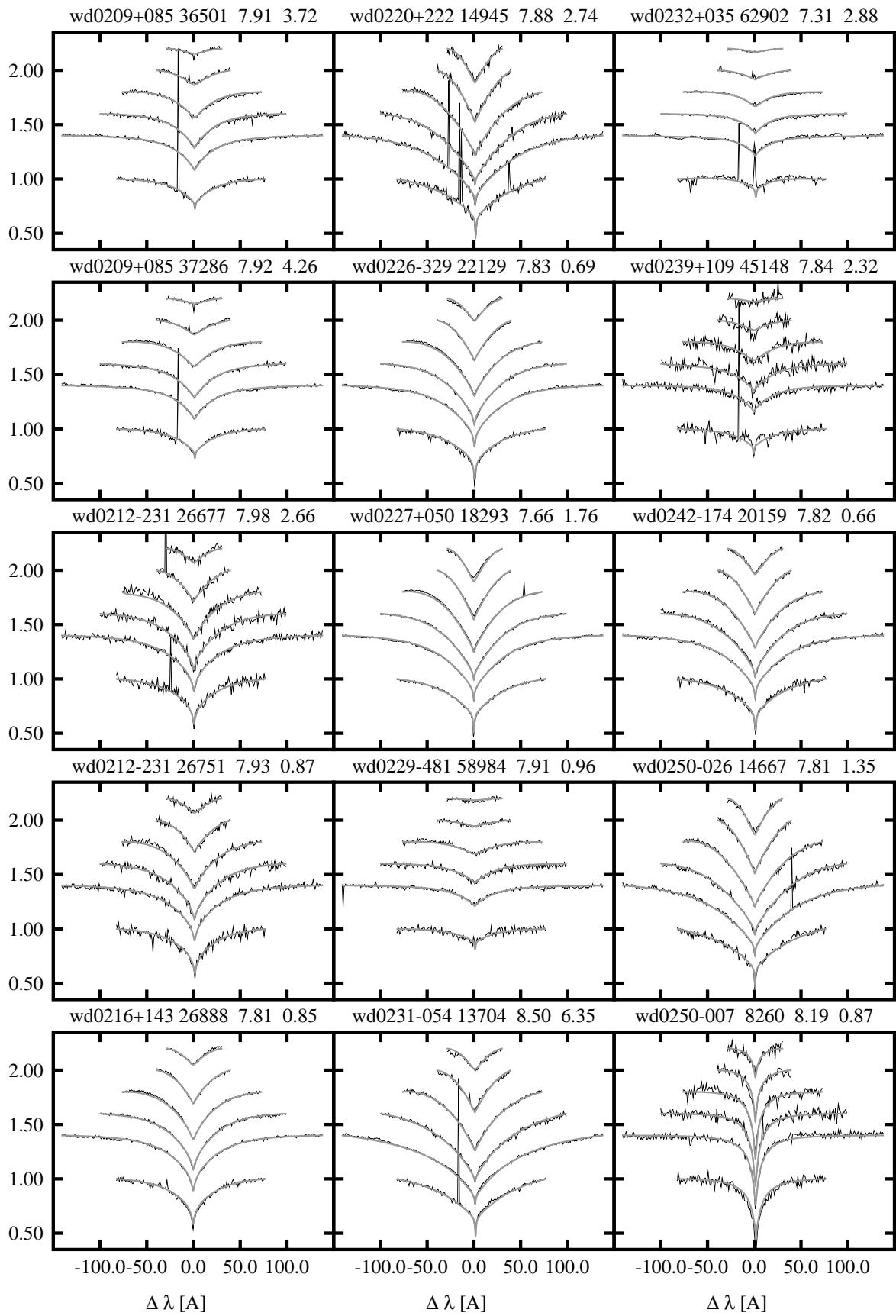
164 APPENDIX G. GRAPHICAL REPRESENTATION OF THE SPY SPECTRA FITS



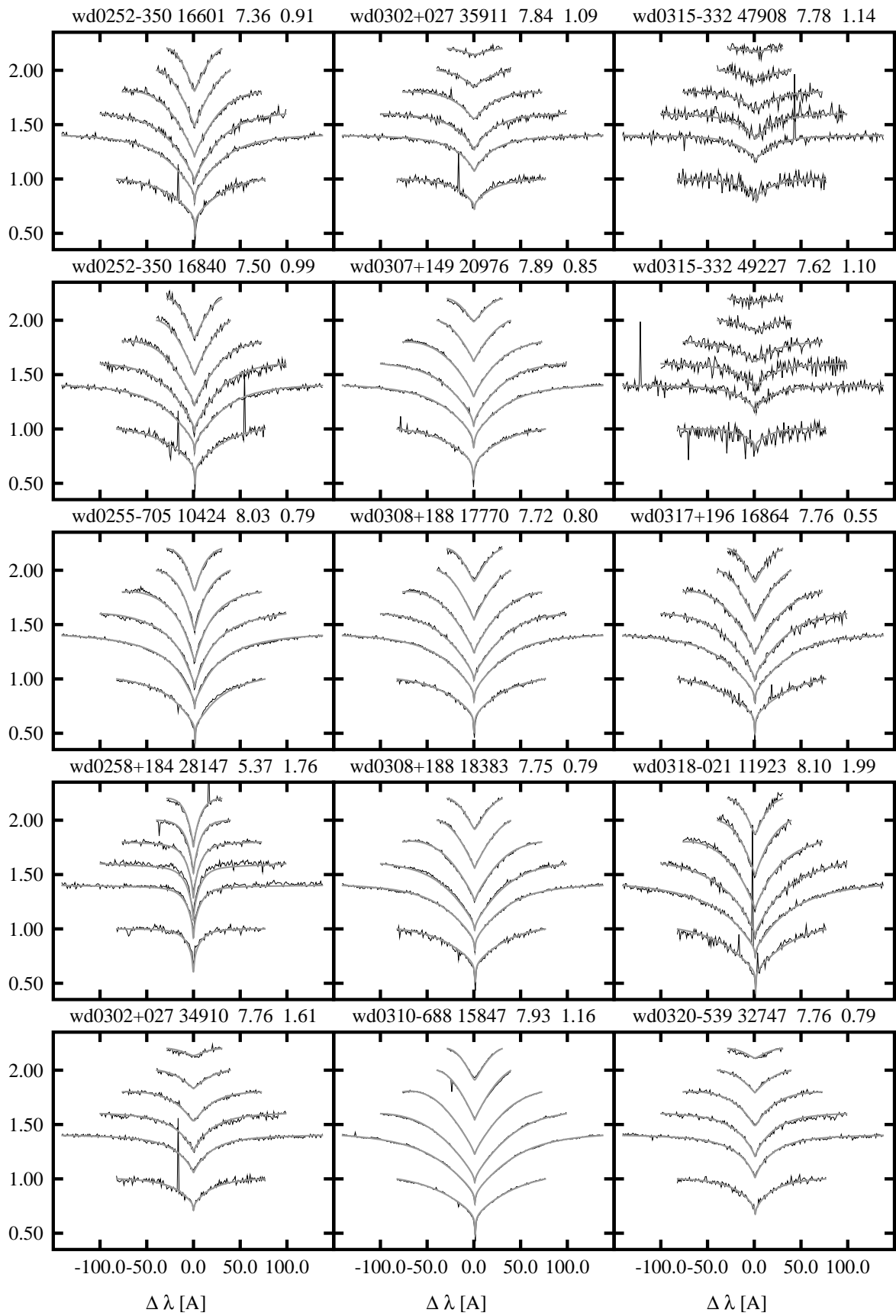


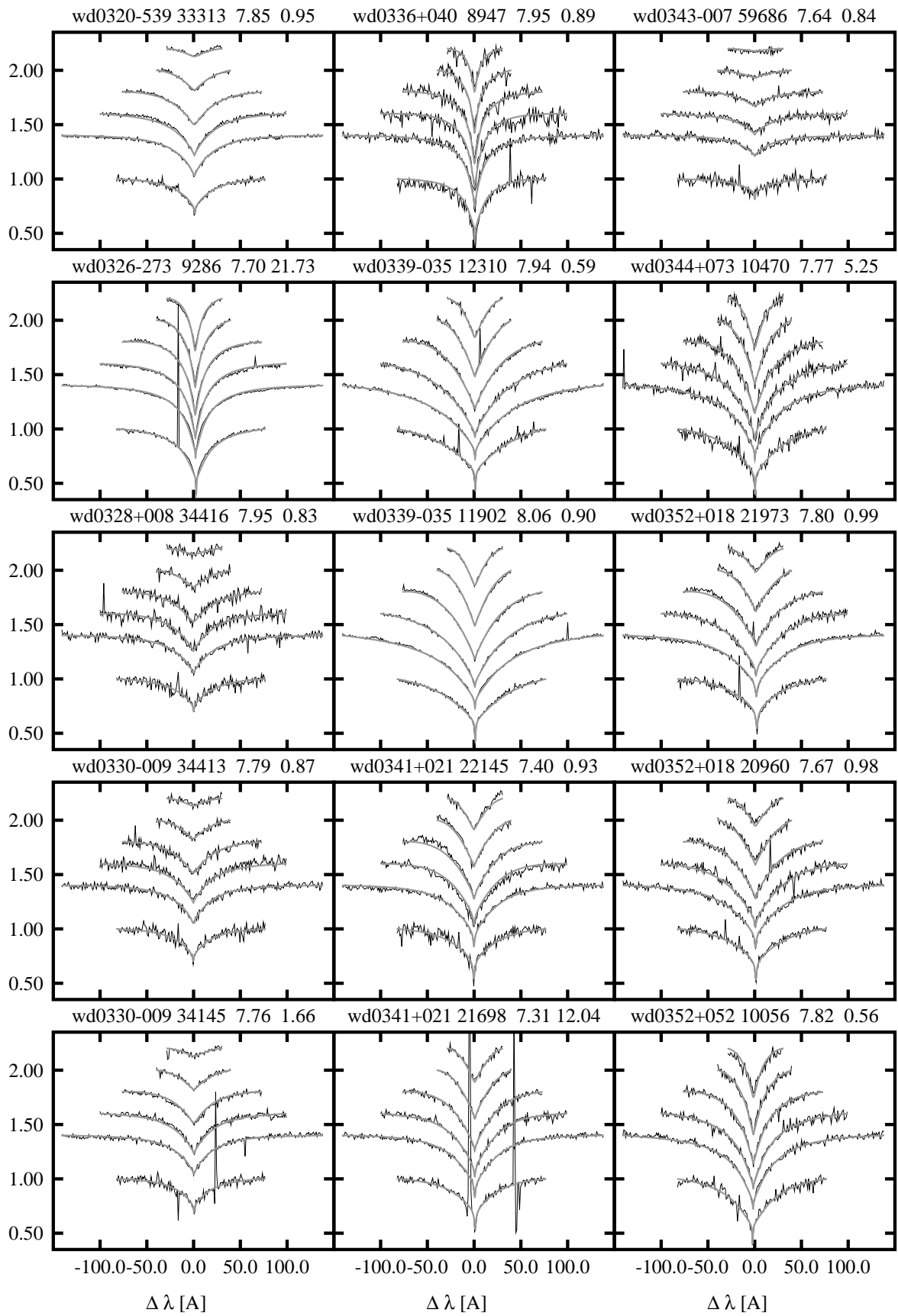
166 APPENDIX G. GRAPHICAL REPRESENTATION OF THE SPY SPECTRA FITS



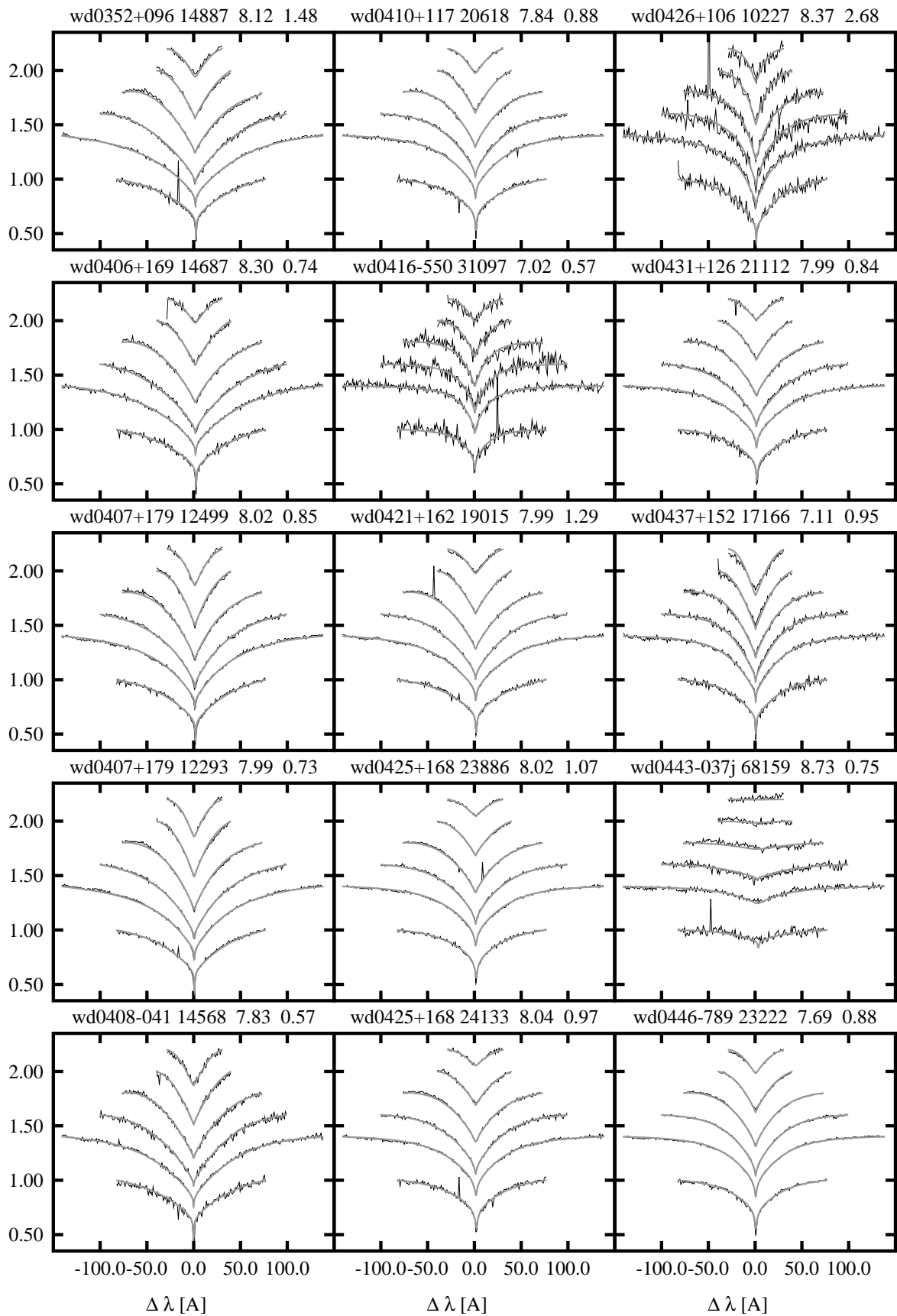


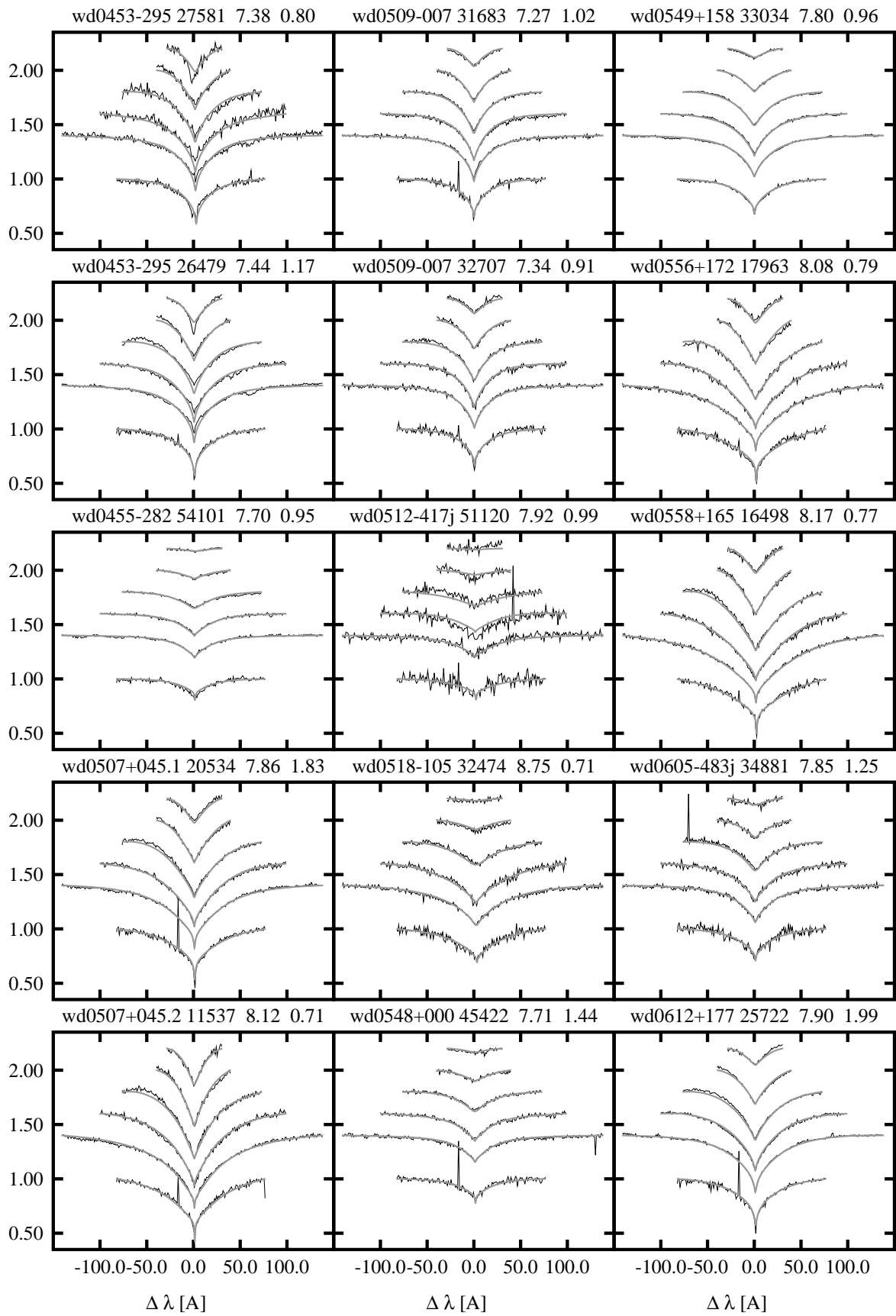
168 APPENDIX G. GRAPHICAL REPRESENTATION OF THE SPY SPECTRA FITS



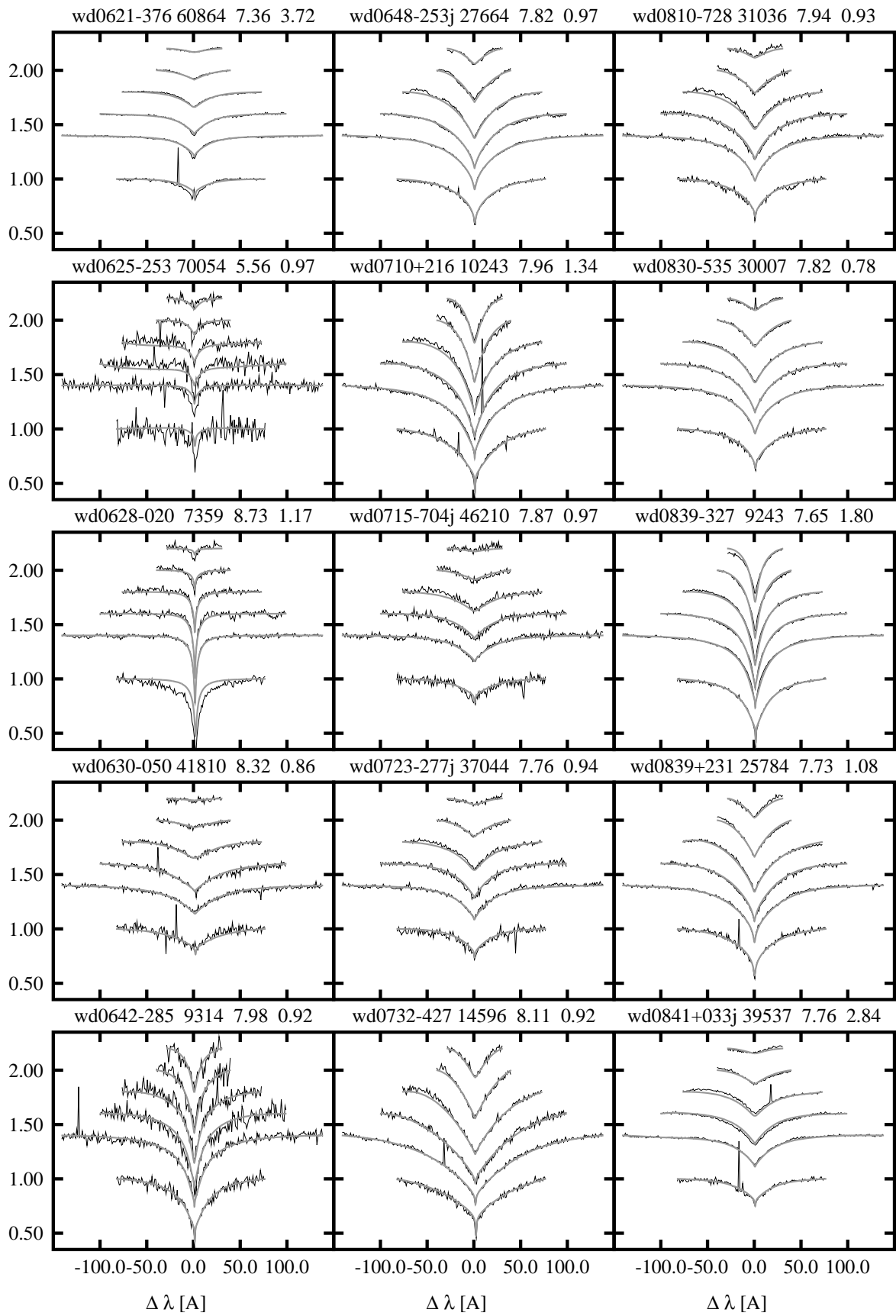


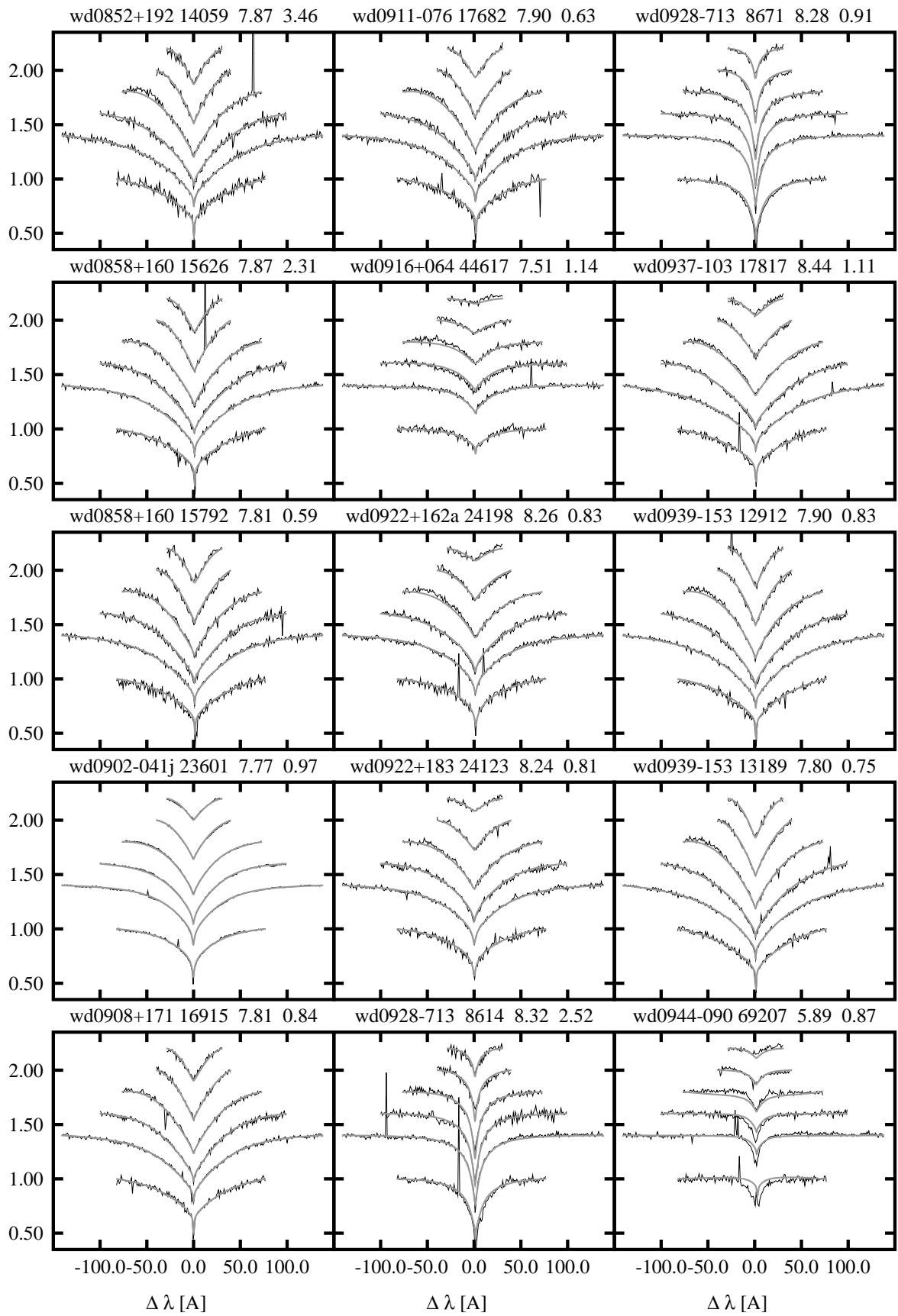
170 APPENDIX G. GRAPHICAL REPRESENTATION OF THE SPY SPECTRA FITS



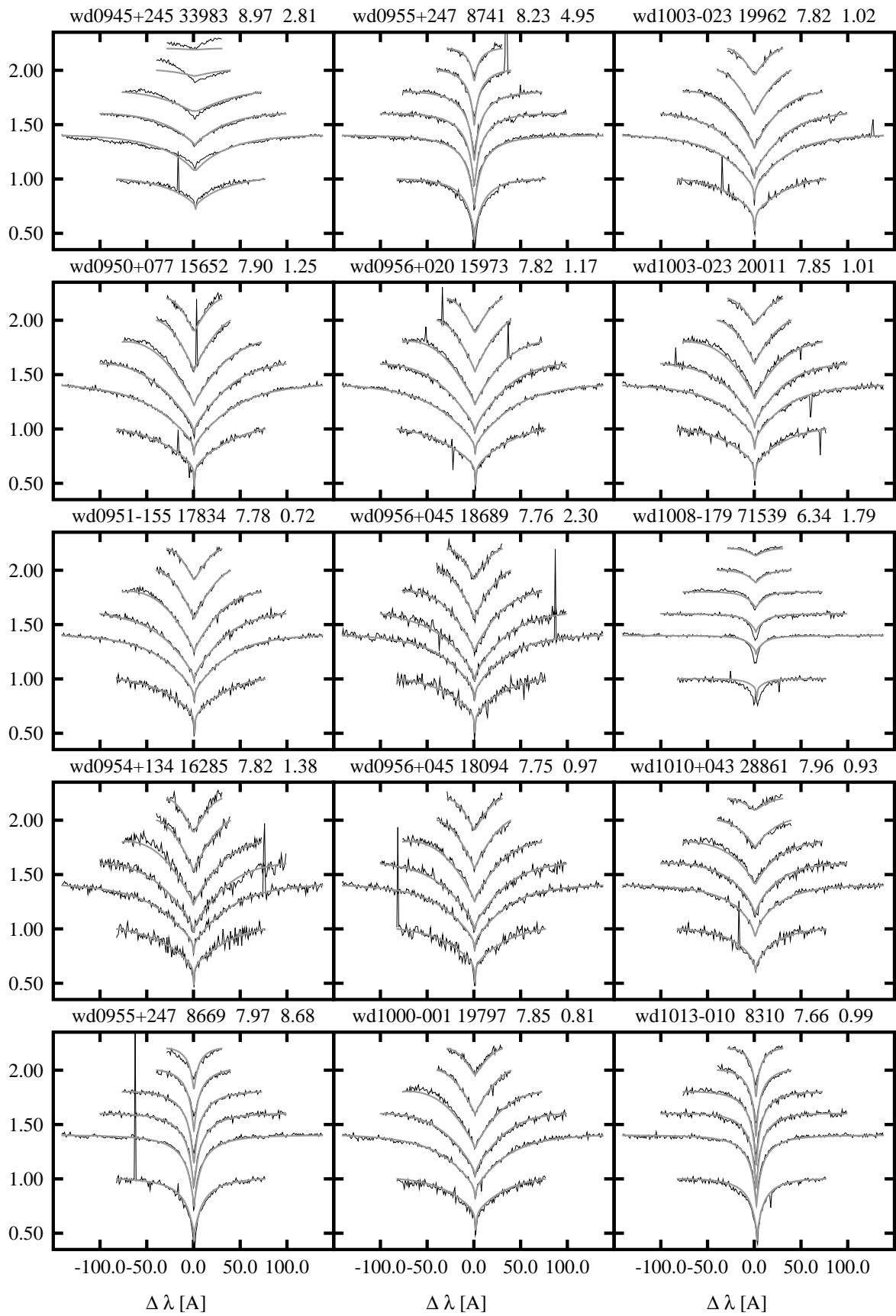


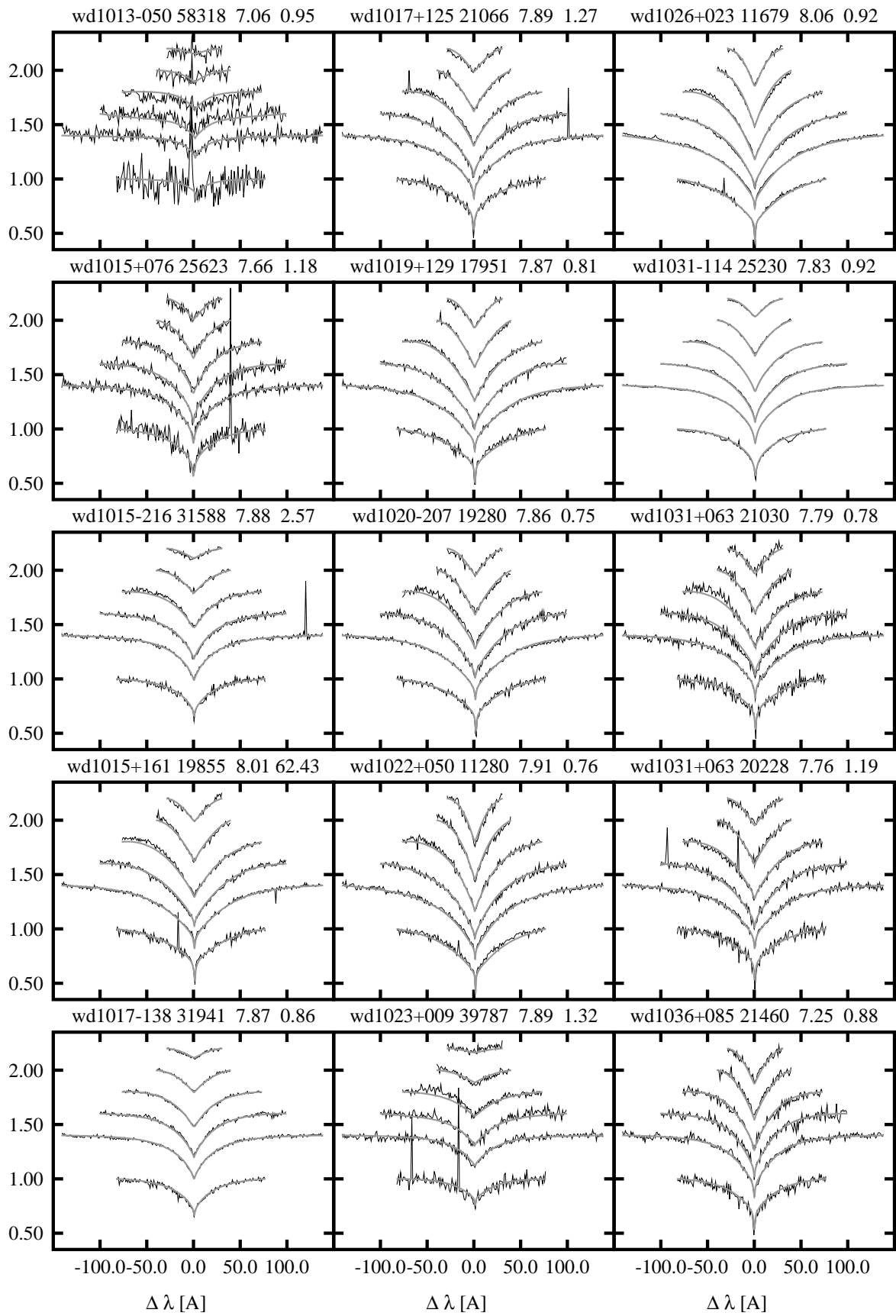
172 APPENDIX G. GRAPHICAL REPRESENTATION OF THE SPY SPECTRA FITS



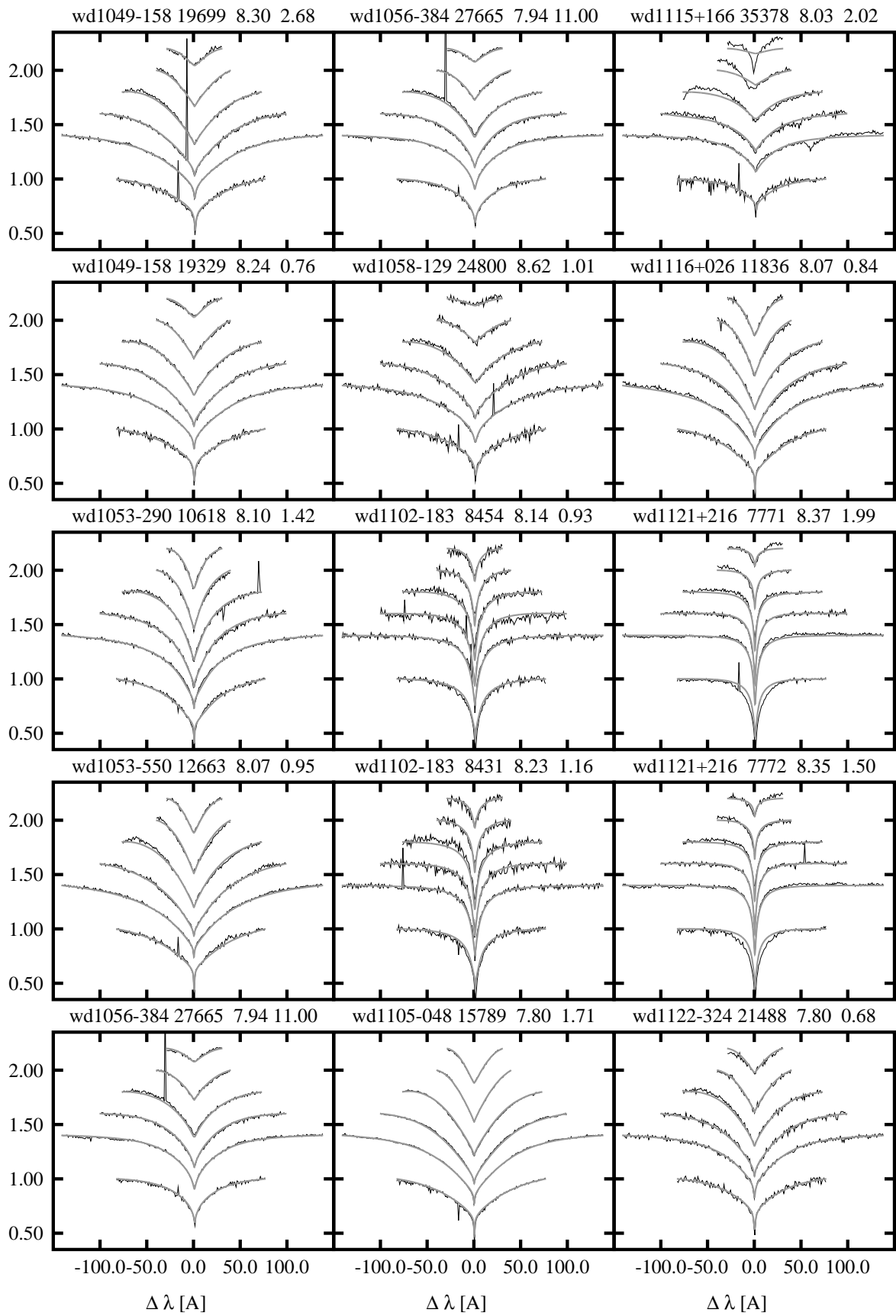


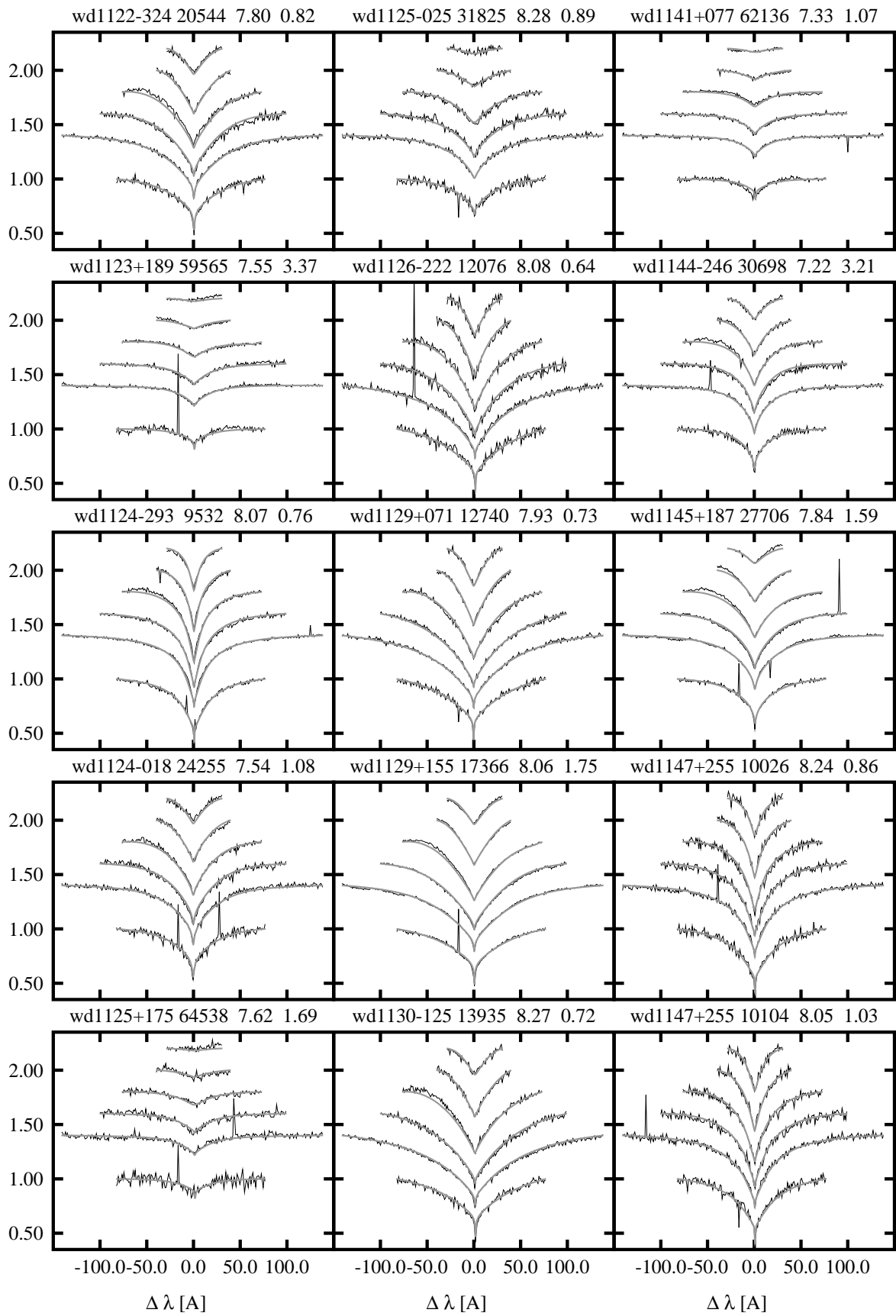
174 APPENDIX G. GRAPHICAL REPRESENTATION OF THE SPY SPECTRA FITS



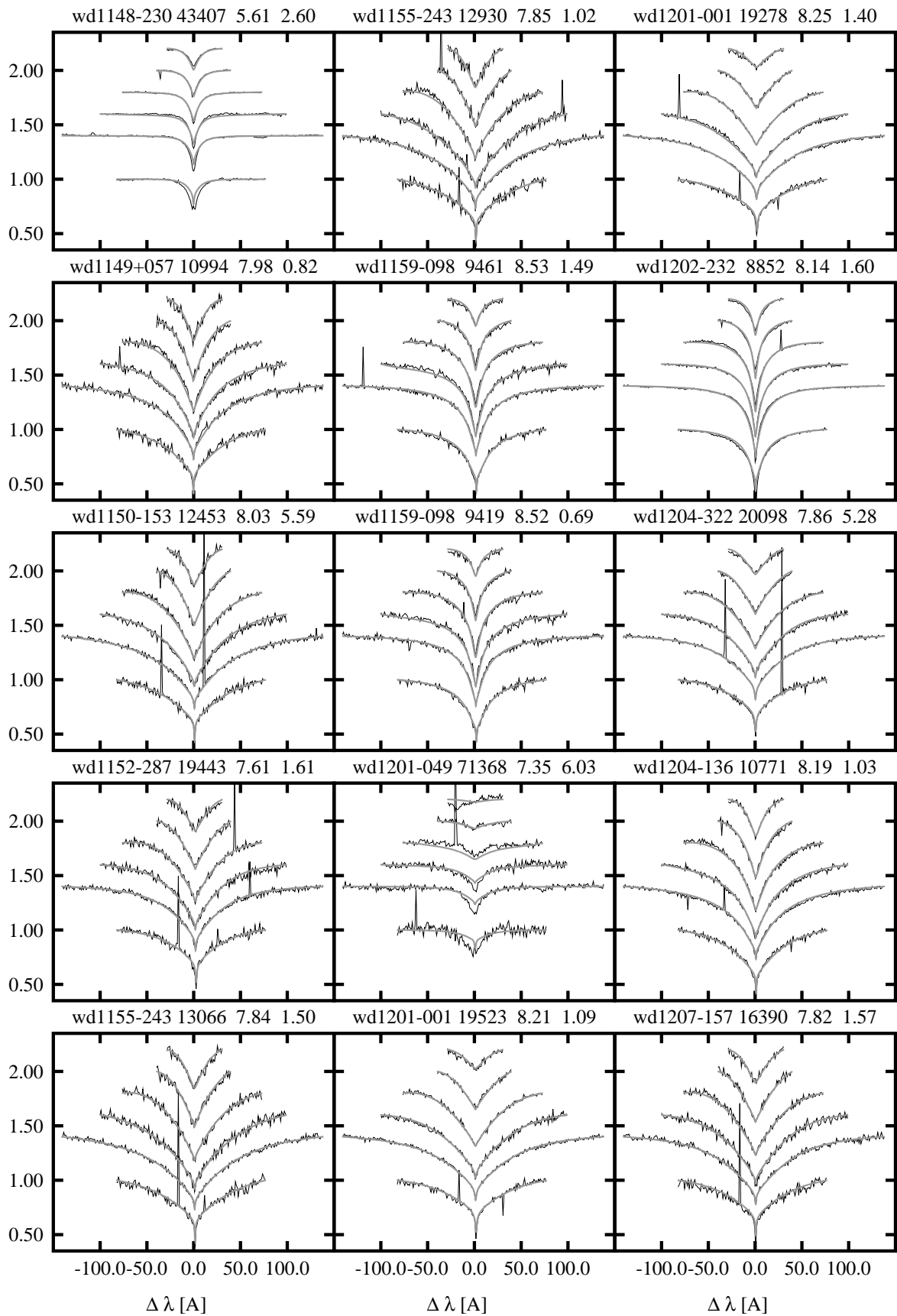


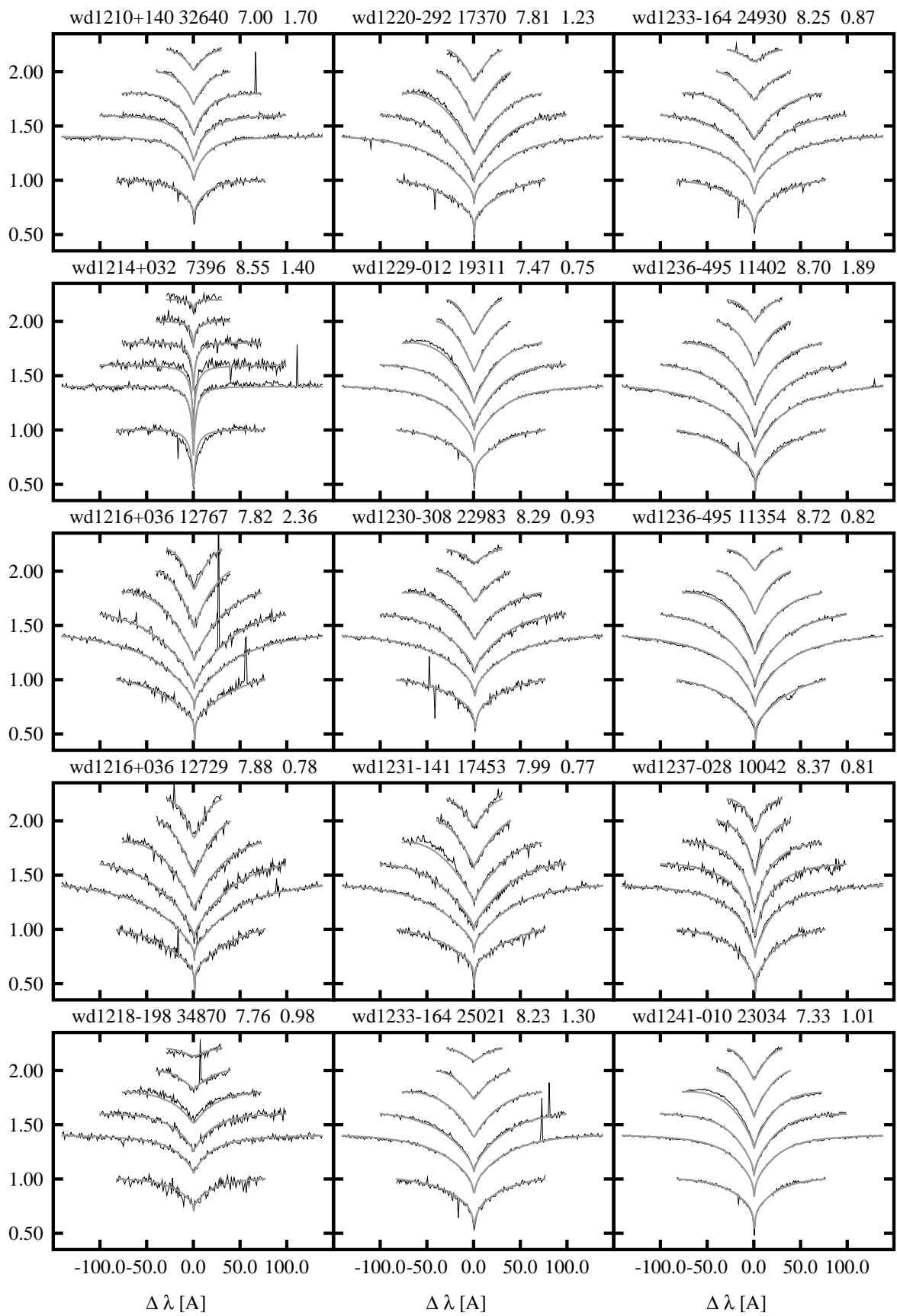
176 APPENDIX G. GRAPHICAL REPRESENTATION OF THE SPY SPECTRA FITS



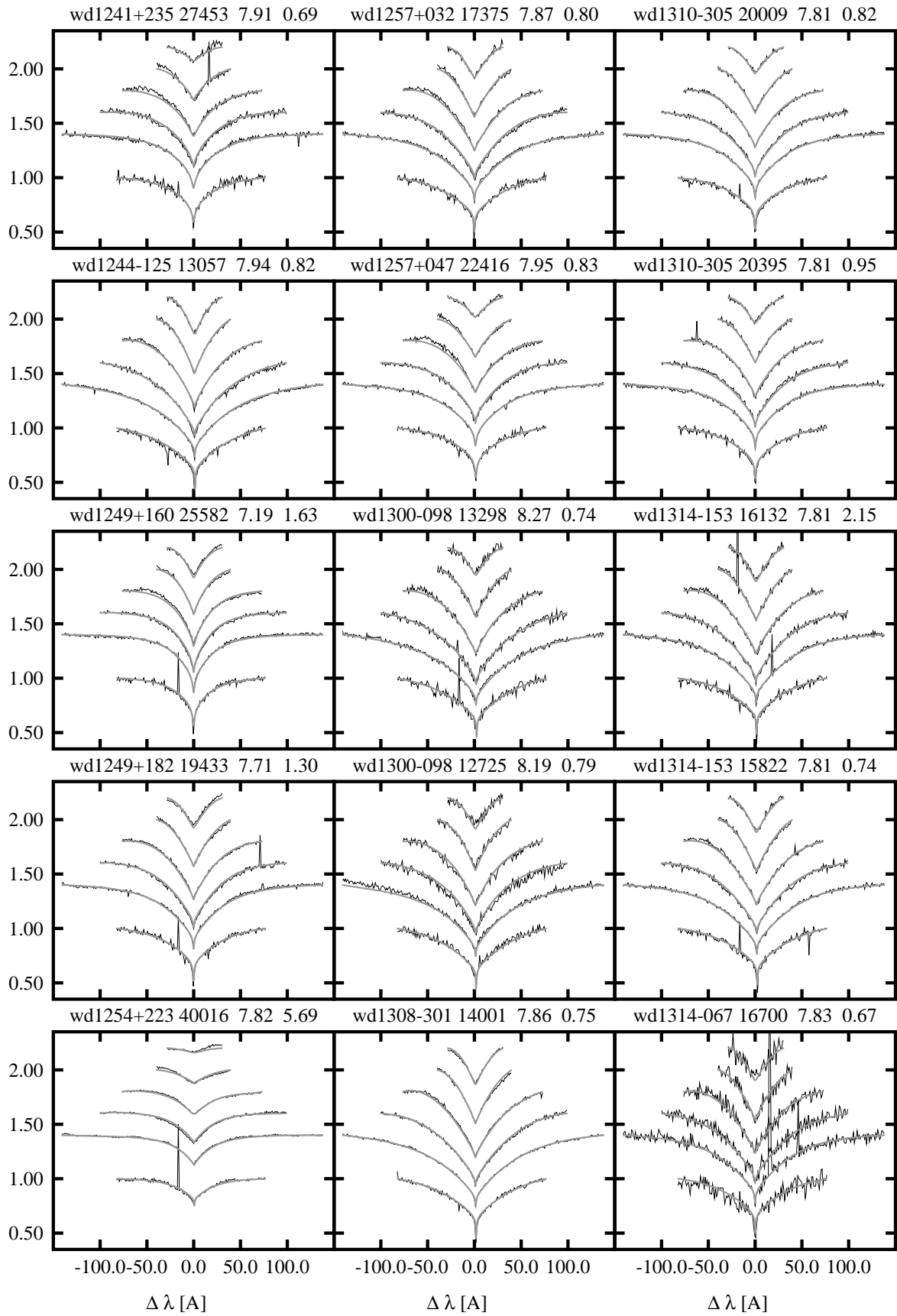


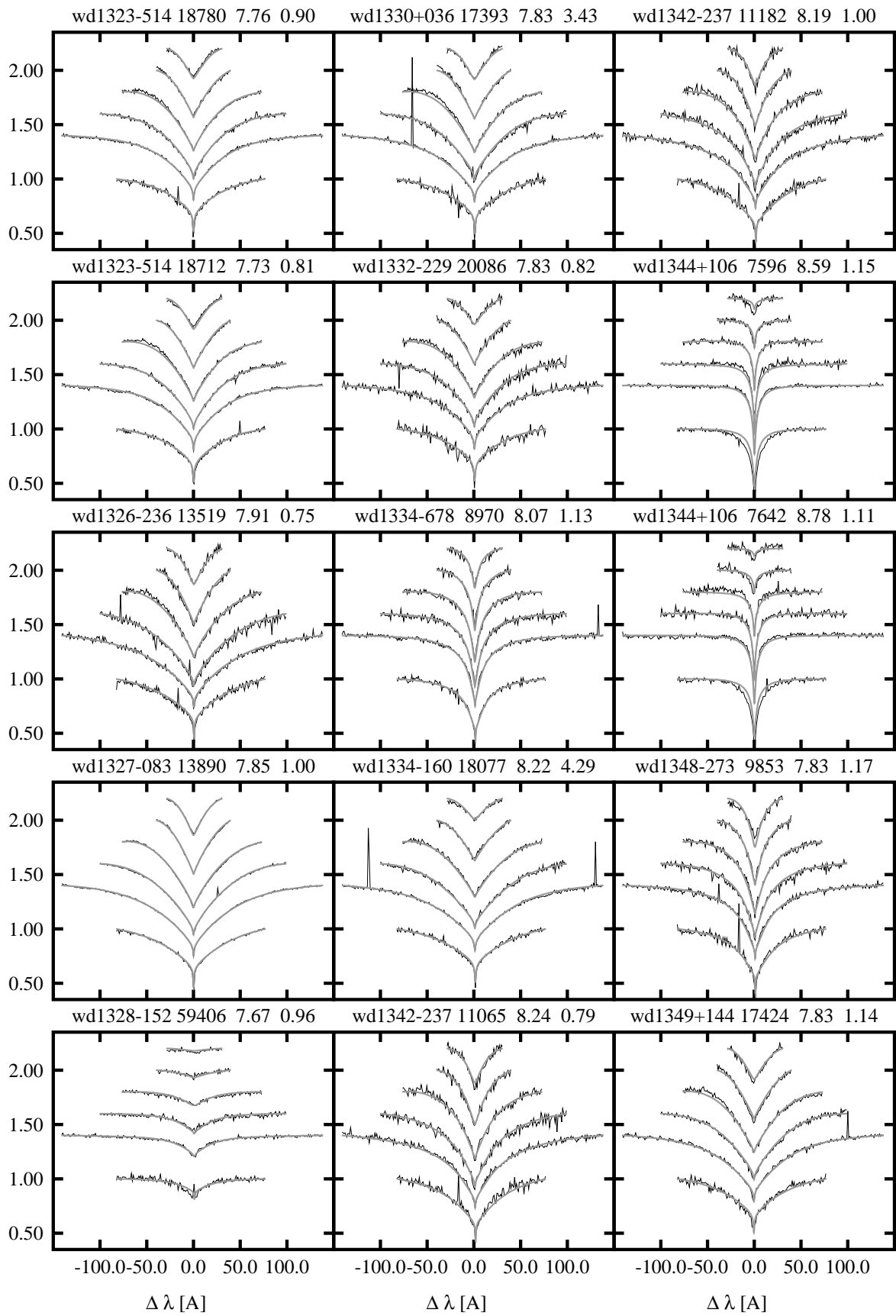
178 APPENDIX G. GRAPHICAL REPRESENTATION OF THE SPY SPECTRA FITS



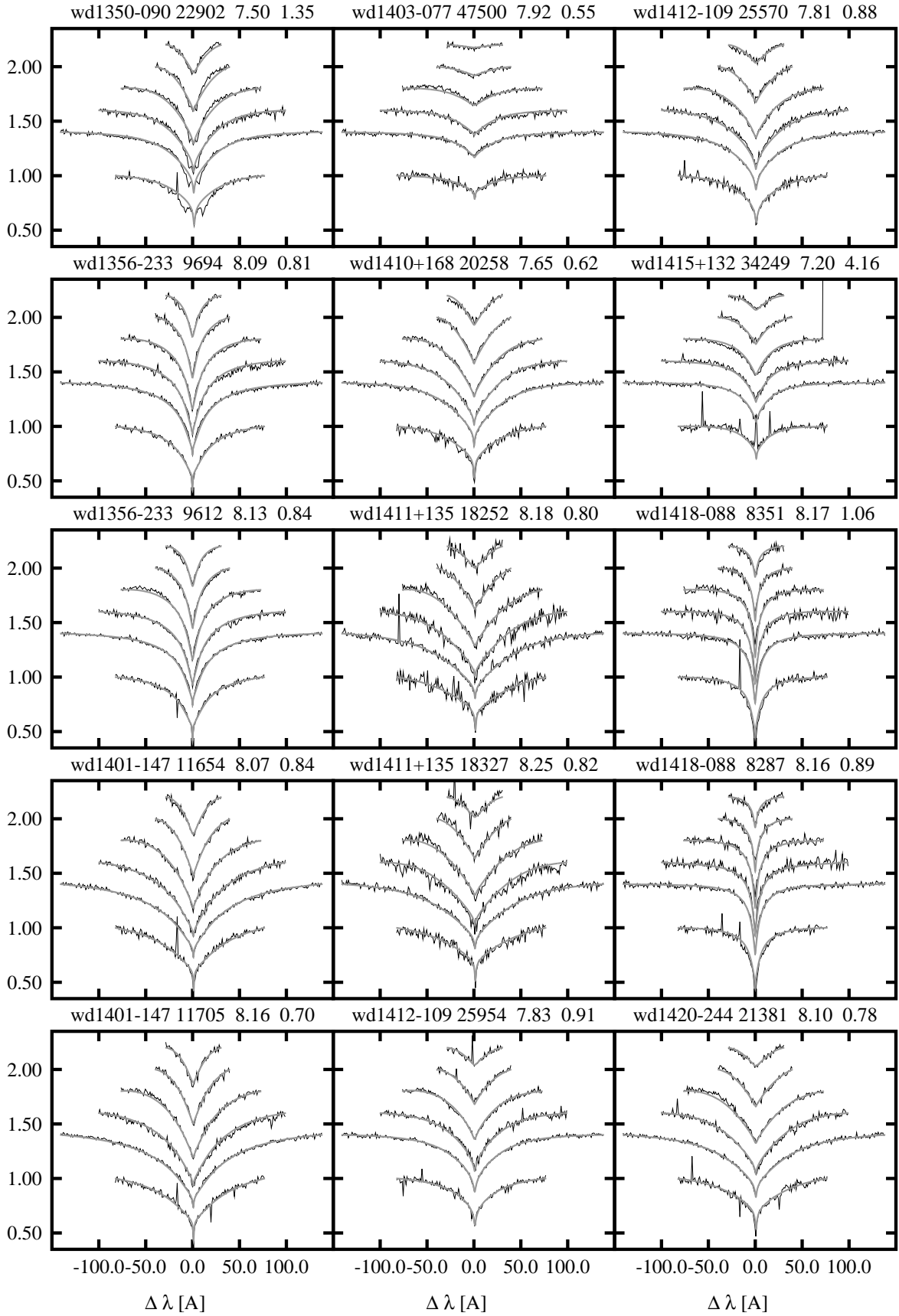


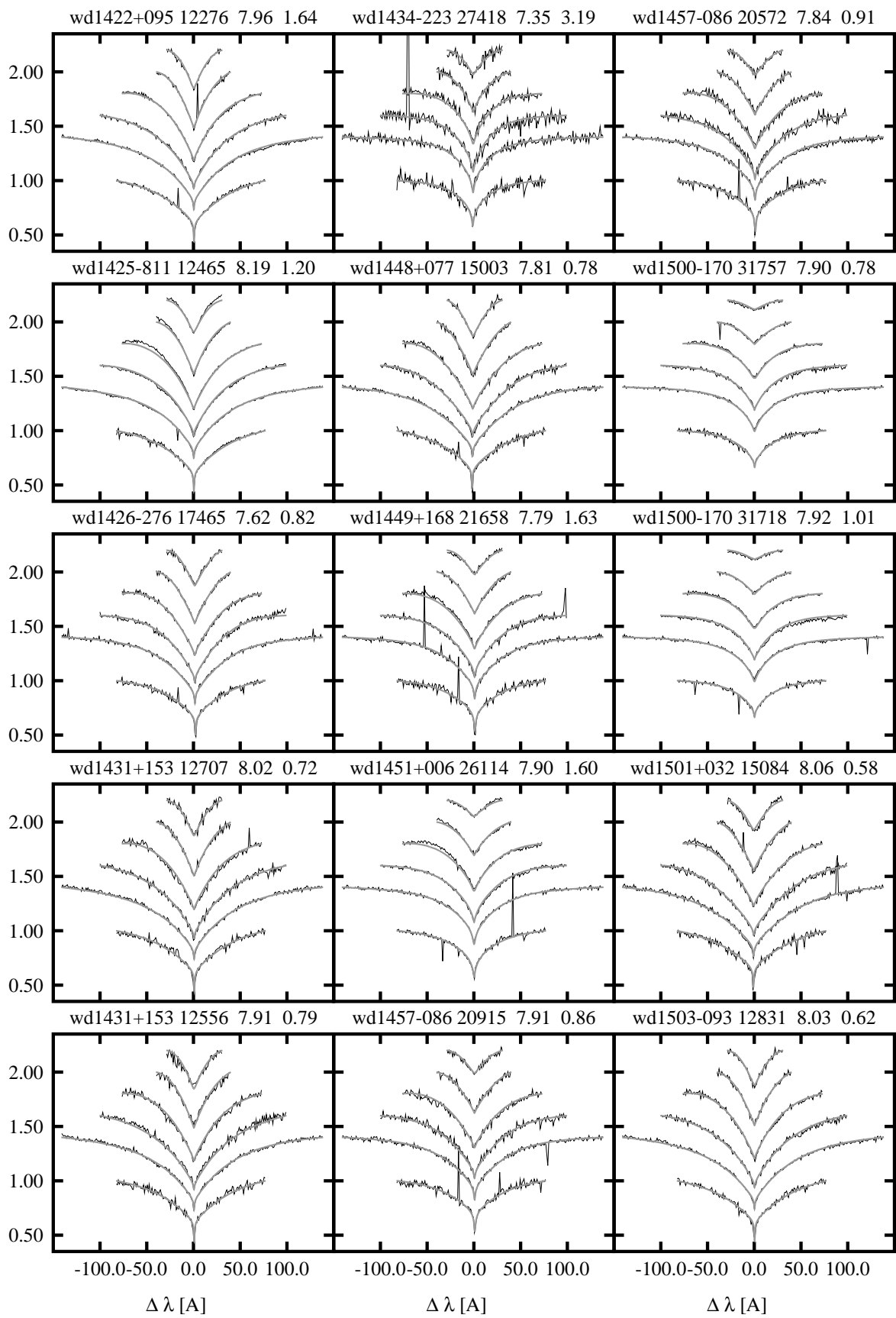
180 APPENDIX G. GRAPHICAL REPRESENTATION OF THE SPY SPECTRA FITS



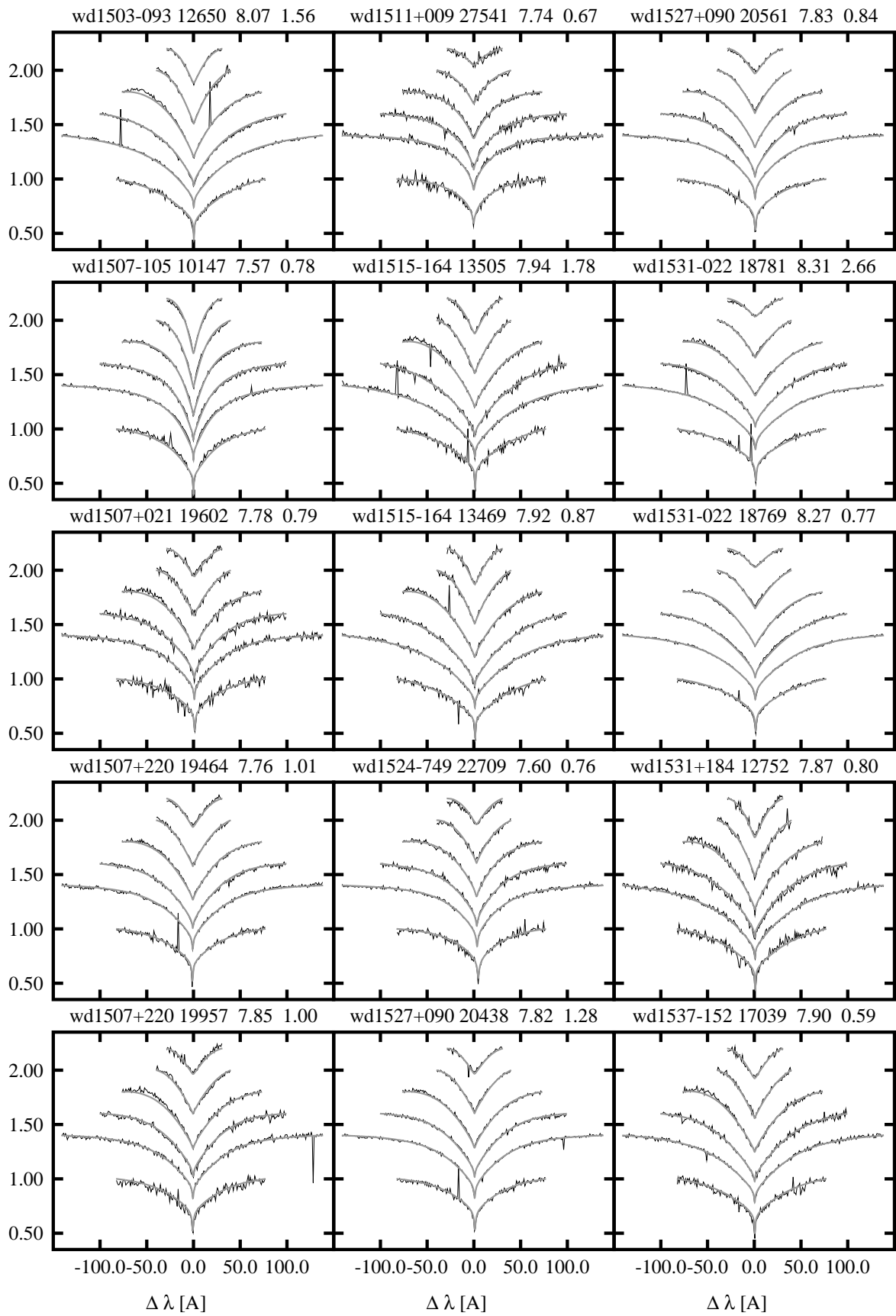


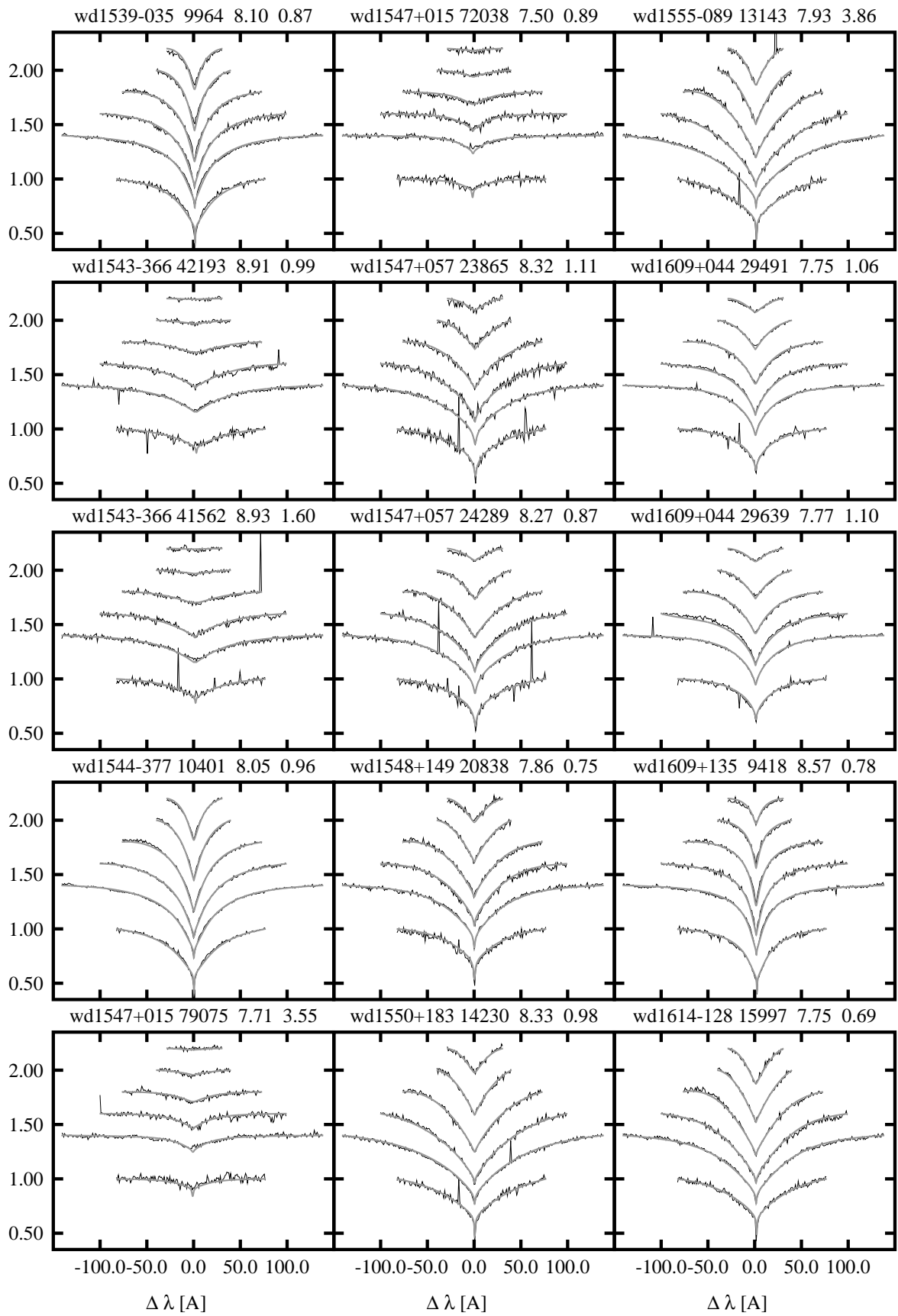
182 APPENDIX G. GRAPHICAL REPRESENTATION OF THE SPY SPECTRA FITS



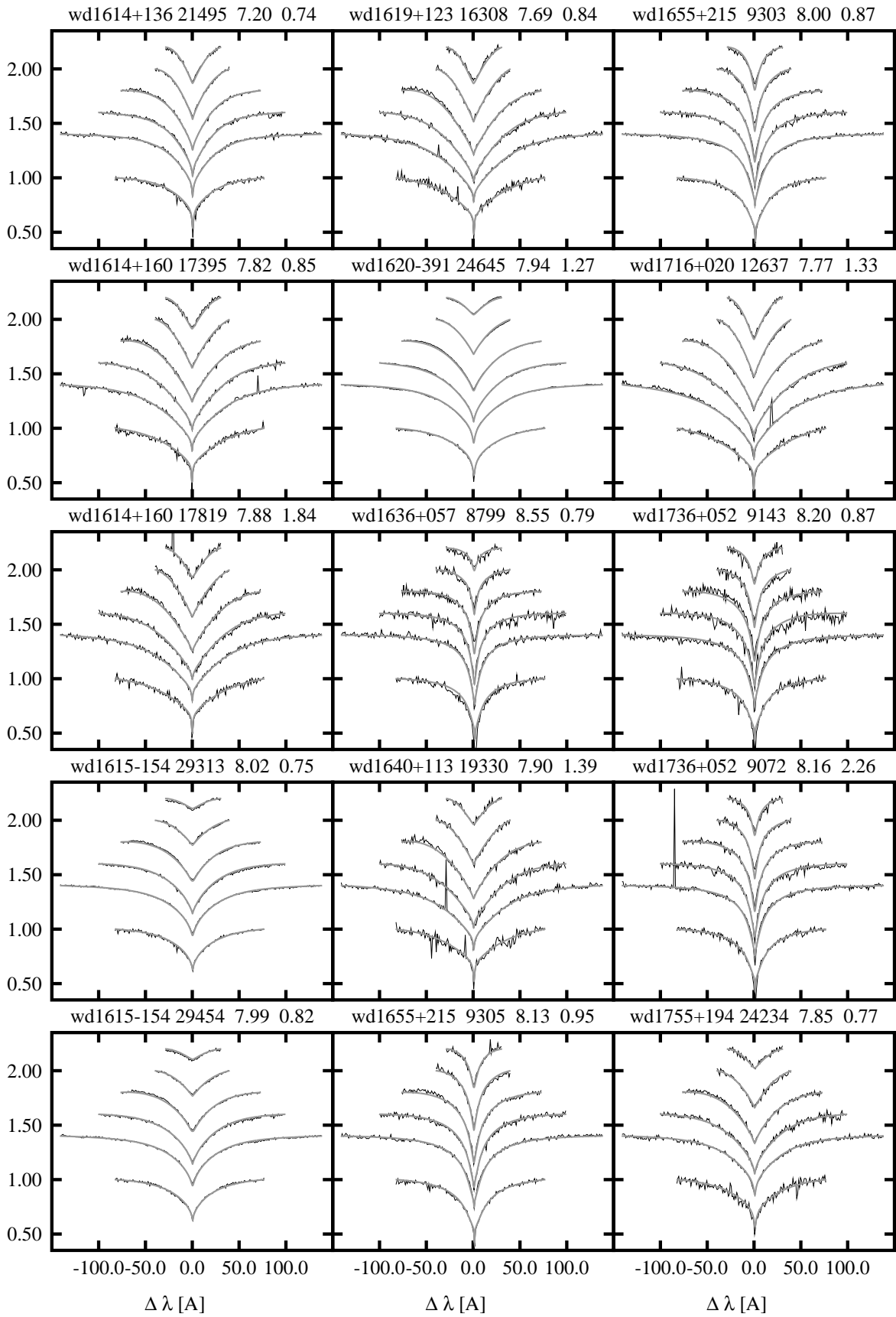


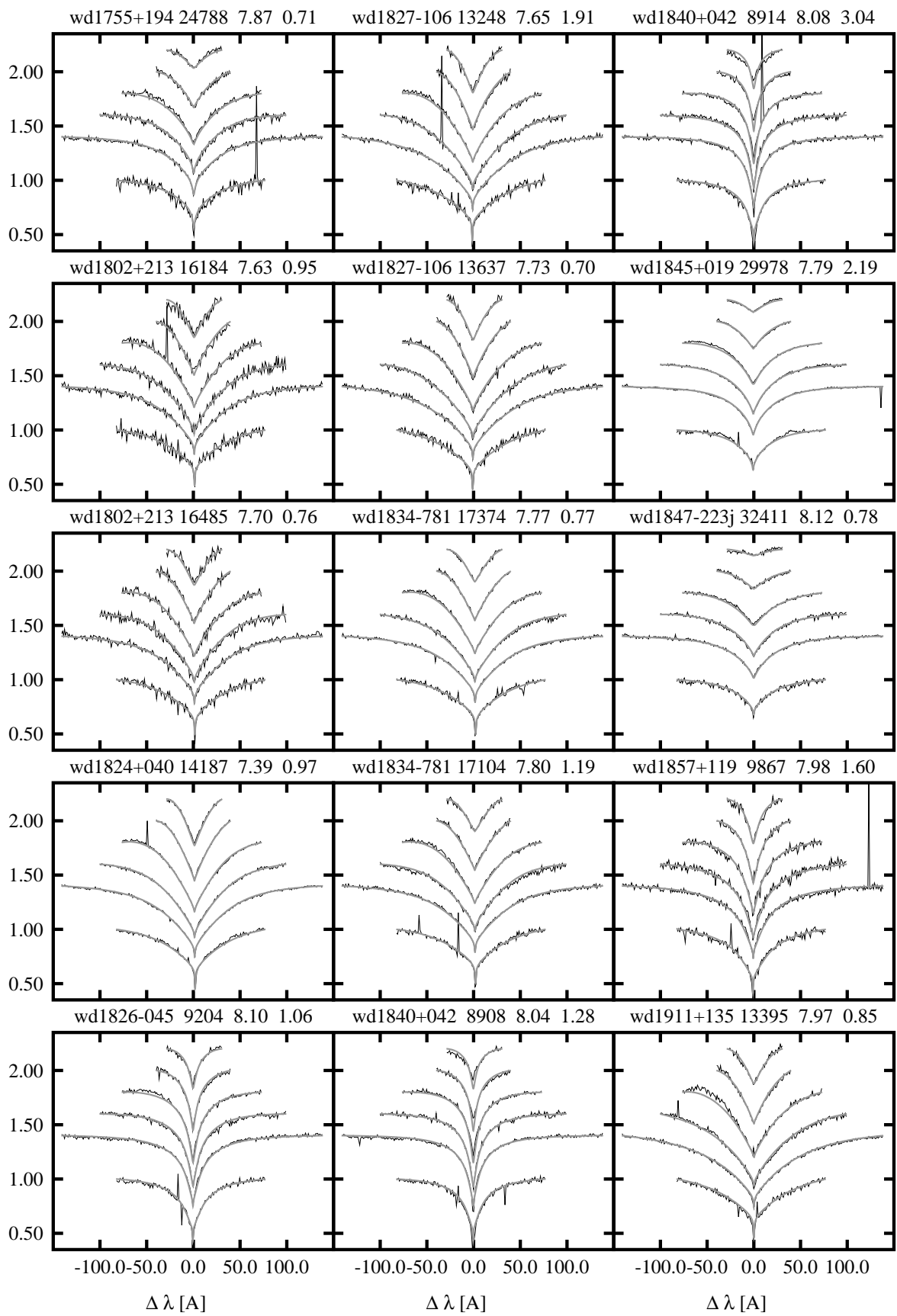
184 APPENDIX G. GRAPHICAL REPRESENTATION OF THE SPY SPECTRA FITS



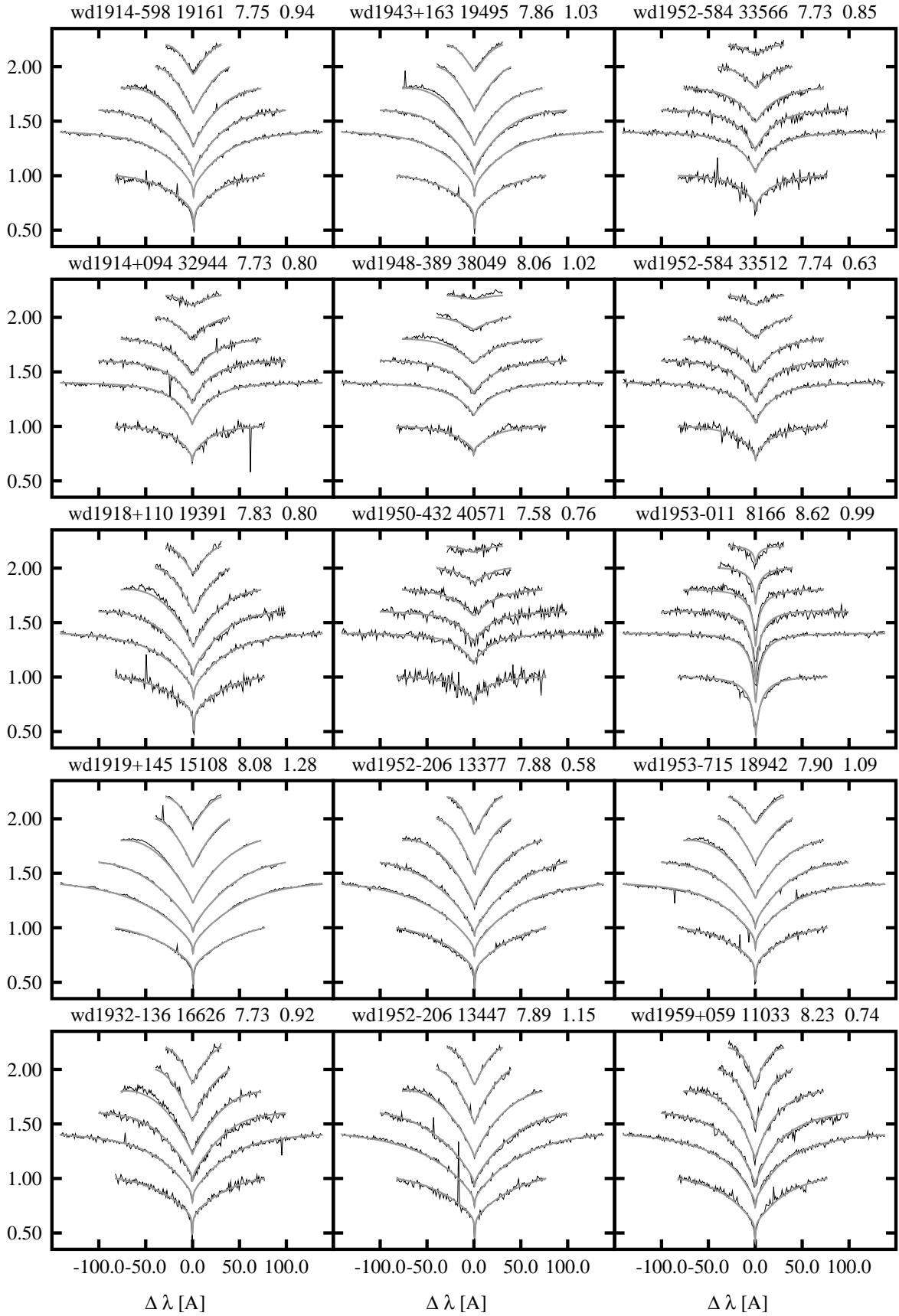


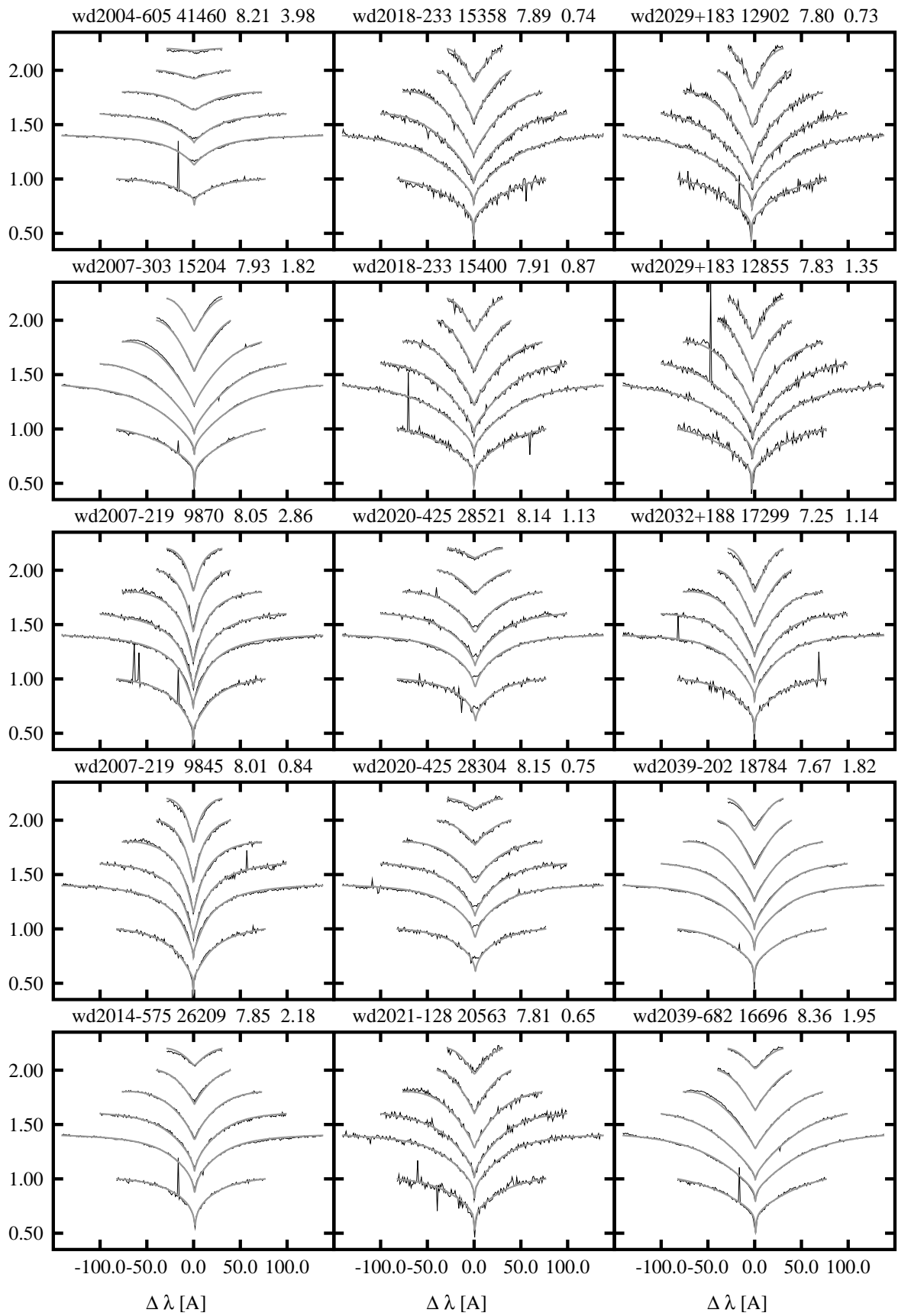
186 APPENDIX G. GRAPHICAL REPRESENTATION OF THE SPY SPECTRA FITS



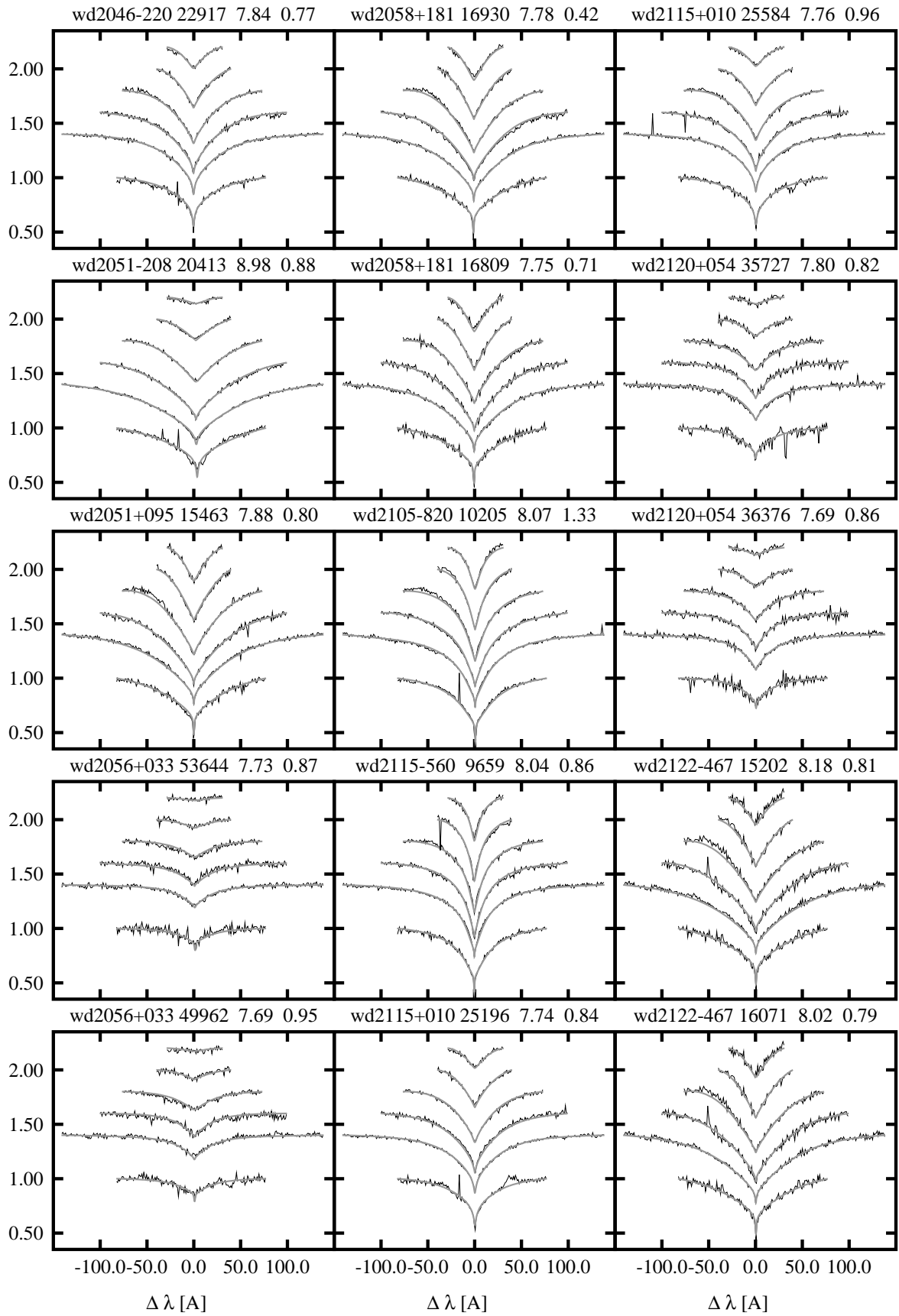


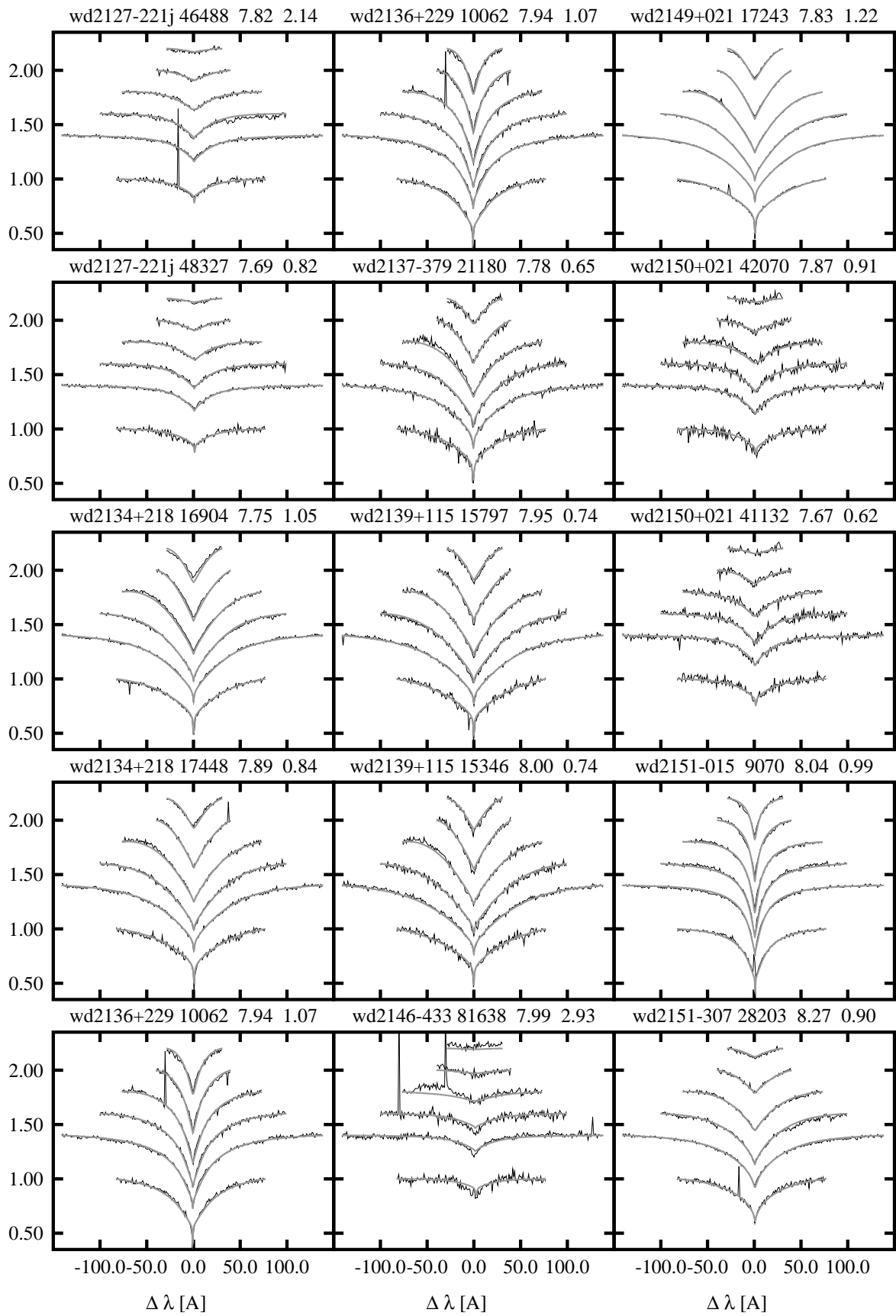
188 APPENDIX G. GRAPHICAL REPRESENTATION OF THE SPY SPECTRA FITS



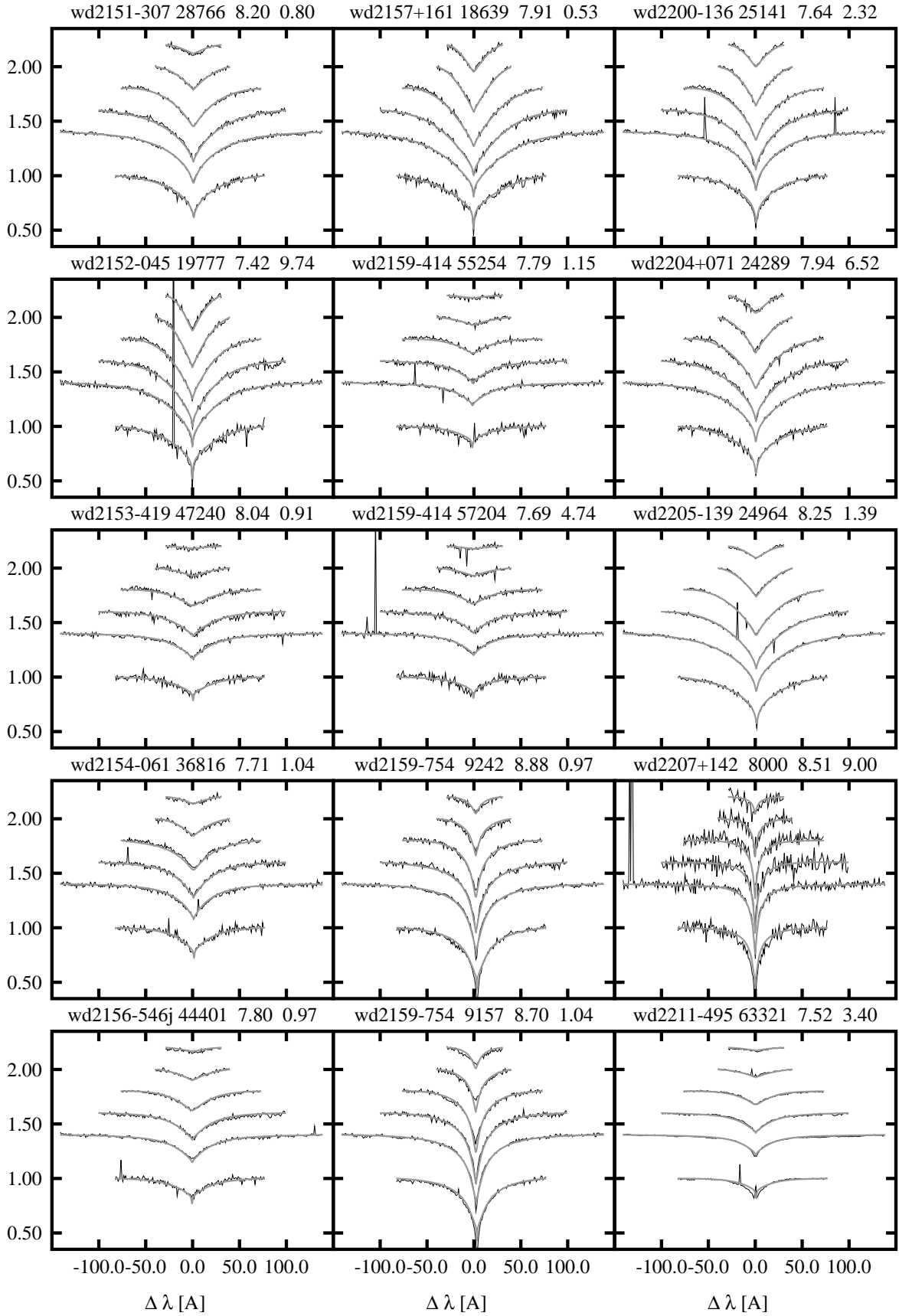


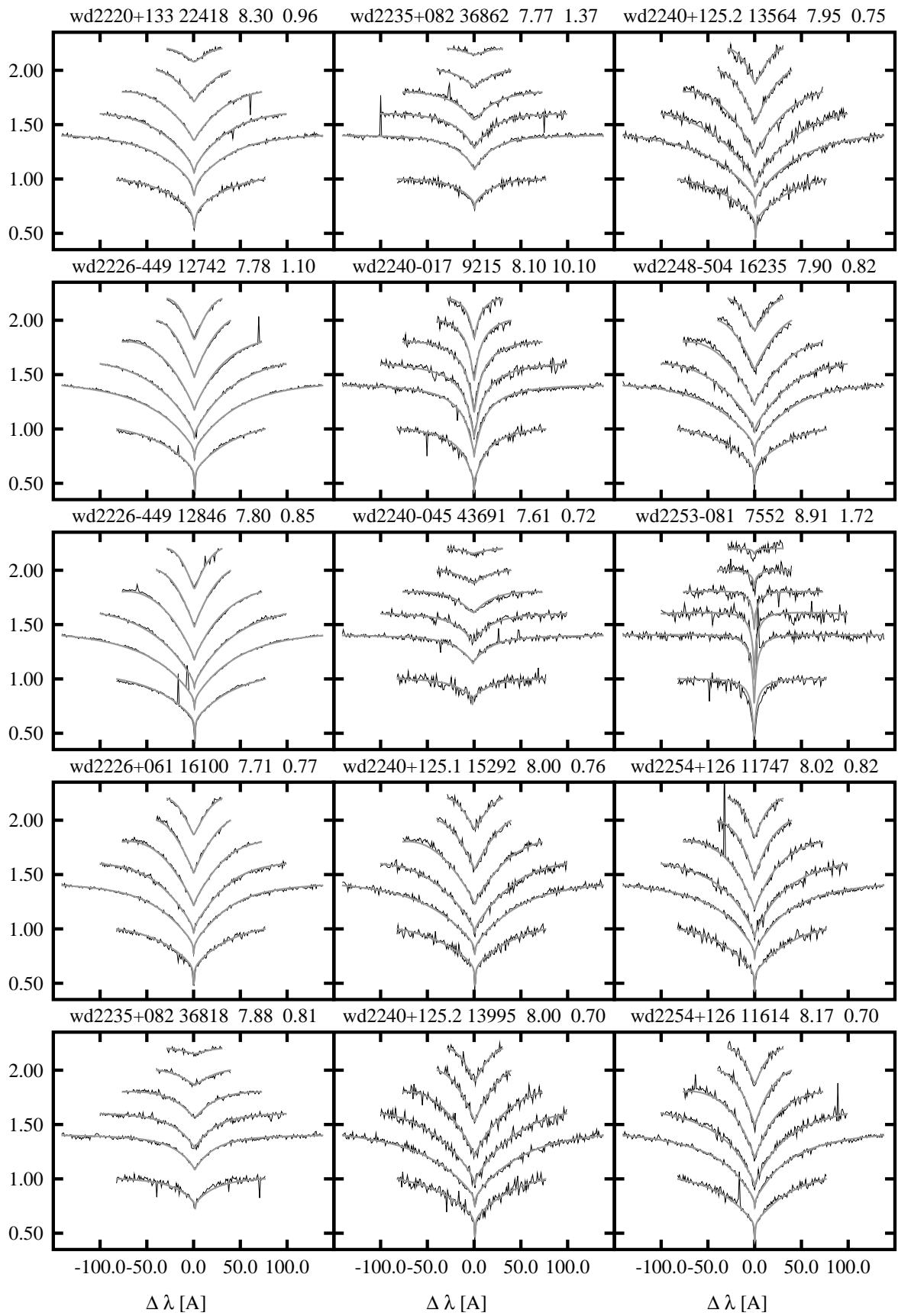
190 APPENDIX G. GRAPHICAL REPRESENTATION OF THE SPY SPECTRA FITS



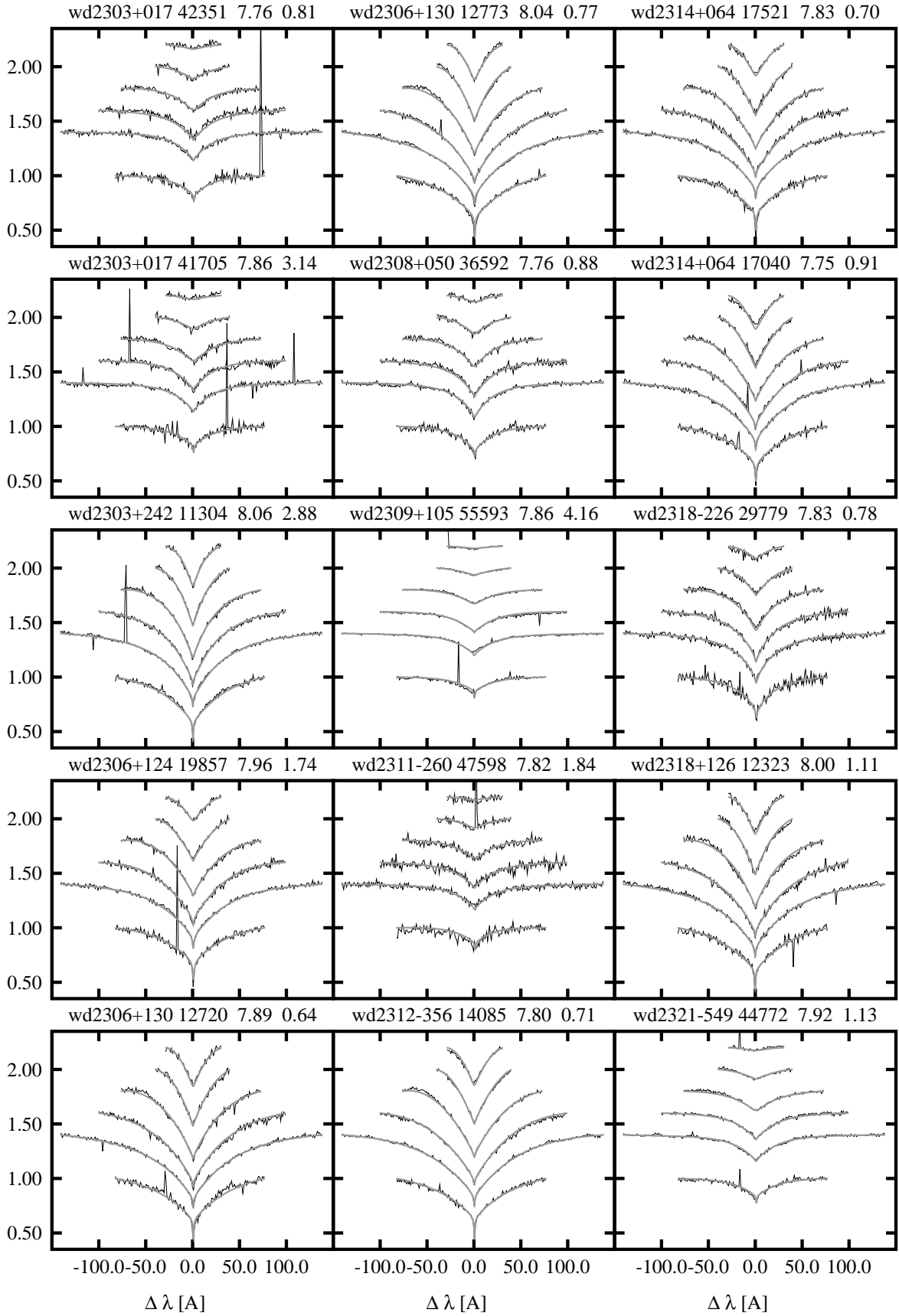


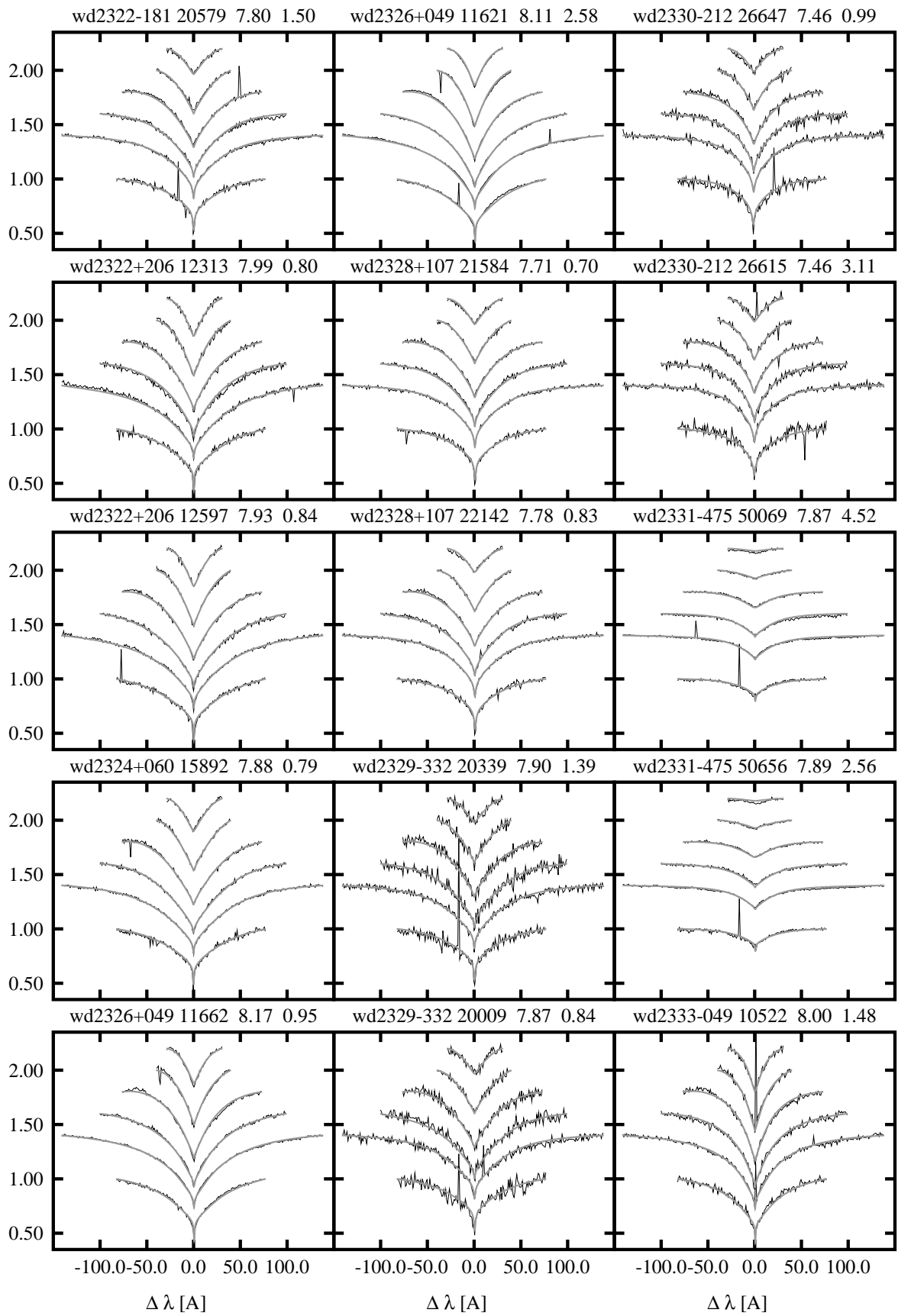
192 APPENDIX G. GRAPHICAL REPRESENTATION OF THE SPY SPECTRA FITS



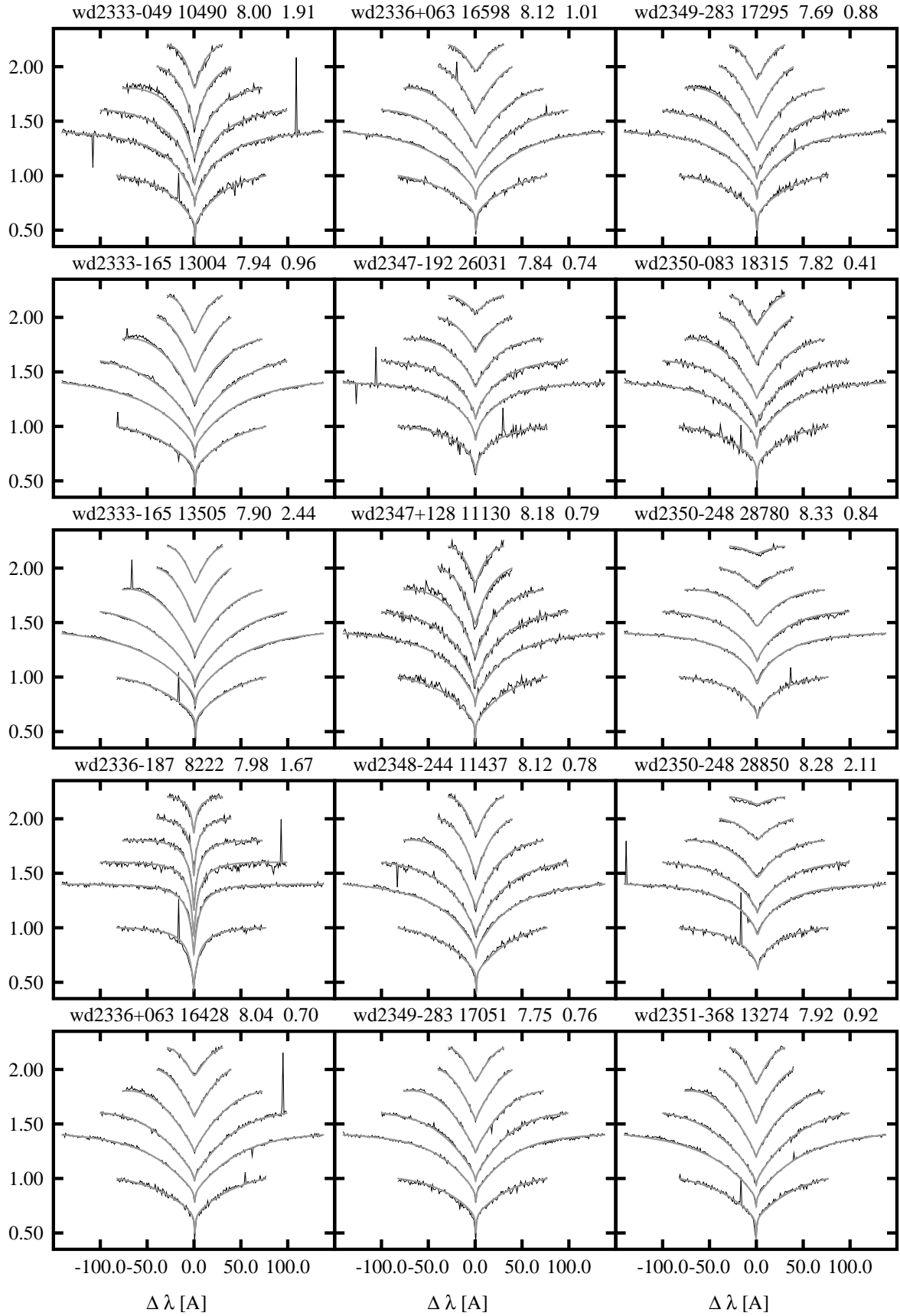


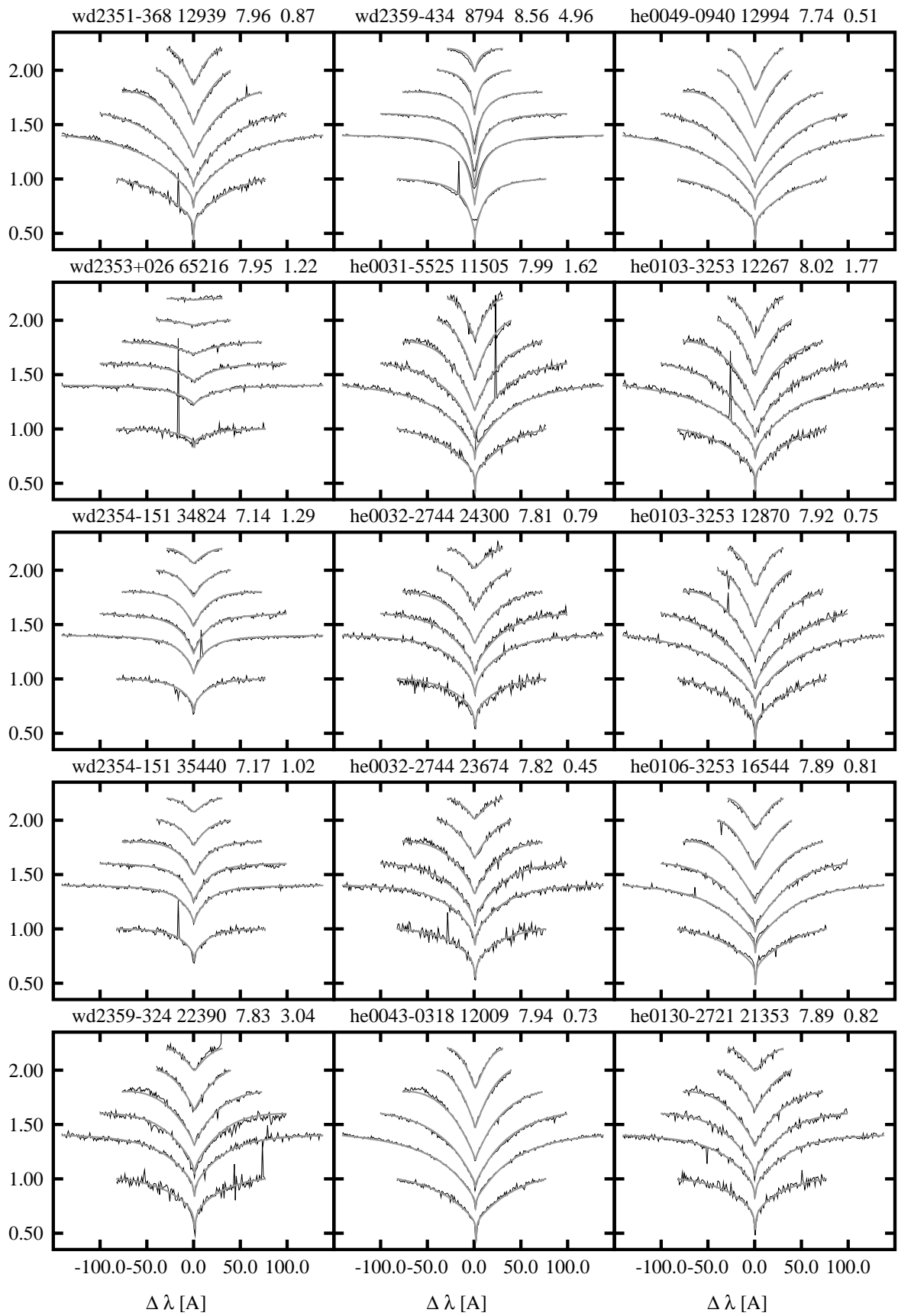
194 APPENDIX G. GRAPHICAL REPRESENTATION OF THE SPY SPECTRA FITS



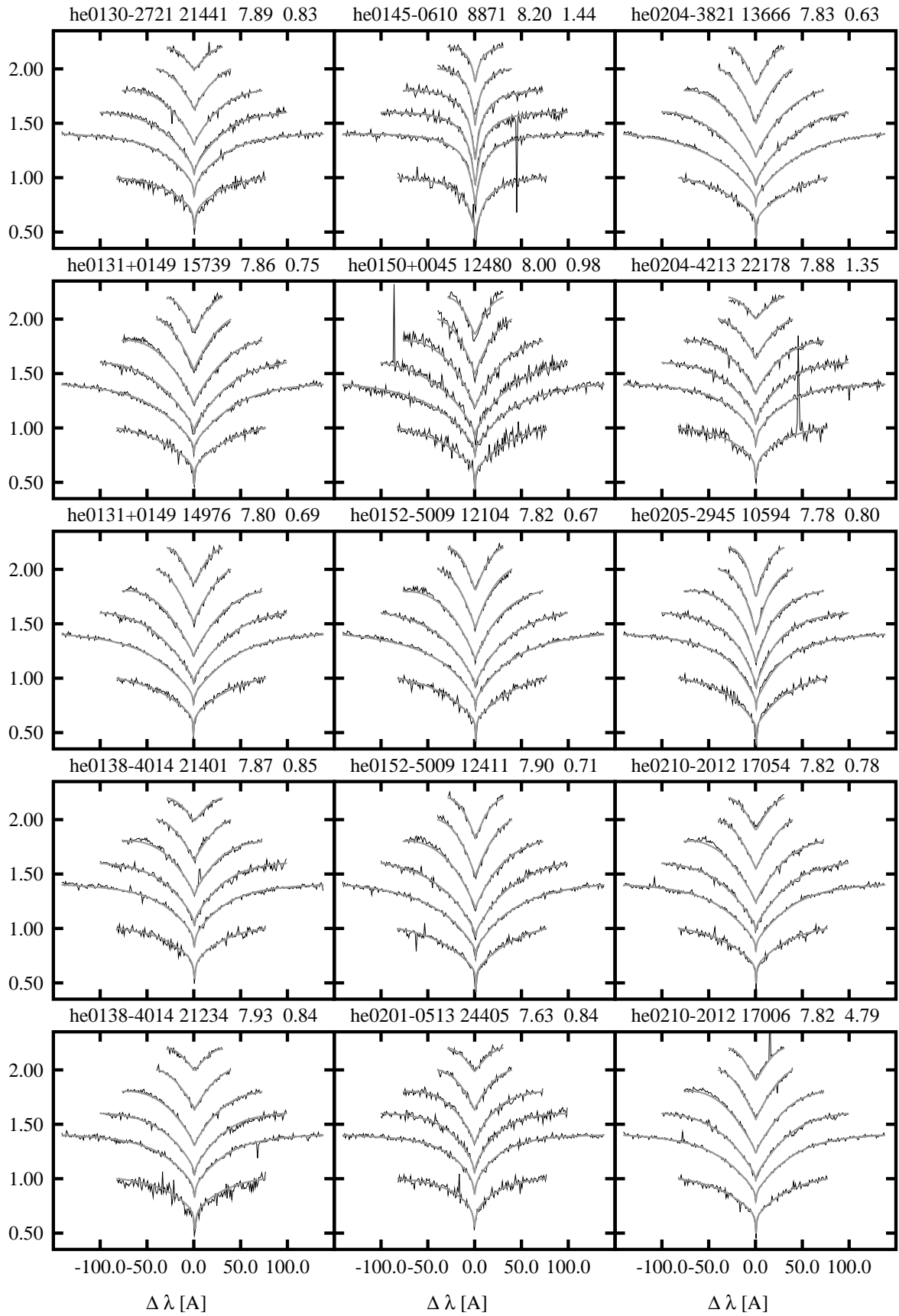


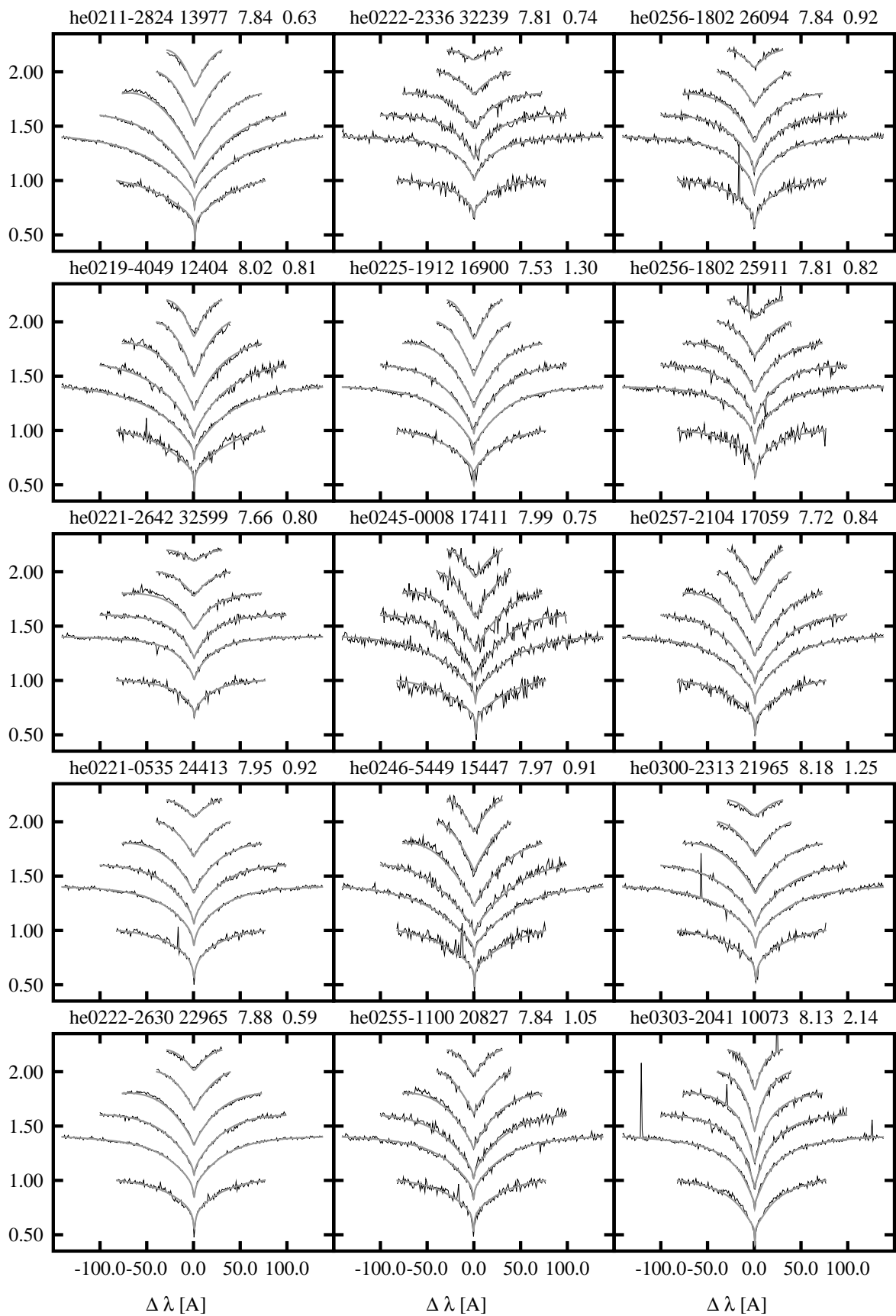
196 APPENDIX G. GRAPHICAL REPRESENTATION OF THE SPY SPECTRA FITS



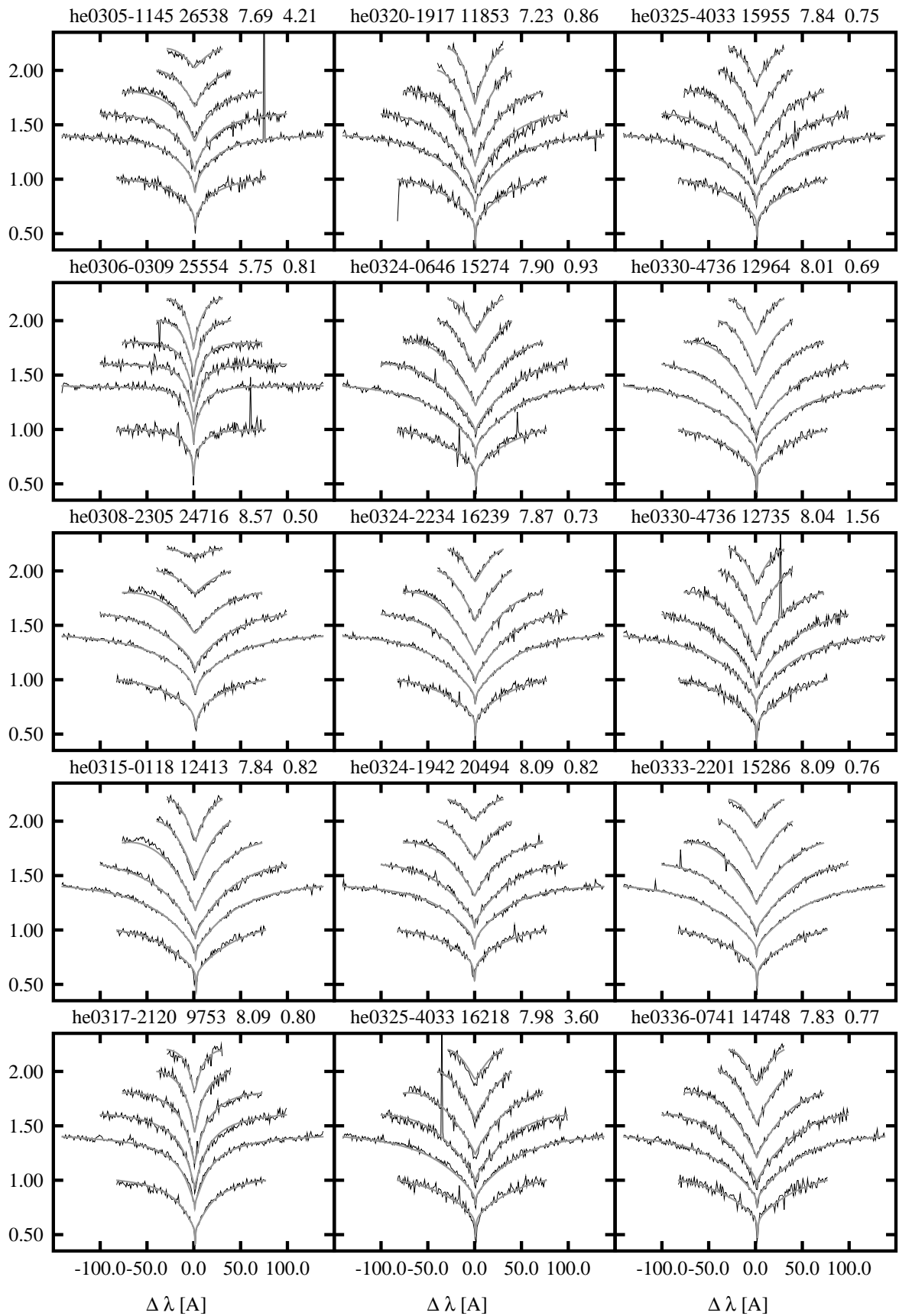


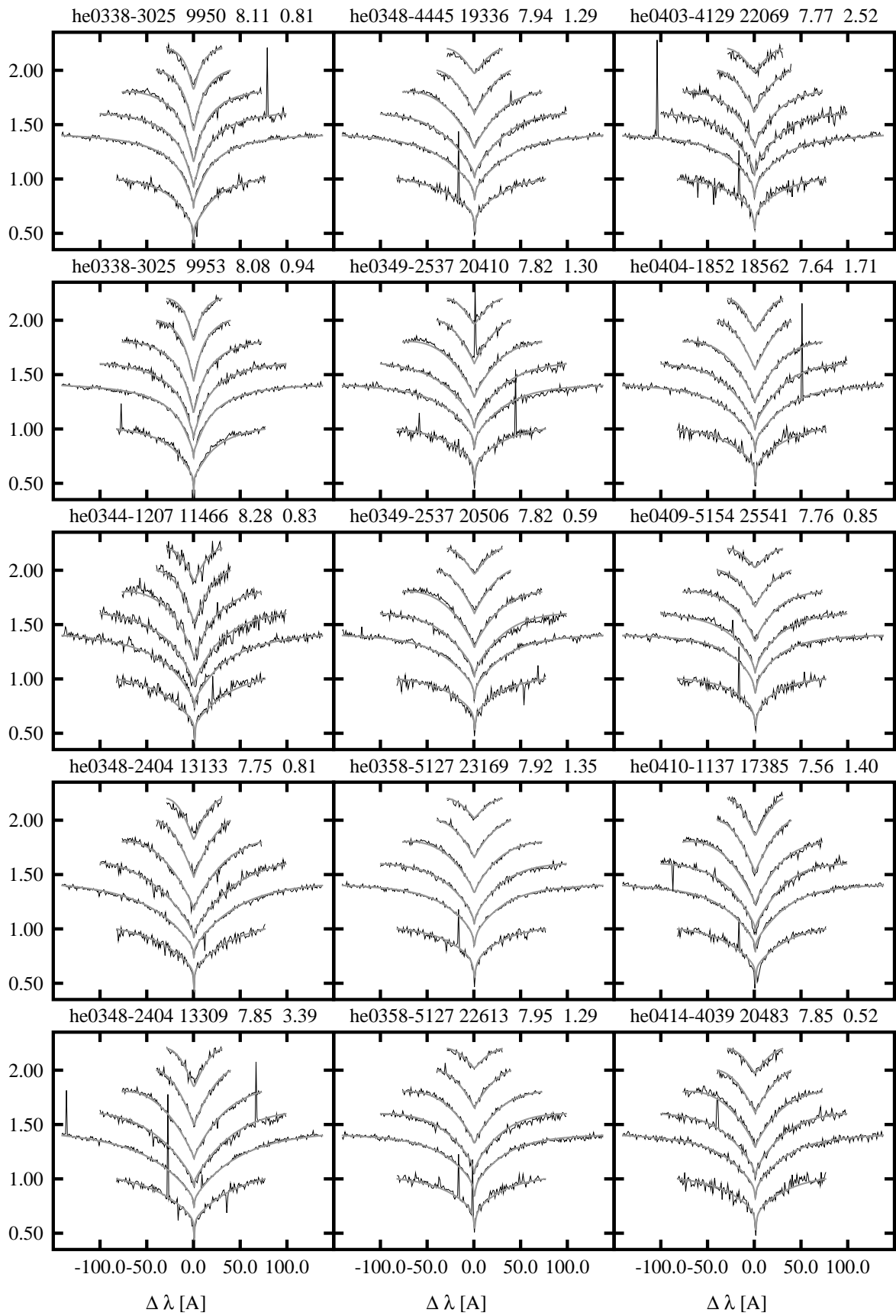
198 APPENDIX G. GRAPHICAL REPRESENTATION OF THE SPY SPECTRA FITS



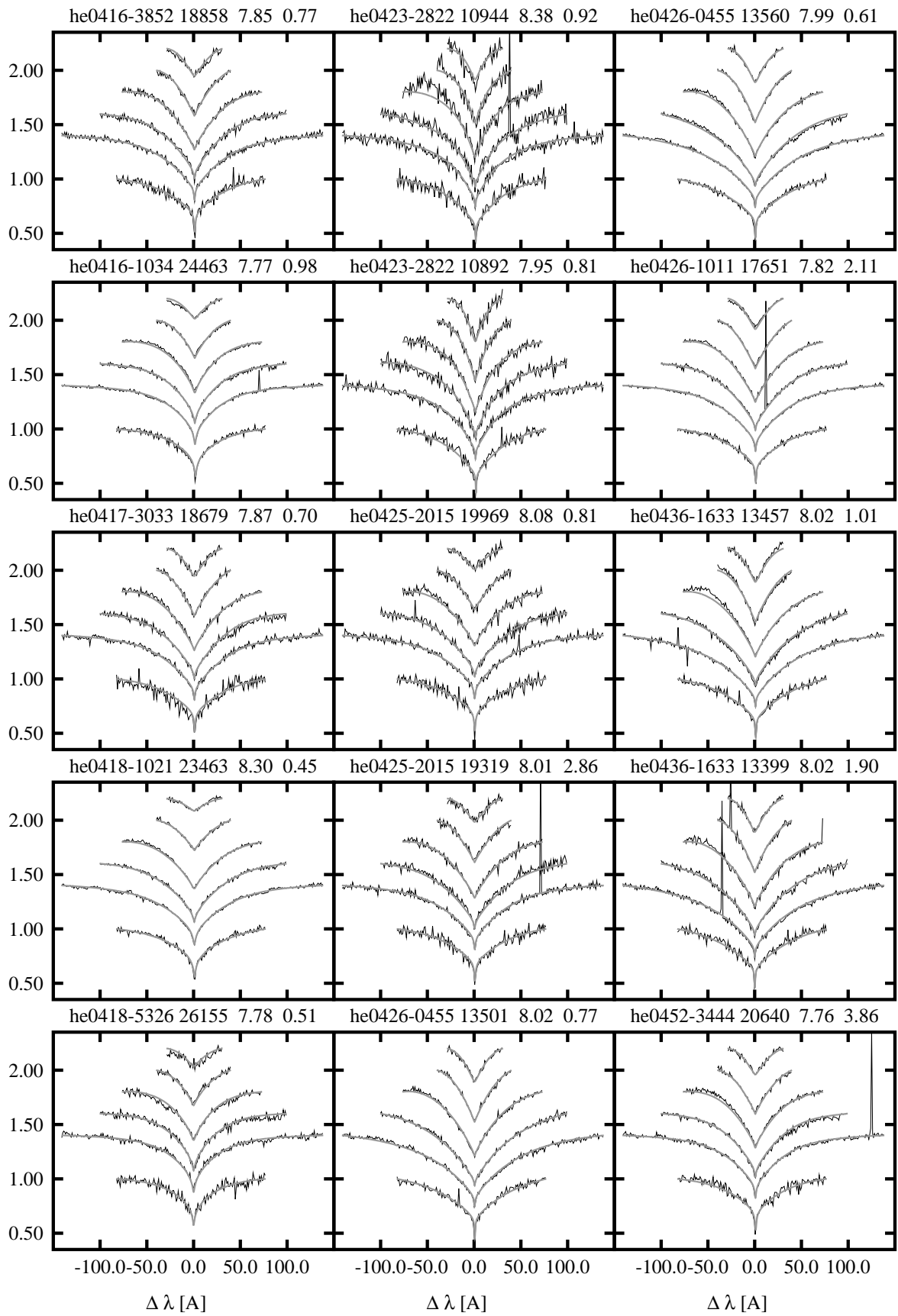


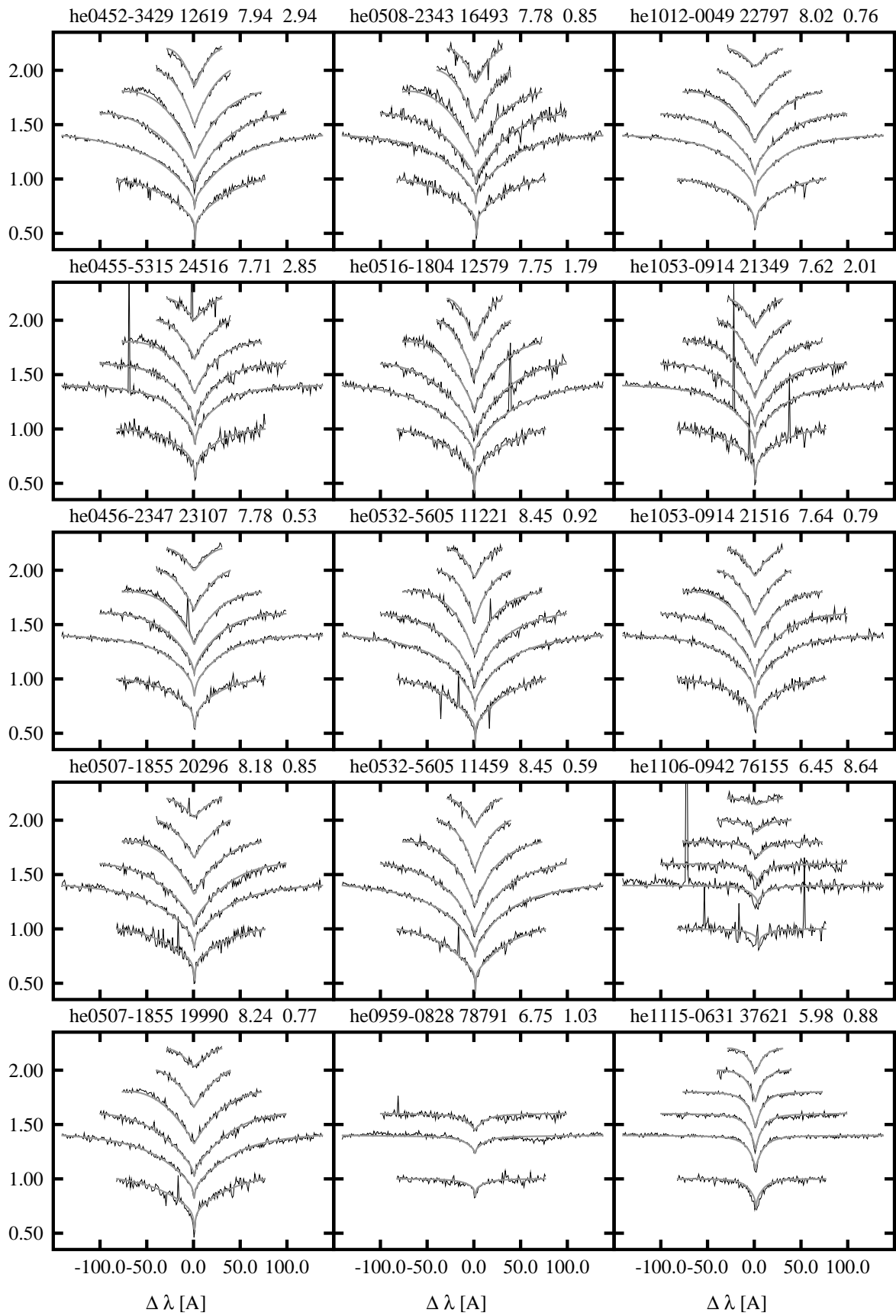
200 APPENDIX G. GRAPHICAL REPRESENTATION OF THE SPY SPECTRA FITS



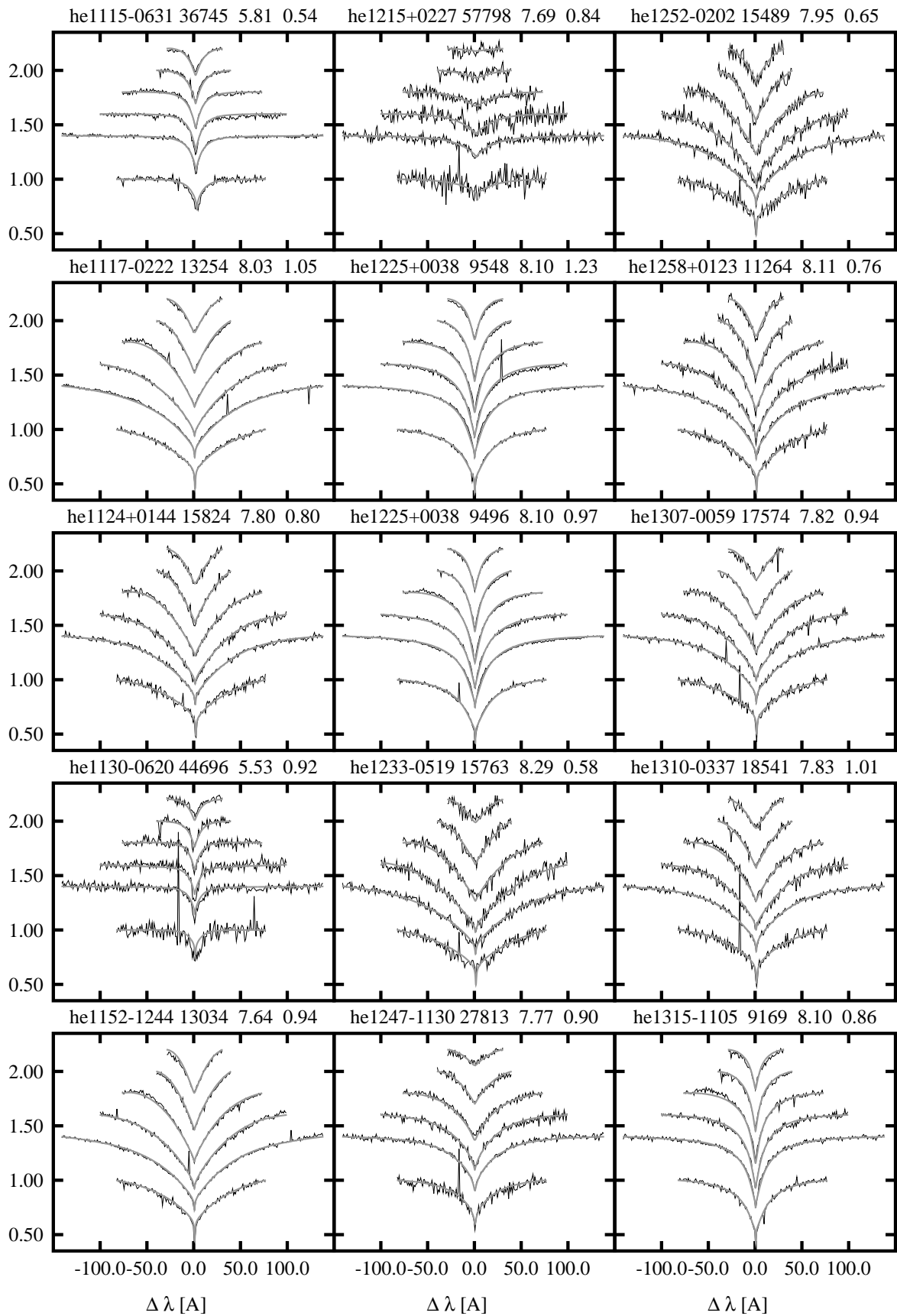


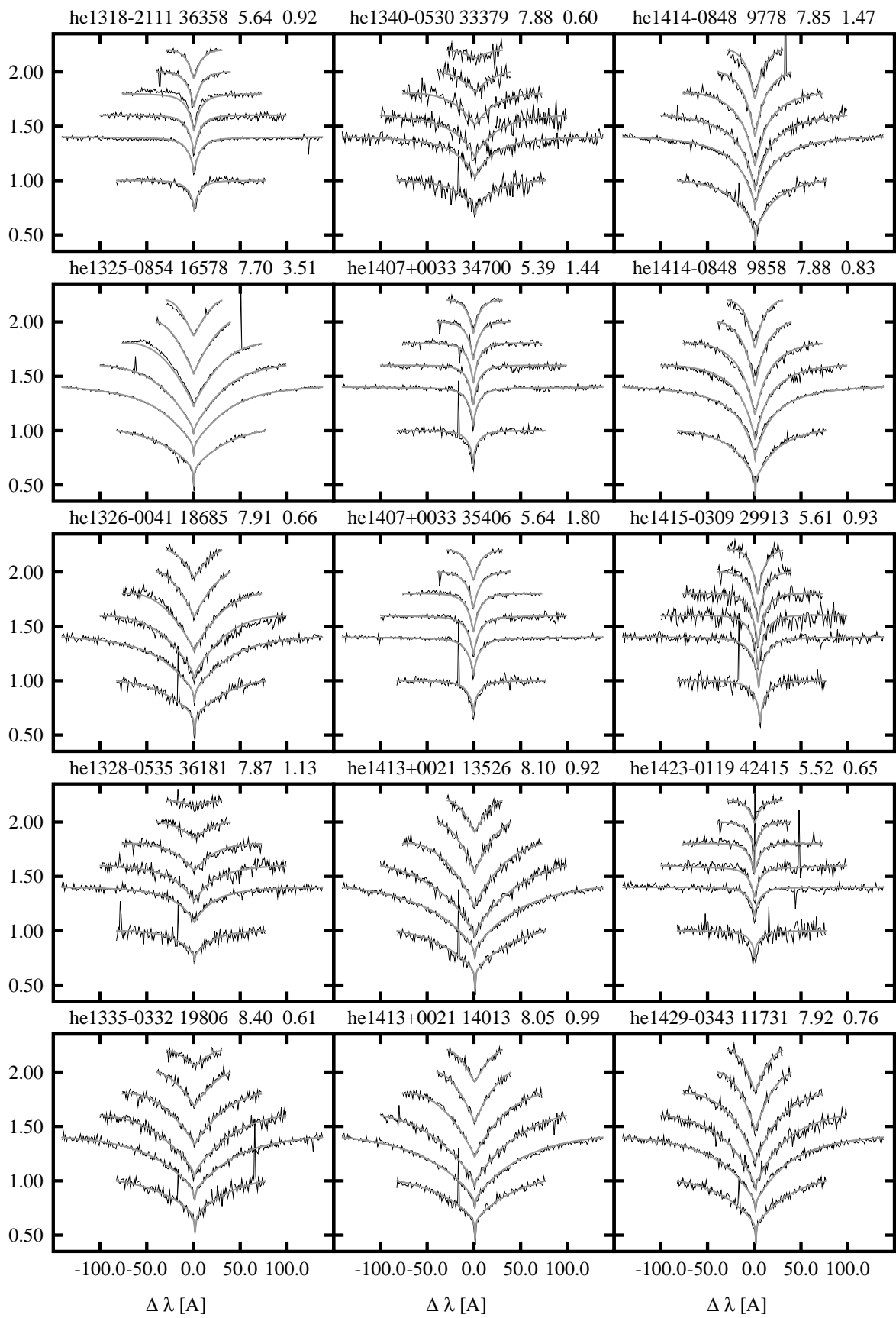
202 APPENDIX G. GRAPHICAL REPRESENTATION OF THE SPY SPECTRA FITS



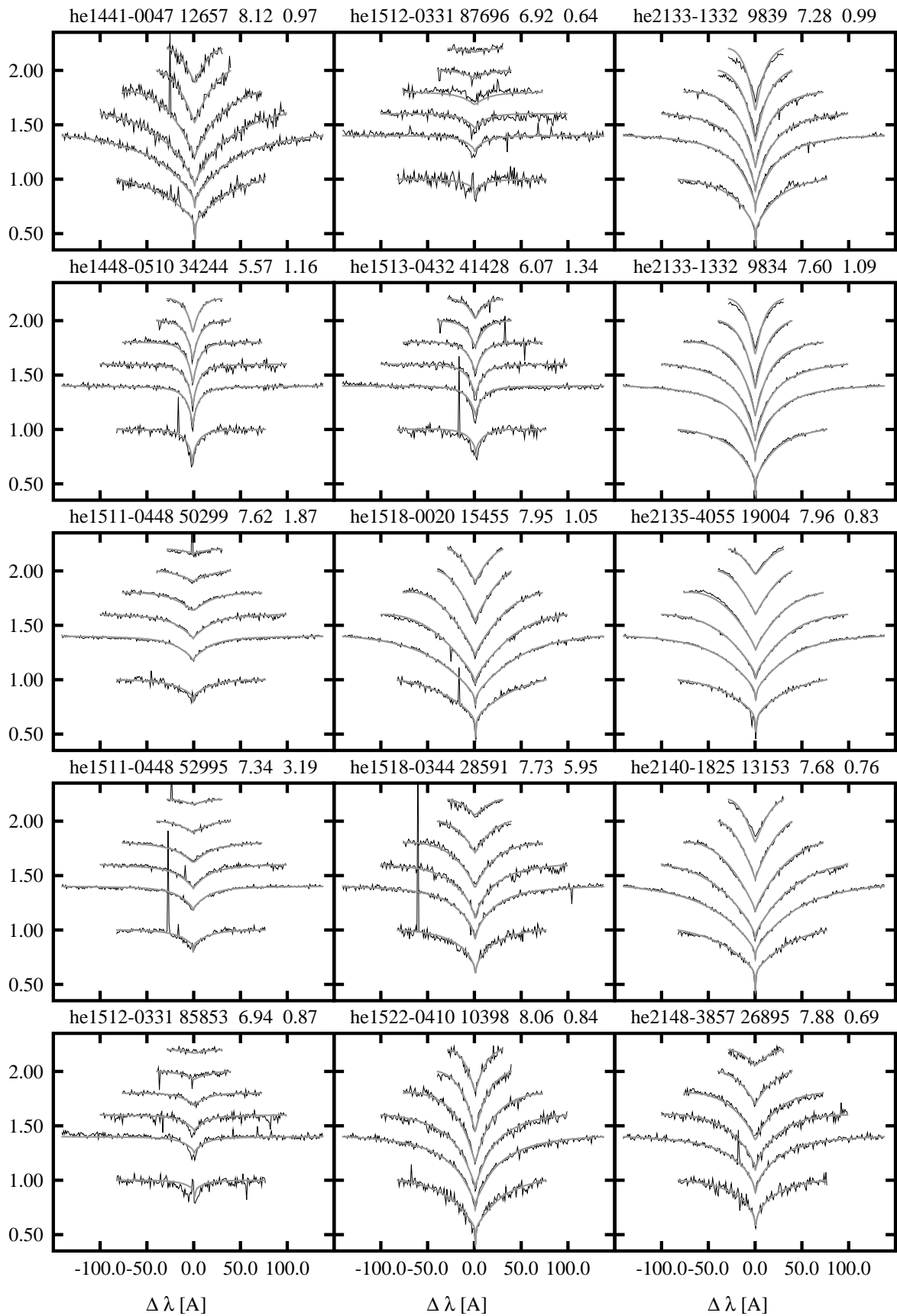


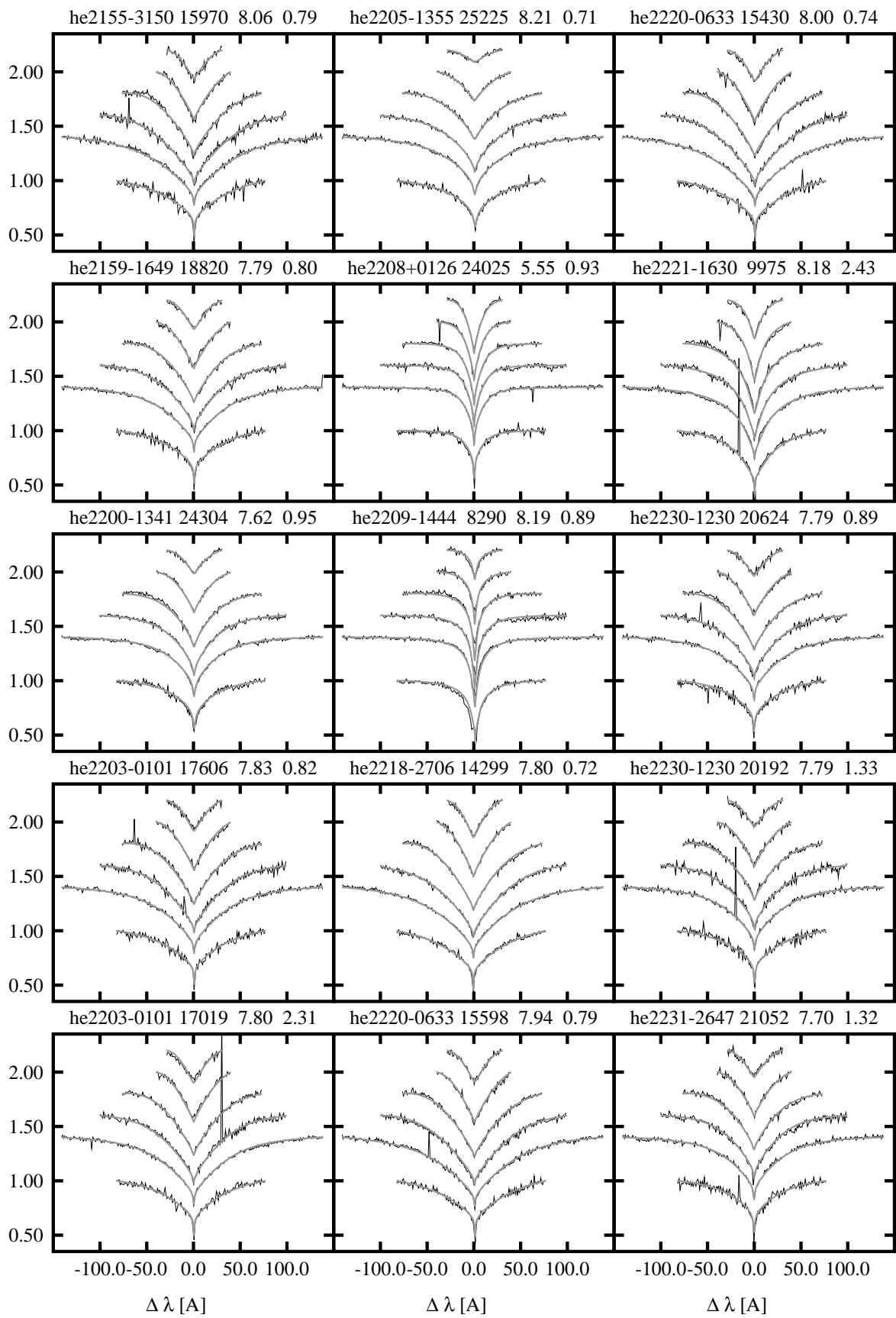
204 APPENDIX G. GRAPHICAL REPRESENTATION OF THE SPY SPECTRA FITS



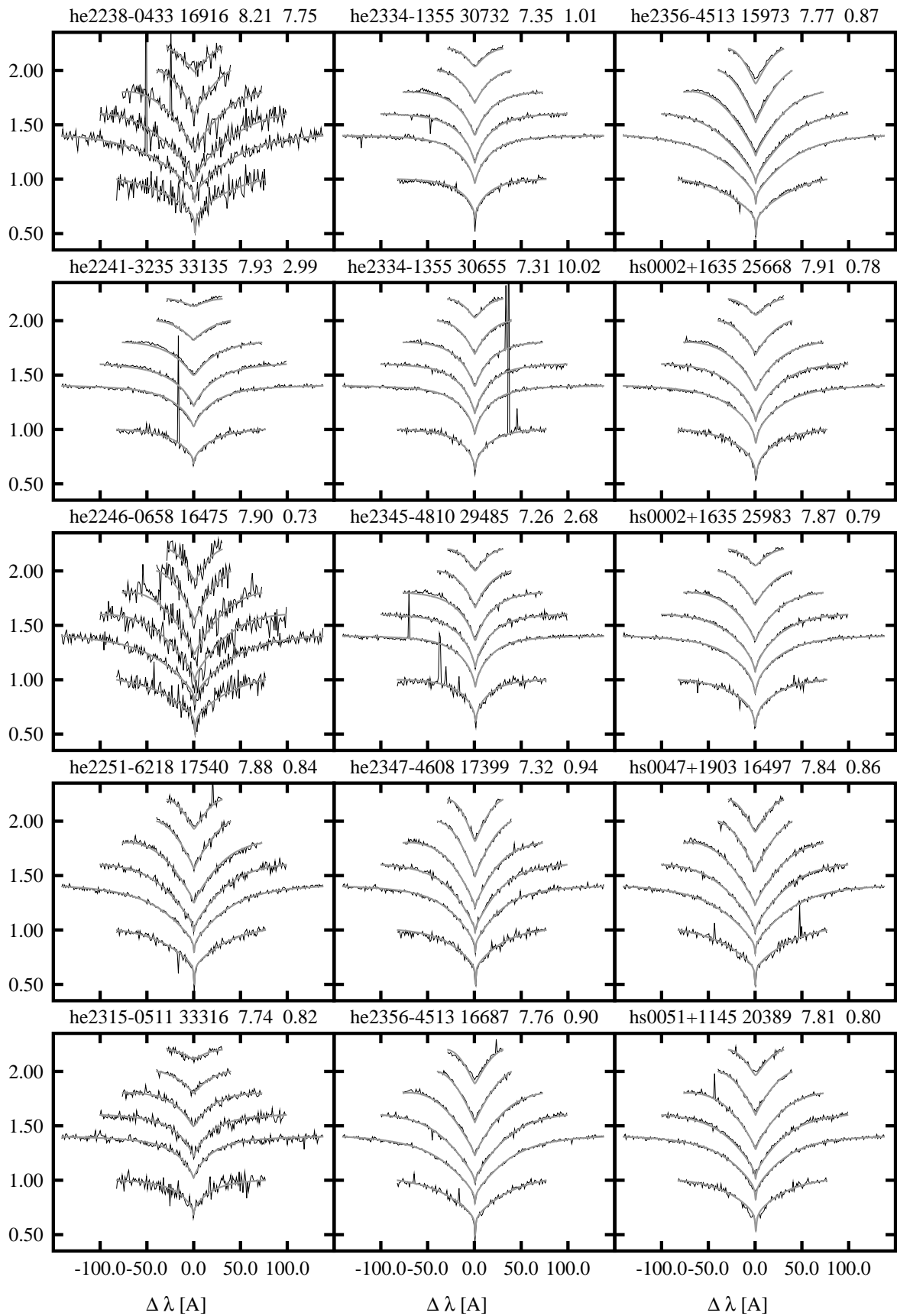


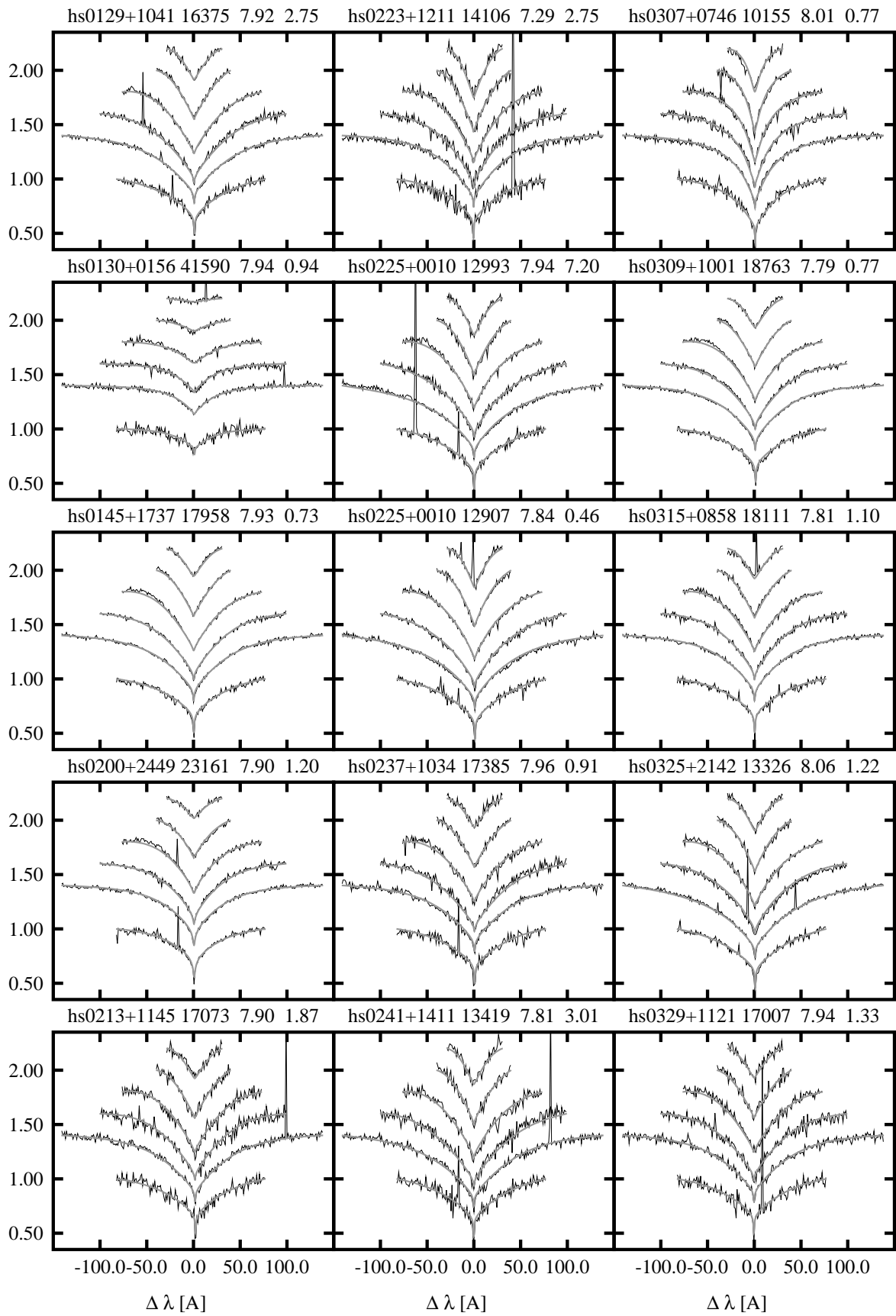
206 APPENDIX G. GRAPHICAL REPRESENTATION OF THE SPY SPECTRA FITS



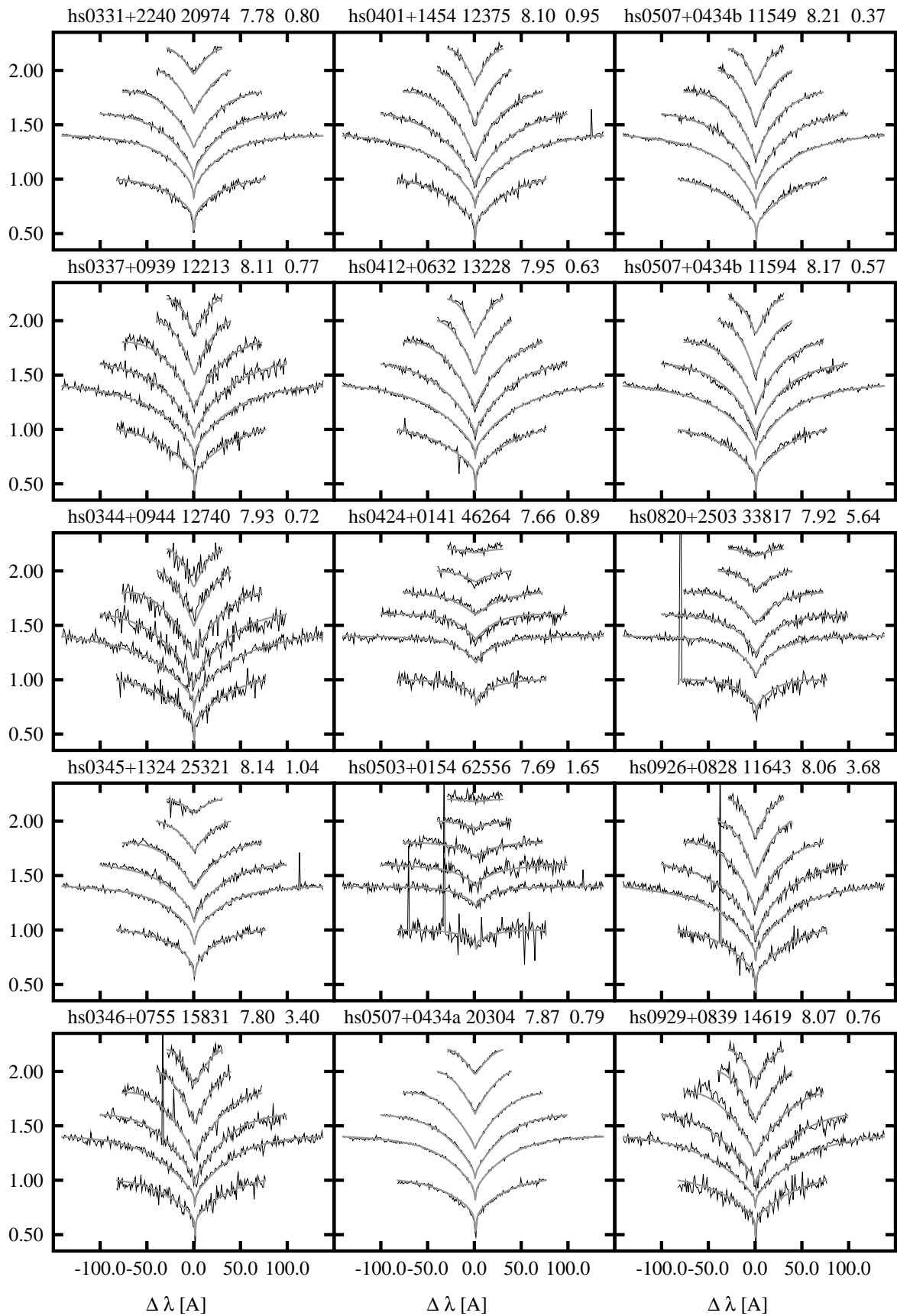


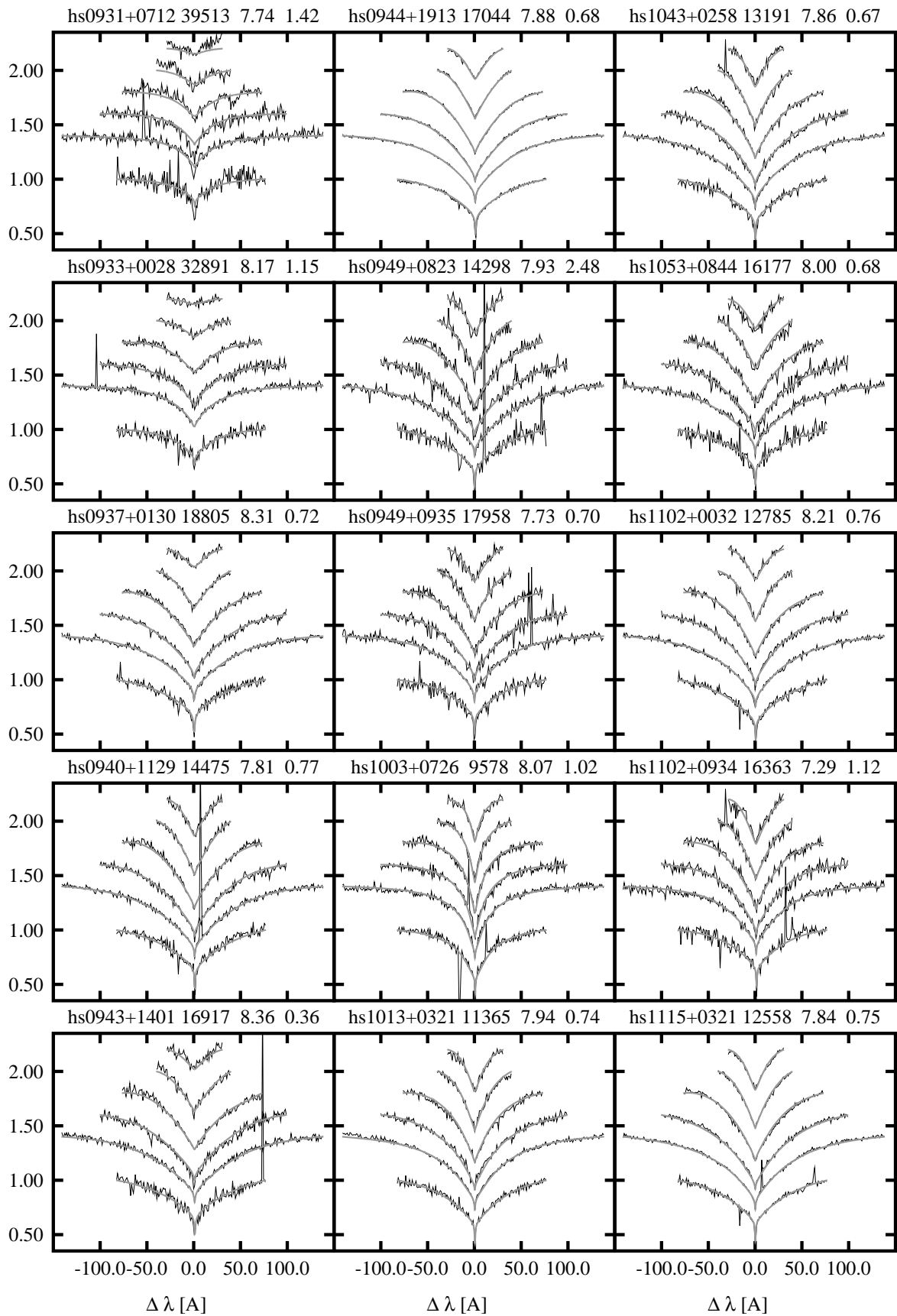
208 APPENDIX G. GRAPHICAL REPRESENTATION OF THE SPY SPECTRA FITS



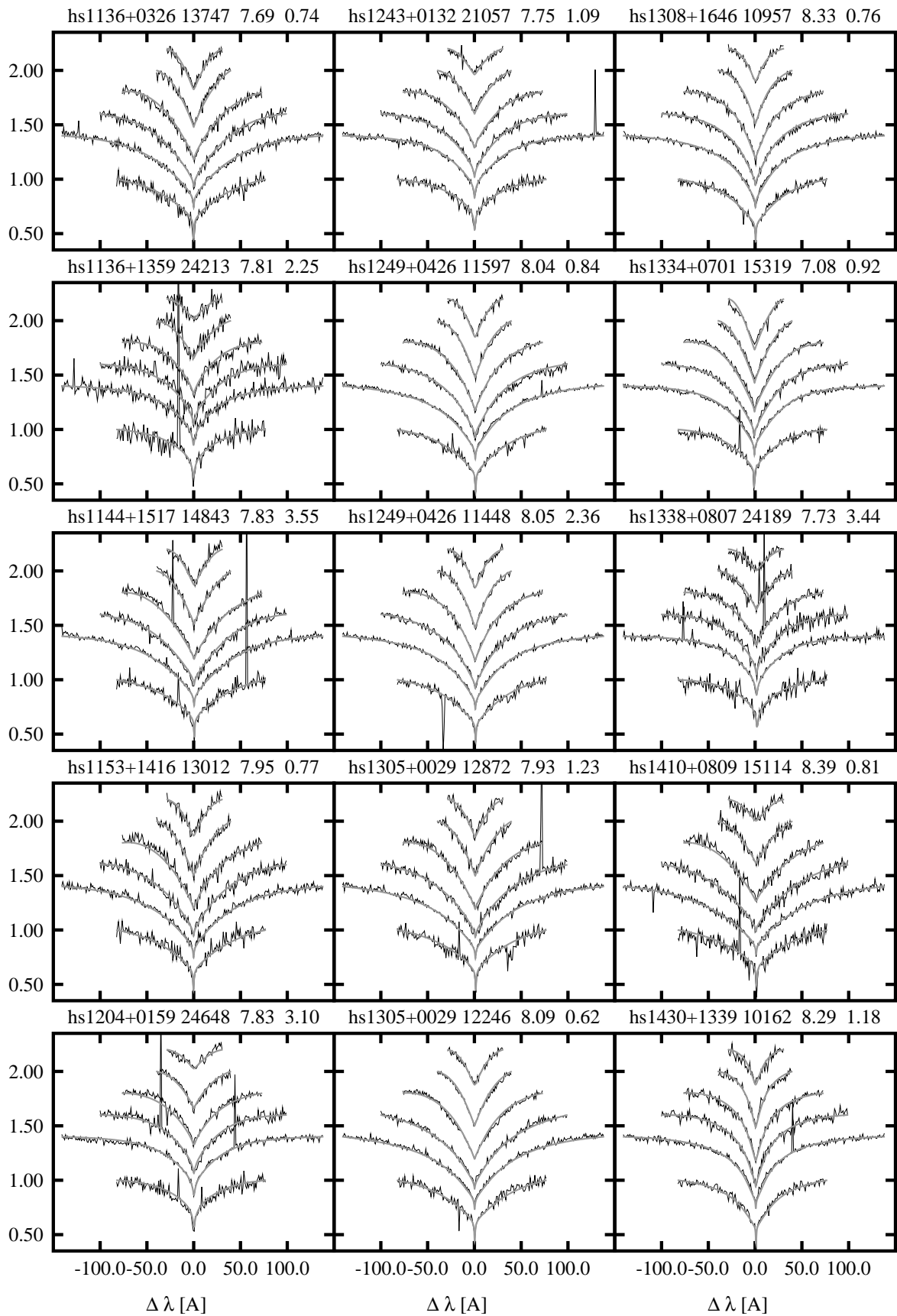


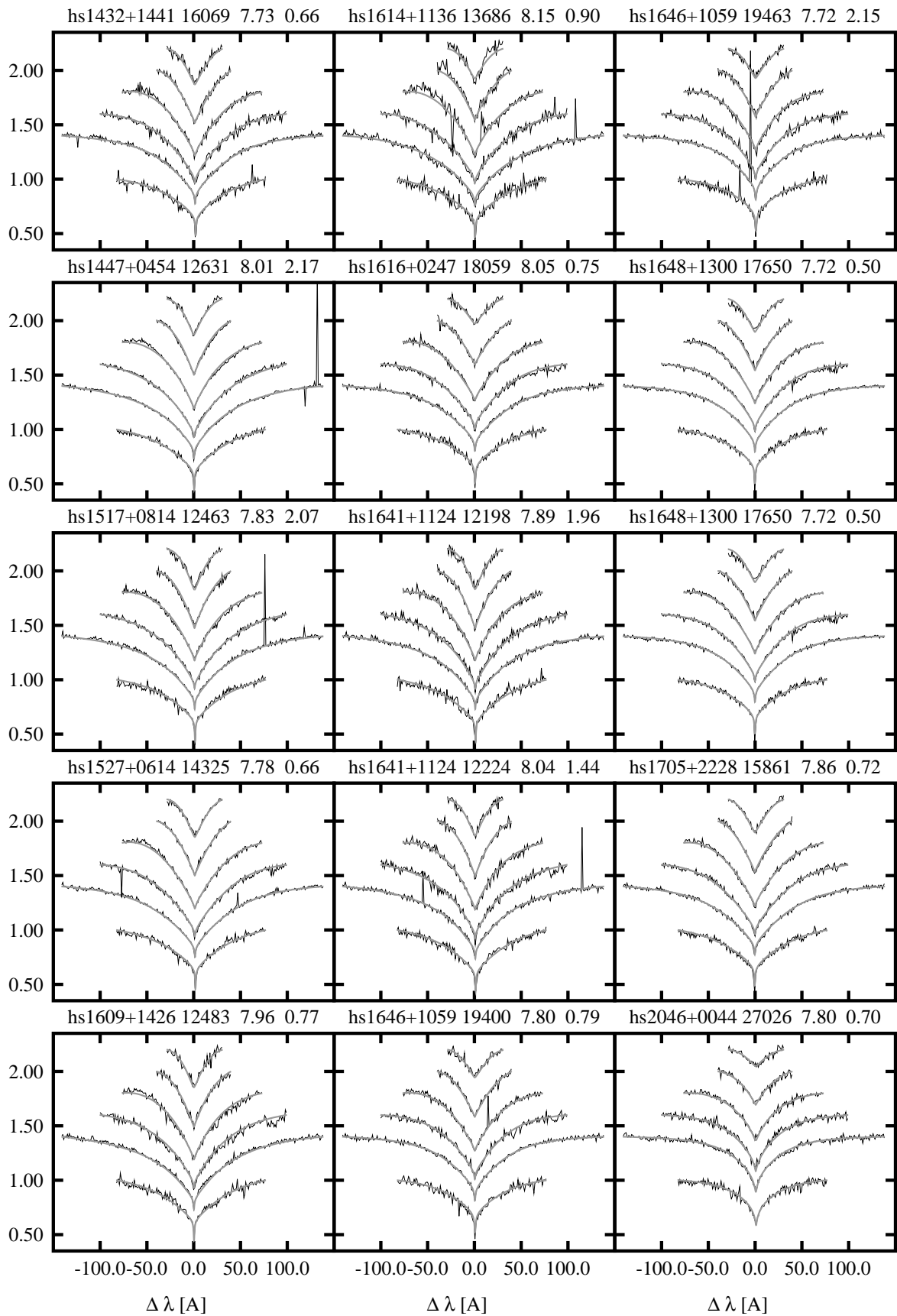
210 APPENDIX G. GRAPHICAL REPRESENTATION OF THE SPY SPECTRA FITS



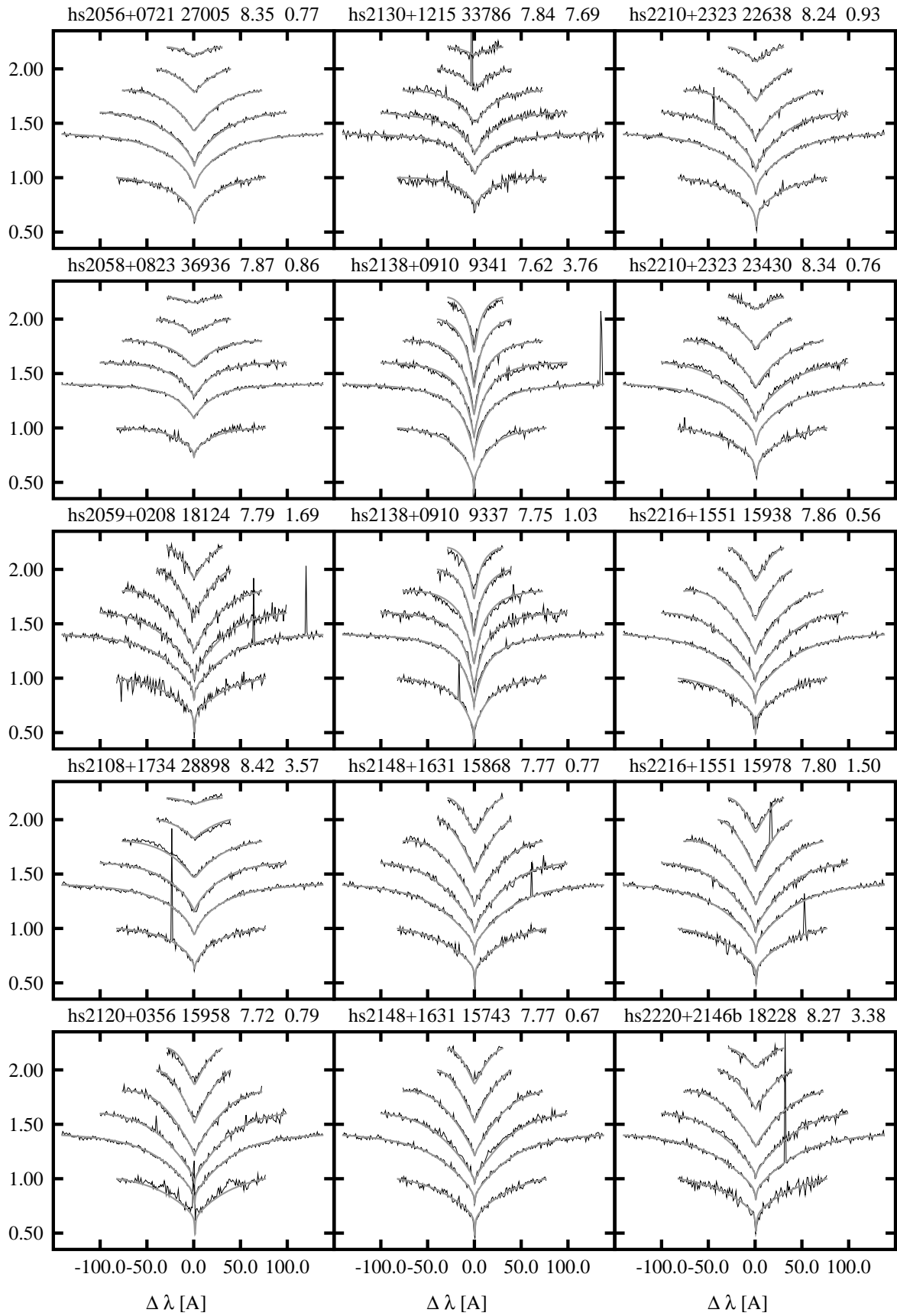


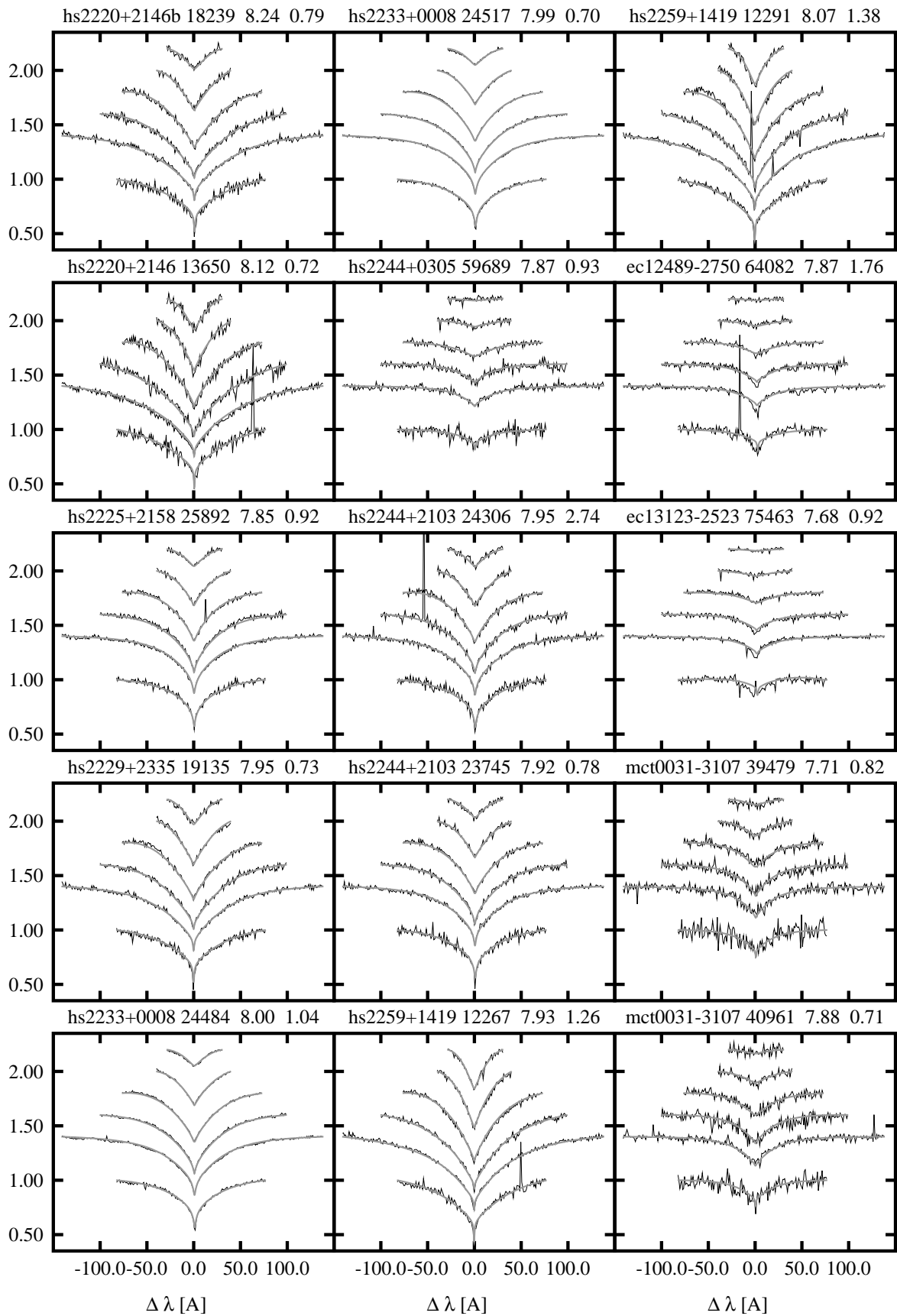
212 APPENDIX G. GRAPHICAL REPRESENTATION OF THE SPY SPECTRA FITS



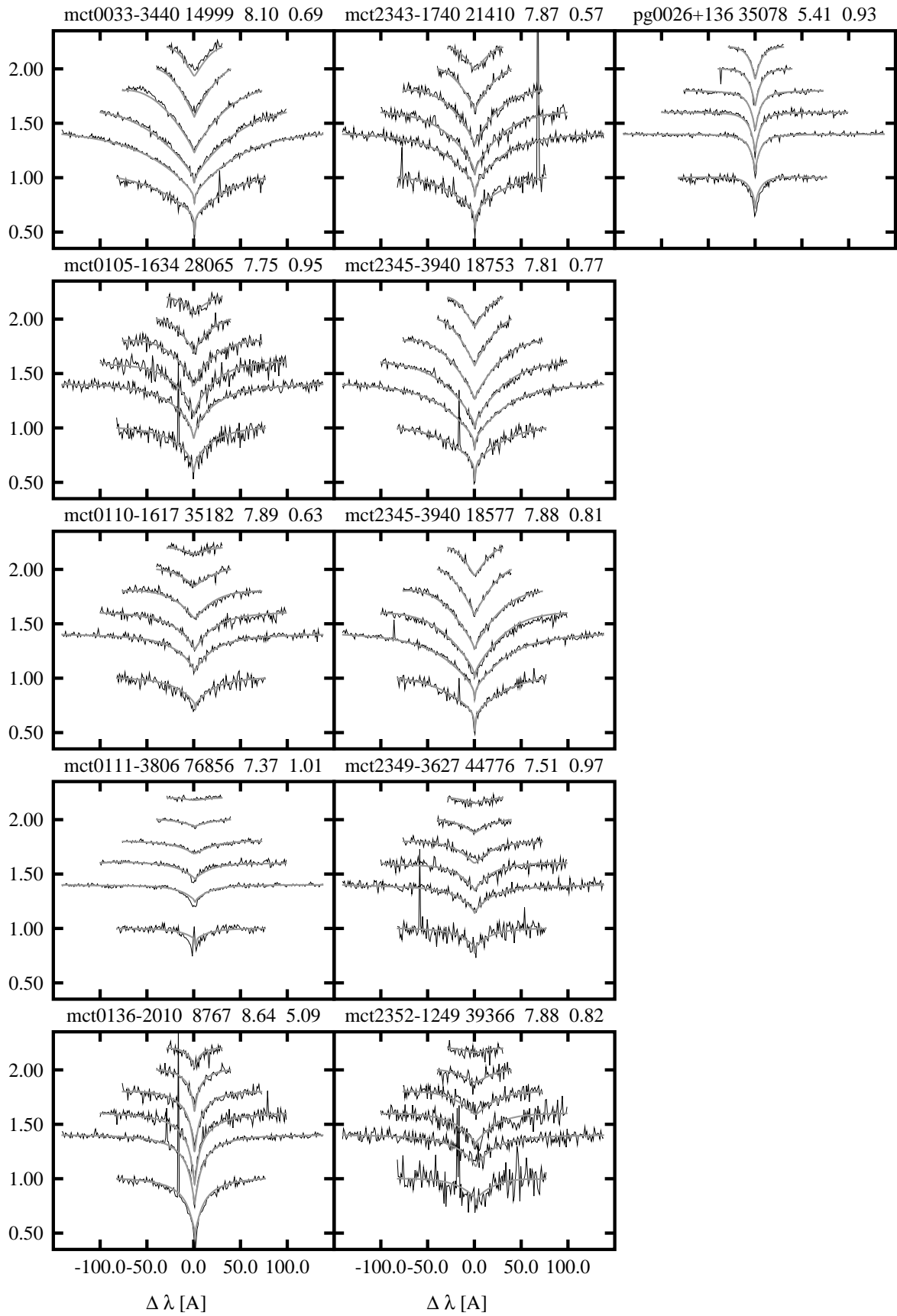


214 APPENDIX G. GRAPHICAL REPRESENTATION OF THE SPY SPECTRA FITS





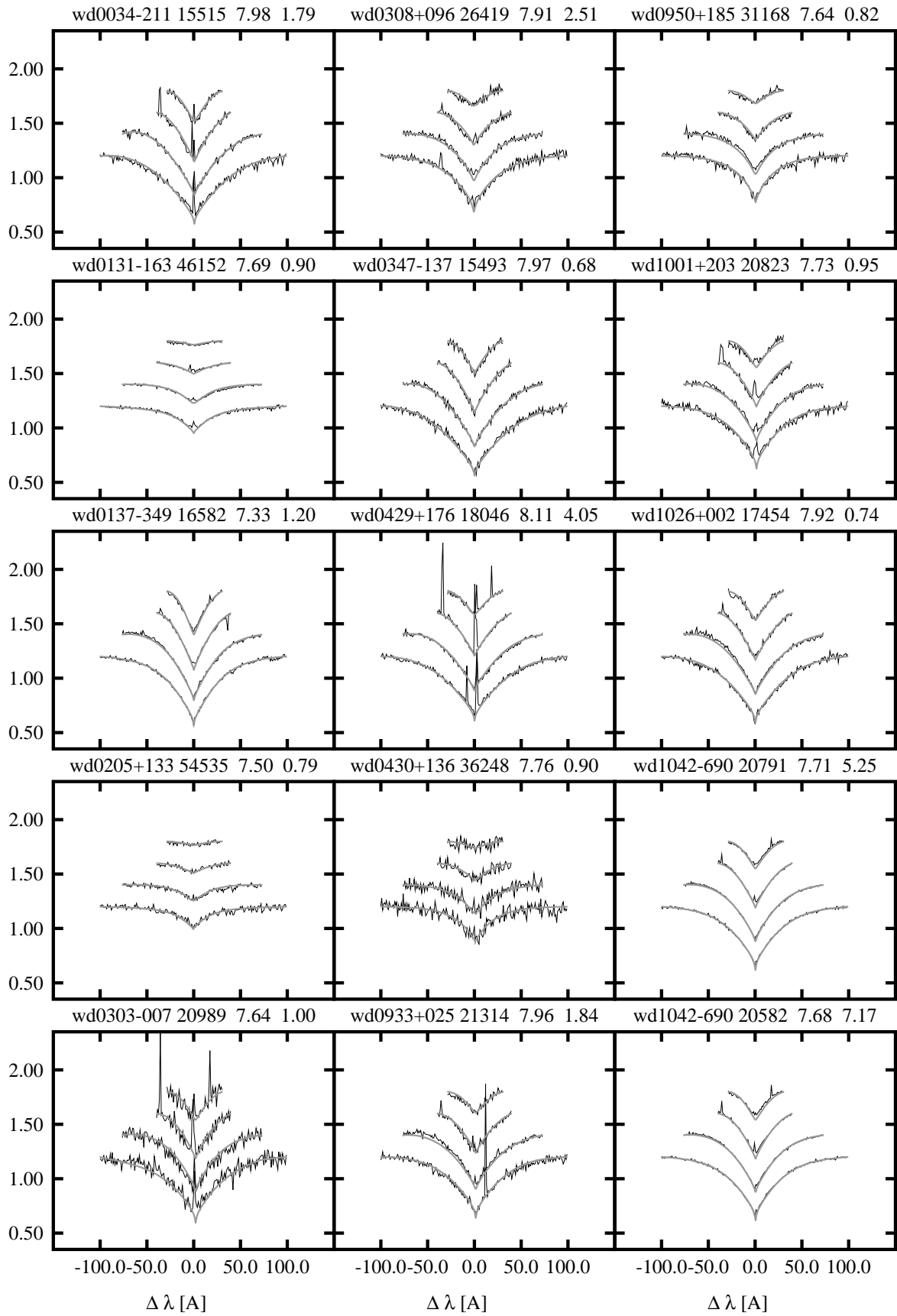
216 APPENDIX G. GRAPHICAL REPRESENTATION OF THE SPY SPECTRA FITS

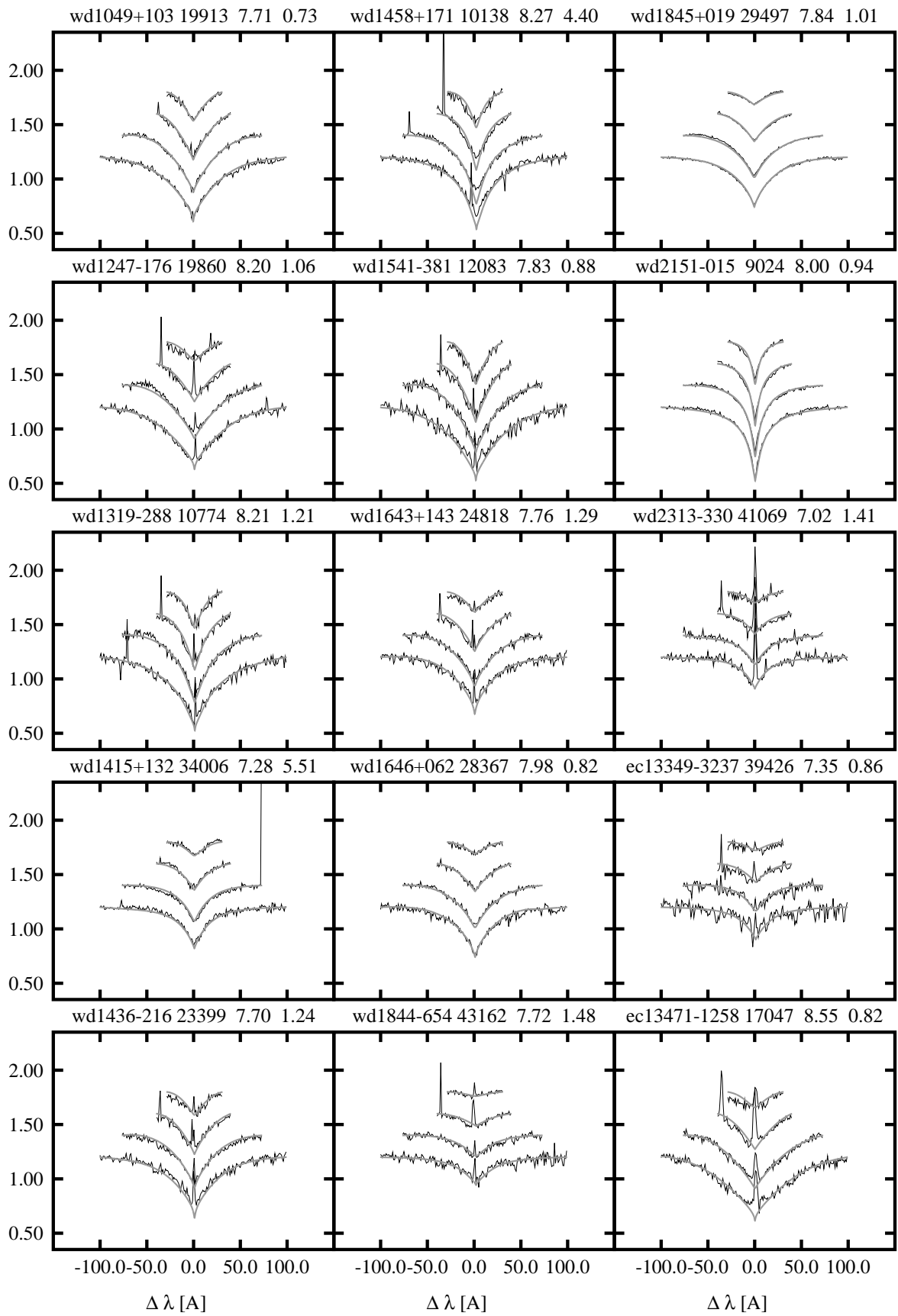


G.2 DA+dM Binaries

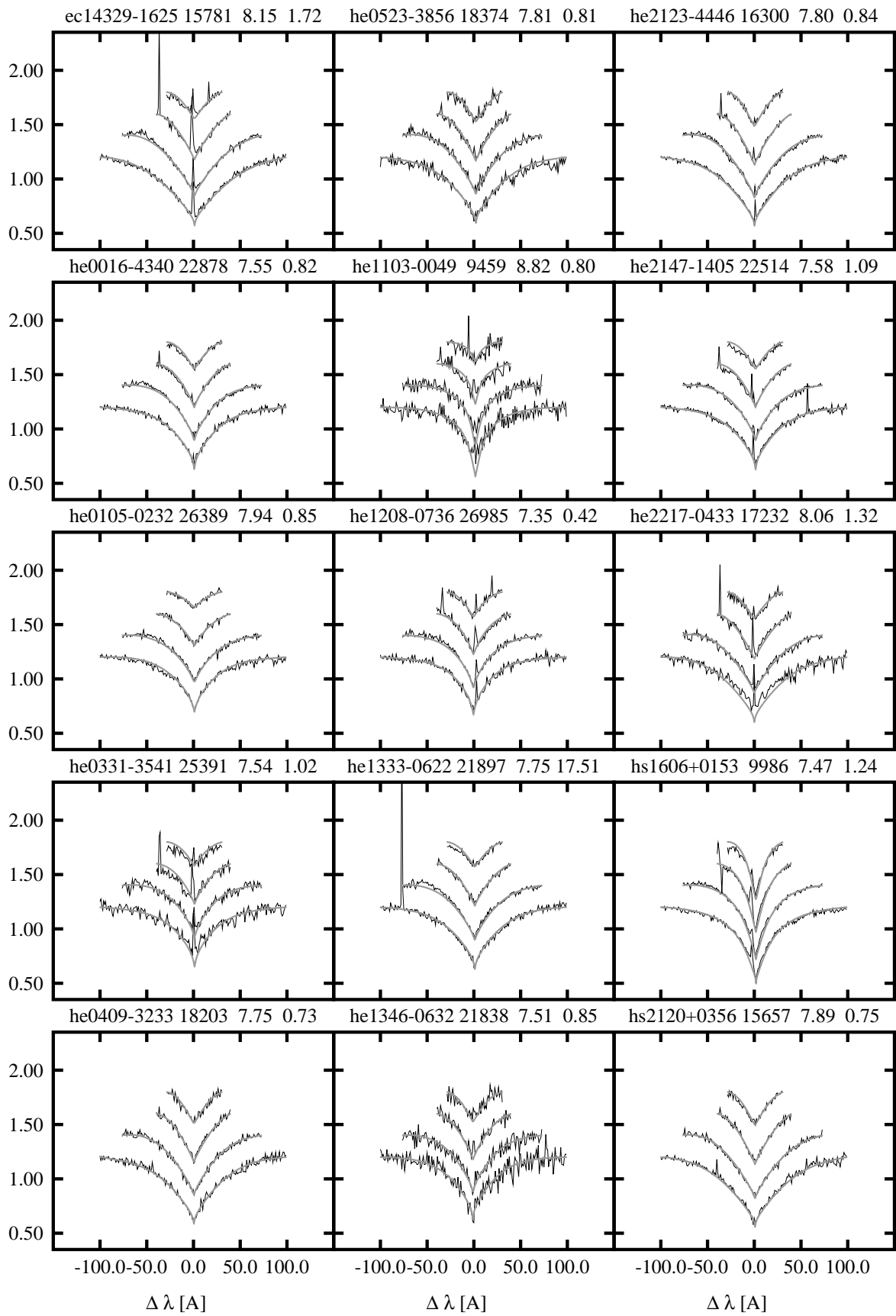
The following three pages display the fits of the DA model spectra to the Balmer lines H γ through H δ of DA+dM spectra, as described in chapter 4. The plots are similar to those in appendix G.1.

218 APPENDIX G. GRAPHICAL REPRESENTATION OF THE SPY SPECTRA FITS





220 APPENDIX G. GRAPHICAL REPRESENTATION OF THE SPY SPECTRA FITS

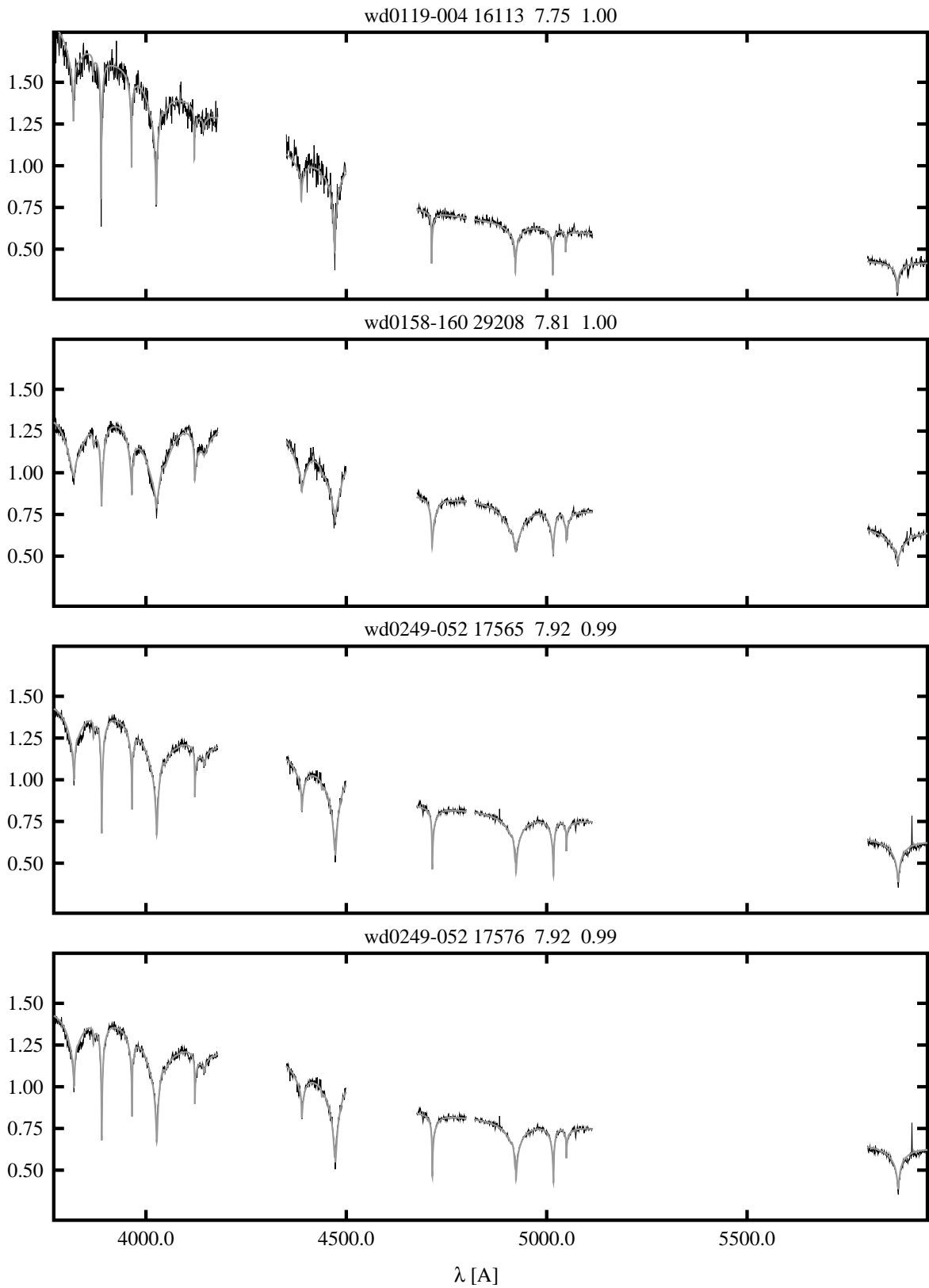


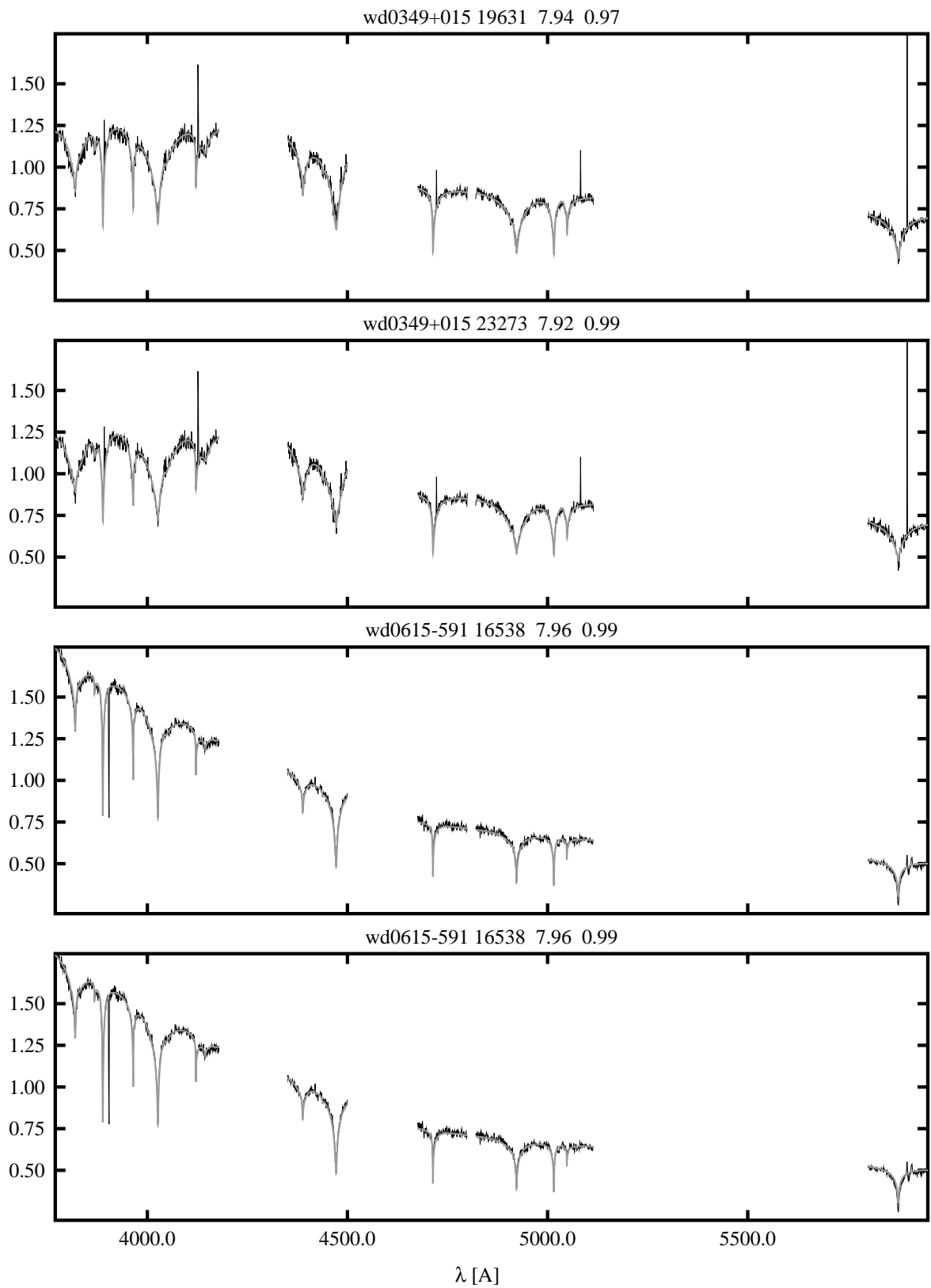
G.3 DB Stars

The fits of DB models to the SPY DB spectra without spectroscopically visible hydrogen are shown on the next pages. Only the spectral regions that were used in the fits are plotted, with the spectra as black and the fits as grey lines. As for the DA spectra, the intensity is given in arbitrary units, and the fit results are listed on top of each panel.

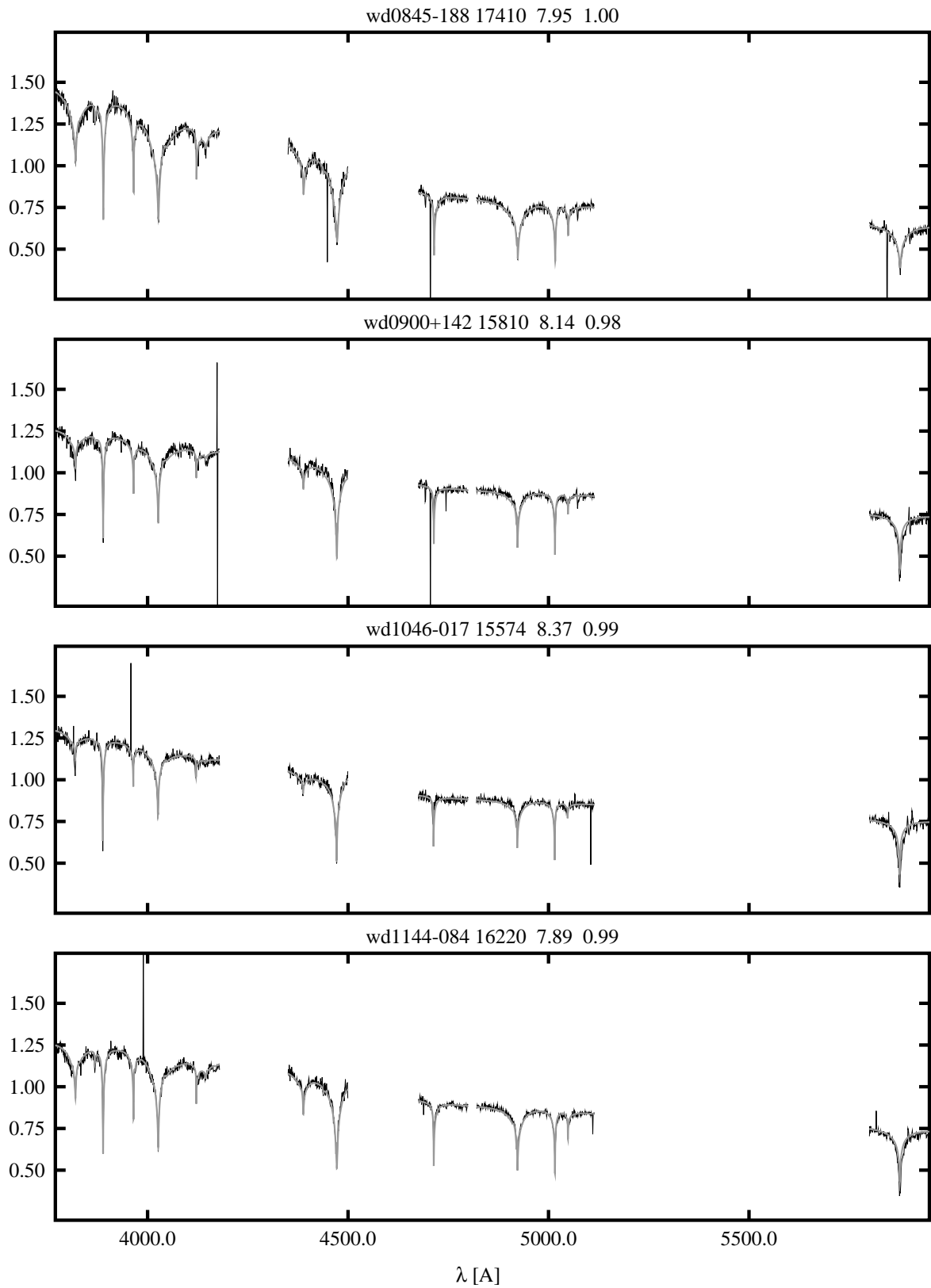
Also included are the fits of the two DB+dM objects WD 1004–178 and HE 0429–1651 for which only the blue part of the spectra was used, as described in chapter 5.

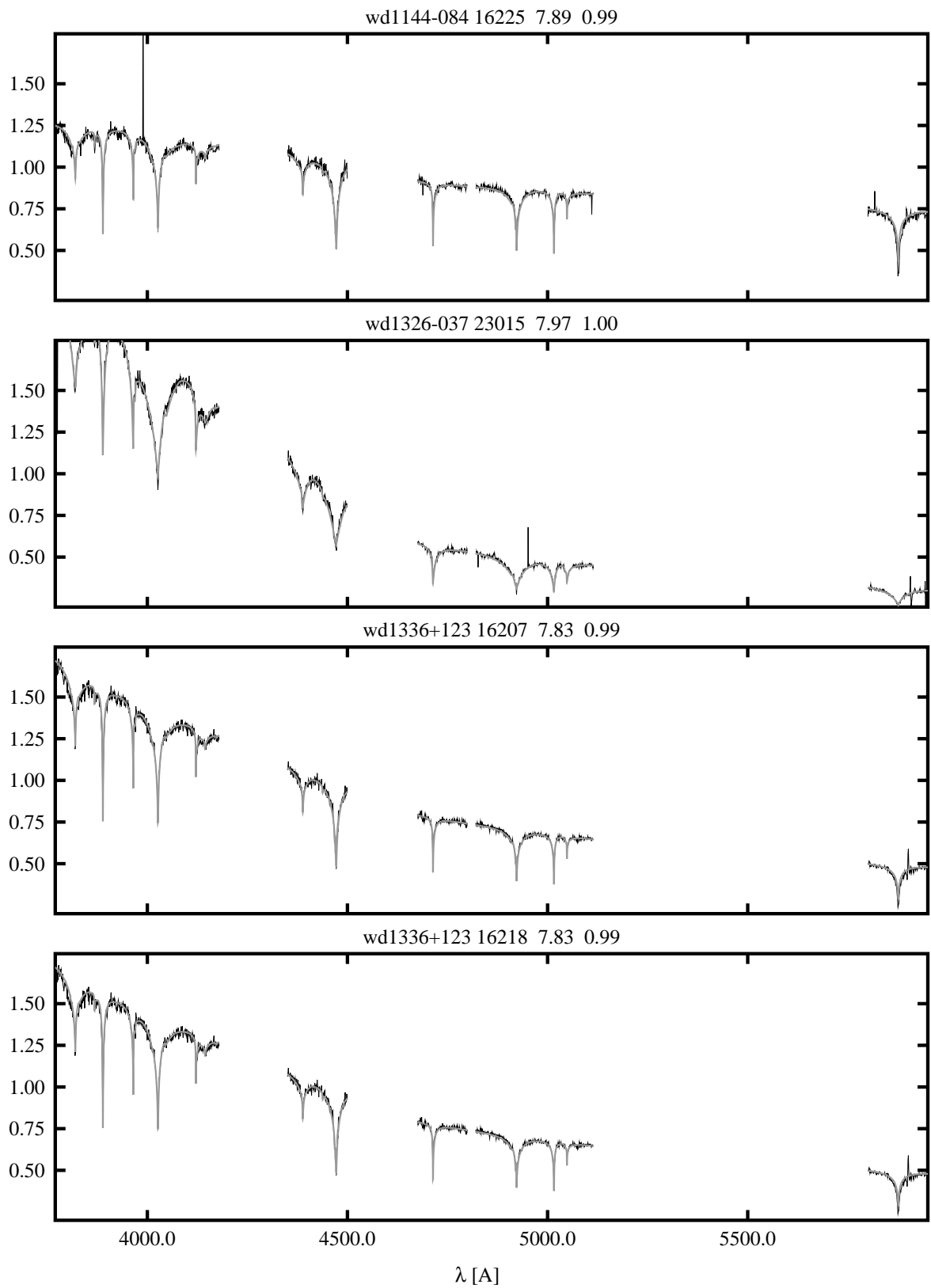
222 APPENDIX G. GRAPHICAL REPRESENTATION OF THE SPY SPECTRA FITS



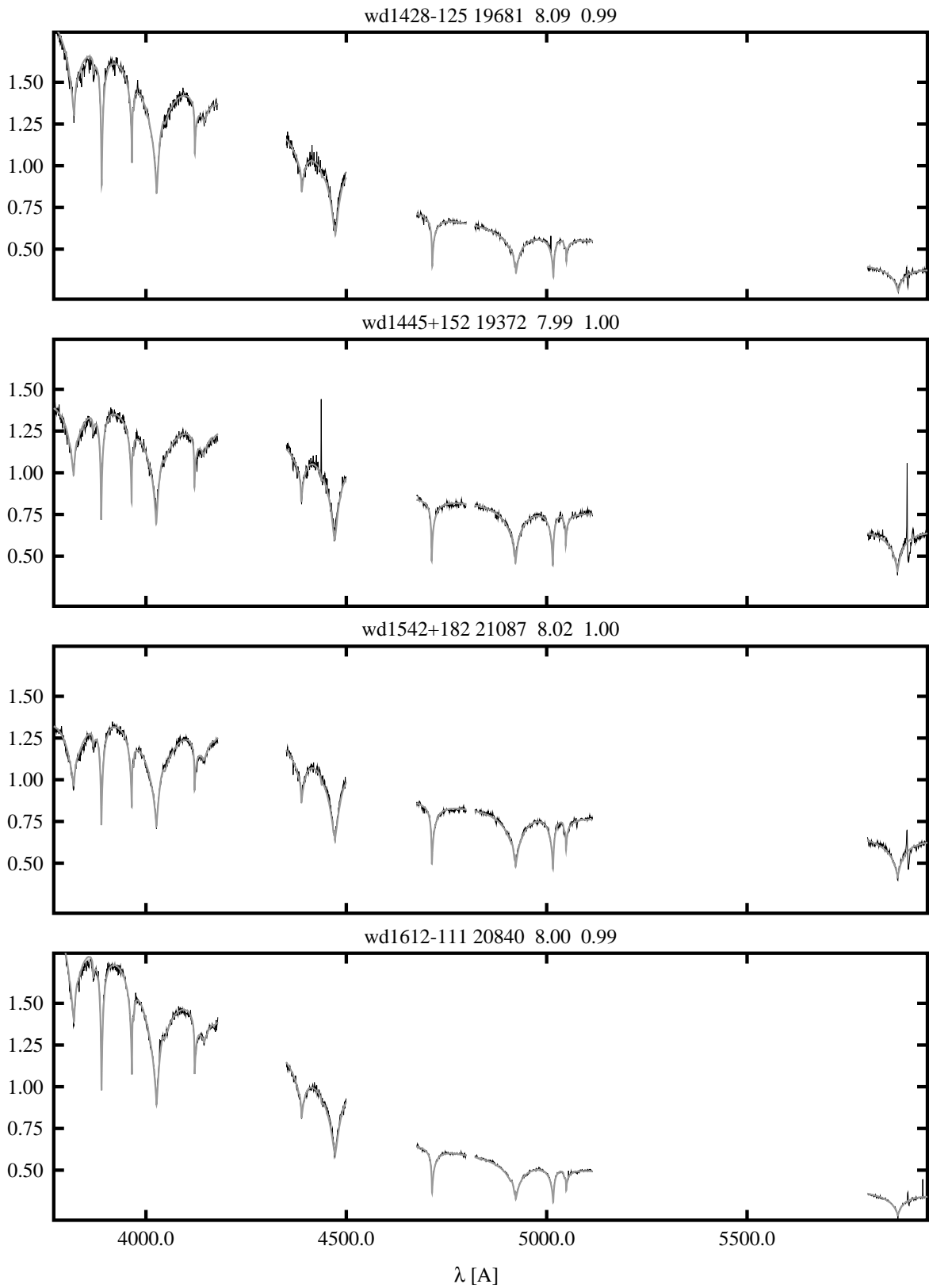


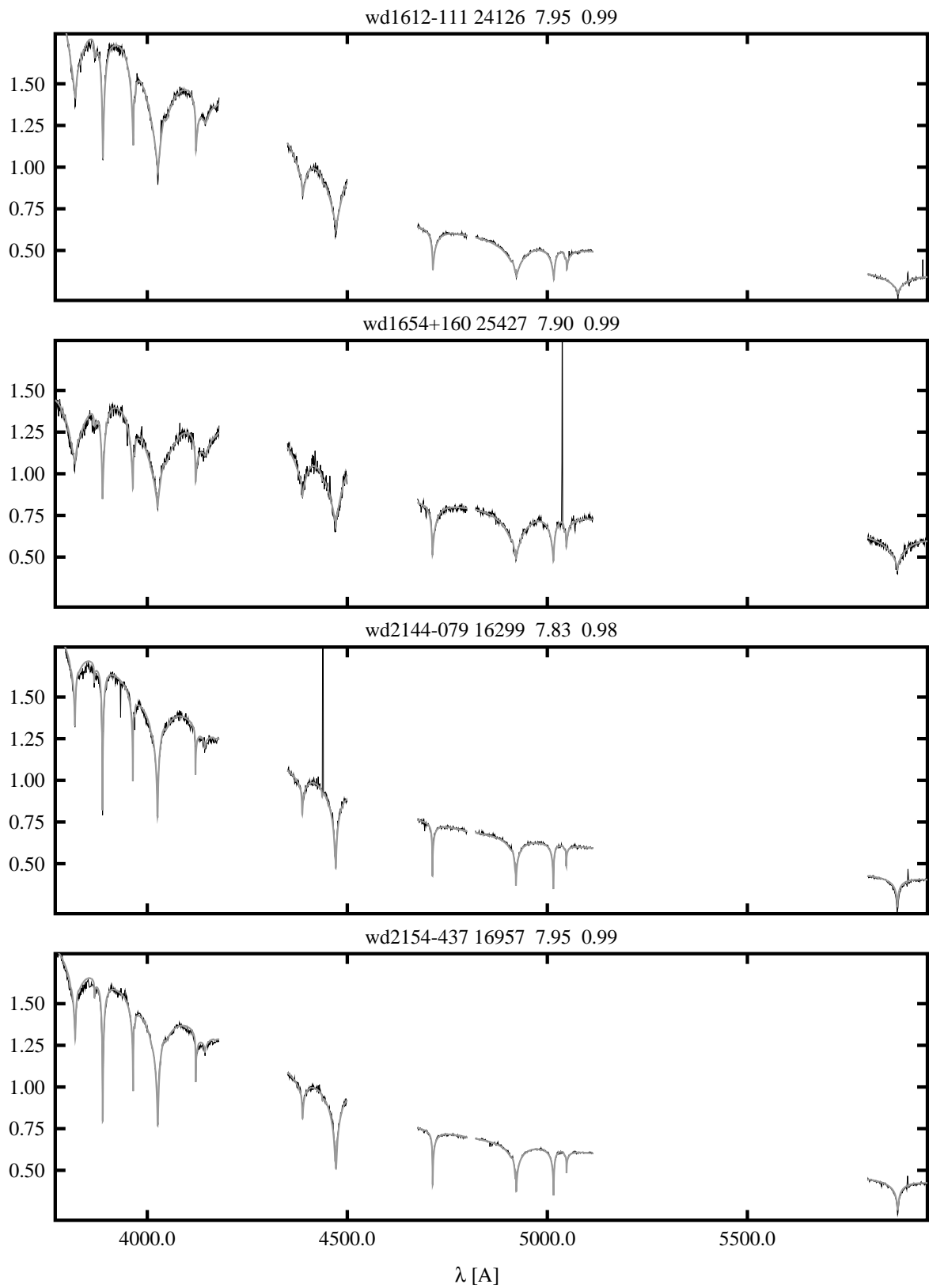
224 APPENDIX G. GRAPHICAL REPRESENTATION OF THE SPY SPECTRA FITS



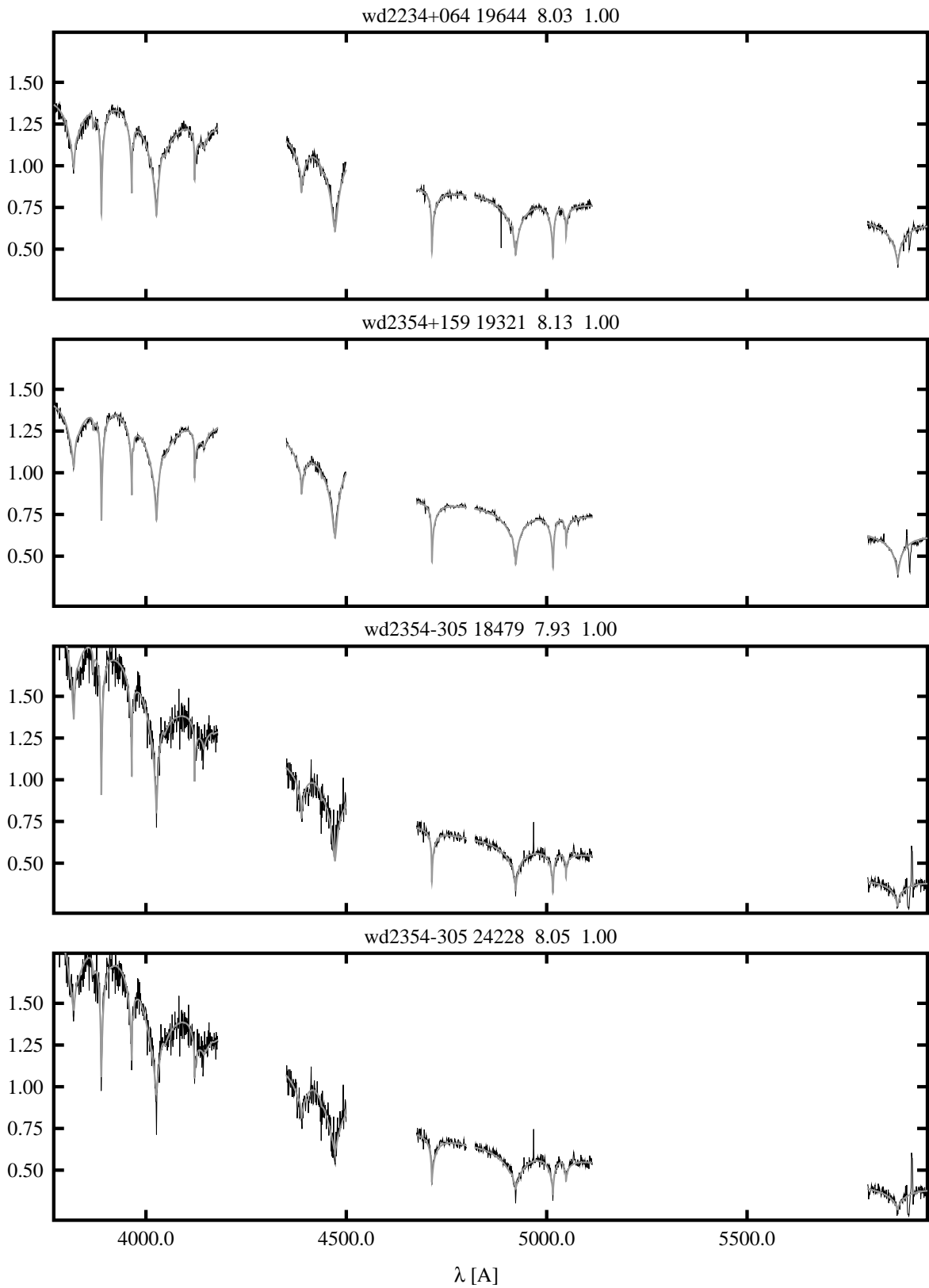


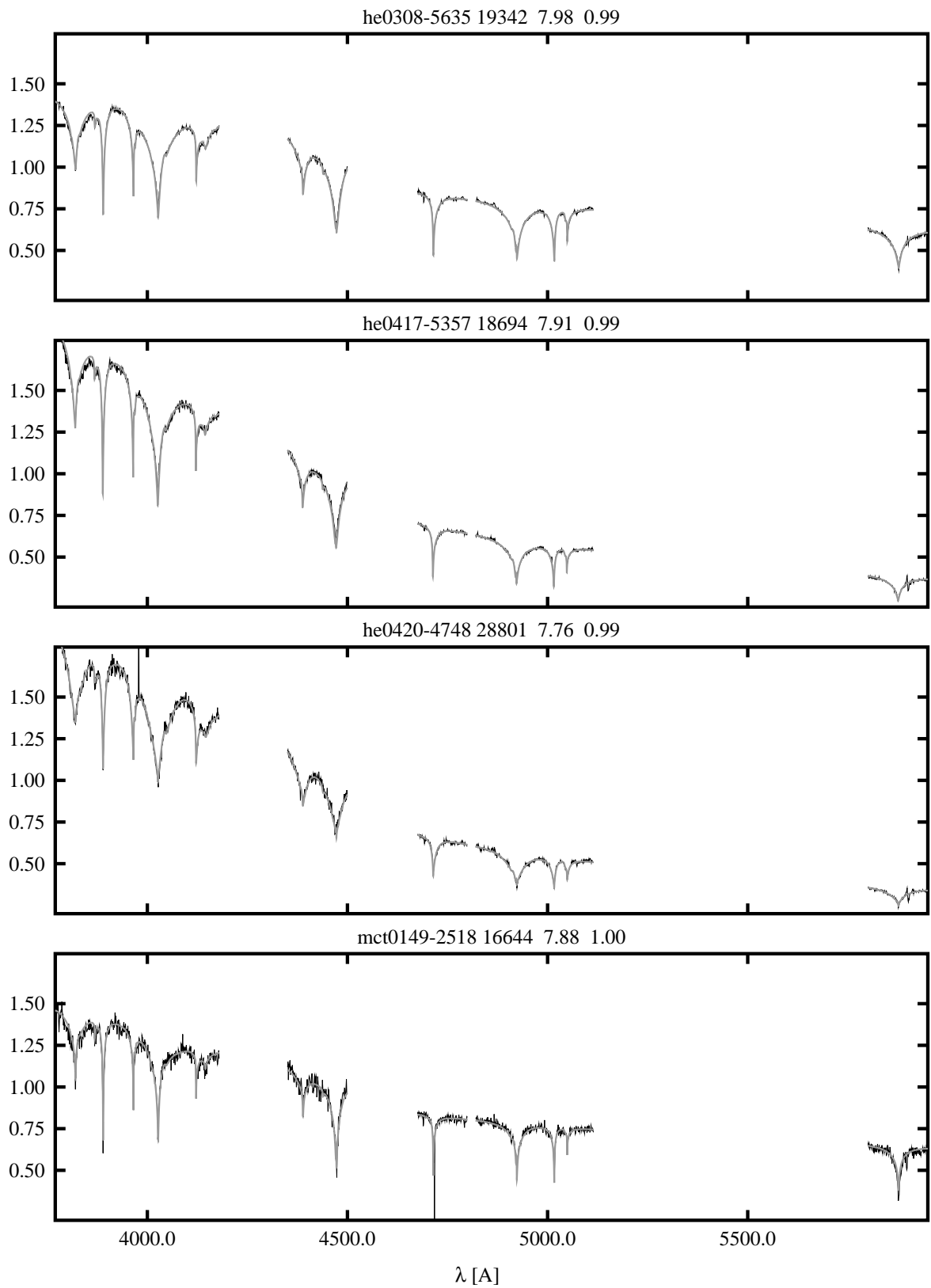
226 APPENDIX G. GRAPHICAL REPRESENTATION OF THE SPY SPECTRA FITS



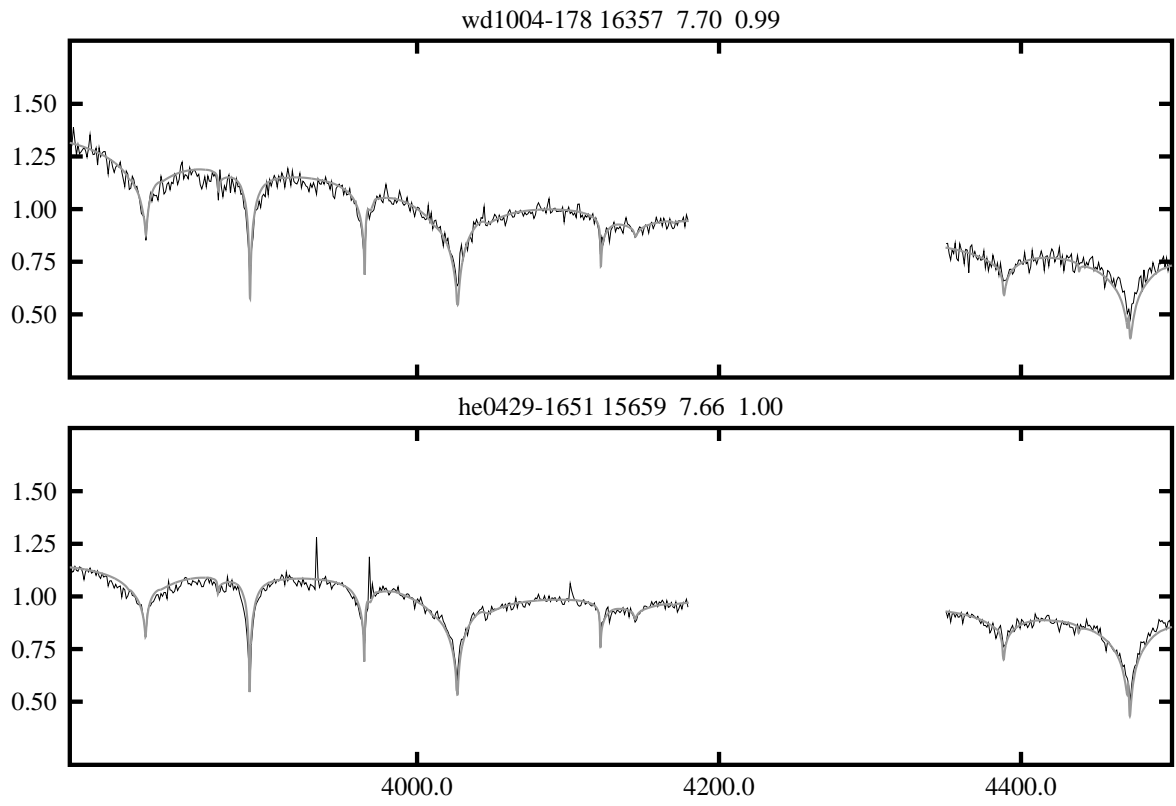


228 APPENDIX G. GRAPHICAL REPRESENTATION OF THE SPY SPECTRA FITS





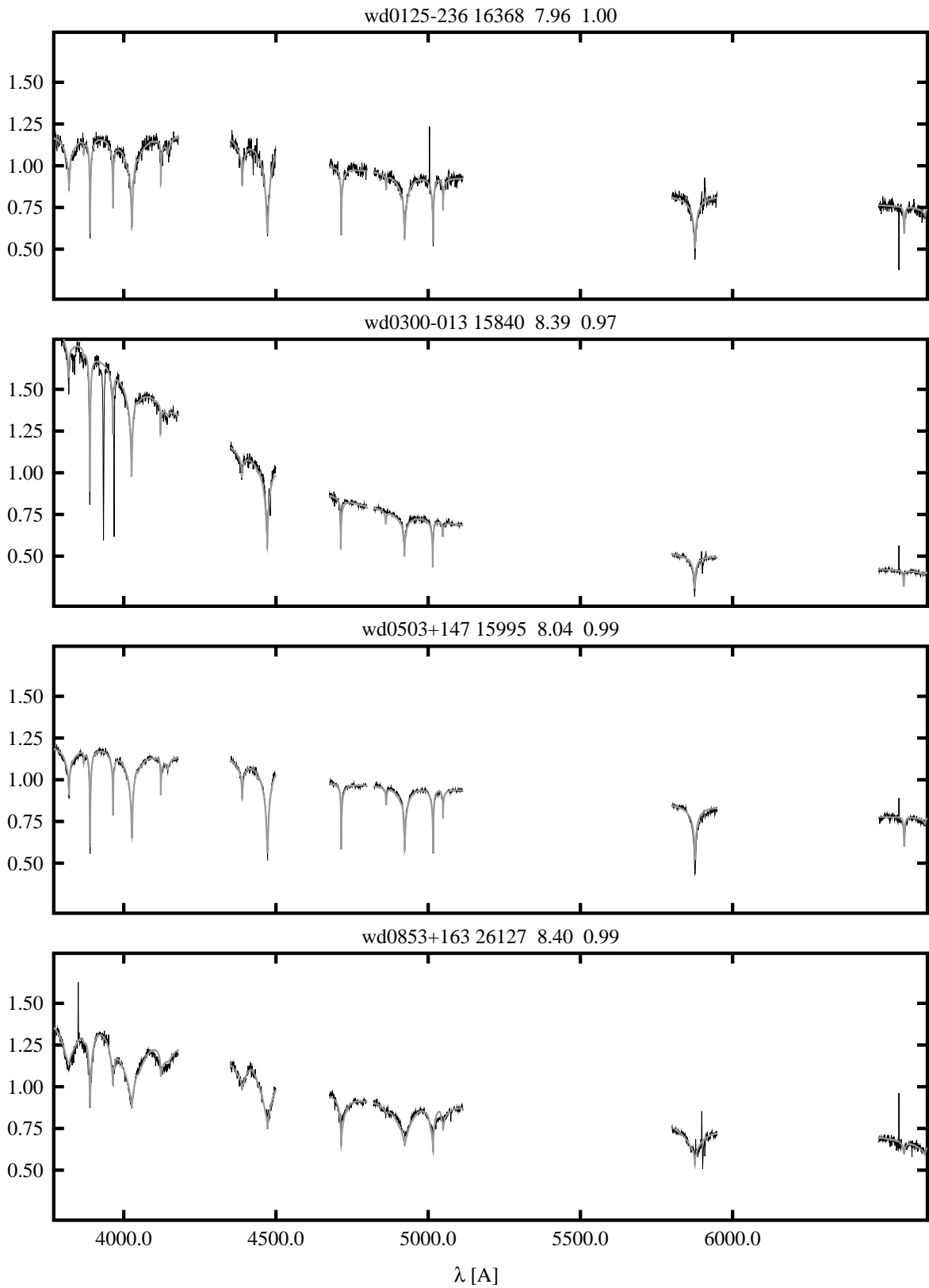
230 APPENDIX G. GRAPHICAL REPRESENTATION OF THE SPY SPECTRA FITS

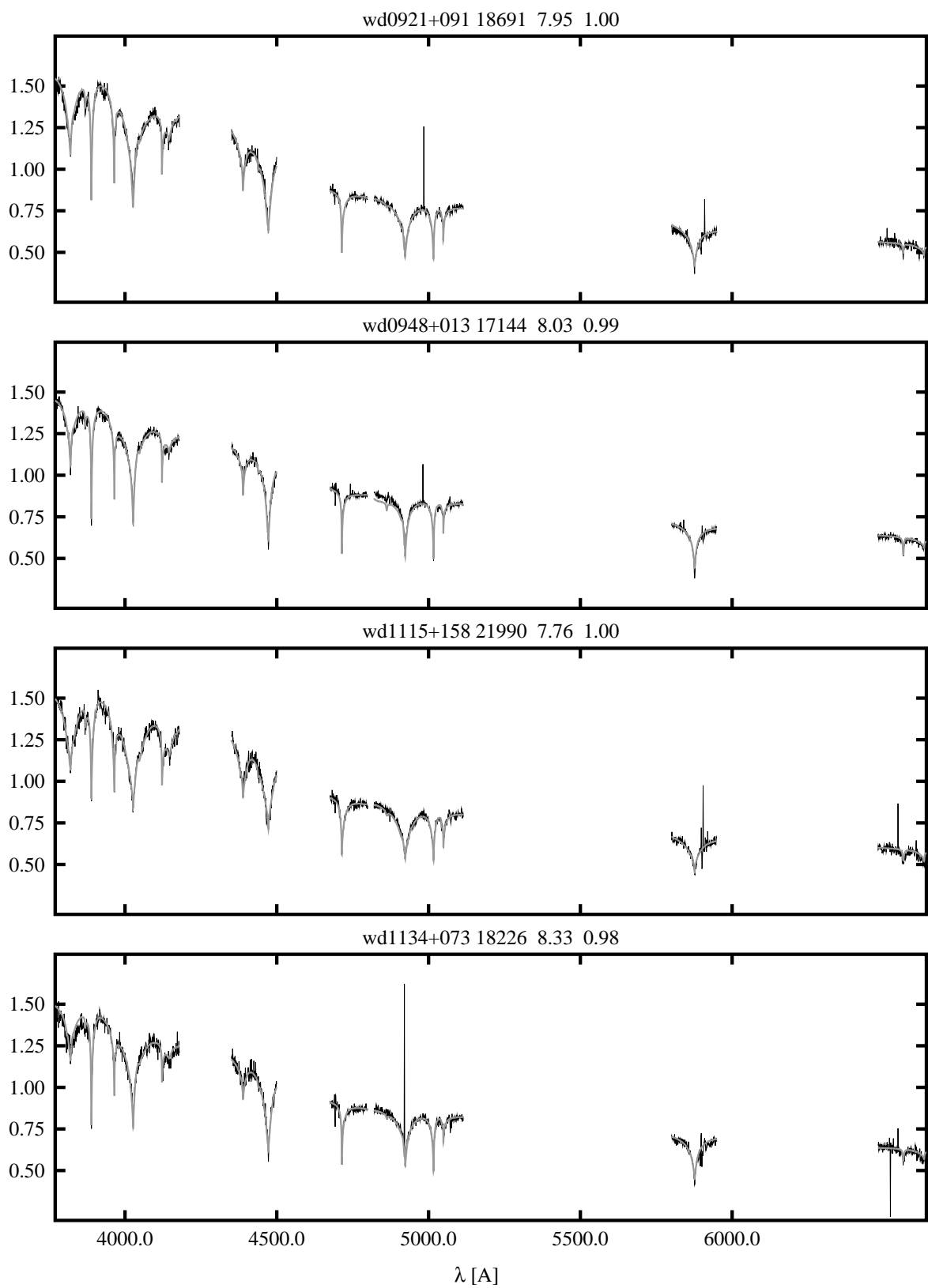


G.4 DBA Stars

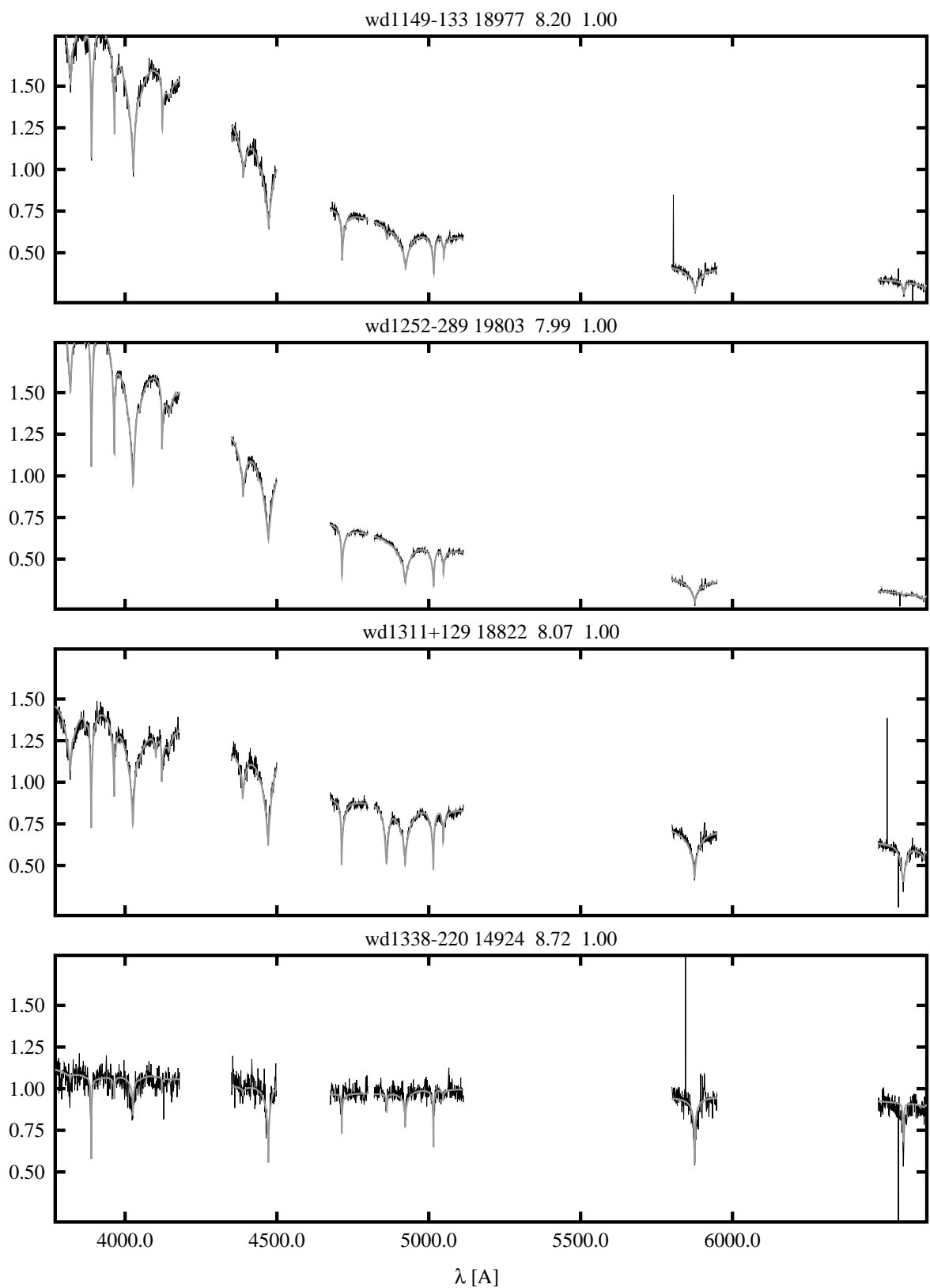
The fits of helium model atmospheres with admixtures of hydrogen to the SPY DBA spectra are shown on the following pages; for each object only one fit, normally that with the lowest χ^2 , is shown. For the DBA stars that exhibit very weak H lines, and for which thus a model atmosphere without hydrogen yields the best fit, nevertheless the $\log y = 5$ fit is shown. The T_{eff} and $\log g$ fit results are given on top of each panel; the $\log y$ values can be found in table C.1.

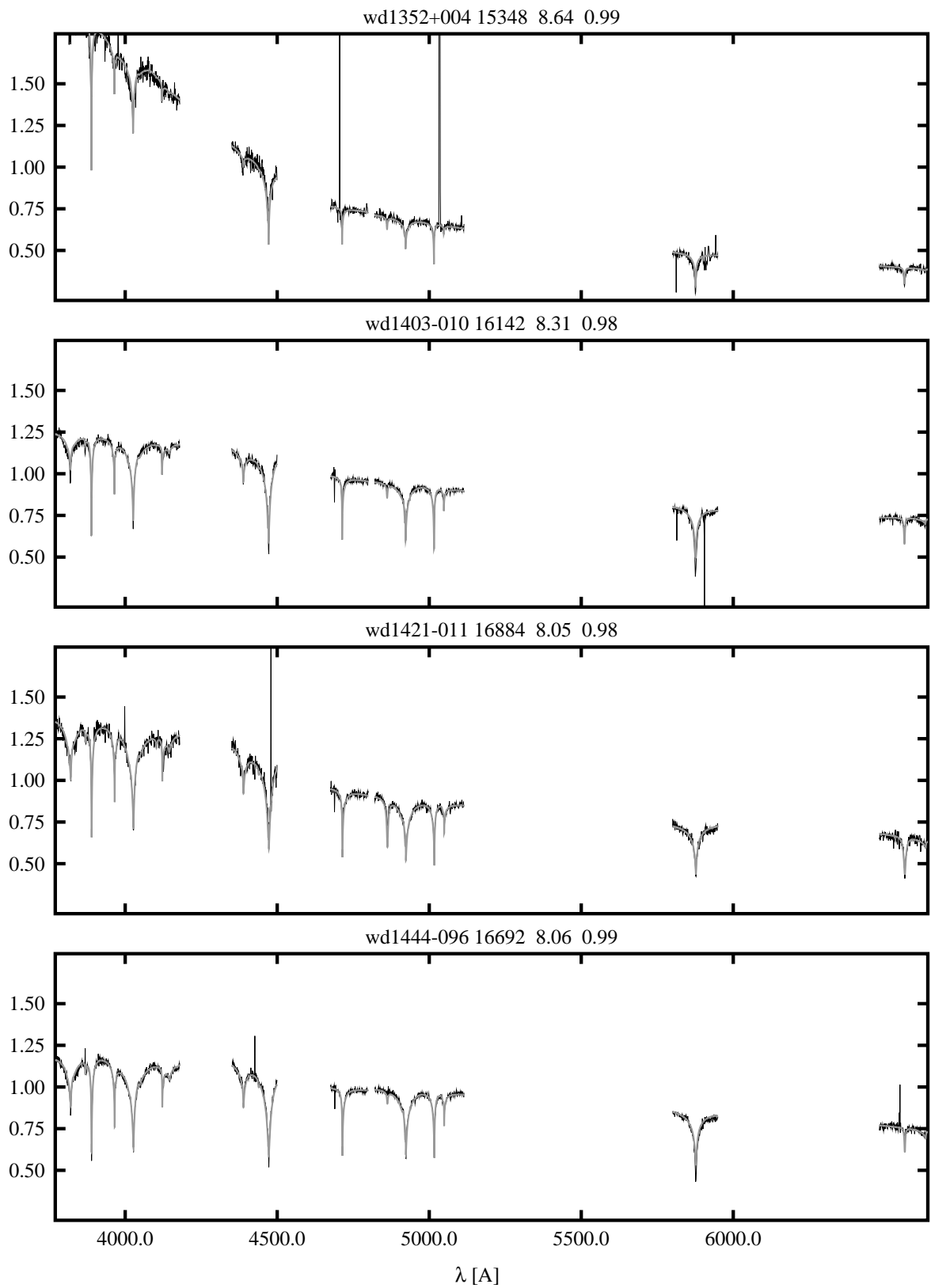
232 APPENDIX G. GRAPHICAL REPRESENTATION OF THE SPY SPECTRA FITS



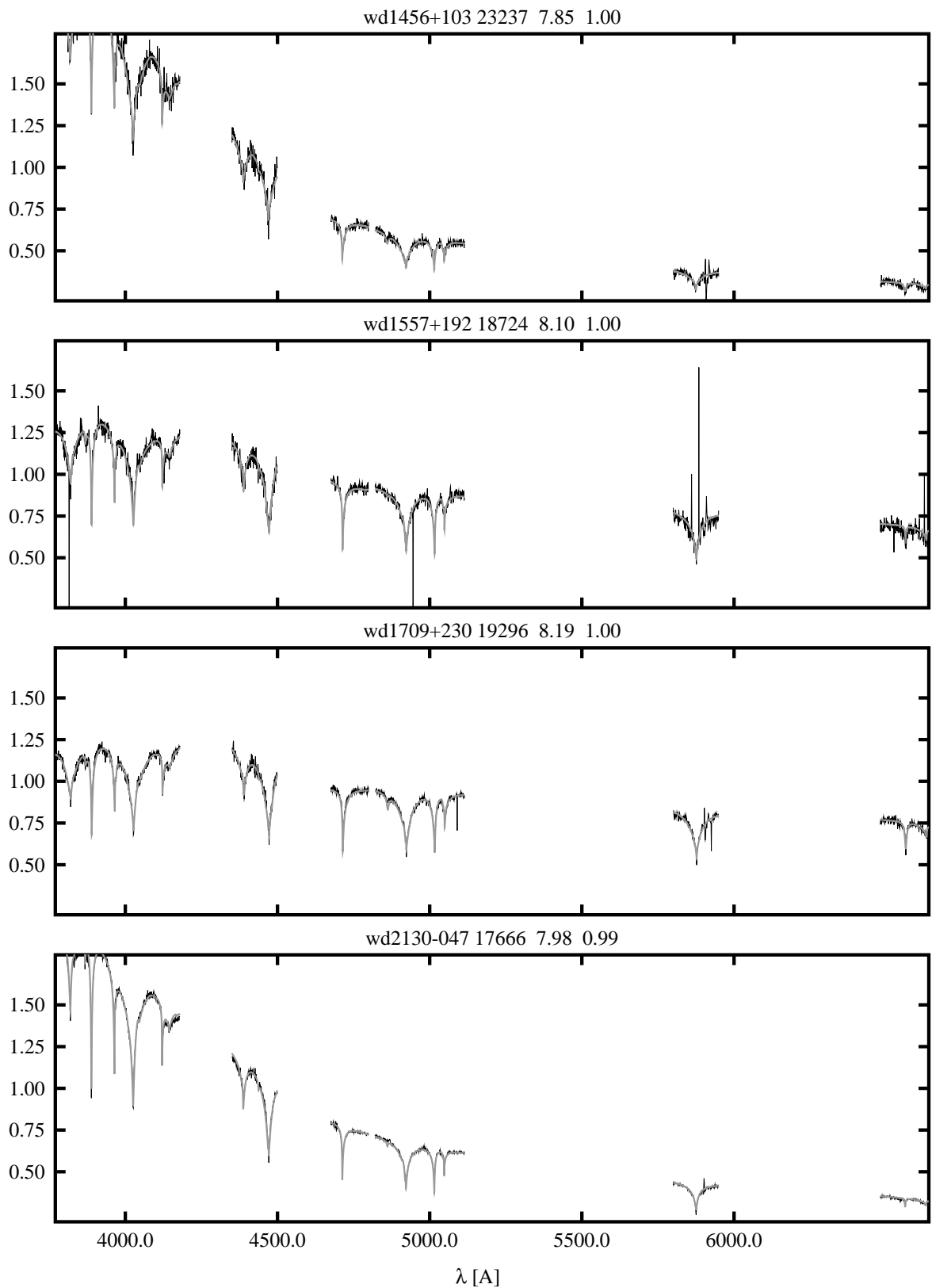


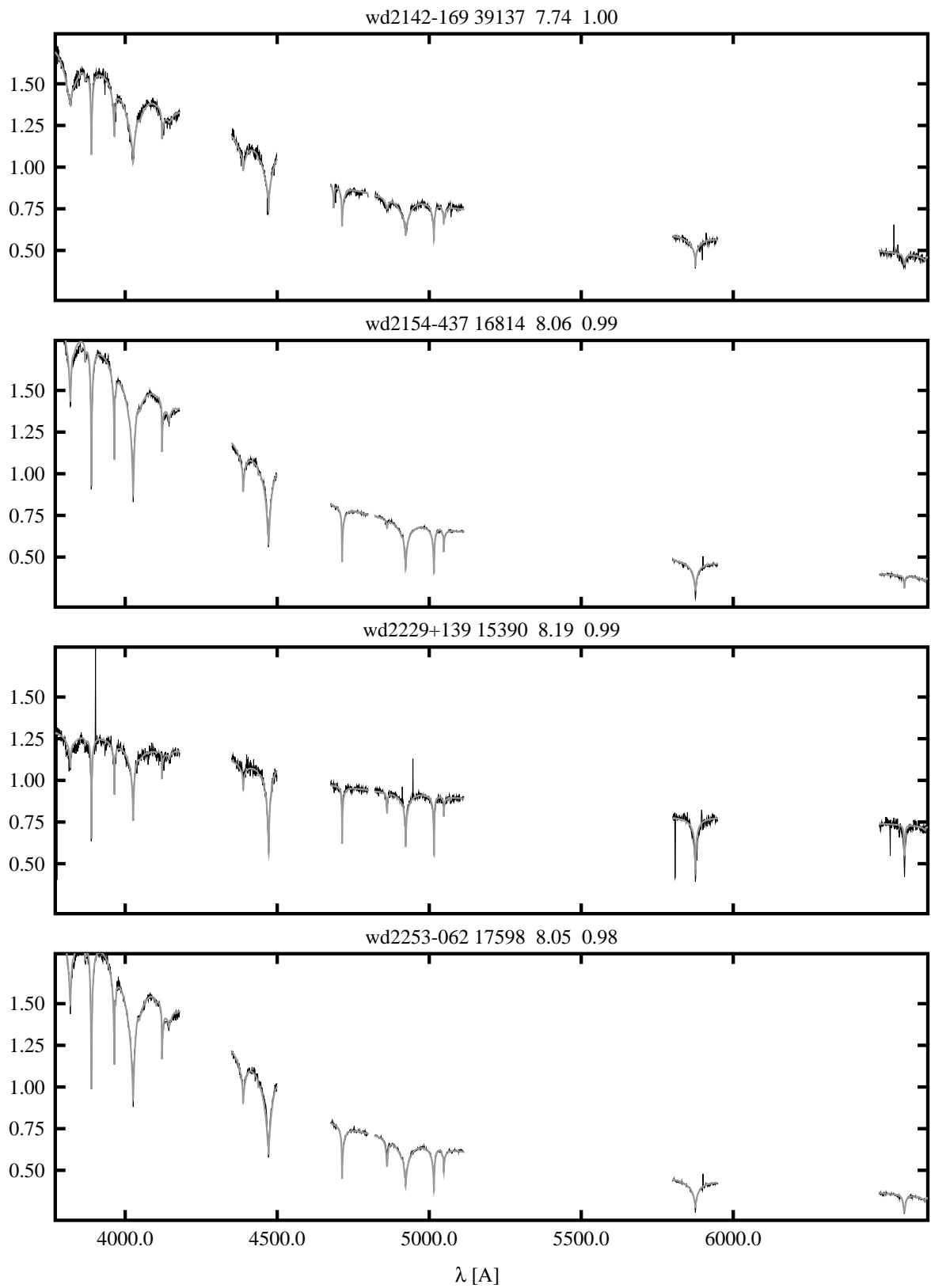
234 APPENDIX G. GRAPHICAL REPRESENTATION OF THE SPY SPECTRA FITS



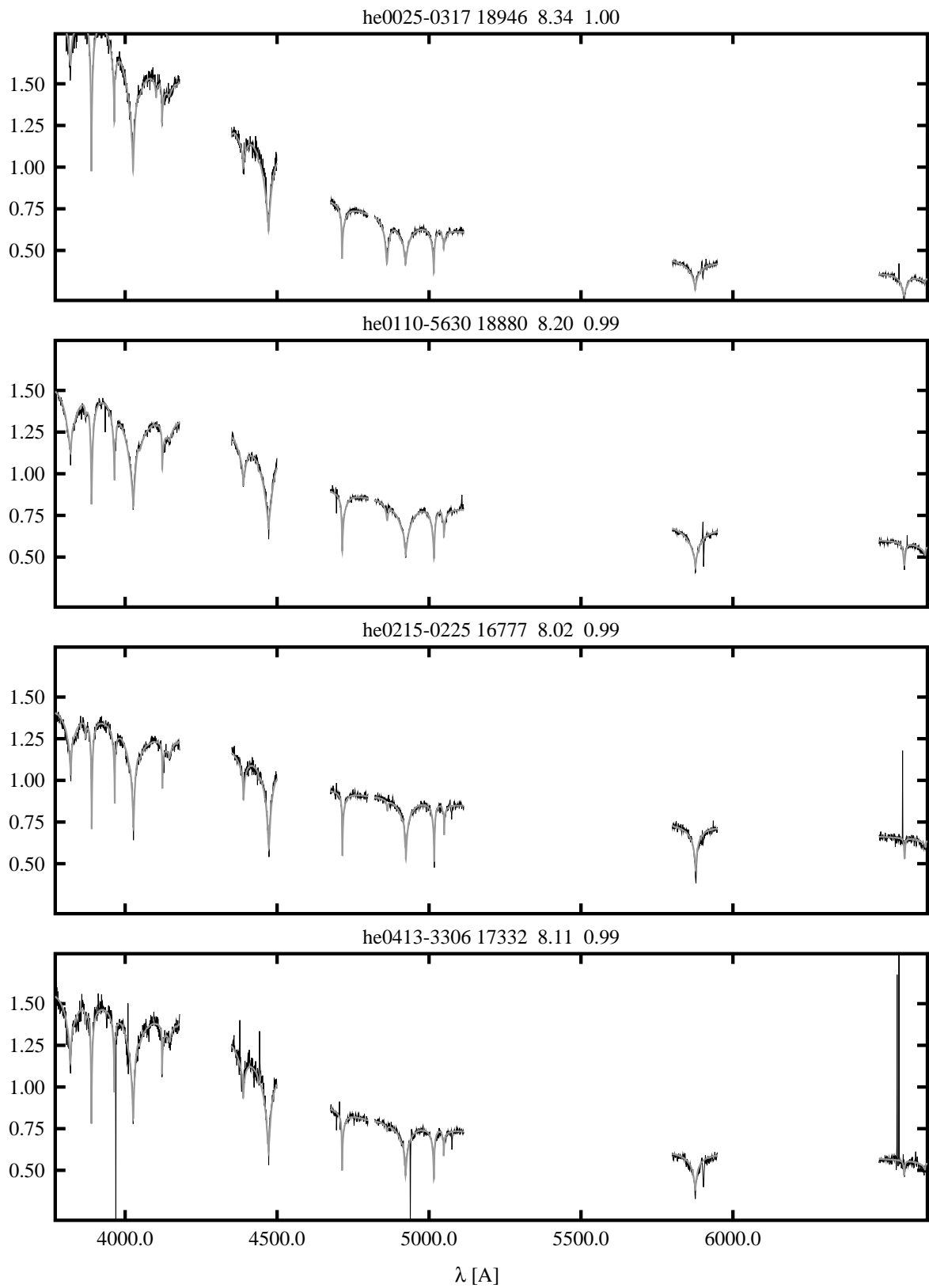


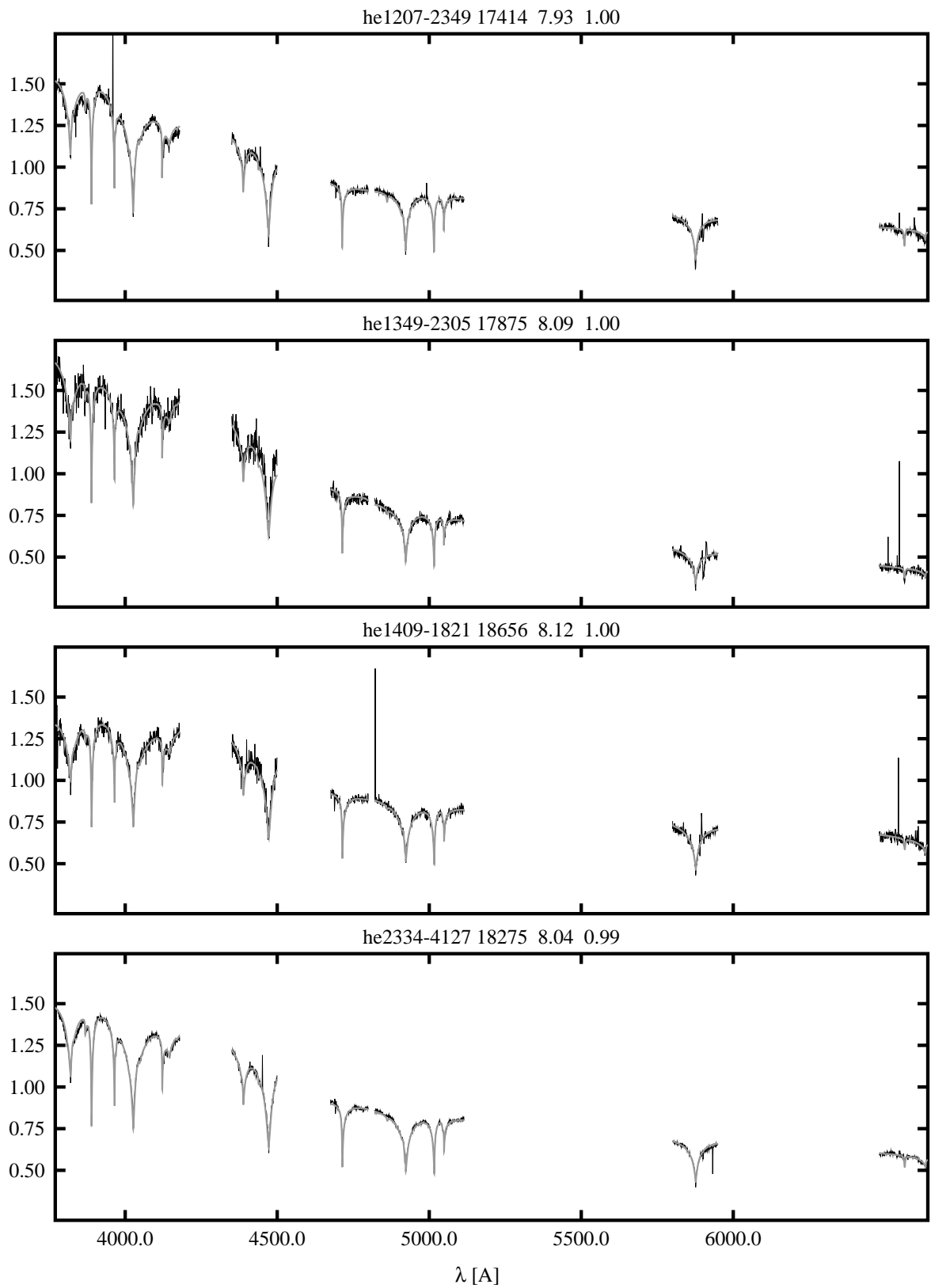
236 APPENDIX G. GRAPHICAL REPRESENTATION OF THE SPY SPECTRA FITS



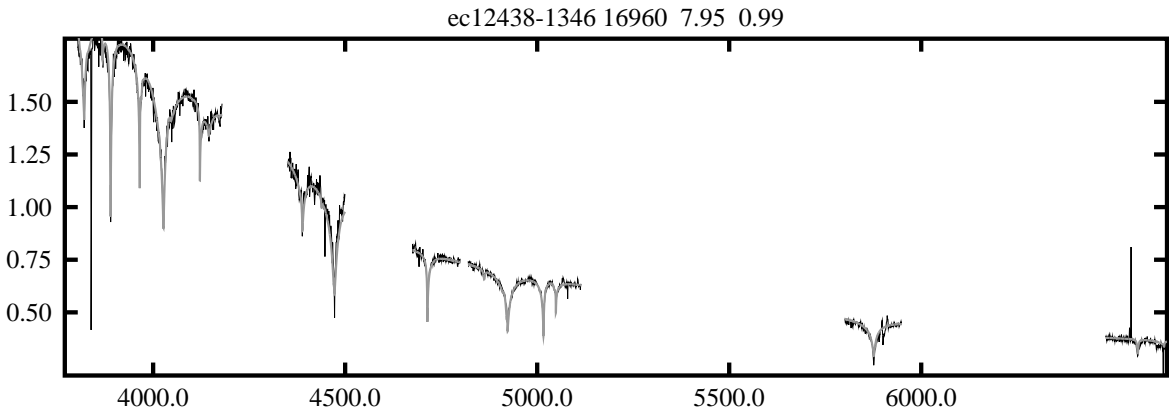


238 APPENDIX G. GRAPHICAL REPRESENTATION OF THE SPY SPECTRA FITS





240 APPENDIX G. GRAPHICAL REPRESENTATION OF THE SPY SPECTRA FITS



Bibliography

- [1] Aznar Cuadrado, R., Jordan, S., Napiwotzki, R. et al. 2004, A&A, 423, 1081
- [2] Bannister, N. 2001, PhD thesis, Univ. of Leicester
- [3] Beauchamp, A., Wesemael, F., Bergeron, P., Liebert, J., & Saffer, R. A. 1996, ASPC, 96, 322
- [4] Beauchamp, A., Wesemael, F., Bergeron, P., et al. 1999, ApJ, 516, 887
- [5] Beers, T. C., Preston, G. W., Shectman, S. A., Doinidis, S. P., & Griffin, K. E. 1992, AJ, 103, 267
- [6] Belczynski, K., Bulik, T., Ruiter, A. J. 2005, ApJ, 629, 915
- [7] Benedict, G. F., McArthur, B. E., Franz, O. G., et al. 2000, AJ, 119, 2382
- [8] Berger, L., Koester, D., Napiwotzki, R., Reid, I., & Zuckerman, B. 2005, A&A, 444, 565
- [9] Bergeron, P., Fontaine, G., Lacombe, P., et al. 1984, AJ, 89, 374
- [10] Bergeron, P., Wesemael, F., Fontaine, G., & Liebert, J. 1990a, ApJ, 351, 21
- [11] Bergeron, P., Liebert, J., Greenstein, J. L. 1990b, ApJ, 361, 190
- [12] Bergeron, P., Saffer, R. A., & Liebert, J. 1992, ApJ, 443, 735
- [13] Bergeron, P., Liebert, J. & Fulbright, M. S. 1995, ApJ, 444, 810
- [14] Bergeron, P., Ruiz, M. T., & Leggett, S. K. 1997, ApJS, 108, 339
- [15] Bergeron, P., Wesemael, F., Saffer, R. A. 2000, PASP, 112, 837
- [16] Bergeron, P., Leggett, S. K., Ruiz, M. T. 2001, ApJS, 133, 413
- [17] Bergeron, P., Fontaine, G., Billères, M., et al. 2004, ApJ, 600, 404
- [18] Bertin, E., & Arnouts, S. 1996, A&AS, 117, 393
- [19] Bessell, M. S. 1979, PASP, 91, 589
- [20] Branch, D., Livio, M., Yungelson, L. R., et al. 1995, PASP, 107, 1019

- [21] Castanheira, B. G., Kepler, S. O., Mullally, F., et al. 2006b, *A&A*, 450, 227
- [22] Castanheira, B. G., Kepler, S. O., Handler, G., & Koester, D. 2006a, *ArXiv Astrophysics e-prints*, arXiv:astro-ph/0602169
- [23] Christlieb, N., Wisotzki, L., Reimers, D., et al. 2001, *A&A*, 366, 898
- [24] Cordes, O. 2005, Dissertation, Univ. Bonn
- [25] Crawford, D. L., & Mander, J. 1966, *AJ*, 71, 114
- [26] Dolez, N., Vauclair, G., Kleinman, S. J., et al. 2006, *A&A*, 446, 237
- [27] Eisenstein, D. J., Liebert, J., Koester, D., et al. 2006, in preparation
- [28] Fey, W., & Bues, I. 1995, *AGAb*, 11, 168
- [29] Finley, D. S., Koester, D., & Basri, G. 1997, *ApJ*, 488, 375
- [30] Fontaine, G., Bergeron, P., Billères, M., & Charpinet, S. 2003, *ApJ*, 591, 1184
- [31] Friedrich, S., Koester, D., Christlieb, N., Reimers, D., & Wisotzki, L. 2000, *A&A*, 363, 1040
- [32] Gianninas, A., Bergeron, P., & Fontaine, G. 2005, *ApJ*, 631, 1100
- [33] Giovannini, O., da Costa, A. F. M., Castanheira, B. G., & Kepler, S. O. 2005, in *ASP Conf. Ser. 334, 14th European Workshop on White Dwarfs*, ed. D. Koester & S. Moehler, 89
- [34] Green, R., Schmidt, M., & Liebert, J. 1986, *ApJS*, 61, 305
- [35] Greenstein, J. L. 1984, *AJ*, 276, 602
- [36] Greenstein, J. L., Liebert, J. W. 1990, *ApJ*, 360, 662
- [37] Hagen, H.-J., Groote, D., Engels, D., & Reimers, D. 1995, *A&AS*, 111, 195
- [38] Heber, U., Napiwotzki, R., Lemke, M., & Edelmann, H. 1997, *A&A*, 324, 53
- [39] Homeier, D., Koester, D., Hagen, H.-J., et al. 1998, *A&A*, 338, 563
- [40] Homeier, D. 2001, Dissertation, Univ. Kiel
- [41] Iben, I., & Tutukov, A. V. 1984, *ApJS*, 54, 335
- [42] Iben, I., & Tutukov, A. V. 1986, *ApJ*, 311, 742
- [43] Johnson, H. L., & Morgan, W. W. 1953, *ApJ*, 117, 353
- [44] Karl, C. A., Napiwotzki, R., Nelemans, G., et al. 2003, *A&A*, 410, 663
- [45] Karl, C. A., Heber, U., & Napiwotzki, R. 2005, in *ASP Conf. Ser. 334, 14th European Workshop on White Dwarfs*, ed. D. Koester & S. Moehler, 369

- [46] Kepler, S. O., Giovannini, O., Kanaan, A., Wood, M. A., & Claver, C. F. 1995, *BaltA*, 4, 157
- [47] Kepler, S. O., Robinson, E. L., Koester, D., et al. 2000, *ApJ*, 539, 379
- [48] Kepler, S. O., Costa, J.E.S, Castanheira, B. G., et al. 2005a, *AJ*, 634, 1311
- [49] Kepler, S. O., Castanheira, B. G., Saraiva, M. F. O., et al. 2005b, *A&A*, 442, 629
- [50] Kilkeny, D. 1986, *Obs.*, 106, 201
- [51] Kilkeny, D., Heber, U., & Drilling, J. S. 1988, *South Afr. Astron. Obs. Circ.*, 12, 1-80
- [52] Kilkeny, D., O'Donoghue, D., Koen, C., Stobie, R. S., & Chen, A. 1997b, *MNRAS*, 287, 867
- [53] Kleinman, S.J. 1999, in *ASP Conf. Ser. 169*, 11th European Workshop on White Dwarfs, ed. J.-E. Solheim & E. G. Meistas, 116
- [54] Kleinman, S. J., Harris, H. C., Eisenstein, D., J., et al. 2004, *ApJ*, 607, 426
- [55] Koester, D., Schulz, H., & Weidemann, V. 1979, *A&A*, 76, 262
- [56] Koester, D., Allard, N. F., & Vauclair G. 1994, *A&A*, 291, L9
- [57] Koester, D., & Vauclair, G. 1997, in *Proceedings of the tenth European Workshop on White Dwarfs*, ed. J. Isern, M. Hernandez & E. Garcia-Berro, Kluwer Academic Publisher, 429
- [58] Koester, D., Dreizler, S., Weidemann, V., & Allard, N. F. 1998, *A&A*, 338,612
- [59] Koester, D., Napiwotzki, R., Christlieb, N., et al. 2001, *A&A*, 378, 556
- [60] Koester, D., Rollenhagen, K., Napiwotzki, R., et al. 2005a, *A&A*, 432, 1025
- [61] Koester, D., Napiwotzki, R., Voss, B., et al. 2005b, *A&A*, 439, 317
- [62] Lamontagne, R., Demers, S., Wesemael, F., Fontaine, G., & Irwin, M. J. 2000, *AJ*, 119, 241
- [63] Liebert, J., Schmidt, G. D., Sion, E. M., et al. 1985, *PASP*, 97, 158
- [64] Liebert, J., Bergeron, P., Schmidt, G. D., & Saffer, R. A. 1993, *ApJ*, 418, 426
- [65] Liebert, J., Bergeron, P., & Holberg, J. B. 2003, *AJ*, 125, 348
- [66] Liebert, J., Bergeron, P., & Holberg, J. B. 2005, *ApJS*, 156, 47
- [67] Lisker, T., Heber, U., Napiwotzki, R., et al. 2005, *A&A*, 430, 223
- [68] Madej, J., Nalezyty, M., & Althaus, L. G. 2004, *A&A*, 419, 5

- [69] Marsh, M. C., Barstow, M. A., Buckley, D. A., et al. 1997, *MNRAS*, 286, 369
- [70] Maxted, P. F. L., Ferrario, L., Marsh, T. R., & Wickramasinghe, D. T. 2000, *MNRAS*, 315, 41
- [71] McCook, G. P., & Sion, E. M. 1999, *ApJS*, 121, 1
- [72] Morales-Rueda, L., Marsh, T. R., Maxted, P. F. L., et al. 2005, *MNRAS*, 359, 648
- [73] Mukadam, A. S., Mullally, F., Nather, R. E., et al. 2004a, *ApJ*, 607, 982
- [74] Mukadam, A. S., Winget, D. E., von Hippel, T., et al. 2004b, *ApJ*, 612, 1052
- [75] Mullally, F., Thompson, S. E., Castanheira, B. G., et al. 2005, *ApJ*, 625, 966
- [76] Napiwotzki, R., Green, P. J., & Saffer, R. A. 1999, *ApJ*, 517, 399
- [77] Napiwotzki, R., Edelmann, H., Heber, U., et al. 2001, *A&A*, 378, 17
- [78] Napiwotzki, R., Koester, D., Nelemans, G., et al. 2002, *A&A*, 378, 17
- [79] Napiwotzki, R., Christlieb, N., Drechsel, H., et al. 2003, *ESO Msngr.*, 112, 25
- [80] Napiwotzki, R., Karl, C. A., Lisker, T., et al. 2004, *Ap&SS*, 291, 321
- [81] Napiwotzki, R., Karl, C. A., Nelemans, G., et al. 2005, in *ASP Conf. Ser. 334*, 14th European Workshop on White Dwarfs, ed. D. Koester & S. Moehler, 375
- [82] Nather, R. E. 1978, *PASP*, 90, 477
- [83] Nather, R. E., Winget, D. E., Clemens, J. C., Hansen, C. J., & Hine, B. P. 1990, *ApJ*, 361, 309
- [84] Nelemans, G., Napiwotzki, R., Karl, C. A., et al. 2005, *A&A*, 440, 1087
- [85] Østensen, R., & Solheim, J.-E. 2000, *BaltA*, 9, 411
- [86] Oswald, T. D., Sion, E. M., Hammond, G., et al. 1991, *AJ*, 101, 583
- [87] Pech, D., Vauclair, G., & Dolez, N. 2006, *A&A*, 446, 223
- [88] Perlmutter, S., Aldering, G., Goldhaber, G., et al. 1999, *ApJ*, 517, 565
- [89] Pauli, E.-M., Napiwotzki, R., Altmann, M., et al. 2003, *A&A*, 400, 877
- [90] Press, W. H., Teukolsky, S. A., Vetterling, W. T., & Flannery, B. P. 1992, *Numerical Recipes*, second edition, The Press Syndicate of the University of Cambridge, Cambridge, New York, Melbourne
- [91] Putney, A. 1997, *ApJS*, 112, 527
- [92] Reimers, D., Jordan, S., Koester, D., et al. 1996, 311, 572
- [93] Riess, A. G., Nugent, P. E., Gilliland, R. L., et al. 2001, *ApJ*, 560, 49

- [94] Robinson, E. L., Nather, R. E., & McGraw, J. T. 1976, *ApJ*, 210, 211
- [95] Schmidt, G. D., Vennes, S., Wickramasinghe, D. T., Ferrario, L. 2001, *MNRAS*, 328, 203
- [96] Sefako, R. R., Glass, I. S., Kilkenny, D., et al. 1999, *MNRAS*, 309, 1043
- [97] Sion, E. M., Greenstein, J. L., Landstreet, J. D., et al. 1983, *ApJ*, 269, 253
- [98] Silvestri, N. M., Oswalt, T. D., Wood, M. A., et al. 2001, *AJ*, 121, 503
- [99] Silvotti, R., Voss, B., Bruni, I., et al. 2005, *A&A*, 443, 195
- [100] Ströer, A., Heber, U., Lisker, T., et al. 2005, in *ASP Conf. Ser. 334, 14th European Workshop on White Dwarfs*, ed. D. Koester & S. Moehler, 309
- [101] Ströer, A., Heber, U., Lisker, T., et al. 2006, in preparation
- [102] Strömgren, B. 1963, *QJRAS*, 4, 8
- [103] Stys, D., Slevinsky, R., Sion, E. M., et al. 2000, *PASP*, 112, 354
- [104] Surmelian, G. L., & O'Connell, R. E. 1974, *AJ*, 193, 705
- [105] Tonry, J. L., Schmidt, B. P., Barris, B., et al. 2003, *ApJ*, 594, 1
- [106] Unsöld, A., & Baschek, B. 2002, *Der neue Kosmos, 7. Auflage*, Springer Verlag, Berlin, Heidelberg, New York
- [107] Vennes, S. 1992, *ApJ*, 390, 590
- [108] Vennes, S., Thejll, P. A., Wickramasinghe, D. T., & Bessell, M. S. 1996, *ApJ*, 467, 782
- [109] Vennes, S., Korpela, E., & Bowyer, S. 1997a, *AJ*, 114, 1567
- [110] Vennes, S., Thejll, P. A., Genova Galvan, R., & Dupuis, J. 1997b, *ApJ*, 480, 714
- [111] Vennes, S. 1999, *ApJ*, 525, 995
- [112] Voss, B., Koester, D., Østensen, R., et al. 2006, *A&A*, 450, 1061
- [113] Webbink, R. F. 1984, *ApJ*, 277, 355
- [114] Weidemann, V., & Koester, D. 1984, *A&A*, 132, 195
- [115] Weidemann, V., & Koester, D. 1995, *A&A*, 297, 216
- [116] Wegner, G. 1983, *AJ*, 88, 1
- [117] Wegner, G., & Nelan, E. P. 1987, *ApJ*, 319, 916
- [118] Wegner, G., & Dupuis 1993, *AJ*, 106, 390

- [119] Werner, K., Wolff, B., Pakull, M. W., et al. 1996, in Proc. Int. Workshop “Supersoft X-ray Sources”, 472, ed. J. Greiner, 131
- [120] Werner, K., Rauch, T., Napiwotzki, R., et al. 2004, A&A, 424, 657
- [121] Wesemael, F., Greenstein, J. L., Liebert, J., et al. 1993, PASP, 105, 761
- [122] Wesemael, F., Bergeron, P., Lamontagne, R., et al. 1994, ApJ, 429, 369
- [123] Whelan, J., & Iben, I. 1973, ApJ, 186, 1007
- [124] Wood, M. A. 1995, in White Dwarfs, Proceedings of the 9th European Workshop on White Dwarfs Held at Kiel, Germany. Lecture Notes in Physics, ed. D. Koester & K. Werner (Springer-Verlag, Berlin, Heidelberg, New York), Vol. 443, p.41
- [125] Wisotzki, L., Koehler, T., Groote, D., & Reimers, D. 1996, A&AS, 115, 227
- [126] Zuckerman, B., Koester, D., Reid, I. N., & Hünsch, M. 2003, ApJ, 596, 477

Acknowledgements

In the first place I have to thank Detlev Koester for offering me the possibility of preparing this thesis, and for his support during the work. I thank Gerard Vauclair and Michel Chevreton for the help in preparing and conducting the observations at Observatoire Haute-Provence, as well as Roy Østensen for supporting me in the preparation of the observations at the Nordic Optical Telescope. My thanks are due to Roberto Silvotti, Barbara G. Castanheira, and Kepler de Souza Oliveira Filho for the independent observations of the candidate ZZ Ceti stars that I forwarded to them.

I also would like to thank Derek Homeier, Ralf Napiwotzki and Uli Heber for helpful discussions about different aspects of the Calar Alto observations and the SPY analysis, as well as Matthias Hünsch, Sabine Möhler, Stefan Jordan and all other current and former members of the stellar astrophysics working group in Kiel for their support and their helpful comments during the last years.

My thanks are furthermore due to all colleagues at the institute for providing the very pleasant working atmosphere, and especially to our system administrator Holger Boll who on a regular basis provided solutions for seemingly unsolvable technical problems.

I thank the Deutsche Forschungsgemeinschaft for supporting my work financially under grant number KO 738/21-2, KO 738/22-1, and KO 738/23-1, as well for financial travel support that made the observations at Calar Alto possible. In the same way I am grateful for financial support in the framework of the OPTICON program that enabled the access and travel to Observatoire Haute-Provence and to the Nordic Optical Telescope.

Finally, my warmest thanks go to my family for the continuous support over all the years.

Lebenslauf

Name: Björn Voss
geboren: 07.10.1976 in Lübeck
Familienstand: ledig
Staatsangehörigkeit: deutsch

Schulbildung: 1983 - 1987 Grund- und Hauptschule Zarpen
1987 - 1996 Carl-Jacob-Burckhardt-Gymnasium Lübeck
1996 Abitur mit den Prüfungsfächern:
Mathematik, Biologie, Englisch und Geschichte

Studium: WS96/97 Immatrikulation im Fach Physik
an der Christian-Albrechts-Universität zu Kiel

WS98/99 Vordiplom mit Nebenfach Informatik
SS01 Diplom-Hauptprüfung mit Nebenfach Informatik

SS01-SS02 Anfertigung der Diplomarbeit "Untersuchung alter of-
fener Sternhaufen mittels Mosaikdaten-Photometrie"
am Institut für Theoretische Physik und Astrophysik der
Christian-Albrechts-Universität zu Kiel

SS02-SS06 Promotion am Institut für Theoretische Physik und As-
trophysik der Christian-Albrechts-Universität zu Kiel

Erklärung

Diese Arbeit wurde von mir nach Inhalt und Form nur unter Zuhilfenahme der angegebenen Hilfsmittel unter Anleitung von Prof. Dr. D. Koester angefertigt. Sie wurde noch nicht an anderer Stelle ganz oder zum Teil im Rahmen eines Prüfungsverfahrens vorgelegt.

Kiel, 30. Mai 2006